Theory of van der Waals materials

from interband coherence to moiré butterflies

Dissertation

zur Erlangung des Grades eines
Doktors der Naturwissenschaften

am Fachbereich Physik der Freien Universität Berlin

vorgelegt von

Kryštof Kolář

Berlin, 2024

Erstgutachter: Prof. Felix von Oppen, PhD
Zweitgutachter: Prof. Dr. Piet W. Brouwer

Tag der Abgabe: 18. Dezember 2024
Tag der Disputation: 24. Februar 2025

Selbstständigkeitserklärung

Name: Kolář
Vorname: Kryštof

Ich erkläre gegenüber der Freien Universität Berlin, dass ich die vorliegende Dissertation selbstständig und ohne Benutzung anderer als der angegebenen Quellen und Hilfsmittel angefertigt habe. Die vorliegende Arbeit ist frei von Plagiaten. Alle Ausführungen, die wörtlich oder inhaltlich aus anderen Schriften entnommen sind, habe ich als solche kenntlich gemacht. Diese Dissertation wurde in gleicher oder ähnlicher Form noch in keinem früheren Promotionsverfahren eingereicht.

Mit einer Prüfung meiner Arbeit durch ein Plagiatsprüfungsprogramm erkläre ich mich einverstanden.

Datum: **Unterschrift**:

Kurzfassung

Das Aufkommen zweidimensionaler Schichtmaterialien brachte das enorme Potenzial mit sich, einstellbare korrelierte Phasen von Materie zu realisieren. Diese Arbeit beschäftigt sich mit der vielfältigen Physik dieser Materialien und konzentriert sich dabei auf Plattformen auf Basis von Graphen und Übergangsmetall-Dichalkogeniden, die in den letzten Jahren bemerkenswerte Fortschritte erfahren haben. Zu den Hauptthemen zählen Interbandkohärenz, Moiré Physik und Elektrostatik.

Als erstes Beispiel betrachtet diese Arbeit geschichtete Materialien als Plattform zur Realisierung von Exzitonenkondensaten, bei denen Elektron-Loch-Paare spontan und kohärent kondensieren. Es wird gezeigt, wie Rastertunnelmikroskopie genutzt werden kann, um die Interbandkohärenz der Exzitonenkondensaten in diesen Materialien zu untersuchen.

Als besonders erfolgreich hat sich das Paradigma des Stapelns und Verdrehens von Materialschichten erwiesen, wodurch ein langwelliges Moiré-Muster und, unter bestimmten Bedingungen, flache Bänder entstehen. Das beste Beispiel hierfür ist Twisted Bilayer-Graphen beim magischen Winkel, das korrelierte Isolatorphasen und Supraleitung aufweist, obwohl eine einzelne Graphenschicht keines von beiden zeigt. Der theoretische Hauptkandidat für den Grundzustand in der Isolatorphase von Twisted Bilayer-Graphen ist der Kramers Intervalley-Coherent Zustand, der einem Exzitonenkondensat ähnelt. In dieser Arbeit zeigen wir, dass dieser Zustand einzigartig vor bestimmten Arten von Störungen durch ein Analogon des Anderson-Theorems geschützt ist.

Über zwei Schichten hinausgehend wurde kürzlich gezeigt, dass verdrehte N-Schicht-Graphen Moiré-Strukturen eine robuste Supraleitung aufweisen, die der von Twisted Bilayer-Graphen ähnelt. Für $N = 4$ und $N = 5$ weist das Phasendiagramm eine robuste supraleitende Tasche auf, die über die vollständige Füllung der flachen Bänder hinausgeht, was ein experimentelles Rätsel darstellt. In dieser Arbeit zeigen wir, wie eine sorgfältige Berücksichtigung der dreidimensionalen Natur des Systems dieses Rätsel auf natürliche Weise erklärt. Ein wichtiges Merkmal geschichteter Materialien ist die Möglichkeit, ihre Dotierung n und das elektrische Verschiebungsfeld D durch Anpassung der oberen und unteren Gate-Spannungen zu steuern, wobei n und D durch lineare Kombinationen der Gate-Spannungen gegeben sind. Während typischerweise angenommen wird, dass die Systemeigenschaften hauptsächlich durch D gesteuert werden, haben neuere Experimente an Graphen-Mehrschichten Eigenschaften gezeigt, die offenbar nur auf eine einzelne Gate-Spannung empfindlich reagieren. Diese Eigenschaften werden im Rahmen dieser Arbeit erklärt.

Das langwellige Moiré-Muster weist eine vergrößerte Einheitszelle auf, und im letzten Teil dieser Arbeit untersuchen wir zwei Konsequenzen daraus. Erstens untersuchen wir die Realraum-Texturen von Wellenfunktionen in Moiré-Systemen, die aufgrund ihrer großen Einheitszelle in lokalen Tunnelexperimenten beobachtbar sind. Zweitens analysieren wir die Wirkung eines Magnetfelds in verdrehten Doppelschicht-Übergangsmetall-Dichalkogeniden, bei denen die große Einheitszelle den Zugang zum sogenannten Hofstadter-Regime ermöglicht.

Abstract

The advent of two-dimensional van der Waals materials brought with it the remarkable potential to realize tunable correlated phases of matter. This thesis delves into the rich physics of these materials, focusing on platforms based on graphene and transition metal dichalcogenides, which have experienced significant progress in recent years. The main themes include interband coherence, moiré physics, and electrostatics.

As a first example, this thesis considers layered materials as a platform to realize exciton condensates, in which electron-hole pairs spontaneously and coherently condense. Characterized by interband coherence, we demonstrate how the exciton condensate phase can be probed using scanning tunneling microscopy.

The paradigm of stacking and twisting layers of materials has been remarkably successful, forming a long-wavelength moiré pattern and producing flat bands under certain conditions. The prime example is magic angle twisted bilayer graphene, which hosts correlated insulating and superconducting phases, even though a single graphene layer does not show either phase. The prime theoretical candidate ground state for the correlated insulators in twisted bilayer graphene is the Kramers intervalley coherent state, which is analogous to an exciton condensate. In this thesis, we find that this state is uniquely protected from certain types of disorder by an analog of Anderson's theorem.

Going beyond bilayers, twisted N-layer graphene moiré structures have recently been shown to exhibit robust superconductivity similar to twisted bilayer graphene. For $N = 4$ and $N = 5$, the phase diagram features a robust superconducting pocket extending beyond full filling of the flat bands, presenting an experimental puzzle. We show in this thesis, how a careful consideration of the three-dimensional nature of the devices, particularly by taking into account out-of-plane electric fields, naturally explains this puzzle. An important feature of layered materials is the ability to control their charge doping, n, and electric displacement field, D, by adjusting top and bottom gate voltages, where n and D are given by linear combinations of the gate voltages. While typically, system properties are assumed to be primarily tuned by D, recent experiments on graphene multilayers revealed features seemingly sensitive only to a single gate voltage. As part of this thesis, we explain these features.

The long-wavelength moiré pattern features an enlarged unit cell, and in the last part of this thesis, we explore two surprising consequences of this. Firstly, we study the real-space textures of wavefunctions in moiré systems, which, due to their large unit cell, are experimentally observable in local tunneling experiments. Secondly, we explore the effect of magnetic field on the topological bands in twisted bilayer transition metal dichalcogenides, where the large unit cell enables access to the so-called Hofstadter regime. We find that the effect of external magnetic field is most dramatic when it "cancels" the effective field arising due to the band topology. Remarkably, for zero-field bands that resemble Landau levels, cancelling the effective field by an external magnetic flux recovers a nearly-free parabolic dispersion.

List of publications

This thesis is based on the following peer-reviewed and published articles.

- Gal Shavit, Kryštof Kolář, Christophe Mora, Felix von Oppen, and Yuval Oreg
  Strain disorder and gapless intervalley coherent phase in twisted bilayer graphene
  Phys. Rev. B 107, L081403 [1]
  https://doi.org/10.1103/PhysRevB.107.L081403
  Section 4.5 of Chapter 4 is based on this work.

- Kryštof Kolář, Gal Shavit, Christophe Mora, Yuval Oreg, and Felix von Oppen,
  Anderson's Theorem for Correlated Insulating States in Twisted Bilayer Graphene
  Phys. Rev. Lett. 130, 076204 [2]
  https://doi.org/10.1103/PhysRevLett.130.076204
  Most of Chapter 4 is based on this work.

- Kryštof Kolář, Yiran Zhang, Stevan Nadj-Perge, Felix von Oppen, and Cyprian Lewandowski
  Electrostatic fate of N-layer moiré graphene
  Phys. Rev. B 108, 195148 [3]
  https://doi.org/10.1103/PhysRevB.108.195148
  Chapter 5 is based on this work.

- Kryštof Kolář, Kang Yang, Christophe Mora, Felix von Oppen
  Hofstadter spectrum of Chern bands in twisted transition metal dichalcogenides
  Phys. Rev. B 110, 115114 [4]
  https://doi.org/10.1103/PhysRevB.110.115114
  Chapter 8 is based on this work.

Additionally, the following articles in preparation are based on work described in this thesis.

- Kryštof Kolář, Felix von Oppen
  Tunneling signatures of interband coherence in exciton condensates
  in preparation [5]
  This publication will contain the results of Chapter 3.

- Kryštof Kolář, Dacen Waters, Joshua Folk, Matthew Yankowitz, and Cyprian Lewandowski,
  The rise of single-gate behavior in Bernal-terminated graphene multilayers
  in preparation [6]
  This publication will contain the results of Chapter 6.

- Kryštof Kolář, Kang Yang, Felix von Oppen, Christophe Mora
  Real-space topology of wavefunctions and absence thereof
  in preparation [7]
  This publication will contain the results of Chapter 7.

Contents

1 Introduction

The experimental realization of an atomically thin monolayer in the form of graphene [8] ignited a transformative era in condensed matter physics [9]. Graphene made it possible to study Dirac particles on a tabletop [10], with carrier density that could be tuned simply by tuning the volatage on a nearby gate. Graphene multilayers also proved interesting. They occur in two forms: in the natural Bernal stacking, and in the metastable rhombohedral stacking. Importantly, in addition to filling fraction, multilayers offered the additional tunability afforded in doubly gated setups by varying the difference between the gate voltages [11–13], effectively tuning the displacement field in the sample. For trilayers and beyond, rhombohedral stacking proved particularly interesting due to the emergence of extremely high density of states [11, 14–16], leading to flat surface states in the infinite layer limit [17].

However, already for bilayers, there is a fascinating possibility of stacking two monolayers at a small angle offset that has led to profoundly rich physics. In this case, interference of the lattices of the two layers creates a beating, or moiré, pattern in real space, significantly enlarging the original unit cell. Importantly, as predicted in seminal works [18, 19], the electronic bands in such devices, denoted twisted bilayer graphene (TBG), undergo significant flattening near the so-called "magic" angle of $\theta = 1.1^\circ$, amplifying electron-electron interactions. However, achieving this precise twist angle was a major experimental challenge, accomplished eventually by Pablo Jarillo-Herrero's group, with groundbreaking discoveries of superconductivity, first in graphene-based systems, and correlated insulating behavior [20, 21]. These findings took the condensed matter community by storm, not least because of the similarity of the phase diagram of twisted bilayer graphene to that of high-temperature superconductors. The initial findings [20, 21] were soon reproduced by other groups and provided more information on the physics of twisted bilayer graphene [22–30], but also pointed towards strong device dependence arising from twist angle and strain uncertainties. Beyond twisted bilayer graphene, experimentalists have also explored other possibilities of twisting and stacking graphene layes, leading to new exciting platforms. For example, in alternating twisted graphene multilayers [23, 31–34], a flat band twisted bilayer graphene-like sector coexists with other, more dispersive sectors. Another example is helical trilayer graphene [35], in which two moiré patterns coexist and relax into macroscopic domains. We also mention twisted double bilayer graphene [36–38], which features strongly correlated topological insulating phases.

A few years after the succesful experimental realization of graphene, the successful exfoliation of monolayers of transition metal dichalcogenides (TMDs) marked another major milestone [39]. Unlike graphene, TMDs, such as $MoTe_2$, WSe_2, and WTe_2, are a family of semiconductors

with strong spin-orbit coupling and diverse electronic properties. Given the absence of free carriers, the community was particularly interested in their optical properties [40, 41], which are dominated by transitions involving excitons, bound states of electrons and holes, as in two-dimensional materials the exciton binding energy is enhanced compared to bulk materials.

Thanks to their remarkable excitonic properties, TMD layers provided a deep material push to the effort to find an exciton condensate [42–44], an elusive state of matter in which excitons spontaneously condense in a coherent fashion [45–48]. Furthermore, TMD layers allowed the possibility to engineer bilayer structures with an insulating spacer [49–51], which allow the spatial separation of electrons and holes, as originally proposed for double quantum wells. Compared to these quantum wells, however, TMD bilayers offer greater tunability, allowing interlayer electric field and interlayer bias to be varied at will.

Inspired by the success of twisted bilayer graphene, researchers extended the twisting and stacking paradigm to transition metal dichalcogenides. Compared to twisted bilayer graphene, TMDs have the additional possibly of stacking different material layers, leading to so-called heterobilayers. Interestingly, for heterobilayers, a moiré (beating) pattern emerges already at zero twist angle, arising due to the differing lattice constant of the two constituent layers. This proposal has been the subject of some very interesting experiments, exhibiting the first example of the quantum anomalous Hall effect without magnetic doping [52, 53], as well as simulating the famous Hubbard model [54]. Twisted homobilayer TMDs, consisting of the same underlying TMD, have arguably proven even more remarkable. Following the theoretical prediction of flat and detached topological bands [55], experiments on twisted TMD bilayers showed Mott insulating phases [56], superconductivity [57, 58], quantum criticality [59], and, most remarkably, the integer and fractional quantum anomalous Hall effects [60–64]. Very recently, experiments on twisted TMD bilayers suggested a fractional quantum spin Hall effect of holes [65] and appeared to feature multiple flat bands of equal Chern number in a given valley [65, 66], resembling Landau levels.

Motivated by these remarkable discoveries, in this thesis, we delve into the world of layered materials, with a focus on moiré systems. Figure 1.1 presents a schematic diagram of the topics covered and some of the connections between them. We begin by introducing moiré models and deriving the continuum models for twisted bilayer graphene and twisted bilayer transition metal dichalcogenides in Chapter 2.

In the following Chapter 3, we focus on one of the conceptually simplest proposals, that of an exciton condensate phase in monolayer and bilayer systems, primarily composed out of transition metal dichalcogenides. We exploit the fact that in these systems, surface probes can in fact probe bulk properties, by virtue of their two-dimensional nature. A natural such probe is scanning tunneling microscopy (STM). We show how STM can be used to extract vital properties of the exciton condensate phase both for monolayer and bilayer condensates. For monolayers, we find that coherent exciton condensation manifests in interband coherence, which can be probed by STM. In bilayers, although interband coherence between layers does not manifest directly in STM, the presence of excitons can be inferred from an additional tunneling peak.

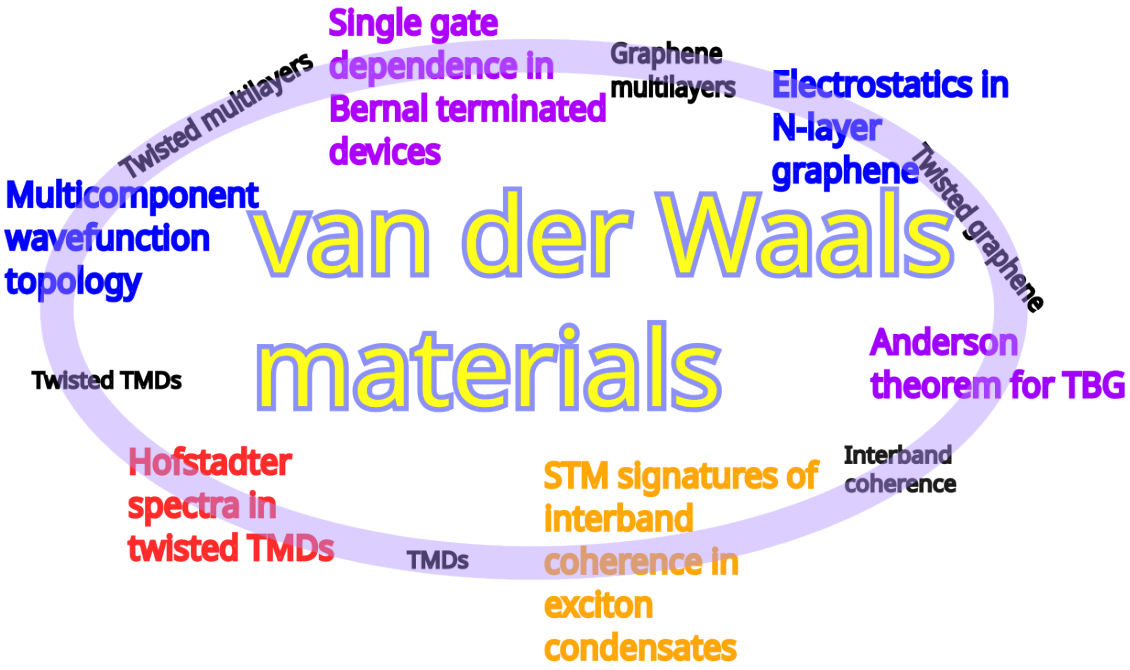

Figure 1.1: Schematic showing the six parts of this thesis and their primary connections

The next Chapter 4 builds on interband coherence, but this time in the context of moiré systems. In particular, it studies the effects of disorder on interband coherence in twisted bilayer graphene. We find that a prime candidate state, the Kramers intervalley coherent state is directly analogous to an s-wave superconductor, and derive a corresponding Anderson theorem for this state.

In the following Chapter 5, we consider the addition of multiple layers, focusing on structures with an alternating arrangement of twist angles. These arrangements exhibit similar physics to twisted bilayer graphene, but feature higher magic angles, facilitating experimental realization. Surprisingly, while superconductivity in twisted bilayer graphene typically vanishes when more than three charge carriers per unit cell are present, in twisted pentalayer graphene, it persists up to five carriers per unit cell. In Chapter 5, we resolve this discrepancy using electrostatics and a powerful insight regarding vertical distributions of charges.

The next Chapter 6 moves to a different class of moiré systems from the graphene family. These involve Bernal or rhombohedrally stacked graphene layers, such as twisted double bilayer graphene and rhombohedral pentalayer graphene aligned with hexagonal boron nitride (hBN). Exhibiting a plethora of interesting correlated phases, these systems have recently attracted great experimental interest [16, 36–38, 67]. One experimental mystery present in these diverse devices was the presence of diagonal features in the filling-displacement field plane, apparently tuned by a single gate only. In Chapter 6, we explain this feature for both twisted double bilayer graphene

and rhombohedral pentalayer graphene, pointing to its origin in the local Bernal stacking commont to both systems.

In the next Chapter 7, we study the real-space properties of multi-component wavefunctions, relevant both to twisted graphene devices and to twisted bilayer transition metal dichalcogenides, forming a natural bridge between the two main platforms of this thesis. Defining a real-space Chern number, we find that it can only be non-trivial for wavefunctions with zeroes in the unit cell, a situation which naturally occurs in the chiral limit of twisted bilayer graphene, as well as the adiabatic limit of twisted bilayer transition metal dichalcogenides.

In the final Chapter 8, we zoom in on twisted bilayer TMDs, investigating their behavior under large external magnetic fields, and completing the circle of Figure 1.1. A unique feature of moiré systems is that their large unit cells allow for the experimental realization of the Hofstadter regime, where magnetic fluxes on the order of a flux quantum thread each unit cell. Our most notable finding is that, counterintuitively, the bands of twisted bilayer TMDs can simplify under an applied magnetic field. In particular, we find that when minus one flux quantum is threaded per unit cell, topological flat bands turn into nearly-free parabolic bands.

2 Background

In this Chapter, we introduce the continuum models of moiré systems that form the backbone of much of this thesis.

2.1 Principles of construction of a moiré Hamiltonian for twisted structures

Consider a monolayer system with a basis of lattice vectors $\mathbf{c}_1, \mathbf{c}_2$ forming a triangular lattice, and a single layer Bloch Hamiltonian $\mathrm{H}_{\text{mono}}(\mathbf{k})$. The first step to construct a Hamiltonian for a twisted bilayer is to consider how a single layer is affected upon twisting. Under a rigid rotation by angle θ, implemented in real space by a rotation matrix

$$R(\theta) = \begin{pmatrix} \cos\theta & -\sin\theta \\ \sin\theta & \cos\theta \end{pmatrix}, \tag{2.1}$$

the single-particle Hamiltonian of the rotated system also rotates as

$$\mathrm{H}^{\theta}_{\text{mono}}(\mathbf{k}) = \mathrm{H}_{\text{mono}}(R(\theta)\mathbf{k}). \tag{2.2}$$

Let us now consider two layers stacked on top of each other and rotate the top layer by $\theta/2$ and the bottom layer by $-\theta/2$ with respect to the unrotated positions. Then, we have the following single particle Hamiltonians for the bottom and top layers:

$$\mathrm{H}^{b}_{\text{mono}}(\mathbf{k}) = \mathrm{H}^{-\theta/2}_{\text{mono}}(\mathbf{k}) \tag{2.3}$$
$$\mathrm{H}^{t}_{\text{mono}}(\mathbf{k}) = \mathrm{H}^{\theta/2}_{\text{mono}}(\mathbf{k}). \tag{2.4}$$

In addition, each layer $l = t, b$ will experience an effective potential and will be able to tunnel into the other layer. The continuum model can now be constructed by assuming that the effective potentials and tunneling only depend on the local relative displacement $\mathbf{d}(\mathbf{r})$ of the

top layer relative to the bottom layer. Then, we can write a general twisted bilayer continuum Hamiltonian

$$H_M = \begin{pmatrix} \mathrm{H}^b_{\mathrm{mono}}(\mathbf{k}) + V^b[\mathbf{d}(\mathbf{r})] & T[\mathbf{d}(\mathbf{r})] \\ T^\dagger[\mathbf{d}(\mathbf{r})] & \mathrm{H}^t_{\mathrm{mono}}(\mathbf{k}) + V^t[\mathbf{d}(\mathbf{r})] \end{pmatrix}, \tag{2.5}$$

where $V^{l=b/t}(\mathbf{d})$ are the potentials on the bottom/top layer and $T(\mathbf{d})$ is the tunneling term. An important property of the potentials and tunnelings is that changing the displacement $\mathbf{d}$ by a lattice vector should leave them invariant as follows:

$$V^l(\mathbf{d} + \mathbf{c}_1) = V^l(\mathbf{d} + \mathbf{c}_2) = V^l(\mathbf{d}) \tag{2.6}$$

$$T(\mathbf{d} + \mathbf{c}_1) = T(\mathbf{d} + \mathbf{c}_2) = T(\mathbf{d}). \tag{2.7}$$

For a twisted bilayer at twist angle θ, supposing we start at zero displacement, $\mathbf{d} = 0$ at $\mathbf{r} = 0$, the displacement of the top layer with respect to the bottom layer at position $\mathbf{r}$ is then

$$\mathbf{d}(\mathbf{r}) = [R(\theta) - 1]\mathbf{r}. \tag{2.8}$$

For simplicity, in what follows, we will make the small angle approximation

$$[R(\theta) - 1]\mathbf{r} \approx \theta \hat{z} \times \mathbf{r}, \tag{2.9}$$

with $\hat{z}$ the unit vector along the out-of-plane z-direction. This implies, that as functions of the real-space position, $\mathbf{r}$, the tunneling and layer potentials are in fact periodic under translations by the enlarged, moiré, lattice vectors:

$$\mathbf{a}_1 = -\frac{1}{\theta}\hat{z} \times \mathbf{c}_1 \tag{2.10}$$

$$\mathbf{a}_2 = -\frac{1}{\theta}\hat{z} \times \mathbf{c}_2. \tag{2.11}$$

This enlarged periodicity reflects real space beating (moiré) patterns, shown in Fig. 2.1a. The corresponding moiré reciprocal basis is

$$\mathbf{G}_1 = -\frac{1}{A_{\mathrm{UC}}}\hat{z} \times \mathbf{a}_2 \tag{2.12}$$

$$\mathbf{G}_2 = \frac{1}{A_{\mathrm{UC}}}\hat{z} \times \mathbf{a}_1, \tag{2.13}$$

where

$$A_{\mathrm{UC}} = |\mathbf{a}_1 \times \mathbf{a}_2| \tag{2.14}$$

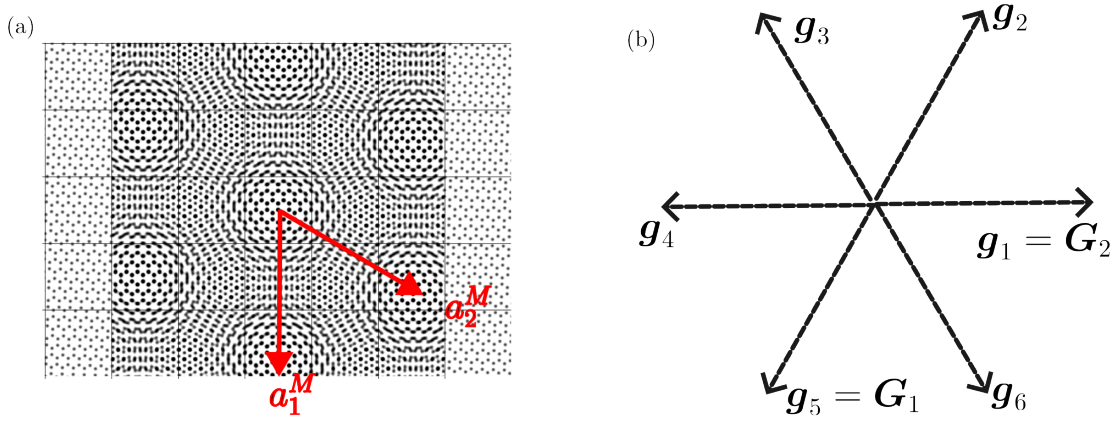

Figure 2.1: (a) The moiré pattern showing the moiré lattice vectors $\mathbf{a}_1$, $\mathbf{a}_2$. (b) Reciprocal space plot of the first shell reciprocal lattice moiré vectors $\mathbf{g}_1, \ldots, \mathbf{g}_6$.

is the moiré unit cell area. The moiré reciprocal basis satisfies

$$\mathbf{G}_i \cdot \mathbf{a}_j = 2\pi\delta_{ij}. \tag{2.15}$$

This emergent moiré periodicity allows us to expand the potentials and tunnelings in a Fourier expansion in the moiré lattice vectors $\mathbf{g}$, which are given as linear combinations of $\mathbf{G}_1$ and $\mathbf{G}_2$. In particular, we have:

$$V^l(\mathbf{r}) = \sum_{\mathbf{g}} V^l_{\mathbf{g}} e^{i\mathbf{g}\cdot\mathbf{r}} \tag{2.16}$$

$$T(\mathbf{r}) = \sum_{\mathbf{g}} T_{\mathbf{g}} e^{i\mathbf{g}\cdot\mathbf{r}}, \tag{2.17}$$

where typically one only considers elements to be nonzero for a finite set of $\mathbf{g}$ with small enough $\mathbf{g}$. In particular, most studies take $\mathbf{g}$ to lie in the first moiré reciprocal shell, satisfying $|\mathbf{g}| \leq |\mathbf{G}_1|$. In addition to the zero Fourier mode, $\mathbf{g} = 0$, there are six nonzero vectors in the first shell. We label these vectors as $\mathbf{g}_j$ for $j \in \{1, \ldots, 6\}$. $\mathbf{g}_1 \equiv \mathbf{G}_2 = (4\pi\theta/(\sqrt{3}a_0), 0)$, and $\mathbf{g}_j$ are defined as the $j-1$-th counterclockwise C_{6z} rotations of $\mathbf{g}_1$. We illustrate these basis vectors in Fig. 2.1b. Using the reciprocal lattice vectors, the moiré Brillouin zone can be constructed in the standard way.

Importantly, the values of the coefficients at different values of $\mathbf{g}$ are related by symmetries. In the following two Sections, we consider two typical twisted bilayer systems – twisted bilayer TMDs and twisted bilayer graphene, and construct their continuum Hamiltonians using their symmetries.

2.2 Twisted bilayer transition metal dichalcogenides

Transition metal dichalcogenides are semiconductors with strong spin-orbit coupling. The spin-valley locked active valleys for WSe_2 and $MoTe_2$ are at the K and K' points, which are at momenta $\boldsymbol{K} = (\frac{4\pi}{3a_0}, 0)$ and $\boldsymbol{K'} = (-\frac{4\pi}{3a_0}, 0)$ with a_0 the lattice constant. Since we can use time-reversal symmetry to relate the Hamiltonians in the two valleys, we focus on a K valley in what follows. In the K-valley, we have a parabolic dispersion with the following single-particle quadratic Hamiltonian

$$\mathrm{H}_{\text{mono}}(\mathbf{k}) = \frac{\hbar^2(\mathbf{k} - \boldsymbol{K})^2}{2m^*}, \tag{2.18}$$

where m^* is the effective mass in the effective mass approximation. Considering a bilayer, and applying rotations by $\pm\theta/2$ to the top and bottom layers, we obtain the top and bottom layer single-particle Hamiltonians

$$\mathrm{H}^b_{\text{mono}}(\mathbf{k}) = \frac{\hbar^2(\mathbf{k} - \boldsymbol{K^b})^2}{2m^*} \tag{2.19}$$

$$\mathrm{H}^t_{\text{mono}}(\mathbf{k}) = \frac{\hbar^2(\mathbf{k} - \boldsymbol{K^t})^2}{2m^*}, \tag{2.20}$$

where $\boldsymbol{K_b} = R(-\theta/2)\boldsymbol{K}$ is the position of the rotated bottom layer K-point and $\boldsymbol{K^t} = R(\theta/2)\boldsymbol{K}$ is the position of the K-point of the top layer. We plot the positions of the rotated K-points in Fig. 2.2a, together with the reciprocal vectors $\mathbf{g}_5, \mathbf{g}_6$.

Twisted bilayer TMDs are symmetric under three-fold rotations around the z-axis (C_{3z}), under time-reversal ($\mathcal{T}$), and under two-fold rotations around the y-axis (C_{2y}), which swaps the layers. To constrain the Hamiltonian in a single valley, only valley preserving symmetries are necessary. A convenient choice is C_{3z} and $C_{2y}\mathcal{T}$.

Consider first the symmetry constraints on the layer potentials, which are best obtained by considering the real space actions of symmetries. C_{3z} imposes that

$$V^l(\mathbf{r}) = V^l(C_{3z}\mathbf{r}), \tag{2.21}$$

which constrains the Fourier coefficients as follows:

$$V^l_{\mathbf{g}} = V^l_{C_{3z}\mathbf{g}}. \tag{2.22}$$

The reality of $V^l(\mathbf{r})$ implies that

$$V^l_{\mathbf{g}} = (V^l_{-\mathbf{g}})^*. \tag{2.23}$$

Finally, $C_{2y}\mathcal{T}$ gives the following constraint

$$V^t(x, y) = V^b(-x, y), \tag{2.24}$$

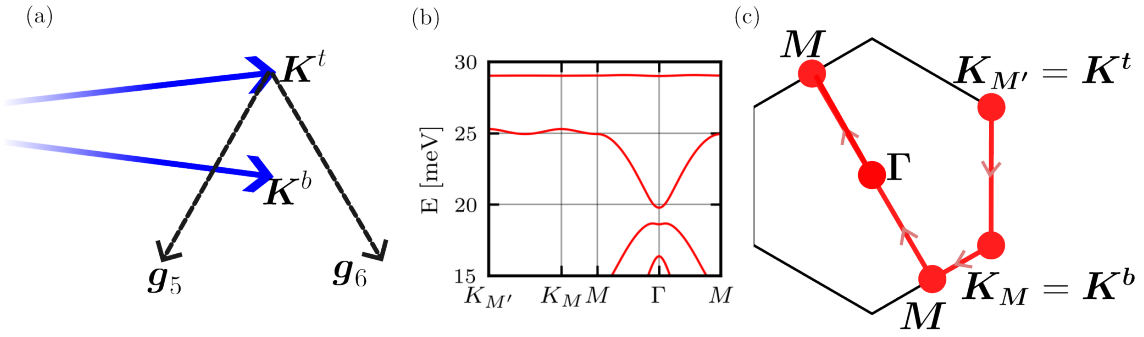

Figure 2.2: (a) Illustration of the rotated top and bottom layer K-points, together with the two reciprocal vectors $\mathbf{g}_5, \mathbf{g}_6$, which are relevant for interlayer tunneling. (b) Band structure plot for twisted bilayer WSe_2 at twist angle $\theta = 1.43°$. (c) Sketch of the moiré brillouin zone, together with the path in reciprocal space used to plot band structures in this work.

which in Fourier space obtains

$$V^t_{\mathbf{g}} = V^b_{C_{2y}\mathbf{g}}. \tag{2.25}$$

This in particular shows that the constant $\mathbf{g} = 0$ Fourier mode can be neglected as it is equal in both layers due to $C_{2y}\mathcal{T}$ symmetry.

Remarkably, in the first harmonic approximation, in which one takes only the first shell of reciprocal vectors, the potentials are parametrized by only two parameters: an amplitude V, and a phase ψ. The layer potentials then read:

$$V^b(\mathbf{r}) = \left(V e^{i\psi} \sum_{j=1,3,5} e^{i\mathbf{r}\cdot\mathbf{g}_j} \right) + h.\,c. \tag{2.26}$$

$$V^t(\mathbf{r}) = \left(V e^{-i\psi} \sum_{j=1,3,5} e^{i\mathbf{r}\cdot\mathbf{g}_j} \right) + h.\,c., \tag{2.27}$$

where $h.\,c.$ denotes the complex conjugate. We now turn to the symmetry constraints on the tunneling term $T(\mathbf{r})$, which is more subtle than the layer potentials, which could be obtained simply by considering the real space actions of symmetries. To obtain the symmetry constraints for the tunneling terms, we need to define the basis of kets $|\mathbf{k}, t\rangle$ and $|\mathbf{k}, b\rangle$, which correspond to momentum eigenstates at momentum $\mathbf{k}$ in the top and bottom layers, respectively, where $\mathbf{k}$ will typically lie close to the K-valley momentum $\boldsymbol{K}$.

Let us now discuss the representation of C_{3z} symmetry on the basis of states expanded around the K-valley. C_{3z} rotates momentum by 120°, but, crucially, with respect to the K-point of each given layer. Formally, it acts on momentum eigenstates in the two layers as follows:

$$C_{3z}\,|\boldsymbol{K^b} + \mathbf{k}, b\rangle = |\boldsymbol{K^b} + C_{3z}\mathbf{k}, b\rangle \tag{2.28}$$

$$C_{3z}\,|\boldsymbol{K^t} + \mathbf{k}, t\rangle = |\boldsymbol{K^t} + C_{3z}\mathbf{k}, t\rangle\,. \tag{2.29}$$

However, to have a Bloch periodic Hamiltonian, we need to measure momentum with respect to a common origin. Let us therefore measure momentum $\mathbf{k}$ with respect to the bottom layer Dirac point, so that the total momentum is written as $\boldsymbol{K^b} + \mathbf{k}$. In this convention, we obtain the following non-trivial representation for C_{3z} symmetry on the top layer wavefunctions:

$$\begin{aligned} C_{3z} \left| \boldsymbol{K^b} + \mathbf{k}, t \right\rangle &= C_{3z} \left| \boldsymbol{K^t} - \Delta \boldsymbol{K} + \mathbf{k}, t \right\rangle && (2.30) \\ &= \left| \boldsymbol{K^t} + C_{3z}(-\Delta \boldsymbol{K} + \mathbf{k}), t \right\rangle && (2.31) \\ &= \left| \boldsymbol{K^b} + \Delta \boldsymbol{K} - C_{3z} \Delta \boldsymbol{K} + C_{3z}\mathbf{k}, t \right\rangle && (2.32) \\ &= \left| \boldsymbol{K^b} - \mathbf{g}_5 + C_{3z}\mathbf{k}, t \right\rangle , && (2.33) \end{aligned}$$

where we defined $\Delta \mathbf{K} = \boldsymbol{K^t} - \boldsymbol{K^b}$ as the relative momentum shift between the valleys of the two layers. Note that if we measure momentum with respect to the bottom layer, C_{3z} acting on wavefunctions in the top layer, in addition to rotating momentum, implements also a momentum boost by $-\mathbf{g}_5$. With this, we obtain the following C_{3z} constraint on the tunneling term:

$$T_{\mathbf{g}} = T_{\mathbf{g}_5 + C_{3z}\mathbf{g}}. \tag{2.34}$$

In particular the additional momentum boost implies that a purely spatially uniform tunneling term is not allowed by C_{3z} symmetry. Concentrating again on the Fourier components of smallest magnitude, assuming T_0 is nonzero, we see that we have $T_0 = T_{\mathbf{g}_5} = T_{\mathbf{g}_6}$. Therefore, the simplest symmetry allowed tunneling term is

$$T(\mathbf{r}) = w(1 + e^{\mathbf{g}_5 \cdot \mathbf{r}} + e^{\mathbf{g}_6 \cdot \mathbf{r}}), \tag{2.35}$$

where the real constant w parametrizes the strength of interlayer tunneling. We illustrate these tunnelings in Fig. 2.2a, where a particle at the K-valley of the top layer can either tunnel without a momentum transfer, or it can pick up a boost by $\mathbf{g}_5$ or $\mathbf{g}_6$. Altogether, we obtain the twisted bilayer TMD Hamiltonian in the K-valley in the first harmonic approximation:

$$H^K_{tTMD} = \begin{pmatrix} -\frac{\hbar^2(\mathbf{k} - \boldsymbol{K^b})^2}{2m^*} + V^b(\mathbf{r}) & w(1 + e^{i\mathbf{g}_5 \cdot \mathbf{r}} + e^{i\mathbf{g}_6 \cdot \mathbf{r}}) \\ w(1 + e^{-i\mathbf{g}_5 \cdot \mathbf{r}} + e^{-i\mathbf{g}_6 \cdot \mathbf{r}}) & -\frac{\hbar^2(\mathbf{k} - \boldsymbol{K^t})^2}{2m^*} + V^t(\mathbf{r}) \end{pmatrix}, \tag{2.36}$$

where $V^b(\mathbf{r})$ is given in Eq. (2.26) and $V^t(\mathbf{r})$ is given in Eq. (2.27).

For physically relevant parameters, this continuum model leads to valley-resolved topological flat bands [55]. The physical reason for this is that the real-space texture defined by the tunneling and potential terms forms a real-space skyrmion, and particles tracking the skyrmion experience an effective magnetic field. We will describe this picture in more detail in Chapter 7. As an example, consider the parameters obtained in Ref. [68] as an illustrative example. The parameters for twisted bilayer WSe_2 are $(a_0, m^*, V, \psi, w) = (0.332\,\mathrm{nm}, 0.43\,\mathrm{m_e}, 9\,\mathrm{meV}, -128°, 18\,\mathrm{meV})$, where m_e is the bare electron mass. We plot the band structures at twist angle $\theta = 1.43°$ in

Fig. 2.2b, which shows a flat detached Chern number one band. The band structures are plotted along a path in the moiré Brilloun zone, shown in Fig. 2.2c. Note that conventionally, the K-points of the two layers are referred to as the moiré K_M and moiré $K_{M'}$ points, so that we identify $\boldsymbol{K^t} = K_{M'}$ and $\boldsymbol{K^b} = K_M$.

2.3 Twisted bilayer graphene

For twisted bilayer graphene, we have a Dirac Hamiltonian at each valley. We start with unrotated layers with a Dirac cone of a single spin-valley flavor at momentum $\boldsymbol{K} = (\frac{4\pi}{3a_0}, 0)$, with a_0 the monolayer lattice constant, with the following single-particle Dirac Hamiltonian:

$$\mathrm{H}_{\text{mono}}(\mathbf{k}) = v_F(\mathbf{k} - \boldsymbol{K}) \cdot \boldsymbol{\sigma}, \tag{2.37}$$

where $v_F = 542.1\,\mathrm{meV} \cdot \mathrm{nm}$ is the graphene Dirac velocity and where $\boldsymbol{\sigma}$ is the vector of Pauli-matrices in sublattice space.

Considering a bilayer, and applying rotations by $\pm\theta/2$ to the top and bottom layers, we obtain the top and bottom layer single-particle Hamiltonians

$$\mathrm{H}^b_{\text{mono}}(\mathbf{k}) = v_F[R(-\theta/2)\mathbf{k} - \boldsymbol{K^b}] \cdot \boldsymbol{\sigma} \tag{2.38}$$

$$\mathrm{H}^t_{\text{mono}}(\mathbf{k}) = v_F[R(\theta/2)\mathbf{k} - \boldsymbol{K^t}] \cdot \boldsymbol{\sigma}, \tag{2.39}$$

where we note that the rotations acting on momentum $\mathbf{k}$ in the Hamiltonians for the two layers have a very small effect on the band structure and are often neglected.

Twisted bilayer graphene is symmetric under three-fold rotations around the z-axis (C_{3z}), under time-reversal ($\mathcal{T}$), and under two-fold rotations around the x, y, and z-axes (C_{2x}, C_{2y}, C_{2z}). To constrain the Hamiltonian in a single valley, only valley preserving symmetries are necessary, of which a convenient choice is C_{3z}, $C_{2z}\mathcal{T}$, and C_{2x}.

In discussing symmetries, it is most natural to measure the momentum in each layer with respect to its respective Dirac point [69]. While in this way our Hamiltonian and eigenfunctions cease being Bloch periodic, we can always come back to the original representation. The Bloch non-periodicity manifests in the interlayer tunneling terms, which have to be modified as follows.

$$T(\mathbf{r}) \to T(\mathbf{r})e^{i\Delta\boldsymbol{K}\cdot\mathbf{r}} = \sum_{\mathbf{g}} T_{\mathbf{g}} e^{i(\mathbf{g}+\Delta\boldsymbol{K})\cdot\mathbf{r}}, \tag{2.40}$$

with the meaning that if the electron tunnels from the top to the bottom layer, it additionally gains momentum $\Delta\boldsymbol{K}$, as a result of the different momentum origins. The Hamiltonian now

acts on 4-component wavefunctions $\Psi(\mathbf{r})$ which are the slowly varying envelope functions expanded around each layer's Dirac cone in the K valley:

$$\Psi(\mathbf{r}) = [\Psi^{b,A}(\mathbf{r}), \Psi^{b,B}(\mathbf{r}), \Psi^{t,A}(\mathbf{r}), \Psi^{t,B}(\mathbf{r})]^T. \tag{2.41}$$

The representations of intravalley symmetries on $\Psi(\mathbf{r})$ are as follows:

$$C_{3z}\Psi(\mathbf{r}) = e^{i2\pi/3\sigma_z}\Psi(C_{3z}\mathbf{r}) \tag{2.42}$$
$$C_{2z}\mathcal{T}\Psi(\mathbf{r}) = \sigma_x\Psi^*(-\mathbf{r}) \tag{2.43}$$
$$C_{2x}\Psi(\mathbf{r}) = \sigma_x\mu_x\Psi(C_{2x}\mathbf{r}), \tag{2.44}$$

where the C_{3z} representation is the standard representation on a Dirac Hamiltonian and where μ_x is the Pauli-x matrix in layer space.

The potential matrices give rise to periodic scalar and vector potentials, which typically arise due to lattice corrugation [70, 71]. However, in the most elementary approach, such terms are neglected [19], therefore we set $V^{t/b}(\mathbf{r}) = 0$ for the continuum model of TBG.

The symmetry constraints on the tunneling terms due to C_{3z}, $C_{2z}\mathcal{T}$, and C_{2x} are respectively:

$$T(\mathbf{r}) = e^{i2\pi/3\sigma_z}T(C_{3z}\mathbf{r})e^{-i2\pi/3\sigma_z} \tag{2.45}$$
$$T(\mathbf{r}) = \sigma_x T(C_{2z}\mathbf{r})^*\sigma_x \tag{2.46}$$
$$\sigma_x T(C_{2x}\mathbf{r})\sigma_x = T^\dagger(\mathbf{r}). \tag{2.47}$$

The simplest possible tunneling term is a spatially uniform tunneling term $T_{\mathbf{g}=0}$, which for TBG is a matrix in sublattice space. However, just like for twisted TMDs, C_{3z} enforces that if $T_{\mathbf{g}=0} \neq 0$, $T_{\mathbf{g}_5}$ and $T_{\mathbf{g}_6}$ are necessarily also nonzero. To see this, note that in the non-periodic gauge currently chosen $T_{\mathbf{g}=0}$ actually has a nontrivial spatial dependence $e^{i\Delta\boldsymbol{K}\cdot\mathbf{r}}$. Under C_{3z}, this spatial dependence maps to $e^{iC_{3z}\Delta\boldsymbol{K}\cdot\mathbf{r}}$ and $e^{i(C_{3z})(C_{3z})\Delta\boldsymbol{K}\cdot\mathbf{r}}$, which corresponds precisely to $\mathbf{g} = \mathbf{g}_5$ and $\mathbf{g} = \mathbf{g}_6$, recovering the result obtained for TMDs in a Bloch periodic gauge. The spatial dependence of the three tunneling terms in the non-periodic gauge is now at wavevectors

$$\boldsymbol{q_1} \equiv \Delta\boldsymbol{K} \tag{2.48}$$
$$\boldsymbol{q_2} \equiv C_{3z}\Delta\boldsymbol{K} \tag{2.49}$$
$$\boldsymbol{q_3} \equiv C_{3z}^2\Delta\boldsymbol{K}, \tag{2.50}$$

which form an equilateral triangle, shown in Fig 2.3a.

In TBG, C_{3z} therefore imposes that

$$T_{\mathbf{g}_5} = e^{i2\pi/3\sigma_z}T_0e^{-i2\pi/3\sigma_z} \tag{2.51}$$
$$T_{\mathbf{g}_6} = e^{i4\pi/3\sigma_z}T_0e^{-i4\pi/3\sigma_z}, \tag{2.52}$$

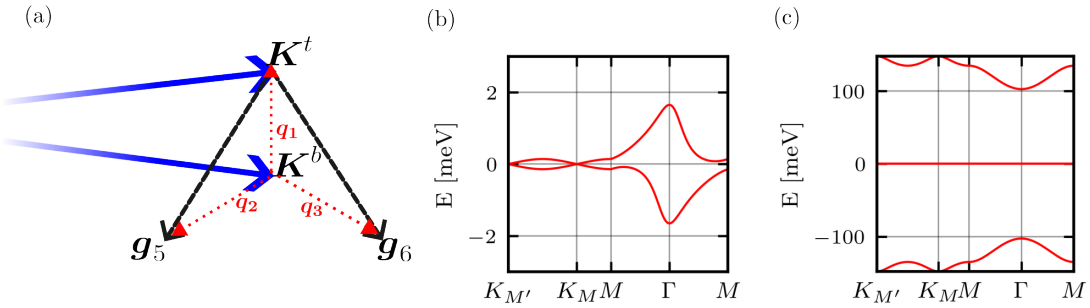

Figure 2.3: (a) The two Dirac points, together with the three tunneling vectors in the non Bloch-periodic gauge. (b) Band structure of twisted bilayer graphene at $\theta = 1.09°$, with lattice corrugation $c = 0.7$, showing extremely flat bands. (c) Band structure of twisted bilayer graphene at $\theta = 1.09°$ in the chiral limit, that is, with lattice corrugation $c = 0$, showing perfectly flat bands with a large gap to the remote bands.

where the factors of $e^{i2\pi/3\sigma_z}$ arise due to the C_{3z} representation on the Dirac Hamiltonian.

We now use $C_{2z}\mathcal{T}$ and C_{2x} to constrain T_0, from which we can then obtain $T_{\mathbf{g}_5}$ and $T_{\mathbf{g}_6}$ using C_{3z}. $C_{2z}\mathcal{T}$ restrains $T_{\mathbf{g}=0}$ as follows:

$$\sigma_x T^*_{\mathbf{g}=0}\sigma_x = T_{\mathbf{g}=0}, \tag{2.53}$$

where the complex conjugation arises due to the antinuitary nature of the symmetry. Finally, C_{2x} constrains $T_{\mathbf{g}=0}$ as follows:

$$\sigma_x T^\dagger_{\mathbf{g}=0}\sigma_x = T_{\mathbf{g}=0}. \tag{2.54}$$

Taken together, this constrains $T_{\mathbf{g}=0}$ to have the following form:

$$T_{\mathbf{g}=0} = w_{AA}\sigma_0 + w_{AB}\sigma_x + w_3 i\sigma_z, \tag{2.55}$$

where w_{AA} parametrizes the strength of intra-sublattice tunneling, w_{AB} that of inter-sublattice tunnelling, while w_3 is an $O(\theta)$ term corresponding to an asymmetry between $A \leftrightarrow A$ and $B \leftrightarrow B$ tunneling [72], but which we will presently neglect. The tunneling term in the Bloch non-periodic gauge for TBG therefore reads:

$$T(\mathbf{r}) = (w_{AA}\sigma_0 + w_{AB}\sigma_x)e^{i\mathbf{q}_1\cdot\mathbf{r}} + (w_{AA}\sigma_0 + w_{AB}\sigma_x e^{2\pi i/3\sigma_z})e^{i\mathbf{q}_2\cdot\mathbf{r}} + \\ + (w_{AA}\sigma_0 + w_{AB}\sigma_x e^{4\pi i/3\sigma_z})e^{i\mathbf{q}_3\cdot\mathbf{r}}, \tag{2.56}$$

where it can be noted that the exponential factors multiplying σ_x simply put the corresponding complex phases on the off-diagonal of the σ_x matrix. Putting everything together, we arrive at the famous Bistritzer-Macdonald Hamiltonian [19] in the K-valley:

$$H_{TBG}^{K} = \begin{pmatrix} v_F \mathbf{k} \cdot \boldsymbol{\sigma} & T(\mathbf{r}) \\ T^{\dagger}(\mathbf{r}) & v_F \mathbf{k} \cdot \boldsymbol{\sigma} \end{pmatrix}. \tag{2.57}$$

Typically, we take $w_{AB} \approx 110\,\mathrm{meV}$, while $w_{AA} = c w_{AB}$, where the factor c accounts for lattice relaxation. At small twist angles, this Hamiltonian leads to two detached bands near charge neutrality per spin and valley. At the magic angle, the typical energy scale for the Dirac term ($v_F|\Delta\mathbf{K}|$) is approximately equal to the typical tunneling scale (w_{AB}):

$$w_{AB} \approx v_F|\Delta\mathbf{K}| = v_F|\boldsymbol{K}^{\boldsymbol{t}} - \boldsymbol{K}^{\boldsymbol{b}}| = v_F \theta^{\text{magic}} \frac{4\pi}{3a_0}, \tag{2.58}$$

from which one can find the magic angle condition as $\theta^{\text{magic}} \approx \frac{w_{AB}}{v_F}\frac{3a_0}{4\pi} \approx 1.09^{\circ}$. We plot the bands of TBG at this angle in Fig. 2.3b, showing their extremely small bandwidth.

An interesting situation arises when the lattice relaxation factor c is set to zero, $c = 0$. In this limit, denoted the chiral limit, the Hamiltonian enjoys a new chiral antisymmmetry, which we denote as $\mathcal{C} = \sigma_z$. Indeed, for $c = 0$, the Hamiltonian of Eq. (2.57) only consists of σ_x and σ_y Pauli matrices, which anticommute with $\mathcal{C}$. In this limit, at the special magic angles, not only does the Dirac velocity vanish. In fact, as shown in Fig. 2.3c, the entire band becomes flat [73].

There is another antiunitary particle-hole antisymmetry, denoted $\mathcal{P}$ [74–77]. $\mathcal{P}$ anticommutes with the Hamiltonian of Eq. (2.57). Just like the chiral antisymmetry, this one is in fact not a physical symmetry, and it only emerges when the small relative rotations in the Dirac Hamiltonians in Eq. (2.38) are neglected, as we have done in writing Eq. (2.57).

$\mathcal{P}$ acts as follows

$$\mathcal{P}\Psi(\mathbf{r}) = i\mu_y \sigma_x \Psi^*(\mathbf{r}), \tag{2.59}$$

with μ_y the Pauli-y matrix in layer space. To check that $\mathcal{P}$ indeed anticommutes with the TBG Hamiltonian, it is easiest to consider the combination $C_{2z}\mathcal{T}\mathcal{P}$. Since $C_{2z}\mathcal{T}$ is a symmetry, if this combination anticommutes, $\mathcal{P}$ must be an antisymmetry. Remarkably, $C_{2z}\mathcal{T}\mathcal{P}$ acts very simply as

$$C_{2z}\mathcal{T}\mathcal{P}\Psi(\mathbf{r}) = i\mu_y \Psi(-\mathbf{r}), \tag{2.60}$$

which confirms the required property if it is noted that $T^{\dagger}(\mathbf{r}) = T(-\mathbf{r})$.

2.4 Alternating twisted graphene multilayers

A natural extension of twisted bilayer graphene is to stack twisted bilayers on top of each other, creating a structure periodic in the vertical direction with a period of two layers, having the same moiré structure as a twisted bilayer. From this stack, one can then remove the top layer, obtaining an analogous system with an odd number of layers.

This system is denoted alternating twisted multilayer graphene, and its Hamiltonian in the K-valley reads [78, 79]:

$$H_{\text{sp}}^{K} = \begin{pmatrix} v_F \mathbf{k}\cdot\boldsymbol{\sigma} & T(\mathbf{r}) & 0 & \cdots \\ T^{\dagger}(\mathbf{r}) & v_F \mathbf{k}\cdot\boldsymbol{\sigma} & T^{\dagger}(\mathbf{r}) & \\ 0 & T(\mathbf{r}) & v_F \mathbf{k}\cdot\boldsymbol{\sigma} & \\ \vdots & & & \ddots \end{pmatrix}, \tag{2.61}$$

where we consider N layers, and where as above we neglected the relative rotations of the Dirac Hamiltonians and we take $T(\mathbf{r})$ from Eq. (2.56).

Just like one solves a particle in a well problem, we solve this problem by first solving the infinite layer problem and then restricting to the finite system. For a system of infinite vertical extent, we define a momentum along the z-direction, $k_z \in (-\pi, \pi]$, which corresponds to the eigenvalues of vertical translations by two layers. Using this, we define the effective bottom and top layer wavefunctions in layer space (in what follows, we suppress the sublattice and real-space indices, since they are not affected) at vertical momentum k_z as

$$|b, k_z\rangle = \sum_{l \text{ odd}} e^{ik_z l/2} |l\rangle \tag{2.62}$$

$$|t, k_z\rangle = \sum_{l \text{ even}} e^{ik_z l/2} |l\rangle , \tag{2.63}$$

where $|l\rangle$ corresponds to layer l. In this basis, the Hamiltonian at the K-valley decomposes into different blocks for each value of k_z:

$$H_{TNG}^{K}(k_z) = \begin{pmatrix} v_F \mathbf{k}\cdot\boldsymbol{\sigma} & 2\cos(k_z/2) T(\mathbf{r}) \\ 2\cos(k_z/2) T^{\dagger}(\mathbf{r}) & v_F \mathbf{k}\cdot\boldsymbol{\sigma} \end{pmatrix}, \tag{2.64}$$

resembling the TBG Hamiltonian of Eq. (2.57), but with a rescaled tunneling term.

This decomposition into sectors holds even for a finite system, but now the sectors rather than being plane waves will be standing waves, formed as superpositions of k_z and $-k_z$ states, which have the same effective Hamiltonian. The vertical wavefunctions for the finite systems

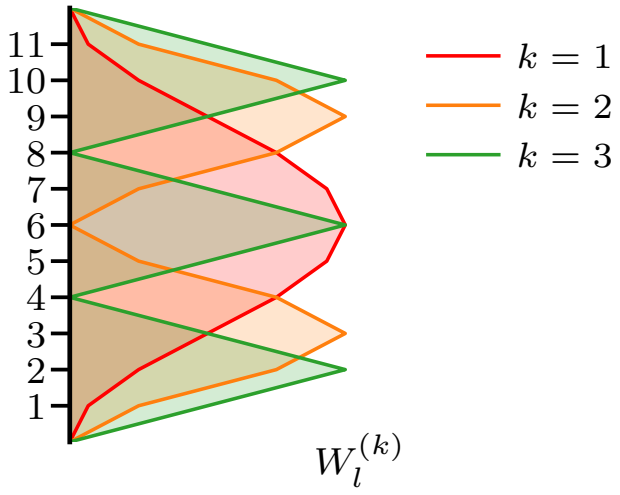

Figure 2.4: Schematics of layer charge distribution (See Eq. (2.72)) for $N = 11$, showing the three sectors with lowest effective twist angle, $k = 1$: red, $k = 2$: orange, $k = 3$: green. In experiment to date, $k = 1$ is the flattest, "magic" sector.

are obtained by imposing that they vanish on layers $l = 0$ and $l = N + 1$ of the infinite system. Vanishing on $l = 0$ implies that we need to consider odd parity wavefunctions only:

$$|b, k_z, -\rangle = \sum_{l \text{ odd}} \sin(k_z l/2) \, |l\rangle \tag{2.65}$$

$$|t, k_z, -\rangle = \sum_{l \text{ even}} \sin(k_z l/2) \, |l\rangle \, . \tag{2.66}$$

Vanishing on $l = N + 1$ leads to the following quantization condition for k_z:

$$k_z = \frac{2\pi k}{N+1}, \tag{2.67}$$

with $k = 1, \ldots \lfloor N/2 \rfloor$ an integer, which labels the TBG-like sectors. For N odd, there is an additional a decoupled sector, having $k = \frac{N+1}{2}$. For this sector, $|t, k_z, -\rangle$ of Eq. (2.66) vanishes. Therefore, there is only one effective layer in this sector. Its Hamiltonian is just the Dirac Hamiltonian of the underlying graphene. We denote this sector for N odd as the MLG-like sector.

To obtain the unitary basis transformation into the basis of sectors, in which the Hamiltonian is block diagonal, we need to normalize the layer wavefunctions. The normalized wavefunctions for sector k with $k = 1, \ldots \lfloor N/2 \rfloor$ read:

$$|b, k\rangle = \sqrt{\frac{4}{N+2}} \sum_{l \text{ odd}} \sin\left(\frac{\pi k l}{N+1}\right) |l\rangle \tag{2.68}$$

$$|t, k\rangle = \sqrt{\frac{4}{N+2}} \sum_{l \text{ even}} \sin\left(\frac{\pi k l}{N+1}\right) |l\rangle \,, \tag{2.69}$$

while for N odd, we have a $k = (\lfloor N/2 \rfloor + 1)$-th MLG-like sector with vector:

$$|b, k = \lfloor N/2 \rfloor + 1\rangle = \sqrt{\frac{2}{N+2}} \sum_{l \text{ odd}} \sin\left(\frac{\pi k l}{N+1}\right) |l\rangle \tag{2.70}$$

Using this, we define the $N \times N$ basis transformation matrix V_{TNG} in layer space as follows:

$$V_{\text{TNG}} = (|b, k = 1\rangle \,, |t, k = 1\rangle \,, |t, k = 2\rangle \ldots), \tag{2.71}$$

where we think of $|b/t, k\rangle$ as N-dimensional column vectors.

Using the normalized wavefunctions, and assuming that in a TBG-like sector the particles are equally likely to be in the effective bottom as in the effective top layer, we obtain the effective layer distribution of sector k as

$$W_l^{(k)} = \frac{2}{N+1} \sin^2\left(\frac{\pi k l}{N+1}\right), \tag{2.72}$$

which we plot for $N = 11$ in Fig. 2.4, showing a typical particle-in-a-box behavior. As will be discussed in Chapter 5, these differing vertical distributions will prove important for the electrostatic properties of these systems.

The tunneling term in the TBG-like sector k is rescaled by

$$\Lambda_k = 2 \cos\left(\frac{\pi k}{N+1}\right), \tag{2.73}$$

leading to the effective twist angle

$$\theta_k^{\text{eff}} = \theta / \Lambda_k, \tag{2.74}$$

which has profound experimental consequences. By setting $\theta_{k=1}^{\text{eff}} = \theta^{\text{magic}}$, we see that the physical magic angle is enhanced by a factor $\Lambda_{k=1} = 2\cos\left(\frac{\pi}{N+1}\right)$. Crucially, larger angles are more robust to disorder, providing an experimental advantage. With an increasing number of layers, there is a continuum of twist angles [78] , with the largest density of twist angles close to the minimal θ_k^{eff} (attained for $k = 1$). We show an example band structure for $N = 11$ in

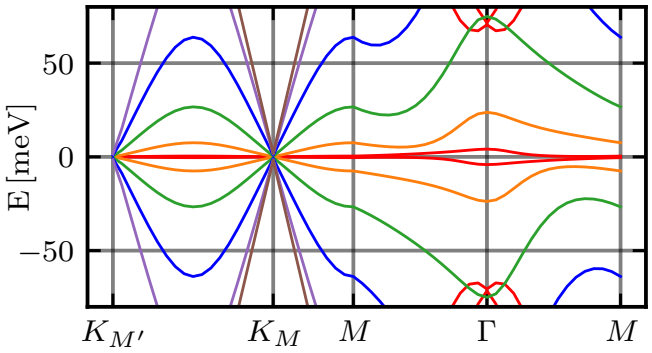

Figure 2.5: Band structure of magic angle TNG for $N = 11$.

Fig. 2.5, where the $k = 1$ sector is at the magic angle and other sectors are progressively more dispersive as their effective twist angle progressively increases according to Eq. (2.74).

The proposal discussed in this Section was first realized for the case of three layers [23, 33, 80], which hosts a set of flat bands coexisting with a graphene-like Dirac cone. Twisted trilayer graphene devices exhibit strongly-coupled superconductivity tunable by an out-of-plane displacement field. More recently, twisted N-layer graphene (TNG) devices have been successfully fabricated for up to $N = 5$ layers [31, 32], which we will discuss in Chapter 5.

3 Tunneling signatures of interband coherence in exciton insulators

In this Chapter, motivated by the experimental advanced on layered materials, we explore the tunneling signatures of interband coherence in exciton insulators. These results will be included in a publication in preparation, Ref. [5].

Excitons – bound pairs of electron and hole – are expected to form spontaneously in the ground state of an intrinsic narrow-gap semiconductor if the binding energy E_b of an isolated exciton exceeds the band gap E_G between the conduction and valence bands [45–48]. When E_G is close to E_b, the exciton density n_{ex} is small and the internal structure of the excitons becomes immaterial. They effectively realize a gas of pointlike bosons, with the residual overlap of excitons inducing a finite exciton compressibility. This gas is expected to undergo Bose-Einstein condensation (BEC) at low temperatures [47]. The formation of the condensate affects the noninteracting band structure only mildly by increasing the gap E_g. However, the associated emergence of interband coherence spontaneously breaks the separate charge conservation symmetries of the conduction and valence bands, permitting exciton superflow under suitable conditions. As the exciton density increases, the system eventually crosses over into a Bardeen-Cooper-Schrieffer (BCS) regime, in which overlapping bare valence and conduction bands spontaneously develop an excitation gap.

While exciton condensates have been studied for almost sixty years, recent years have seen a surge of interest in exciton insulators driven by the emergence of breakthrough materials. Recent work on monolayers of $ZrTe_2$ [42] and WTe_2 [43, 44], bilayer transition metal dichalcogenides [49–51], and bulk $Ta_2Pd_3Te_5$ [81, 82] presented evidence for exciton-insulator formation, improving upon earlier candidate materials such as Ta_2NiSe_5 [83–86] and $TiSe_2$ [87, 88]. Unequivocal detection of an exciton insulators is challenging since it is a state with spontaneous mixing of conduction and valence bands [46, 89, 90]. If this band mixing occurs between bands with a finite momentum offset, it generically couples to the lattice [89], which can also drive band mixing. Recently, Refs. [42, 91, 92] doubt a purely excitonic origin of the states observed in Ta_2NiSe_5 and $TiSe_2$, suggesting instead a lattice driven mechanism. Bilayer condensates in which conduction and valence bands are localized to separate layers, do not couple to the lattice [93, 94], while the recent experiments on $ZrTe_2$ [42] and $Ta_2Pd_3Te_5$ [82] rely on careful modelling to preclude a lattice-driven phase. Experiments on monolayer WTe_2 [43, 44] argued based on transport anomalies and did not observe any lattice distortion, possibly as a result of the specific spin ordering [95].

Diverse experimental techniques were used to probe candidate materials for exciton-insulator formation. Angle-resolved photoemission spectroscopy (ARPES) [42, 82, 83, 87, 92, 96] mapped band structures, and the spontanoues opening of a gap at small temperatures was taken as evidence. Bilayer systems, with extraordinary tunability afforded by bias voltages and external gates [97, 98], allowed the thermodynamic measurement of exciton density as a function of the band gap E_G [49–51]. Furthermore, bilayer systems allow exciton superflow to be probed, manifesting in perfect Coulomb drag [99, 100], similarly to quantum Hall bilayer condensates [101–104]. Notably, ARPES, thermodynamic and transport measurements as global probes are sensitive to disorder. For example, Ref. [49] obtained a compressibility peak upon onset of exciton formation, potentialy due to sample disorder.

A natural tool to study local features with high spatial and energy resolution is scanning tunneling microscopy (STM). STM has, however, been used in the study of excitonic states only in a limited way, primarily to confirm a gapped state [42, 43, 81, 82, 84, 96]. The usefulness of STM beyond establishing gapped states was highlighted by recent experiments on bulk $Ta_2Pd_3Te_5$ [81] and on flat band graphene based systems [105–107]. These state-of-the-art experiments utilized STM to probe finite-momentum interband coherence, which arises as a secondary excitonic order in $Ta_2Pd_3Te_5$ [81], or as a ground state inter-valley coherent order in graphene platforms [76, 108–110].

Here we theoretically study how STM can be applied to study excitonic insulators, going beyond the paradigm of establishing a gapped state. To emphasize this point, we focus on the BEC regime, in which there is a gap even in the absence of exciton formation. In fact this low exciton density regime has two advantages compared to BCS. Firstly, the effect of exciton-lattice coupling is smaller [46], rendering a lattice-driven transition less likely. Secondly, screening effects are negligible for small electron-hole density. On the other hand, screening is crucial in the BCS regime, particularly in bilayer devices, in which it causes an early transition into an electron-hole plasma as the density increases [111, 112].

In monolayer samples (Fig 3.1a), in which excitonic coherence happens between conduction and valence bands offset by a certain momentum (so that the band gap is indirect), lattice-symmetry breaking spatial oscillations in the tunneling signal are expected – which occur, depending on the spin-ordering, in the spin-resolved or spin-averaged tunneling. These oscillations reflect excitons forming a coherent condensate. Importantly, we show that the combination of spatially averaged and oscillatory components of tunneling allows the exciton wavefunction to be determined. Furthermore, we predict finite peaks (rather than divergences as in the BCS regime) at the band edge in the spatially averaged tunneling, obtaining analytical expressions for their shape, finding sharper peaks on the heavier band side.

In a bilayer sample, the tip electrons only directly couple to the top layer, as shown Fig. 3.1b. Assuming the conduction band is in the top layer and the valence band in the bottom layer, the presence of excitons enables a new type of tunneling process, depicted in Fig. 3.1b. In this process, an electron in the conduction band in the top layer bound into an exciton tunnels into

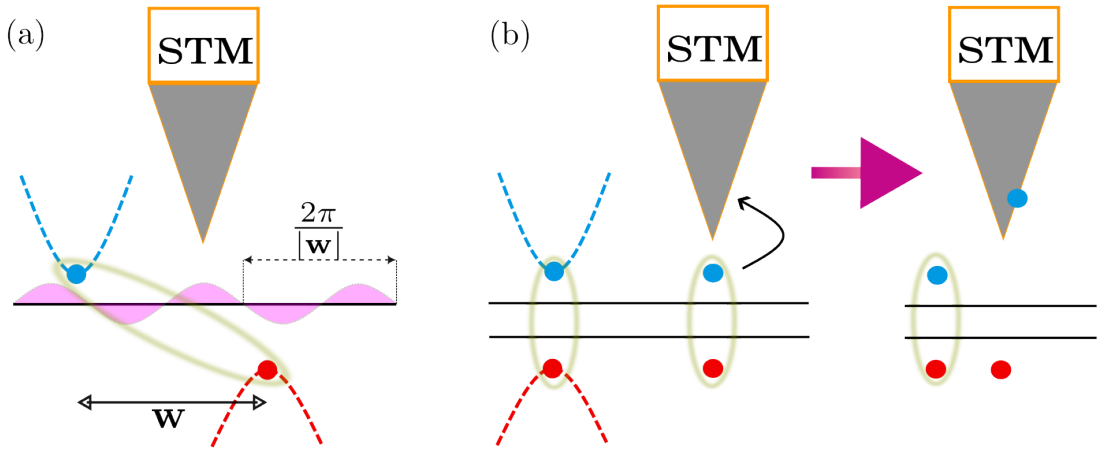

Figure 3.1: (a) Schematics of STM tunneling into a monolayer. The tip can effectively tunnel into both bands. A shift of the conduction and valence bands by wavevector $\mathbf{w}$ in momentum space, leads to additional wavelength $\frac{2\pi}{|\mathbf{w}|}$ spatial oscillations in the STM signal, which allow the exciton wavefunction to be determined. (b) Schematics of a tunneling experiment into a bilayer exciton condensate. The tip electrons can only directly tunnel into the top layer. Exciton condensation enables a process in which a conduction electron bound in an exciton tunnels out, leaving behind a spare valence hole, leading to an additional peak in tunneling spectra.

the tip, leaving behind a hole in the bottom layer. This process is only possible if excitons are present, and leads to an additional peak in the tunneling conductance.

This Chapter is structured as follows. In Section. 3.1, we introduce the basic model of an exciton insulator, including a solution using mean-field decoupling and a perturbative low-density solution. In Section 3.2, we introduce the framework for discussing scanning tunneling microscopy measurements. In Section 3.3, we study the tunneling signatures in a minimal spinless monolayer exciton insulator, and present a method of recovering the exciton wavefunction. In Section 3.4, we discuss signatures in bilayer exciton condensates. In Section 3.5, we discuss the complications due to the spin degree of freedom. We conclude with a discussion in Sec. 3.6.

3.1 Exciton condensates

In this Section, we first introduce the basic model of an exciton insulator in Subsection 3.1.1, In the following Subsection 3.1.2, we introduce the mean-field decoupling. Finally, in Subsection 3.1.3, we undertake a perturbative solution in the low exciton density limit.

3.1.1 Basic model

We begin our discussion with an elementary two-band model of exciton condensation [46, 90], which neglects the spin degree of freedom. It describes the conduction and valence bands within the effective-mass approximation,

$$\epsilon^c_{\mathbf{k}} = \frac{\hbar^2\mathbf{k}^2}{2m_c} + \frac{1}{2}E_G \tag{3.1}$$

$$\epsilon^v_{\mathbf{k}} = -\frac{\hbar^2\mathbf{k}^2}{2m_v} - \frac{1}{2}E_G. \tag{3.2}$$

We assume that the bands are isotropic with effective mass m_c (m_v) of the conduction (valence) band and band gap E_G. The momenta $\mathbf{k}$ are measured from the respective band extrema. Assuming charge neutrality, we omit a chemical potential term.

In terms of underlying Bloch functions, the conduction and valence band operators $c^\dagger_{\mathbf{k},c}$ and $c^\dagger_{\mathbf{k},v}$ are given as

$$c^\dagger_{\mathbf{k},i} = \int d\mathbf{r}\, \frac{e^{i(\mathbf{k}+\mathbf{w}_i)\cdot\mathbf{r}}}{\sqrt{N_{\mathrm{UC}}}} u_{\mathbf{k}+\mathbf{w}_i,i}(\mathbf{r})\psi^\dagger(\mathbf{r}), \tag{3.3}$$

where $\psi^\dagger(\mathbf{r})$ creates an electron at position $\mathbf{r}$, N_{UC} is the number of unit cells, $\mathbf{w}_i$ is the location of the band extremum of band $i = c, v$, and $u_{\mathbf{k}+\mathbf{w}_i,i}(\mathbf{r})$ is the periodic part of the Bloch function normalized within the unit cell. The extrema of conduction and valence band are offset in momentum by $\mathbf{w} = \mathbf{w}_c - \mathbf{w}_v$. With a view towards van der Waals materials, we assume the Bloch states to be perfectly localized along the z-direction, with band i localized at z_i. We choose $z_c = 0$, so that $z_c = z_v = 0$ for monolayers and $z_v < 0$ for a bilayer. For this choice, the conduction-band layer is above the valence-band layer as in Fig. 3.1b.

Including the Coulomb interaction, the Hamiltonian takes the form

$$\begin{aligned}\hat{H} = &\sum_{\mathbf{k}} \epsilon^c_{\mathbf{k}} c^\dagger_{\mathbf{k},c} c_{\mathbf{k},c} + \sum_{\mathbf{k}} \epsilon^v_{\mathbf{k}} c^\dagger_{\mathbf{k},v} c_{\mathbf{k},v} \\ &+ \frac{1}{2A}\sum_{\mathbf{q}} :V_{cc}(\mathbf{q})\rho_{\mathbf{q},c}\rho_{-\mathbf{q},c} + V_{cv}(\mathbf{q})\rho_{\mathbf{q},c}\rho_{-\mathbf{q},v} + (c \leftrightarrow v): + E_C.\end{aligned} \tag{3.4}$$

Here, A is the sample area, normal ordering is with respect to the intrinsic semiconductor (i.e., conduction-band electrons and valence-band holes), and $V_{ij}(\mathbf{q})$ is the unscreened Coulomb interaction for bands i, j,

$$V_{ij}(\mathbf{q}) = \frac{e^2}{2\epsilon\epsilon_0|\mathbf{q}|}\exp(-|\mathbf{q}|\cdot|z_i - z_j|), \tag{3.5}$$

with the electron charge e, vacuum permittivity ϵ_0, and a background relative dielectric constant ϵ. We included the electrostatic charging energy E_C of a parallel-plate capacitor

$$E_C = \frac{1}{2AC_G} : \hat{N}_{\text{ex}}^2 :, \tag{3.6}$$

with the interlayer capacitance per unit area $C_G = \frac{\epsilon\epsilon_0}{e^2}|z_c - z_v|^{-1}$ and the exciton number operator $\hat{N}_{\text{ex}} = \frac{1}{2}\sum_{\mathbf{k}}(c^\dagger_{\mathbf{k},c}c_{\mathbf{k},c} - c_{\mathbf{k},v}c^\dagger_{\mathbf{k},v})$. (The charging energy E_C vanishes for a monolayer condensate.) Finally, $\rho_{\mathbf{q},c}/\rho_{\mathbf{q},v}$ denotes the electron density in the conduction/valence band.

The Hamiltonian in Eq. (3.4) assumes the dominant term approximation, which neglects the momentum dependence of wavefunction overlaps and interband scattering [46]. In this approximation, the electron density is just the sum of the densities

$$\rho_{\mathbf{q},i} = \sum_{\mathbf{k}} c^\dagger_{\mathbf{k},i}c_{\mathbf{k}+\mathbf{q},i} \tag{3.7}$$

in the two bands. Neglecting the momentum dependence of band overlaps is equivalent to approximating $u_{\mathbf{k}+\mathbf{w}_i,i}(\mathbf{r}) \simeq u_{\mathbf{w}_i,i}(\mathbf{r})$. This is justified when $u_{\mathbf{k}+\mathbf{w}_i,i}(\mathbf{r})$ is slowly varying with $\mathbf{k}$ on the scale of the inverse Bohr radius of the excitons. In what follows, we also use the simplified notation $u_{\mathbf{w}_i,i}(\mathbf{r}) \to u_i(\mathbf{r})$. In general, the electron density involves mixed terms involving both conduction and valence band operators, leading to interband scattering. For monolayer systems, these can be neglected when conduction and valence bands are offset by a finite momentum $\mathbf{w}$ (Fig 3.1a) and the Coulomb potential $V_{\mathbf{w}} \propto 1/|\mathbf{w}|$ is suppressed relative to intraband contributions [46]. For bilayer systems with conduction and valence bands residing in different layers, the neglect of interband scattering is justified by the vanishing overlap between the conduction and valence band wavefunctions [94, 113, 114] (Fig. 3.1b).

Within the dominant term approximation (DTA), interband scattering is neglected and the model has separate charge-conservation symmetries for conduction and valence electrons. Interband coherence spontaneously breaks these separate symmetries, leaving only overall charge conservation. In monolayer systems, interband coherence results in spatial density modulations at the wavevector $\mathbf{w}$, forming a charge density wave (CDW) within the spinless model. The origin of this CDW is arbitrary, leading to a gapless Goldstone mode. However, interband scattering (neglected in the DTA) explicitly breaks the separate charge conservation symmetries and generally pins the origin of the CDW, gapping out the Goldstone mode. Consequently, while monolayer exciton condensates spontaneously break the lattice translation symmetry, the independent charge conservation symmetries are explicitly broken by interband scattering terms in the interaction.

3.1.2 Mean-field solution

The Coulomb attraction between electrons in the conduction band and holes in the valence leads to spontaneous condensation of electron-hole pairs (excitons) as the band gap E_G is re-

duced below the exciton binding energy E_b [46–48]. In the BEC limit, we can view $\sum_{\mathbf{k}} \phi_{\mathbf{k}} c^\dagger_{\mathbf{k},c} c_{\mathbf{k},v}$ as the creation operator of an exciton with the (normalized, so that $\frac{1}{A}\sum_{\mathbf{k}} \phi^2_{\mathbf{k}} = 1$) hydrogenic 1s wave function $\phi_{\mathbf{k}}$ in momentum representation. The corresponding Bose-condensed state takes the form [90]

$$|\Psi_\lambda\rangle = \exp\left(\lambda \sum_{\mathbf{k}} \phi_{\mathbf{k}} c^\dagger_{\mathbf{k},c} c_{\mathbf{k},v}\right) |\mathrm{IS}\rangle \,, \tag{3.8}$$

where $|\mathrm{IS}\rangle = \prod_{\mathbf{k}} c^\dagger_{\mathbf{k},v} |\mathrm{vac}\rangle$ is the ground state of the intrinsic semiconductor. The eigenvalue λ of the coherent state controls the exciton density, with $n_{\mathrm{ex}} = |\lambda|^2$ in the dilute limit.

More generally, the exciton wave function $\phi_{\mathbf{k}}$ can be viewed as a variational parameter [90]. Expanding the exponential, the (normalized) coherent state can be rewritten as

$$|\Psi_\lambda\rangle = \Pi_{\mathbf{k}} (u_{\mathbf{k}} c^\dagger_{\mathbf{k},v} + v_{\mathbf{k}} c^\dagger_{\mathbf{k},c}) |\mathrm{vac}\rangle \,, \tag{3.9}$$

where

$$u_{\mathbf{k}} = \frac{1}{\sqrt{1+\lambda^2\phi^2_{\mathbf{k}}}} \tag{3.10}$$

$$v_{\mathbf{k}} = \frac{\lambda\phi_{\mathbf{k}}}{\sqrt{1+\lambda^2\phi^2_{\mathbf{k}}}}. \tag{3.11}$$

This shows that the BEC ansatz is in fact a Hartree-Fock approximation in terms of the variational Slater determinant $|\Psi_\lambda\rangle$, which is not limited to the BEC limit.

The optimal Slater determinant is obtained by mean-field decoupling the full interacting Hamiltonian of Eq. (3.4). This leads to the mean-field Hamiltonian [46, 90, 113]

$$\hat{H}_{\mathrm{MF}} = \sum_{\mathbf{k}} \begin{pmatrix} c^\dagger_{\mathbf{k},c} & c^\dagger_{\mathbf{k},v} \end{pmatrix} h_{\mathrm{mf}} \begin{pmatrix} c_{\mathbf{k},c} \\ c_{\mathbf{k},v} \end{pmatrix} \;;\; h_{\mathrm{mf}} = \begin{pmatrix} \bar{\epsilon}^c_{\mathbf{k}} & \Delta_{\mathbf{k}} \\ \Delta_{\mathbf{k}} & \bar{\epsilon}^v_{\mathbf{k}} \end{pmatrix}. \tag{3.12}$$

Here, the single-particle energies

$$\bar{\epsilon}^c_{\mathbf{k}} = \epsilon^c_{\mathbf{k}} - \frac{1}{A}\sum_{\mathbf{k}'} V_{cc}(\mathbf{k}-\mathbf{k}') \langle c^\dagger_{\mathbf{k}',c} c_{\mathbf{k}',c}\rangle + \frac{n_{\mathrm{ex}}}{2C_G}, \tag{3.13}$$

$$\bar{\epsilon}^v_{\mathbf{k}} = \epsilon^v_{\mathbf{k}} + \frac{1}{A}\sum_{\mathbf{k}'} V_{vv}(\mathbf{k}-\mathbf{k}') \langle c_{\mathbf{k}',v} c^\dagger_{\mathbf{k}',v}\rangle - \frac{n_{\mathrm{ex}}}{2C_G} \tag{3.14}$$

are renormalized by Fock and (for bilayer systems) interlayer capacitance terms, $n_{\mathrm{ex}} = \langle \hat{N}_{\mathrm{ex}}\rangle / A$ denotes the exciton density, and

$$\Delta_{\mathbf{k}} = -\frac{1}{A}\sum_{\mathbf{k}} V_{cv}(\mathbf{k}-\mathbf{k}') \langle c^\dagger_{\mathbf{k}',c} c_{\mathbf{k}',v}\rangle \tag{3.15}$$

measures the strength of interband coherence. We choose the order parameter to be real, which can be achieved by a suitable gauge transformation. Above, $\langle \hat{O} \rangle$ denotes the expectation value of an operator $\hat{O}$ in the trial state in Eq. (3.9). The self-consistent ground state of Eq. (3.12) is the Slater determinant, which minimizes the expectation value of the full Hamiltonian [115].

According to Koopman's theorem, the mean-field Hamiltonian h_{mf} in Eq. (3.12) describes the single-particle excitations [116]. This yields two bands with energies

$$E_{\mathbf{k},\pm} = \frac{\bar{\epsilon}^c_{\mathbf{k}} + \bar{\epsilon}^v_{\mathbf{k}}}{2} \pm \sqrt{\left(\frac{\bar{\epsilon}^c_{\mathbf{k}} - \bar{\epsilon}^v_{\mathbf{k}}}{2}\right)^2 + \Delta^2_{\mathbf{k}}}. \tag{3.16}$$

and eigenvectors $(u_{\mathbf{k}}, -v_{\mathbf{k}})$ for the upper $(+)$ and $(v_{\mathbf{k}}, u_{\mathbf{k}})$ for the lower $(-)$ band. The corresponding Bogoliubov operators are

$$d^\dagger_{\mathbf{k},+} = u_{\mathbf{k}} c^\dagger_{\mathbf{k},c} - v_{\mathbf{k}} c^\dagger_{\mathbf{k},v}, \tag{3.17}$$

$$d^\dagger_{\mathbf{k},-} = v_{\mathbf{k}} c^\dagger_{\mathbf{k},c} + u_{\mathbf{k}} c^\dagger_{\mathbf{k},v}. \tag{3.18}$$

The mean-field Hamiltonian in Eq. (3.12), written in terms of these operators is diagonal:

$$\hat{H}_{MF} = \sum_{\mathbf{k},\alpha=\pm} E_{\mathbf{k},\alpha} d^\dagger_{\mathbf{k},\alpha} d_{\mathbf{k},\alpha}. \tag{3.19}$$

At charge neutrality, all $d^\dagger_{\mathbf{k},-}$ orbitals are occupied, while all $d^\dagger_{\mathbf{k},+}$ orbitals are empty. Thus, the mean-field ground state is simply

$$\begin{aligned} |\mathrm{GS}\rangle &= \Pi_{\mathbf{k}} (u_{\mathbf{k}} c^\dagger_{\mathbf{k},v} + v_{\mathbf{k}} c^\dagger_{\mathbf{k},c}) \, |\mathrm{vac}\rangle \\ &= \Pi_{\mathbf{k}} (u_{\mathbf{k}} + v_{\mathbf{k}} c^\dagger_{\mathbf{k},c} c_{\mathbf{k},v}) \, |\mathrm{IS}\rangle \, , \end{aligned} \tag{3.20}$$

where the first line emphasizes the Hartree-Fock nature and the second the electron-hole pairing of $|\mathrm{GS}\rangle$. Using the expectation values $\langle c^\dagger_{\mathbf{k},c} c_{\mathbf{k},c} \rangle = \langle c_{\mathbf{k},v} c^\dagger_{\mathbf{k},v} \rangle = v^2_{\mathbf{k}}$ and $\langle c^\dagger_{\mathbf{k},c} c_{\mathbf{k},v} \rangle = u_{\mathbf{k}} v_{\mathbf{k}}$ in this state, the self-consistency equation reads

$$\begin{aligned} \left(\frac{\hbar^2 \mathbf{k}^2}{2m} + E_g + \frac{1}{A} \sum_{\mathbf{k}} \frac{v^2_{\mathbf{k}}}{C_G} - \frac{2}{A} \sum_{\mathbf{k}'} V_{cc}(\mathbf{k} - \mathbf{k}') v^2_{\mathbf{k}'} \right) u_{\mathbf{k}} v_{\mathbf{k}} = \\ = \left[\frac{1}{A} \sum_{\mathbf{k}'} V_{cv}(\mathbf{k} - \mathbf{k}') u_{\mathbf{k}'} v_{\mathbf{k}'} \right] (u^2_{\mathbf{k}} - v^2_{\mathbf{k}}), \end{aligned} \tag{3.21}$$

with the reduced mass $m = m_c m_v / (m_c + m_v)$.

We briefly make several comments. The excitonic ground state in Eq. (3.20) is reminiscent of the BCS ground state of superconductivity. Indeed, it has been suggested that decreasing E_G into the semimetallic regime leads to a BCS state of electrons and holes [90]. However, this

mean-field picture faces a series of subtleties. First, exciton-exciton interactions are generically attractive at large distances, resulting in a tendency of excitons to form molecules, which can in turn undergo BEC [111, 117–119]. Second, depending on details, the gas phase can be unstable to the formation of liquid droplets of excitons [120, 121]. Last, for increasing electron-hole densities, screening effects reduce the effective electron-hole attraction [112, 114, 122–125].

For bilayer condensates, biexciton and liquid-droplet formation are irrelevant, as the out-of-plane dipole moment of the excitons, represented by Eq. (3.6), renders the exciton-exciton interaction repulsive [113]. However, pairing is weakened due to the reduced interband Coulomb interaction, so that pairing is suppressed by screening effects at smaller densities [123–125], likely rendering only the BEC regime accessible.

In monolayer samples, weakly bound biexcitons should form at the smallest densities [111, 117–119] and a theory based on excitons is, strictly speaking, not valid. However, as biexcitonic binding is weak, we neglect this complication. At large densities, the electron-hole liquid renders the BCS regime inaccessible unless there is strong exciton-lattice coupling. However, such a phase would not classify as a pure interaction-driven exciton insulator. In contrast, lattice distortion in the BEC regime is small [46].

3.1.3 Low exciton density solution

For both monolayers and bilayers, we will focus on the low-exciton-density (BEC) regime, where we can exploit a systematic expansion of the mean-field solution [47, 90]. For $E_G > E_b$, there is only the trivial solution $u_{\mathbf{k}} = 1, v_{\mathbf{k}} = 0$. For $E_G < E_b$, there will be a finite density of excitons in the ground state given by $n_{\text{ex}} = \frac{1}{A}\sum_{\mathbf{k}} v_{\mathbf{k}}^2$. To lowest order in the low-density limit (small $v_{\mathbf{k}}$), Eq. (3.21) reduces to the excitonic Schrödinger equation [90]

$$\frac{\hbar^2 k^2}{2m} v_{\mathbf{k}} - \frac{1}{A}\sum_{\mathbf{k}'} V_{cv}(\mathbf{k}-\mathbf{k}') v_{\mathbf{k}'} = -E_G v_{\mathbf{k}}. \tag{3.22}$$

This equation is solved by setting $E_G = E_b$, the binding energy of the corresponding ground state (hydrogenic 1s) wavefunction $v_{\mathbf{k}} = \lambda\phi_{\mathbf{k}}$. At this order, one therefore recovers the bosonic coherent state of the excitons in Eq. (3.8).

The exciton density is determined by considering higher-order contributions in Eq. (3.21), assuming $v_{\mathbf{k}}$ is small. Since λ has units of $[\text{distance}]^{-1}$, the appropriate dimensionless expansion parameter is in fact λa_B^*, with the natural lengthscale of the system being the Bohr radius, $a_B^* = \frac{4\pi\epsilon_0\epsilon\hbar^2}{e^2 m}$. Physically, $\lambda a_B^* \ll 1$ is equivalent to $n_{\text{ex}}(a_B^*)^2 \ll 1$, the low exciton density limit.

While the small expansion parameter is λa_B^*, for clarity of notation, we write our expansion in terms of λ instead. We know from Eq. (3.22) that to lowest order, $v_{\mathbf{k}} = \lambda\phi_{\mathbf{k}}$ and $E_G = E_b$. Assuming this lowest-order solution, we expand to higher orders.

$$v_{\mathbf{k}} = \lambda\phi_{\mathbf{k}} + \lambda^2 v_{\mathbf{k}}^{(2)} + \lambda^3 v_{\mathbf{k}}^{(3)} + \dots \tag{3.23}$$

$$u_{\mathbf{k}} = \sqrt{1 - v_{\mathbf{k}}^2} \tag{3.24}$$

$$E_G = E_b + \lambda E_G^{(1)} + \lambda^2 E_G^{(2)} + \dots, \tag{3.25}$$

where we choose the functions $\phi_{\mathbf{k}}$, $v_{\mathbf{k}}^{(2)}$,$v_{\mathbf{k}}^{(3)}$,$\dots$ to be orthogonal to each other, and where $v_{\mathbf{k}}^{(n)} \propto (a_B^*)^n$ as a result of expanding in terms of λ and not λa_B^*.

To order λ^2, Eq. (3.21) reads:

$$E_G^{(1)}\phi_{\mathbf{k}} + \frac{\hbar^2\mathbf{k}^2}{2m}v_{\mathbf{k}}^{(2)} - \frac{1}{A}\sum_{\mathbf{k}'} V_{cv}(\mathbf{k}-\mathbf{k}')v_{\mathbf{k}'}^{(2)} = -E_b v_{\mathbf{k}}^{(2)}. \tag{3.26}$$

Projecting onto $\phi_{\mathbf{k}}$ and using Eq. (3.22), we obtain $E_G^{(1)} = 0$. Without $E_G^{(1)}$, we recover the lowest order Eq. (3.22) for $v_{\mathbf{k}}^{(2)}$, so that $v_{\mathbf{k}}^{(2)} \propto \phi_{\mathbf{k}}$, implying $v_{\mathbf{k}}^{(2)}$ can be absorbed into $\phi_{\mathbf{k}}$. Therefore, we set $v_{\mathbf{k}}^{(2)} = 0$.

To order λ^3, Eq. (3.21) reads:

$$\begin{aligned}\left[E_G^{(2)} + \frac{1}{A}\sum_{\mathbf{k}'}\frac{\phi_{\mathbf{k}'}^2}{C_G} - \frac{2}{A}\sum_{\mathbf{k}'}\left\{V_{cc}(\mathbf{k}-\mathbf{k}')\phi_{\mathbf{k}'}^2 - \phi_{\mathbf{k}}V_{cc}(\mathbf{k}-\mathbf{k}')\phi_{\mathbf{k}'}\right\}\right]\phi_{\mathbf{k}} + \\ + \left[(\frac{\hbar^2\mathbf{k}^2}{2m} + E_b)\phi_{\mathbf{k}} - \frac{1}{A}\sum_{\mathbf{k}'}V_{cv}(\mathbf{k}-\mathbf{k}')\phi_{\mathbf{k}'}\right]\frac{\phi_{\mathbf{k}}^2}{2} + \\ + \frac{\hbar^2\mathbf{k}^2}{2m}v_{\mathbf{k}}^{(3)} - \frac{1}{A}\sum_{\mathbf{k}'}V_{cv}(\mathbf{k}-\mathbf{k}')v_{\mathbf{k}'}^{(3)} = -E_b v_{\mathbf{k}}^{(3)}.\end{aligned} \tag{3.27}$$

Firstly, note that the second line vanishes by merit of Eq. (3.22). Secondly, multiplying by $\phi_{\mathbf{k}}$ and summing over $\mathbf{k}$ removes the $v_{\mathbf{k}}^{(3)}$ term, allowing $E_G^{(2)}$ to be evaluated as:

$$E_G^{(2)} = -\frac{1}{C_G} + \frac{2}{A^2}\sum_{\mathbf{k},\mathbf{k}'}\left[V_{cc}(\mathbf{k}-\mathbf{k}')\phi_{\mathbf{k}}^2\phi_{\mathbf{k}'}^2 - \phi_{\mathbf{k}}^3 V_{cv}(\mathbf{k}-\mathbf{k}')\phi_{\mathbf{k}'}\right], \tag{3.28}$$

where we used that $\phi_{\mathbf{k}}$ is normalized.

The exciton compressibility $\frac{d\mu_{\text{ex}}}{dn_{\text{ex}}} = -\frac{dE_G}{dn_{\text{ex}}} = -E_G^{(2)}$ is obtained by noting that $n_{\text{ex}} = \lambda^2 + O(\lambda^6)$, and is given by the following expression

$$\frac{d\mu_{\text{ex}}}{dn_{\text{ex}}} = \frac{1}{C_G} - \frac{2}{A^2}\sum_{\mathbf{k},\mathbf{k}'}\left[V_{cc}(\mathbf{k}-\mathbf{k}')\phi_{\mathbf{k}}^2\phi_{\mathbf{k}'}^2 - \phi_{\mathbf{k}}^3 V_{cv}(\mathbf{k}-\mathbf{k}')\phi_{\mathbf{k}'}\right], \tag{3.29}$$

where the first term is due to the geometric capacitance and reflects the dipole-dipole repulsion of excitons in bilayers, the second term is the intraband exchange energy gain, while the last term is the inter-band exchange repulsion.

In the monolayer case with $1/C_G = 0$ and a 2D Coulomb interaction, Eq. (3.22) can be solved analytically, giving the binding energy of $E_b = 4\text{Ry}^*$ (in terms of the excitonic Rydberg constant Ry^*), and the wavefunction

$$\phi_{\mathbf{k}} = a_B^*\sqrt{2\pi}\frac{1}{(1+(ka_B^*)^2/4)^{\frac{3}{2}}}, \tag{3.30}$$

where a_B^* is the excitonic Bohr radius. Furthermore, knowledge of this wavefunction allows the sums over $\mathbf{k}$ and $\mathbf{k}'$ in Eq. (3.29) to be performed, obtaining the numerical value of the exciton compressibility

$$\left.\frac{d\mu_{\text{ex}}}{dn_{\text{ex}}}\right|_{\text{monolayer}} \approx 6.0\,\text{Ry}^*(a_B^*)^2. \tag{3.31}$$

Knowledge of the wavefunction also allows the pairing term $\Delta_{\mathbf{k}}$ to be evaluated

$$\Delta_{\mathbf{k}} = \sum_{\mathbf{k}'}\frac{1}{A}V_{cv}(\mathbf{k}-\mathbf{k}')u_{\mathbf{k}'}v_{\mathbf{k}'} \approx \sum_{\mathbf{k}'}\frac{1}{A}V_{cv}(\mathbf{k}-\mathbf{k}')\lambda\phi_{\mathbf{k}'}^{1\text{s}}. \tag{3.32}$$

Comparing with the excitonic Schrödinger equation, Eq. 3.22, we can also write this as

$$\Delta_{\mathbf{k}} = \left(\frac{\hbar^2\mathbf{k}^2}{2m} + E_b\right)\lambda\phi_{\mathbf{k}}^{1\text{s}}. \tag{3.33}$$

Finally, we also evaluate the intraband Fock term, which reads

$$\Sigma_{\text{Fock}}(\mathbf{k}') = \frac{1}{A}\sum_{\mathbf{k}}V_{vv}(\mathbf{k}-\mathbf{k}')(v_{\mathbf{k}})^2 = \frac{1}{A}\sum_{\mathbf{k}}V_{cc}(\mathbf{k}-\mathbf{k}')(v_{\mathbf{k}})^2. \tag{3.34}$$

To evaluate it in the low density limit, we plug in $v_{\mathbf{k}}$ from Eq. (3.23). To order λ^2, we obtain

$$\Sigma_{\text{Fock}}(\mathbf{k}) \approx \frac{1}{4\pi^2}\int d\mathbf{k}' V_{vv}(\mathbf{k}-\mathbf{k}')(\lambda\phi_{\mathbf{k}'}^{1\text{s}})^2. \tag{3.35}$$

For general $\mathbf{k}$, this integral cannot be evaluated analytically. We can nevertheless analytically obtain a Taylor expansion of $\Sigma_{\text{Fock}}(\mathbf{k})$ giving

$$\Sigma_{\text{Fock}}(\mathbf{k})/\text{Ry}^* \approx \frac{3\pi^2}{2} n_{\text{ex}} (a_B^*)^2 - \frac{15\pi^2}{32} n_{\text{ex}} (a_B^*)^2 (k a_B^*)^2 + \dots, \tag{3.36}$$

where ... stand for terms of order $\mathcal{O}[(ka_B^*)^4]$. Keeping only terms up to $(ka_B^*)^2$ implies that these expressions are only accurate for $\mathbf{k} \approx 0$ – close to the band edge. In Subsection 3.3.1 below, we will use the above expression to evaluate the mean-field energies $E_{\mathbf{k},\pm}$ and densities of states in the low density limit.

3.2 Tunneling probes

Let us denote $\psi(\mathbf{r}_{\text{tip}})$ the electron operator at the position of the tip, and assume the system to be in an initial state $|i\rangle$ of energy E_i. Then, the tunneling conductance at tip-sample bias V is according to Fermi's golden rule given by

$$\frac{\mathrm{d}I}{\mathrm{d}V} = \frac{2\pi}{\hbar} t^2 e^2 g_s \nu_0 \sum_f \Big[|\langle f| \psi^\dagger(\mathbf{r}_{\text{tip}}) |i\rangle|^2 \delta(E_f - E_i + eV) + \\ + |\langle f| \psi(\mathbf{r}_{\text{tip}}) |i\rangle|^2 \delta(E_i - E_f + eV) \Big], \tag{3.37}$$

where t is the tunneling amplitude, ν_0 is the tip density of states per spin, and $g_s = 2$ is a factor accounting for spin degeneracy. The sum is over final many-body states $|f\rangle$ having energy E_f.

For a fermionic mean-field system, the above expression can be considerably simplified. First, by inverting Eq. (3.3), the electron operator $\psi(\mathbf{r}_{\text{tip}})$ is expanded in terms of the band operators:

$$\psi^\dagger(\mathbf{r}_{\text{tip}}) = \sum_{\mathbf{k}} \sum_i \frac{1}{\sqrt{N_{\text{UC}}}} e^{-i(\mathbf{k}+\mathbf{w}_i)\cdot\mathbf{r}_{\text{tip}}} u^*_{\mathbf{k}+\mathbf{w}_i,i}(\mathbf{r}_{\text{tip}}) c^\dagger_{\mathbf{k},i}. \tag{3.38}$$

Next, projectors onto each mean-field band α at momenutm $\mathbf{k}$ are defined as:

$$P^{(\alpha)}_{i,j}(\mathbf{k}) = \langle i|\mathbf{k},\alpha\rangle \langle \mathbf{k},\alpha|j\rangle, \tag{3.39}$$

where $|\mathbf{k},\alpha\rangle$is the solution of the mean-field Hamiltonian at $\mathbf{k}$ with energy $E_{\mathbf{k},\alpha}$. For the spinless exciton system of Sec. 3.1, we have the following projectors onto the upper and lower bands ($\alpha = \pm$) at $\mathbf{k}$:

$$P^{+}(\mathbf{k}) = \begin{pmatrix} u_{\mathbf{k}} \\ -v_{\mathbf{k}} \end{pmatrix} \begin{pmatrix} u_{\mathbf{k}} & -v_{\mathbf{k}} \end{pmatrix} = \begin{pmatrix} u_{\mathbf{k}}^2 & -u_{\mathbf{k}}v_{\mathbf{k}} \\ -u_{\mathbf{k}}v_{\mathbf{k}} & v_{\mathbf{k}}^2 \end{pmatrix} \tag{3.40}$$

$$P^{-}(\mathbf{k}) = \begin{pmatrix} v_{\mathbf{k}} \\ u_{\mathbf{k}} \end{pmatrix} \begin{pmatrix} v_{\mathbf{k}} & u_{\mathbf{k}} \end{pmatrix} = \begin{pmatrix} v_{\mathbf{k}}^2 & u_{\mathbf{k}}v_{\mathbf{k}} \\ u_{\mathbf{k}}v_{\mathbf{k}} & u_{\mathbf{k}}^2 \end{pmatrix}, \tag{3.41}$$

which encode all the information about the eigenstates of the mean-field Hamiltonian, Eq. (3.12).

Using this framework, the tunneling conductance at sample-tip bias V can be compactly written as a sum over the mean-field eigenstates:

$$\frac{\mathrm{d}I}{\mathrm{d}V} = \frac{2\pi}{\hbar} t^2 e^2 g_s \nu_0 \,\mathrm{Tr}\left[\frac{\Phi(\mathbf{r}_{\text{tip}})}{A} \sum_{\mathbf{k},\alpha} P^{(\alpha)}(\mathbf{k}) \delta(E_{\mathbf{k},\alpha} - eV)\right], \tag{3.42}$$

where we defined a matrix of wavefunctions at the position of the tip as

$$\left[\Phi(\mathbf{r}_{\text{tip}})\right]_{i,j} = A_{\text{UC}} e^{i(\mathbf{w}_j - \mathbf{w}_i)\cdot\mathbf{r}_{\text{tip}}} u^{*}_{\mathbf{w}_i,i}(\mathbf{r}_{\text{tip}}) u_{\mathbf{w}_j,j}(\mathbf{r}_{\text{tip}}), \tag{3.43}$$

where A_{UC} denotes the unit cell area. Note that in this equation, the weak dependence on momentum $\mathbf{k}$ of periodic parts of the Bloch functions $u_{\mathbf{w}_i+\mathbf{k},i}(\mathbf{r})$ was neglected. The advantage of the above expression is that it separates the real-space dependence on the band wavefunctions, encoded in $\Phi(\mathbf{r}_{\text{tip}})$, from the dependence on the solution of the mean-field equations, which is to a large extent (entirely in the dominant-term approximation) independent of the detailed structure of the band wavefunctions. The diagonal components of $\Phi(\mathbf{r}_{\text{tip}})$ are squared moduli of wavefunctions and have the lattice periodicity, while off-diagonal comonents have additional oscillations at wavevector $(\mathbf{w}_i - \mathbf{w}_j)$ if $\mathbf{w}_i \neq \mathbf{w}_j$. These off-diagonal terms lead to signatures of translational symmetry breaking in monolayer condensates.

Spatial averaging in this framework is straightforward. Assuming the tip tunnels at $z = 0$, we obtain the spatial average of $\Phi(\mathbf{r}_{\text{tip}})$, which is the only term depending on $\mathbf{r}_{\text{tip}}$ in Eq. (3.42), as follows:

$$\frac{1}{A}\int_{\text{z=0}} d\mathbf{r}_{\text{tip}}\, \Phi(\mathbf{r}_{\text{tip}}) = \mathrm{Diag}(\delta_{z_j,0}), \tag{3.44}$$

where $\delta_{z_j,0}$ is one for layers states localized at $z = 0$ and zero otherwise.

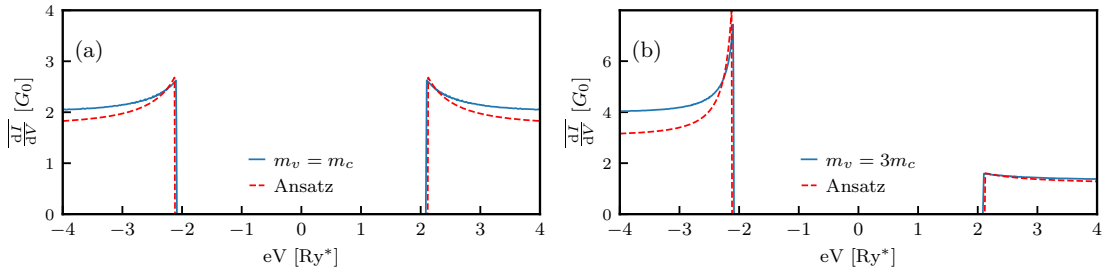

Figure 3.2: Spatially averaged DOS for a monolayer [Eq. (3.45)]. Numerical results (blue) are compared to analytical results from Eqs. (3.49),(3.50), working at $n_{\text{ex}} = 0.025\,(a_B^*)^{-2}$ (a) for equal masses, $m_c = m_v$ (b) for unequal masses, $m_v = 3m_c$.

For a monolayer, we have that $z_j = 0$ for each j, and the right hand side becoms the identity matrix. The spatially averaged $\frac{\mathrm{d}I}{\mathrm{d}V}$ (denoted $\overline{\frac{\mathrm{d}I}{\mathrm{d}V}}$) is then

$$\left.\overline{\frac{\mathrm{d}I}{\mathrm{d}V}}\right|_{\text{monolayer}} = \frac{2\pi}{\hbar} t^2 e^2 g_s \nu_0 \frac{1}{A} \sum_{\mathbf{k},\alpha} \delta(E_{\mathbf{k},\alpha} - eV), \tag{3.45}$$

measuring the total density of states (DOS).

Since neither the tunneling amplitude t nor the tip density of states ν_0 are directly experimentally accessible, we express our results in terms of:

$$G_0 = g_s \frac{m}{\hbar^3} t^2 e^2 \nu_0, \tag{3.46}$$

which corresponds to a spatially averaged conductance into a parabolic band with mass m. Experimentally, this conductance can be obtained from the normal state conductances into the conduction and valence bands, which differ from the above equation only by the replacement $m \to m_c$ for the conduction band and $m \to m_v$ for the valence band.

Note that strictly speaking, $E_{\mathbf{k},\alpha}$ in Eq. (3.42) should be measured with respect to the chemical potential, as the tip bias physically corresponds to the difference of electrochemical potentials of the sample and the tip. For a gapped system like an exciton condensate, the chemical potential can be anywhere in the gap, with position tunable by a back gate, so that there is no natural choice of chemical potential. Therefore, we do not include it, noting that our $\frac{\mathrm{d}I}{\mathrm{d}V}$ spectra hold up to an overall energy shift.

3.3 Tunneling into monolayer exciton condensates – spinless case

Let us now consider a spinless monolayer, in which the conduction band minimum and valence band maximum are offset by a wavevector $\mathbf{w} = \mathbf{w}_c - \mathbf{w}_v$, see Figure 3.1a. For simplicity, and

to emphasize the essential physics, we assume in this section that $\mathbf{w}$ is incommensurate with the lattice. The wavefunction matrix at $\mathbf{r}$ is

$$\Phi^{\text{spinless}}(\mathbf{r}) = A_{\text{UC}} \begin{pmatrix} |u_c(\mathbf{r})|^2 & e^{-i\mathbf{w}\cdot\mathbf{r}} u_c^*(\mathbf{r}) u_v(\mathbf{r}) \\ e^{i\mathbf{w}\cdot\mathbf{r}} u_c(\mathbf{r}) u_v^*(\mathbf{r}) & |u_v(\mathbf{r})|^2 \end{pmatrix}, \tag{3.47}$$

which has oscillatory off-diagonal components breaking lattice periodicity. Due to the structure of Eq. (3.42), therefore, if the projector matrices $P^{\pm}(\mathbf{k})$ have off-diagonal components, the spatial dependence of $\frac{\mathrm{d}I}{\mathrm{d}V}$ will break lattice translation symmetry.

In this Section, we first discuss spatially averaged tunneling in Subsection 3.3.1. We subsequently discuss the spatial dependence of $\frac{\mathrm{d}I}{\mathrm{d}V}$ in Subsection 3.3.2. We conclude with Subsection 3.3.3, which presents a method to extract the exciton wavefunction by combining the spatially averaged and spatially dependent measurements.

3.3.1 Spatially averaged tunneling

As shown in Eq. (3.45), spatially averaged tunneling in a monolayer probes the total density of states. We can obtain analytical insights by using the perturbative solution in the low exciton density limit, Eq. (3.23). In this limit, we obtained the value of the pairing term $\Delta_{\mathbf{k}}$ in Eq. (3.33), the value of the intraband Fock renormalizations in Eq. (3.36), as well as the exciton compressibility in Eq.(3.31). Together, these are sufficient to obtain the mean-field energies, defined in Eq. (3.16), to linear order in n_{ex}.

Firstly, to linear order in n_{ex}, the gap increases to

$$E_{0,+} - E_{0,-} = \left[4 - 6.0\tilde{n}_{\text{ex}} + 16\pi\tilde{n}_{\text{ex}} - 3\pi^2\tilde{n}_{\text{ex}}\right] \text{Ry}^*, \tag{3.48}$$

where we defined the exciton density in atomic units as $\tilde{n}_{\text{ex}} = n_{\text{ex}}(a_B^*)^2$. The first two terms are the single-particle band gap $E_G = E_b - \frac{d\mu_{\text{ex}}}{dn_{\text{ex}}} n_{\text{ex}}$, where $E_b = 4\,\text{Ry}^*$ is the monolayer binding energy, and where $\frac{d\mu_{\text{ex}}}{dn_{\text{ex}}} = (6.0)\,\text{Ry}^*(a_B^*)^2$ is the inverse exciton compressibility, obtained in Eq. (3.31). The third term, $(16\pi\tilde{n}_{\text{ex}})\,\text{Ry}^*$, is the increase of the interacting gap due to a finite pairing term $\Delta_{\mathbf{k}}$ on the off-diagonals in Eq. (3.12). To evaluate it, we use the analytical expression of Eq. (3.33). The last term, $(-3\pi^2\tilde{n}_{\text{ex}})\,\text{Ry}^* = -2\Sigma_{\text{Fock}}(\mathbf{k}=0)$, is due to the intraband Fock term of Eq. (3.36) evaluated at $\mathbf{k} = 0$. This term acts to reduce the gap.

Secondly, the tunneling conductance $\frac{\mathrm{d}I}{\mathrm{d}V}$ at positive bias is

$$\overline{\frac{\mathrm{d}I}{\mathrm{d}V}}(eV > 0) = G_0\Theta(eV - E_{0,+}) \left[\frac{m}{m_c} + \frac{15\pi^2}{64}\tilde{n}_{\text{ex}} - \frac{256\pi\tilde{n}_{\text{ex}}}{\left(4 + \frac{m_c}{m}(eV - E_{0,+})/\text{Ry}^*\right)^3}\right]^{-1}, \tag{3.49}$$

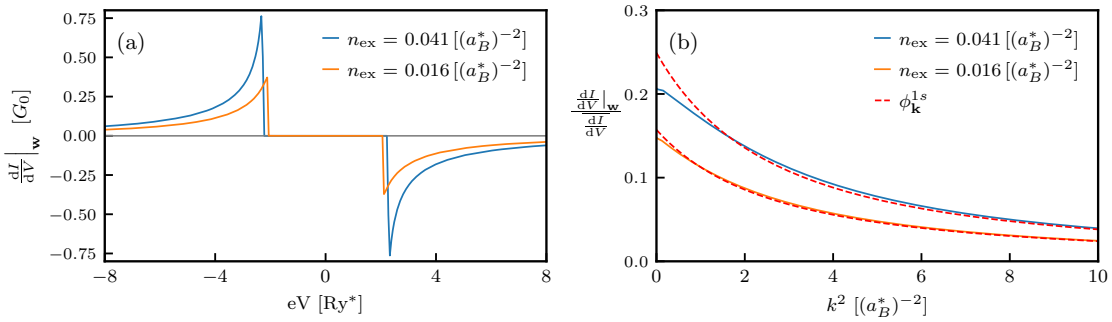

Figure 3.3: (a) Wavevector $\mathbf{w}$ component of $\frac{\mathrm{d}I}{\mathrm{d}V}$ at $n_{\text{ex}} = 0.041(a_B^*)^{-2}$ (orange) and $n_{\text{ex}} = 0.041(a_B^*)^{-2}$ (blue). We take $m_c = m_v$. (b) Wavefunction deduced from a combination of oscillating and average $\frac{\mathrm{d}I}{\mathrm{d}V}$, plotted as a function of $k^2 = \frac{e\bar{I}}{G_0\,\mathrm{Ry}^*}(a_B^*)^{-2}$, cf. Eq. (3.56). Shown in dashed red is the analytical wavefunction, Eq. (3.30) multiplied by a constant to fit the inferred wavefunctions.

while at negative bias, it is

$$\overline{\frac{\mathrm{d}I}{\mathrm{d}V}}(eV<0) = G_0\Theta(E_{0,-}-eV) \left[\frac{m}{m_v} + \frac{15\pi^2}{64}\tilde{n}_{\text{ex}} - \frac{256\pi\tilde{n}_{\text{ex}}}{\left(4+\frac{m_v}{m}(E_{0,-}-eV)/\mathrm{Ry}^*\right)^3}\right]^{-1}, \quad (3.50)$$

where the first term in square brackets is the non-interacting term, the second term is a mass renormalization due to the intraband Fock term, and the third term is due to the excitonic pairing, leading to a peak in the tunneling signal at the band edge. Note that the above results were obtained using a Taylor expansion of the intraband Fock term around $\mathbf{k} = 0$ given in Eq. (3.36), meaning they are only valid close to the band edge ($eV \approx E_{0,\pm}$).

The main conclusion to be drawn from Eqs. (3.49) and (3.50) is that for differing conduction and valence band masses, the peak at the band edge will be more pronounced for the heavier band. Numerical solution of the mean-field equations, shown in Figs. 3.2a,b confirms these analytical expectations. In these plots, we compare the analytical results (shown in red) with Hartree-Fock numerical simulations (shown in blue) for equal (a) and different (b) masses. The analytical expressions match well close to the band edge, accurately capturing the more pronounced effect of excitons on the heavier side. On the other hand, further away from the band edge, the analytical and numerical results deviate. This is a result of using a Taylor expanded expression for the intraband Fock [Eq. (3.36)], leading to large deviations for $|eV| \to \infty$, where we expect the non-interacting density of states to be recovered. Our Taylor expanded expression for the intraband Fock term, however, wrongly predicts a mass renormalization in this limit.

3.3.2 Tunneling current oscillations

Studying the spatial Fourier transform of $\frac{\mathrm{d}I}{\mathrm{d}V}$ reveals exciton-driven oscillations at wavevector $\mathbf{w}$ and more generally at $\mathbf{w}+\mathbf{G}$ for a reciprocal lattice vector $\mathbf{G}$:

$$\left.\frac{\mathrm{d}I}{\mathrm{d}V}\right|_{\mathbf{w}+\mathbf{G}} = \frac{2\pi}{\hbar}t^2e^2g_s\nu_0\,\langle u_{\mathbf{w}_v,v}|u_{\mathbf{w}_c+\mathbf{G},c}\rangle \frac{1}{A}\sum_{\mathbf{k}} u_{\mathbf{k}}v_{\mathbf{k}}[\delta(E_{\mathbf{k},-}-eV)-\delta(E_{\mathbf{k},+}-eV)], \quad (3.51)$$

where the wavefunction overlap is defined as

$$\langle u_{\mathbf{w}_v,v}|u_{\mathbf{w}_c+\mathbf{G},c}\rangle = \int_{\mathrm{UC}} d\mathbf{r}\, u_v^*(\mathbf{r})e^{i\mathbf{G}\cdot\mathbf{r}}u_c(\mathbf{r}), \quad (3.52)$$

with UC denoting the unit cell. This overlap typically decays quickly with $\mathbf{G}$, implying the strongest signal at $\mathbf{w}$. A crucial difference from the spatially averaged result of Eq. (3.45) is the additional weight factor $u_{\mathbf{k}}v_{\mathbf{k}}$.

In the low exciton density limit, the perturbative solution of Sec. 3.1.2 gives

$$u_{\mathbf{k}}v_{\mathbf{k}} \approx \sqrt{An_{\mathrm{ex}}}\phi_{\mathbf{k}}^{1s}, \quad (3.53)$$

with the exciton wavefunction $\phi_{\mathbf{k}}^{1s}$ given in Eq. 3.30. We plot the oscillatory component in Figure 3.3a for two representative values of the exciton density n_{ex}, where we use the value $\langle u_{\mathbf{w}_c,c}|u_{\mathbf{w}_v,v}\rangle = \frac{1}{2}$ for the band overlap, modelling a scenario in which the conduction and valence bands have similar orbital character. Note that due to the $u_{\mathbf{k}}v_{\mathbf{k}}$ factor, the oscillatory signal decays quickly away from the band edge.

These lattice-symmetry breaking oscillations in $\frac{\mathrm{d}I}{\mathrm{d}V}$ are a signature of a coherent exciton condensate in the BEC limit, and are analogous to the Kekulé pattern observed recently in graphene devices [105–107]. Importantly, these oscillations would not be present for an incoherent exciton gas [114], which occurs at elevated temperatures.

3.3.3 Recovering the wavefunction

Remarkably, by combining the spatially averaged and wavevector-$\mathbf{w}$ measurements, the exciton wavefunction can be recovered as follows. Firstly, the wavevector $\mathbf{w}$ measurement $\frac{\mathrm{d}I}{\mathrm{d}V}\big|_{\mathbf{w}}$ [Eq. (3.51)] is divided by the spatially averaged measurement $\overline{\frac{\mathrm{d}I}{\mathrm{d}V}}$ [Eq. (3.45)], cancelling the density of states factor. Assuming a rotationally symmetric solution (suggested by the fact that the exciton ground state is the symmetric 1s state), we obtain at positive bias

$$\left.\frac{\mathrm{d}I}{\mathrm{d}V}\right|_{\mathbf{w}} \Big/ \overline{\frac{\mathrm{d}I}{\mathrm{d}V}}(V>0) \propto \Theta(eV-E_+^0)u_{k(V)}v_{k(V)}, \quad (3.54)$$

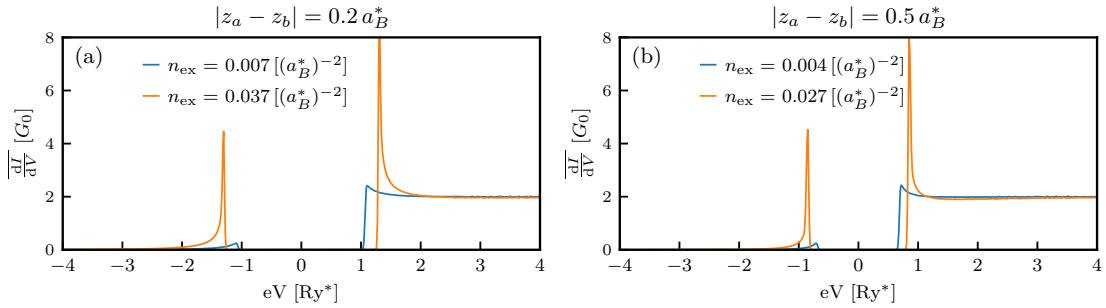

Figure 3.4: (a) Spatially averaged $\frac{\mathrm{d}I}{\mathrm{d}V}$ into a bilayer EC for $|z_a - z_b| = 0.2\,a_B^*$ for two values of n_{ex}. The appearance of a peak at negative bias is a highlight of exciton condensation, whose integrated weight gives n_{ex}. (b) Like (a) but with $|z_a - z_b| = 0.5\,a_B^*$. The integrated weight of the negative bias peak yields n_{ex}, cf. Eq. (3.59). For both plots, we take $m_c = m_v$.

where $k = |\mathbf{k}|$. The function $k(V)$ is for $eV > E_+^0$ defined implicitly as

$$E_{k(V),+} = eV, \tag{3.55}$$

where monotonicity of $E_{k,+}$ was assumed, which is a natural assumption in the BEC regime.

Secondly, a change of variables from bias to momentum needs to be performed. To that end, we use that the total spatially-averaged current $\overline{I}$ at positive bias V can be obtained by integrating $\overline{\frac{\mathrm{d}I}{\mathrm{d}V}}$ from the conduction band bottom up to the bias V. This integral is in turn related to the total number of states up to the momentum $k(V)$ [defined in Eq. (3.55)] corresponding to the bias V as follows

$$\overline{I}(V) = \int_{E_+^0}^{E_{k(V),+}} d(eV)\,\overline{\frac{\mathrm{d}I}{\mathrm{d}V}} = G_0 \frac{\mathrm{Ry}^*}{e}[k(V)a_B^*]^2. \tag{3.56}$$

Noting that $\overline{I}(V)$ is directly observable in an STM experiment, $k(V)$ can be obtained and inverted, allowing the recovery of $u_k v_k$ and therefore [using Eq. (3.53)] also of the exciton wavefunction.

We show the resulting quantity obtained using a numerical mean-field solution as a function of k^2 in Figure 3.3b in blue and orange, comparing to the analytical expectation $\phi_{\mathbf{k}}^{1s}$ of Eq. (3.30), shown in dashed red. For small n_{ex} (shown in orange), the shape can be fit perfectly with the analytical form, where only the overall prefactor of the wavefunction needs to be fit (shown in dashed red). On the other hand, for larger n_{ex} (shown in blue), it deviates for small momenta. This deviation results because $v_{\mathbf{k}}$ becomes large for small momenta $\mathbf{k}$, so that assuming $u_{\mathbf{k}} \approx 1$ as in Eq. (3.53) is no longer valid. Nevertheless, we conclude that in the low exciton density limit, spatial oscillations in the STM signal, in addition to establishing an exciton condensate, enable the form of the exciton wavefunction to be recovered.

3.4 Tunneling into a bilayer exciton condensate

In a bilayer setup, only the conduction band is tunneled into, cf. Figure 3.1b. In this case $u_{\mathbf{k},v}(\mathbf{r}_{\text{tip}}) = 0$ vanishes due to the vertical offset and the matrix of wavefunctions $\Phi(\mathbf{r}_{\text{tip}})$ is

$$\Phi(\mathbf{r}_{\text{tip}}) = \begin{pmatrix} |u_c(\mathbf{r}_{\text{tip}})|^2 & 0 \\ 0 & 0 \end{pmatrix}. \tag{3.57}$$

This form implies that there is no lattice translation symmetry breaking – the only spatial dependence is lattice periodic. We therefore concentrate on spatially averaged tunneling, which already shows important differences to averaged tunneling in a monolayer.

The matrix of wavefunctions will pick out the $(1,1)$ component of the projector matrices [Eq. (3.40) and Eq. (3.41)], yielding

$$\overline{\frac{\mathrm{d}I}{\mathrm{d}V}} = \frac{2\pi}{\hbar} t^2 e^2 \nu_0 g_s \frac{1}{A} \sum_{\mathbf{k}} \left[v_{\mathbf{k}}^2 \delta(E_{\mathbf{k},-} - eV) + u_{\mathbf{k}}^2 \delta(E_{\mathbf{k},+} - eV) \right], \tag{3.58}$$

which probes the DOS, but weighted by the factors $(v_{\mathbf{k}})^2$ and $(u_{\mathbf{k}})^2$ for the upper and lower bands, respectively.

In Figures 3.4a and 3.4b, we show the spatially averaged conductance $\overline{\frac{\mathrm{d}I}{\mathrm{d}V}}$ in a bilayer for two values of interlayer distance $\frac{|z_c - z_v|}{a_B^*} = 0.2, 0.5$, respectively. The presence of excitons manifests in the satellite peak emerging at negative bias, arising from the $(v_{\mathbf{k}})^2$ term in Eq. (3.58). Physically, it reflects the exciton-enabled possibility for the conduction band electrons bound to valence holes to tunnel out, leaving behind a spare hole in the valence band, illustrated in Fig. 3.1a. Increasing $|z_c - z_v|$ reduces the exciton binding energy [126], so that the satellite peak and conduction band come closer together, as seen by comparing Fig. 3.4b to Fig. 3.4a.

Integrating $\overline{\frac{\mathrm{d}I}{\mathrm{d}V}}$ across the satellite peak provides a measurement of the local exciton density in the ground state:

$$\overline{I}(V = -\infty) = \int_{E_-^0}^{-\infty} dV \overline{\frac{\mathrm{d}I}{\mathrm{d}V}} = -G_0 4\pi \frac{\mathrm{Ry}^*}{e} n_{\text{ex}}, \tag{3.59}$$

which is particularly useful in inhomogeneous samples where n_{ex} has a spatial variation, rendering global probes inaccurate.

We note that while the presence of an additional peak is a signature that excitons are present, in contrast to the monolayer case, STM in the bilayer setup is not sensitive to exciton coherence. The satellite peak will occur even for an incoherent Bose gas, as the process in Fig. 3.1a does not depend on excitons forming a BEC.

3.5 Tunneling into monolayer exciton condensates – extension to spinful condensates

Since exciton condensates can also possess a spin-structure, in this Section we consider tunneling into a spinful exciton condensate. First, in Subsection 3.5.1, we generalize the framework of Section 3.2 to the spinful case. We then introduce a minimal spinful model of exciton condensates in Subsection 3.5.2, analyzing it in the context of tunneling probes in Subsection 3.5.3.

3.5.1 Tunneling including spin

The spin-structure of exction condensates can be probed by a tip that is partially polarized along a certain spin direction, with the following densities of states for the two spins in the tip:

$$\nu_\uparrow = \nu_0 + \delta\nu/2 \tag{3.60}$$

$$\nu_\downarrow = \nu_0 - \delta\nu/2, \tag{3.61}$$

where $\delta\nu$ parametrizes the difference between the densities of states for the two spins. We define electron operators for the two spins $s = \uparrow / \downarrow$ in the tip

$$\psi_s^\dagger(\mathbf{r}_{\text{tip}}) = \sum_{\mathbf{k}} \sum_i \phi_{\mathbf{k},i}(\mathbf{r}_{\text{tip}}, s) c_{\mathbf{k},i}^\dagger, \tag{3.62}$$

where the band label i also runs over (pseudo-)spin labels. We also define wavefunction matrices for each spin:

$$[\Phi_s(\mathbf{r})]_{i,j} = A_{\text{UC}} e^{i(\mathbf{w}_j - \mathbf{w}_i)\cdot\mathbf{r}} u^*_{\mathbf{w}_i,i}(\mathbf{r}, s) u_{\mathbf{w}_j,j}(\mathbf{r}, s). \tag{3.63}$$

Separating into terms proportional to ν_0 and $\delta\nu$, the local tunneling conductance reads

$$\frac{\mathrm{d}I}{\mathrm{d}V} = \frac{2\pi}{\hbar} t^2 e^2 \operatorname{Tr}\Bigg\{ \left[\nu_0 (\Phi_\downarrow(\mathbf{r}) + \Phi_\uparrow(\mathbf{r})) + \frac{\delta\nu}{2} (\Phi_\uparrow(\mathbf{r}) - \Phi_\downarrow(\mathbf{r})) \right] \frac{1}{A} \sum_{\mathbf{k},\alpha} P^{(\alpha)}(\mathbf{k}) \delta(E_{\mathbf{k},\alpha} - eV) \Bigg\}. \tag{3.64}$$

As we will see, the $\delta\nu$ term probes the spin structure.

3.5.2 Minimal spinful exciton insulator model

The simplest realistic model for an exciton condensate including spin was introducing in [46]. In this time-reversal invariant model, we have doubly (spin) degenerate conduction and valence bands and assume independent spin-rotation symmetry in the conduction and valence band (no spin-orbit coupling). This model can be thought of as two copies of the model of Sec. 3.1.

Time-reversal symmetry forces $\mathbf{w}_c$ and $\mathbf{w}_v$ to be time-reversal invariant momenta so that the momentum difference $\mathbf{w} = \mathbf{w}_c - \mathbf{w}_v$ is also a time-reversal invariant momentum, which we assume to be nonzero. Using the mean-field ground state for the spinless case, Eq. (3.20), one mean-field charge neutral ground state for this spinful model is simply two copies of the spinless solution:

$$|\mathrm{GS}\rangle = \Pi_{\mathbf{k},s=\uparrow,\downarrow}(u_{\mathbf{k}} + v_{\mathbf{k}} c^{\dagger}_{\mathbf{k},c,s} c_{\mathbf{k},v,s}) \, |\mathrm{IS}\rangle \, , \tag{3.65}$$

which has doubly degenerate upper and lower bands with energies given in Equations (3.16).

Using the basis set $\{|\mathbf{k}, c, \uparrow\rangle \, , |\mathbf{k}, c, \downarrow\rangle \, |\mathbf{k}, v, \downarrow\rangle \, |\mathbf{k}, v, \downarrow\rangle\}$, the projector onto the spin-degenerate upper and lower bands is given by a tensor product

$$P^{\pm}_{\mathbb{I}}(\mathbf{k}) \;\; = \;\; P^{\pm}(\mathbf{k}) \otimes \mathbb{I}, \tag{3.66}$$

where $\mathbb{I}$ is the 2-by-2 identity matrix. Explicitly, we have for the upper projector

$$P^{+}_{\mathbb{I}}(\mathbf{k}) \;\; = \;\; \begin{pmatrix} (u_{\mathbf{k}})^2 & 0 & -u_{\mathbf{k}} v_{\mathbf{k}} & 0 \\ 0 & (u_{\mathbf{k}})^2 & 0 & -u_{\mathbf{k}} v_{\mathbf{k}} \\ -u_{\mathbf{k}} v_{\mathbf{k}} & 0 & (v_{\mathbf{k}})^2 & 0 \\ 0 & -u_{\mathbf{k}} v_{\mathbf{k}} & 0 & (v_{\mathbf{k}})^2 \end{pmatrix}, \tag{3.67}$$

and analogously for the lower band projector. Within this model, there is $U(2) \times U(2)$ symmetry, so that other ground states can be generated by rotating the spin axis of conduction/valence bands. In fact, the entire ground state manifold can be generated by the following transformation:

$$\begin{pmatrix} w & 0 \\ 0 & \mathbb{I} \end{pmatrix}, \tag{3.68}$$

where $w \in U(2)$ is a 2-by-2 unitary matrix rotating the spin axis in the conduction band. The projectors are now labeled by the matrix w and read:

$$P^{\pm}_{w}(\mathbf{k}) = \begin{pmatrix} w & 0 \\ 0 & \mathbb{I} \end{pmatrix} P^{\pm}_{\mathbb{I}}(\mathbf{k}) \begin{pmatrix} w^{\dagger} & 0 \\ 0 & \mathbb{I} \end{pmatrix}. \tag{3.69}$$

By analyzing the energetics of different matrices in the presence of terms beyond the dominant term approximation, Halperin and Rice [46] find two candidate ground state matrices. The first, denoted the charge-density wave (CDW), reads:

$$w_{\mathrm{CDW}} = \mathbb{I}, \tag{3.70}$$

while the second, denoted the spin-density wave (SDW), reads:

$$w_{\mathrm{SDW}} = \mathbf{n} \cdot \boldsymbol{\sigma}, \tag{3.71}$$

where $\mathbf{n}$ is a unit vector and $\boldsymbol{\sigma}$ is the vector of Pauli matrices. The CDW state is simply the state in Eq. (3.65), and can be understood as two identical copies of the spinless exciton condensate. For $\mathbf{n} = (0, 0, 1)$, the SDW state also consists of two such copies, but with opposite sign of the order parameter for the two spins. The SDW state for a general $\mathbf{n}$ can then be understood as a rotated version of the $\mathbf{n} = (0, 0, 1)$ state, having opposite sign of the order parameter for the two spin components defined with respect to the direction $\mathbf{n}$.

We note that Halperin and Rice [46] find that at small electron-phonon coupling strength, the SDW state is the ground state, while at large enough electron-phonon coupling, the CDW state becomes the ground state.

3.5.3 Tunneling into the spinful model

For the above spinful model, the sum of the wavefunction matrices for the two spin components is given as

$$\Phi_\uparrow(\mathbf{r}) + \Phi_\downarrow(\mathbf{r}) = \Phi^{\mathrm{spinless}}(\mathbf{r}) \otimes \mathbb{I}, \tag{3.72}$$

while their difference is

$$\Phi_\uparrow(\mathbf{r}) - \Phi_\downarrow(\mathbf{r}) = \Phi^{\mathrm{spinless}}(\mathbf{r}) \otimes \mathbf{m} \cdot \boldsymbol{\sigma}, \tag{3.73}$$

where $\mathbf{m}$ is the spin polarization direction in the tip. The sum contributes to spin-averaged tunneling [proportional to ν_0 in Eq. (3.64)], while the difference contributes to the spin-polarized component [proportional to $\delta\nu$ in Eq. (3.64)].

First, consider spin averaged tunneling [proportional to ν_0 in Eq. (3.64)]. Spatial averaging recovers the spinless answer (discussed in Section 3.3), probing the total density of states. Similarly to the spinless case, excitons will cause spatial oscillations in $\frac{\mathrm{d}I}{\mathrm{d}V}$ at wavevector $\mathbf{w}+\mathbf{G}$. However, since we are assuming time-reversal symmetry, $\mathbf{w}$ is a commensurate wavevector. This implies specifically that $-\mathbf{w}$ and $\mathbf{w}$ are equivalent points in the Brillouin zone. Therefore, both off-diagonal components in Eq. (3.47) contribute to a given Fourier component. With this caveat, the result for the oscillating, spin-averaged component is

$$\left.\frac{\mathrm{d}I}{\mathrm{d}V}\right|_{\mathbf{w}+\mathbf{G}} = \frac{2\pi}{\hbar} t^2 e^2 \nu_0 \langle u_v | u_c \rangle \operatorname{Tr}\left(w + w^\dagger\right) \frac{1}{A} \sum_{\mathbf{k}} u_{\mathbf{k}} v_{\mathbf{k}} [\delta(E_{\mathbf{k},-} - eV) - \delta(E_{\mathbf{k},+} - eV)]. \tag{3.74}$$

Importantly, compared to the spinless model, we have an extra factor $\mathrm{Tr}\big(w + w^\dagger\big)$. For the SDW state, this factor vanishes as the oscillations of the up and down spin exactly cancel. For the CDW state, on the other hand, we recover two times the answer of Subsection 3.3.2. The additional factor of two can be traced back to $-\mathbf{w}$ and $\mathbf{w}$ being equivalent wavevectors in this time-reversal invariant model. On the other hand, in the spinless model, we assumed that $\mathbf{w}$ is an incommensurate wavevector. As in Subsection 3.3.3, the wavefunction can be recovered by combining the oscillatory and spatially averaged signal for the CDW state.

The spin-polarization component [proportional to $\delta\nu$ in Eq. (3.64)] can be evaluated analogously. The spatial average vanishes for both candidate states (CDW and SDW) under consideration, as neither of them has an overall magnetization. However, there is a wavevector-$(\mathbf{w}+\mathbf{G})$ Fourier component, which reads:

$$\left.\frac{\mathrm{d}I}{\mathrm{d}V}\right|_{\mathbf{w}+\mathbf{G}} = \frac{2\pi}{\hbar} t^2 e^2 \frac{\delta\nu}{2} \langle u_v | u_c \rangle \,\mathrm{Tr}\big[\mathbf{m}\cdot\boldsymbol{\sigma}(w+w^\dagger)\big] \\ \frac{1}{A}\sum_{\mathbf{k}} u_{\mathbf{k}} v_{\mathbf{k}} [\delta(E_{\mathbf{k},-} - eV) - \delta(E_{\mathbf{k},+} - eV)]. \quad (3.75)$$

This is only non-vanishing for the SDW order parameter, for which we the trace evaluates as $\mathrm{Tr}\big[\mathbf{m}\cdot\boldsymbol{\sigma}(w+w^\dagger)\big] = 2\mathbf{m}\cdot\mathbf{n}$. The oscillating signal is maximal when the tip magnetization is aligned with the SDW direction. These oscillations in spin-resolved tunneling allow the recovery of the underlying momentum space exciton wavefunction for the SDW state, following the method of Subsection 3.3.3.

3.6 Discussion

To conclude, scanning tunneling microscopy is ideally suited to probe exciton condensation, enabling the extraction of important information like exciton density and exciton wavefunctions. Its local nature enables the focusing on low-disorder regions suitable for exciton condensation, a big advantage compared to angle-resolved photo-emission spectroscopy [42, 83, 87]. Furthermore, our suggested method is especially powerful in combination with sample engineering, which enables a whole range of model parameters to be studied in a single device [127]. While exciton density can also be measured by other means, STM allows the exction density to be measured locally. This provides an important advantage in inhomogeneous samples, where exciton density exhibits spatial variations.

While our focus was on the BEC regime of exciton insulators, we now comment on the possible STM signatures in the regime of higher exciton density. For bilayers, the appearance of a satellite peak is a feature specific to the BEC limit. For increasing carrier density, the conduction band would cross the chemical potential at some point, providing states to tunnel even in the absence of excitonic correlations. In this BCS regime, the main signature would be a gap, which, however, is expected to be strongly affected by screening. For monolayers at larger carrier den-

sities, the oscillatory signal associated with interband coherence should still manifest, but the exciton wavefunction becomes strongly modified due to the presence of other excitons. In the semimetallic regime, furthermore, a spontaneous gap opening due to excitons can be probed by STM, mirroring the current paradigm.

An interesting open question is the effect of finite temperature [114]. At finite temperature, fermionic mean-field in the BEC regime breaks down [90, 128, 129], failing to account for the center-of-mass motion of excitons. Upon increasing temperature, the exciton condensate is expected to undergo a BKT transition, and eventually turn into a classical exciton gas [114]. For a bilayer, this will lead to thermal smearing. However, the satellite peak should persist so long as excitons are present. On the other hand, for a monolayer, quasi-long range order is lost beyond the BKT transition, leading to the disappearance of lattice-symmetry breaking oscillatory components in $\frac{\mathrm{d}I}{\mathrm{d}V}$.

4 Anderson Thoerem for twisted bilayer graphene

The results of most of this Chapter have been published as Ref. [2], co-authored by Gal Shavit, Christophe Mora, Yuval Oreg, and Felix von Oppen. The research was conducted by the author of this thesis and was discussed with the other coauthors. The results of the last Section, Sec. 4.5, of this Chapter have been published as Ref. [1], co-authored by Gal Shavit, Christophe Mora, Yuval Oreg, and Felix von Oppen. The contribution of the author of this thesis was to aid the analysis, in particular to clarify how disorder enters into the toy model considered there.

We move on to moiré systems in the form of twisted bilayer graphene, but continue with the theme of interband coherence. As mentioned in the Introduction, the phase diagram of twisted bilayer graphene is characterized by a plethora of superconducting and correlated insulating phases [20, 25, 29, 30]. The most prominent of these correlated insulators occur at even integer fillings of the moiré flat bands.

A prime candidate state to understand these correlated insulators is the Kramers intervalley coherent (K-IVC) state [76, 108–110, 130–132]. These states exhibit a pattern of magnetization currents, which triple the graphene unit cell, thereby breaking the lattice translation symmetry as well as time reversal. The associated spontaneous interband coherence between the two valleys of the TBG band structure gaps out the moiré Dirac points and induces insulating behavior. A recent work reports evidence for the K-IVC state by measuring the magnetic-field dependence of the thermodynamic gap [133]. In general, the appearance and strength of insulating states tend to be device dependent [29, 30]. A possible explanation for this sample-specific behavior lies in residual disorder associated with random strain or impurity potentials. Thus, it is important to study and understand their effects.

In this Chapter, we focus on understanding the effect of local impurities on the correlated states in TBG. We show that for the K-IVC state, one can systematically classify impurities according to their ability to induce subgap excitations, which diminish or even eliminate the insulating gap. Our discussion is strongly informed by a far-reaching analogy with the familiar problem of classifying impurities in s-wave superconductors [134].

Physically, these analogies can be understood by noting that K-IVC states can be thought of as binding holes in one valley to electrons in the other, akin to excitonic insulators, discussed in the previous Chapter 3. This is analogous to binding time-reversed electrons into Cooper pairs According to Anderson's theorem [134], the ability of impurities to induce subgap excitations in s-wave superconductors is determined by whether or not they respect time-reversal symmetry.

We find that for the K-IVC state, particle-hole symmetry plays the same role as time-reversal symmetry does for superconductors.

In contrast to the K-IVC state, we find that there are no corresponding Anderson theorems for other possible insulating ground states such as the valley polarized and valley Hall states. This Chapter is organized as follows. In Section 4.1, we introduce the projected theory of twisted bilayer graphene, using which the different mean-field ordered states can be formulated. In Section 4.2, we recall the Anderson theorem for s-wave superconductivity. In Section 4.3, we formulate the Anderson theorem for the K-IVC state, classifying disorder according to its transformation properties under symmetries of TBG. We also comment on the possibility of an Anderson theorem for other candidate ground states of TBG. In Sec. 4.4, we classify physically relevant disorder according to their transformation properties and whether they satisfy the prerequisites of our Anderson theorem or not. Finally, in Sec. 4.5, we present the results of a self-consistent calculation based on a toy model of TBG.

4.1 Projected theory of twisted bilayer graphene: symmetries and correlated insulators

In this section we introduce the strong coupling theory of correlated insulators in twisted bilayer graphene, obtained by projecting the TBG Hamiltonian onto the two flat bands in each spin and valley flavor, therefore eight bands in total. Furthermore, we neglect the small relative twist of the Dirac Hamiltonians of the two layers in Eq. (2.38), in order to exploit the emergent (approximate) particle-hole antisymmetry, defined in Eq.(2.59).

To study correlated states, it is advantageous to write the projected Hamiltonian in a special basis, denoted the Chern basis, which diagonalizes the sublattice polarization operator projected onto the flat bands. This is equivalent to projecting onto the flat bands and then adding an infinite staggered mass term projected onto the bands. While in monolayer graphene, such a mass term leads to topologically trivial bands, in twisted bilayer graphene, this mass term in fact leads to topological bands in a given valley, since in a single valley, the two underlying Dirac cones (one for each layer) have the same chirality.

Specifically, ignoring the spin degree of freedom, which will only play a spectator role in what follows, we have four basis states $|u_{\mathbf{k},f,s}\rangle$ at each momentum $\mathbf{k}$, where $s = A/B$ labels the sublattice polarization and $f = K/K'$ the valley degree of freedom.

Let us denote the Pauli matrices acting on the sublattice space as σ_α, and the Pauli matrices in valley space as τ_α. In this notation, the Chern number of a band is given by $C = \sigma_z\tau_z$, which flips sign upon flipping valley as the two valleys are related by time-reversal symmetry.

So far the basis states are determined only by their momentum and the eigenvalues under τ_z and σ_z. There is, however, an arbitrary choice of an overall phase for each state. We can use this arbitrariness to make the representation of the projected time reversal $\mathcal{T}$ and particle-hole $\mathcal{P}$ operators particularly simple. Time reversal flips momentum and preserves sublattice,

which implies that $\mathcal{T}\,|u_{\mathbf{k},K,s}\rangle \propto |u_{-\mathbf{k},K',s}\rangle$. We can now adjust the phases to demand that this proportionality turns into an equality, giving the following simple form for the projected time-reversal operator:

$$\mathcal{T} = \tau_x \mathcal{K}. \tag{4.1}$$

Similarly, the particle-hole antisymmetry preserves valley but flips sublattice and momentum, cf. Eq. (2.59). Therefore, we must have that $\mathcal{P}\,|u_{\mathbf{k},f,A}\rangle \propto |u_{-\mathbf{k},f,B}\rangle$, as well as $\mathcal{P}\,|u_{\mathbf{k},f,B}\rangle \propto |u_{-\mathbf{k},f,A}\rangle$, with possibly different constants of proportionality for different states. Following [76], we choose the basis state phases so that $\mathcal{P}$ is given as

$$\mathcal{P} = i\sigma_y \tau_z \mathcal{K}. \tag{4.2}$$

This choice is natural for the discussion of the K-IVC state, but leads to a more complicated representation of the $C_{2z}\mathcal{T}$ symmetry:

$$C_{2z}\mathcal{T} = e^{i\theta(\mathbf{k})}\sigma_x \mathcal{K}, \tag{4.3}$$

where $\theta(\mathbf{k})$ is an irremovable phase [76].

Another important symmetry is conservation of valley charge, which is associated with invariance under $U(1)$ valley rotations, represented by

$$U_V = e^{i\theta\tau_z}. \tag{4.4}$$

These symmetries allow the projected band Hamiltonian $h(\mathbf{k})$ to be constrained as follows

$$h(\mathbf{k}) = h_0(\mathbf{k})\tau_z + h_x(\mathbf{k})\sigma_x + h_y(\mathbf{k})\sigma_y\tau_z, \tag{4.5}$$

where time-reversal symmetry enforces $h_0(\mathbf{k}) = -h_0(-\mathbf{k})$ and $h_{x,y}(\mathbf{k}) = h_{x,y}(-\mathbf{k})$.

Within the mean-field approximation for the K-IVC state [76], the band Hamiltonian $h(\mathbf{k})$ is complemented by the order parameter $h_{\mathrm{IVC}} = \Delta\sigma_y(\tau_x \cos\theta + \tau_y \sin\theta)$, where θ denotes an arbitrary phase. In view of the associated magnetization currents, the K-IVC state breaks time reversal spontaneously, $\mathcal{T} h_{\mathrm{IVC}} \mathcal{T}^{-1} = -h_{\mathrm{IVC}}$. However, it preserves a modified time-reversal symmetry [76]

$$\mathcal{T}' = i\tau_y \mathcal{K}, \tag{4.6}$$

which concatenates $\mathcal{T}$ with a valley rotation, $\mathcal{T}' = \tau_z\mathcal{T}$. Both $\mathcal{T}$ and valley rotations are symmetries of the single-particle Hamiltonian, so that the mean-field Hamiltonian for the K-IVC state $H(\mathbf{k}) = h(\mathbf{k}) + h_{\mathrm{IVC}}$ conserves the Kramers time reversal $\mathcal{T}'$ (with $\mathcal{T}'^2 = -1$) as a whole.

4.2 Anderson's theorem for s-wave superconductors

To clearly bring out the analogies, as well as differences, between TBG and superconductors, we begin our discussion with a review of Anderson's theorem for s-wave superconductors [134–137], using a formulation which turns out to be adaptable to TBG. Starting from the second-quantized BCS mean-field Hamiltonian $\mathcal{H} = \frac{1}{2}\int d\mathbf{r}\Psi^\dagger(\mathbf{r})H\Psi(\mathbf{r})$, we write the Bogoliubov-de Gennes (BdG) Hamiltonian

$$H = \begin{pmatrix} H_e & \Delta \\ \Delta & H_h \end{pmatrix}, \tag{4.7}$$

in a four-component Nambu formalism, using the basis $\Psi = [\psi_\uparrow, \psi_\downarrow, \psi_\downarrow^\dagger, -\psi_\uparrow^\dagger]$. The normal-state Hamiltonians $H_{e/h}$ for electrons (e) and holes (h) as well as the pairing Δ are matrices in spin space. For s-wave pairing, Δ is proportional to the unit matrix. In the following, we assume that Δ is spatially uniform and chosen to be real.

The BdG Hamiltonian is constrained by antisymmetry under particle-hole conjugation, meaning $\mathcal{P}H\mathcal{P}^{-1} = -H$. As a consequence, the normal-state Hamiltonians of electrons and holes in Eq. (4.7) are related by time reversal $\mathcal{T}$,

$$H_h = -\mathcal{T}H_e\mathcal{T}^{-1}. \tag{4.8}$$

This can be deduced by defining Pauli matrices τ_α and s_α in particle-hole and spin space, respectively. Then, particle-hole conjugation is implemented by $\mathcal{P} = -i\tau_y\mathcal{T} = \tau_y s_y\mathcal{K}$ and squares to unity, $\mathcal{P}^2 = 1$, while time reversal takes the form $\mathcal{T} = is_y\mathcal{K}$ with $\mathcal{T}^2 = -1$ ($\mathcal{K}$ implements complex conjugation).

We separate the normal-state Hamiltonian $H_e = H_0 + U$ into a spatially homogeneous part H_0 and a (local) perturbation U. While we assume $H_0 = \mathcal{T}H_0\mathcal{T}^{-1}$ to be time-reversal symmetric, a general perturbation $U = U_+ + U_-$ can have components $U_\pm = \pm\mathcal{T}U_\pm\mathcal{T}^{-1}$, which are even ($+$) or odd ($-$) under time reversal. Combining these symmetry properties under time reversal with Eq. (4.8), the BdG Hamiltonian in Eq. (4.7) can be written compactly as

$$H = H_0\tau_z + \Delta\tau_x + U_+\tau_z + U_-\tau_0. \tag{4.9}$$

Importantly, one observes that time-reversal-symmetric perturbations anticommute with the order-parameter term, $\{\Delta\tau_x, U_+\tau_z\} = 0$, while the time-reversal breaking term, U_-, commutes.

It can now be seen quite generally that time-reversal-even perturbations do not reduce the BdG gap (Anderson's theorem). Given that antisymmetry under particle-hole conjugation $\mathcal{P}$

enforces the eigenenergies to be symmetric about zero energy, the spectrum can be deduced from the square of H,

$$H^2 = (H_0 + U_+)^2 + \Delta^2, \tag{4.10}$$

implying that the magnitude of the eigenvalues of H is bounded from below by Δ. This argument uses the assumption that the gap remains uniform in the presence of the perturbation, but holds regardless of the particular spatial structure of the impurity potential.

Conversely, perturbations, which are odd under time reversal generally reduce the gap. A uniform Zeeman field described by $U_- = \mathbf{B}\cdot\mathbf{s}$ reduces the gap to $\Delta - |\mathbf{B}|$, provided the normal-state Hamiltonian is spin-rotation invariant. Local magnetic impurities with $U_- = J\mathbf{S}\cdot\mathbf{s}\delta(\mathbf{r})$ are well-known to induce Yu-Shiba-Rusinov states at subgap energies [138–141].

4.3 Anderson's theorem for the Kramers inter-valley coherent state

For twisted bilayer graphene in the K-IVC state we have the mean-field Hamiltonian

$$H(\mathbf{k}) = h(\mathbf{k}) + h_{\mathrm{IVC}}, \tag{4.11}$$

which can be thought of as the analog of the BdG Hamiltonian for the K-IVC state. We will now make the analogies yet more explicit by a change of basis $H \to \mathcal{U}H\mathcal{U}^\dagger$ with

$$\mathcal{U} = \begin{pmatrix} 1 & 0 \\ 0 & i\sigma_y \end{pmatrix}. \tag{4.12}$$

In the new basis, which we refer to as the particle-hole basis, the Chern number becomes $C = \sigma_z$. Transforming the Hamiltonian in this manner, we find

$$H(\mathbf{k}) = H_0(\mathbf{k})\tau_z + \Delta(\tau_x \cos\tilde{\theta} + \tau_y \sin\tilde{\theta}) \tag{4.13}$$

($\tilde{\theta} = \theta + \frac{\pi}{2}$). Here, we make the dependence on the valley Pauli matrices τ_α explicit, while H_0 and Δ are still matrices in sublattice space. We find $H_0(\mathbf{k}) = h_0(\mathbf{k}) + h_x(\mathbf{k})\sigma_x + h_y(\mathbf{k})\sigma_y$ for the single-particle Hamiltonian of the K valley, while Δ is simply proportional to the unit matrix. The transformation (4.12) to the particle-hole basis also changes the explicit forms of the time-reversal and charge-conjugation operations, $\mathcal{T} \to \mathcal{U}\mathcal{T}\mathcal{U}^\dagger$ and $\mathcal{P} \to \mathcal{U}\mathcal{P}\mathcal{U}^\dagger$, which yields $\mathcal{P} = i\sigma_y\mathcal{K}$ and $\mathcal{T}' = -\tau_x\mathcal{P}$.

Equation (4.13) is closely analogous to the BdG Hamiltonian of s-wave superconductors, with particle-hole space replaced by the valley degree of freedom and spin space replaced by sublattice space. In Eq. (4.13), the band Hamiltonian $H_0(\mathbf{k})$ is analogous to the normal-state Hamiltonian. It multiplies τ_z as a consequence of the chiral antisymmetry $\mathcal{P}\mathcal{T} = i\tau_y$ of the

TBG Hamiltonian. Moreover, the term describing K-IVC order is analogous to the pairing term in the BdG Hamiltonian, being offdiagonal in valley and proportional to the unit matrix in sublattice space.

Beyond the structural similarities of the Hamiltonians, there is also a correspondence of symmetries. Interestingly, the roles of time reversal and particle-hole conjugation are essentially reversed. For superconductors, time reversal acts diagonally in particle-hole space, while particle-hole conjugation is offdiagonal. In contrast, in TBG it is time reversal which maps between the two valleys, while particle-hole conjugation acts separately within each valley.

We also note that gauge transformations for superconductors are structurally analogous to U(1) valley rotations in TBG. For superconductors, the BdG Hamiltonian becomes time-reversal symmetric by choosing a gauge, in which Δ is real. In TBG, we can similarly exploit the valley rotation symmetry to choose $\tilde{\theta} = \frac{\pi}{2}$, so that $H(\mathbf{k}) = H_0(\mathbf{k})\tau_z + \Delta\tau_y$. With this choice, the mean-field K-IVC order is also odd under particle-hole conjugation, so that the full Hamiltonian satisfies $\mathcal{P}H(\mathbf{k})\mathcal{P}^{-1} = -H(-\mathbf{k})$. In the following, we make this choice for definiteness. However, just as Anderson's theorem for s-wave superconductors is not specific to a particular gauge, Anderson's theorem for TBG is not limited to this choice.

Armed with this far-reaching correspondence between the BdG Hamiltonian of s-wave superconductors and the K-IVC state of TBG, we now turn to discussing the effects of impurities on the K-IVC state. We consider impurity potentials which are sufficiently smooth on the scale of the atomic lattice, so that they preserve the $U(1)$ valley symmetry. Intervalley scattering can then be neglected and the impurity potential is diagonal in valley space. With this assumption, the low-energy Hamiltonian in the presence of an impurity potential becomes

$$H = H_0\tau_z + \Delta\tau_y + U_-\tau_z + U_+\tau_0. \tag{4.14}$$

Just as for superconductors, the impurity potentials $U_\pm$ are distinguished by their symmetry properties. For superconductors, antisymmetry under particle-hole conjugation is built into the BdG formalism. For this reason, it was sufficient to classify perturbations according to their behavior under time reversal. In contrast, for TBG, both Kramers time reversal and particle-hole conjugation are physical symmetries of the Hamiltonian. Consequently, we now classify perturbations according to their transformation properties under the combined chiral symmetry operation $\mathcal{PT} = i\tau_y$, namely $(\mathcal{PT})U_+\tau_0(\mathcal{PT})^{-1} = U_+\tau_0$ and $(\mathcal{PT})U_-\tau_z(\mathcal{PT})^{-1} = -U_-\tau_z$. (Notice that due to valley rotation symmetry, the impurity terms transform in the same way under $\mathcal{PT}$ and $\mathcal{PT}'$.) By comparing with the discussion of Eq. (4.9), we can now formulate an Anderson's theorem for TBG, our central result: The gap of K-IVC states is robust against valley-preserving perturbations, which are odd under the combined chiral symmetry operation $\mathcal{PT}$. In fact, perturbations which are odd under $\mathcal{PT}$ anticommute with the K-IVC order $\Delta\tau_y$ and cannot reduce the gap. In contrast, similar to time-reversal-breaking impurities in superconductors, perturbations which are even under $\mathcal{PT}$ can induce subgap states in TBG. For perturbations that are local on the moiré scale, this follows as for time-reversal-breaking impu-

rities in s-wave superconductors. A finite density of $\mathcal{PT}$-even impurities can thus suppress or even destroy the K-IVC gap.

So far, our discussion relied on a close structural analogy between the BdG Hamiltonian of s-wave superconductors and the low-energy Hamiltonian of TBG with K-IVC order. More fundamentally, the appearance of an Anderson's theorem in both theories is rooted in the fact that up to $U(1)$ rotations which leave the normal-state Hamiltonian invariant, their order parameters are proportional to a natural antisymmetry of the model, namely $\mathcal{PT}$. For both superconductors and the K-IVC state of TBG, we have $\Delta\tau_y = -i\Delta\mathcal{PT}$. Up to a gauge transformation (superconductors) or a $U(1)$ valley rotation (TBG), this is equivalent to the general order-parameter term $\Delta(\tau_x \cos\theta + \tau_y \sin\theta)$. This form of the order parameter has two important consequences. First, the order-parameter and single-particle terms in the Hamiltonian anticommute, so that the single-particle energies and the order parameter add in quadrature in the mean-field excitation spectrum. Second, this property persists in the presence of disorder, as long as the latter is odd under $\mathcal{PT}$, which is Anderson's theorem. We emphasize that Anderson's theorem does not rely on a specific symmetry of the order parameter, but only on the fact that the order parameter is proportional to a natural unitary antisymmetry of the system in the absence of the spontaneous symmetry breaking.

One should remember that the derivation of Anderson's theorem relies on several assumptions. In particular, one assumes that the order parameter remains spatially uniform and is momentum independent. Similar to anisotropic superconductors, the order parameter of TBG exhibits some momentum dependence [76]. In the presence of momentum dependence, there will be no systematic anticommutation behavior between the order-parameter term and the impurity potential. Then, Anderson's theorem no longer applies in the strict sense, and implies only enhanced, but not full protection of the gap.

We can also consider other candidate insulating ground states, which have been proposed in the literature [142–145].

First, consider an alternative, time-reversal-preserving intervalley coherent state, termed T-IVC. In the particle-hole basis, this state has the order parameter $\Delta\sigma_z(\tau_x \cos\theta + \tau_y \sin\theta)$. The T-IVC gap anticommutes with only one of the three terms of the flat-band Hamiltonian, precluding the derivation of an Anderson's theorem.

The valley-polarized state with order parameter $\Delta\tau_z$ leads to the mean-field Hamiltonian

$$H_{\mathrm{vp}} = H_0\tau_z + \Delta\tau_z + U_-\tau_z + U_+\tau_0 \tag{4.15}$$

in the particle-hole basis. The order-parameter term commutes with the band Hamiltonian, so that a gap emerges only when Δ shifts the flat bands of the two valleys sufficiently far apart in energy. The impurity problem can be considered separately for the two bands and regardless of impurity type, there is no robustness due to an Anderson's theorem.

perturbation	matrix structure	Anderson
layer-even pot.	$\mathbb{I}$	×
layer-odd pot.	μ_z	✓
layer-even sublattice pot.	σ_z	✓
layer-odd sublattice pot.	$\sigma_z\mu_z$	×
layer-even vector pot.	$\sigma_x, \sigma_y\tau_z$	×
layer-odd vector pot.	$\sigma_x\mu_z, \sigma_y\tau_z\mu_z$	✓
tunneling disorder	see text	✓

Table 4.1: Table of time-reversal symmetric perturbations (left column) and their effect on the K-IVC gap. The central column gives the matrix structure in the microscopic graphene basis of TBG, where μ_α, σ_α and τ_α are Pauli matrices in layer, sublattice and valley space, respectively. The right column indicates the validity of Anderson's theorem. The K-IVC gap is protected against perturbations, for which Anderson's theorem is valid. Notice that in this table, we only consider strain-induced vector potentials.

Finally, we consider the valley Hall state with mean field Hamiltonian

$$H_{\mathrm{v}h} = H_0\tau_z + \Delta\sigma_z\tau_z + U_-\tau_z + U_+\tau_0 \tag{4.16}$$

in the particle-hole basis. The order-parameter term anticommutes with the flat-band Hamiltonian $H_0\tau_z$ [see Eq. (4.13)] only in the chiral limit, where $h_0(\mathbf{k}) = 0$ [73]. In this idealized (but experimentally remote) limit, the gap is robust against perturbations, which are purely offdiagonal in sublattice space, e.g., strain disorder.

We therefore find that the K-IVC is distinct from other possible ground states due to the existence of Anderson's theorem for $\mathcal{PT}$-antisymmetric disorder. It is thus conceivable that such kinds of disorder stabilize the K-IVC state relative to competing states.

4.4 Classifying physical perturbations

Above, we phrased our discussion in rather general terms, largely relying on symmetry properties of the TBG flat bands. We now classify perturbations according to their symmetry and tabulate the presence or absence of Anderson's theorem in Table 4.1. For a given behavior under time reversal, it is sufficient to consider their transformation properties under $\mathcal{P}$, which acts separately within each valley.

Usually, we do not know the form of perturbations in the flat-band (i.e., Chern or particle-hole) bases, but rather in the microscopic graphene basis. Within the Bistrizer-MacDonald model [19], the Hamiltonian H_0 is valley diagonal and takes the form

$$H = \begin{pmatrix} v_D \boldsymbol{\sigma} \cdot (\frac{1}{i}\boldsymbol{\nabla} + \mathbf{A}_t) + \phi_t & T(\mathbf{r}) \\ T^\dagger(\mathbf{r}) & v_D \boldsymbol{\sigma} \cdot (\frac{1}{i}\boldsymbol{\nabla} + \mathbf{A}_b) + \phi_b \end{pmatrix} \tag{4.17}$$

for the K-valley. Here, the diagonal and off-diagonal blocks are intra- and inter-layer terms, respectively, and the σ_α refer explicitly to the graphene sublattice. Potential disorder introduces layer- and sublattice-dependent potentials $\phi_{t/b}(\mathbf{r})$. Modulations in the interlayer distance cause variations of the interlayer tunneling terms $T(\mathbf{r})$. Strain introduces vector potentials $\mathbf{A}_{t/b}(\mathbf{r})$ and modifies $T(\mathbf{r})$ [146–148]. In terms of the strain-induced displacements $\mathbf{u}_l(\mathbf{r})$ relative to the uniformly twisted bilayer, the components of the vector potential take the form [147, 148] $(A_l)_\mu = \mathbf{K} \cdot \partial_\mu \mathbf{u}_l + \frac{\beta\sqrt{3}}{2a}(u_{l,xx} - u_{l,yy}, -2u_{l,xy})$. Here, β characterizes the sensitivity of the hopping amplitude to strain-induced displacements and $u_{l,ij}$ is the strain tensor of layer l. Time-reversal symmetry implies that strain-induced vector potentials are odd in valley space, while the scalar potentials are even.

In the microscopic graphene basis of the Bistritzer-MacDonald Hamiltonian in Eq. (4.17), particle-hole conjugation takes the form [76]

$$\mathcal{P} = i\sigma_x\mu_y\mathcal{K}, \tag{4.18}$$

where the μ_α are Pauli matrices in layer space ($\mathcal{PT} = i\tau_x\sigma_x\mu_y$). The validity of Anderson's theorem for various perturbations is now readily established and tabulated in Table 4.1 for time-reversal symmetric perturbations. A sublattice-symmetric potential will commute with $\mathcal{P}$, if it is layer symmetric, and anticommute with $\mathcal{P}$, if it is odd under layer exchange. According to our considerations, we find that layer-symmetric potentials induce subgap states within the K-IVC gap, but layer-odd potentials leave the K-IVC gap intact. These conclusions are reversed for sublattice-odd potentials. Tunneling disorder corresponds to a local variation in the strength of the interlayer tunneling amplitudes and thus in the parameters entering $T(\mathbf{r})$. Consequently, tunneling disorder inherits the $\mathcal{P}$ transformation properties of H_0 and Anderson's theorem applies. Finally, a layer-even vector potential (homostrain) is even under $\mathcal{P}$, while a layer-odd vector potential (heterostrain) is odd. We therefore find that Anderson's theorem applies to (local) heterostrain only.

Anderson's theorem for the K-IVC state can be tested by introducing impurity potentials with different behavior under $\mathcal{PT}$. Local $\mathcal{PT}$-even perturbations will in general induce subgap states, which can be probed directly using scanning tunneling microscopy.

4.5 Abrikosov-Gor'kov treatment of disorder in the K-IVC state – a toy model

In this final Section we illustrate on a simple model how disorder can lead to the destruction of K-IVC order. We use methods originally developed for disordered superconductors developed by Abrikosov and Gor'kov [149], which are reviewed in Ref. [135]. The remarkable result of that treatment of magnetic impurities in an s-wave suprconductor is that in addition to completely destroying superconductivity for large disorder strength, for intermediate disorder strength, it leads to a peculiar regime of "gapless" superconductivity, in which the gap of the superconductor is filled with bound states, but it still exhibits superconducting properties.

Given the analogy of the K-IVC with an s-wave superconductor, it is natural to extend this approach to the K-IVC state. Here we summarize the main results, which are published as Ref. [1].

To allow for analytical understanding, we use a simplified toy model form of the K-IVC Hamiltonian, $H^{toy}(\mathbf{k})$, expanding the single-particle dispersion of Eq. (4.5) around the Dirac points (two for each valley):

$$H^{toy}(\mathbf{k}) = u(k_x\sigma_x\tau_z + k_y\sigma_y) + \Delta_{ivc}\sigma_x\tau_x\rho_z\cdot, \tag{4.19}$$

where in addition to sublattice σ and valley τ degrees of freedom, we need to consider the mini-valley degree of freedom ρ, corresponding to the Dirac points originating from the two layers in twisted bilayer graphene. Importantly, u in this theory is the renormalized TBG Dirac velocity $u \ll v_F$, and $\mathbf{k}$ is only defined up to a cutoff, which leads to slight complications as follows. We take a cutoff k^{max}, corresponding to cutoff energy $W = uk^{max}$, which is the flat band bandwidth. If we have a system with N_{UC} unit cells, we require that for each unit cell there is one state per valley and sublattice, sampling uniformly among the phase space volume $2\pi(k^{max})^2$ (factor of two for mini-valley). This is important when converting sums over momenta to integrals, which can be done by replacing $\sum_{\mathbf{k}} \to \frac{N_{\mathrm{UC}}}{2\pi(k^{max})^2}\int d\mathbf{k}$. Note also that in this expansion, the K-IVC order parameter has a slightly different form than above. However, the crucial property that it anticommutes with the kinetic (Dirac) term, is preserved. Arguably, this toy model is just a caricature of the real problem, but it has the advantage of being easily solvable.

The clean Green's function for this system is simply

$$\begin{aligned} G^{clean}(\mathbf{k},\omega_n) &= \left(i\omega_n - H^{toy}(\mathbf{k})\right)^{-1} && (4.20)\\ &= -\frac{i\omega_n + u(k_x\sigma_x\tau_z + k_y\sigma_y) + \Delta_{ivc}\sigma_x\tau_x\rho_z}{(u|\mathbf{k}|)^2 + {\Delta_{ivc}}^2 + {\omega_n}^2}, && (4.21)\end{aligned}$$

where ω_n is a fermionic Matsubara frequency.

In this model, homostrain disorder couples as

$$\mathcal{U}_{\mathbf{q}}^{homo} = u(A_{x,\mathbf{q}}\sigma_x + A_{y,\mathbf{q}}\sigma_y\tau_z), \tag{4.22}$$

while heterostrain couples as

$$\mathcal{U}_{\mathbf{q}}^{hetero} = u(A_{x,\mathbf{q}}\sigma_x\rho_z + A_{y,\mathbf{q}}\sigma_y\tau_z\rho_z), \tag{4.23}$$

in line with the interpretation that ρ microscopically corresponds to layer. We now immediately see the consequence of the Anderson's theorem derived above in that heterostrain anticommutes with the order parameter, and does not decrease the single-particle gap. Homostrain, on the other hand, commutes, and can reduce the gap.

We assume a white noise distribution for the disorder, defining the disorder energy scale Γ as

$$\Gamma = \frac{N_{\mathrm{UC}}u^2}{W}\left\langle \mathbf{A}_{\mathbf{q}}^{\dagger}\cdot\mathbf{A}_{\mathbf{q}}\right\rangle_{dis.}, \tag{4.24}$$

where as usual, the Fourier components have to scale inversely with system size, and the x and y-components of $\mathbf{A}$ are independent. The Abrikosov-Gor'kov method uses the self-consistent Born approximation (SCBA) for the disorder potential. The Green's function in this approach reads

$$G(\mathbf{k},\omega_n) = \left(i\omega_n - H^{toy}(\mathbf{k}) - \hat{\Sigma}_{SCBA}(\mathbf{k},\omega_n)\right)^{-1}, \tag{4.25}$$

where the disorder in the SCBA contributes a self-energy term:

$$\hat{\Sigma}_{SCBA}(\mathbf{k},\omega) = \left\langle \sum_{\mathbf{p}} \mathcal{U}_{\mathbf{k}-\mathbf{p}}G(\mathbf{p},\omega_n)\mathcal{U}_{\mathbf{p}-\mathbf{k}}\right\rangle_{dis.}, \tag{4.26}$$

where $\langle\cdot\rangle_{dis.}$ denotes disorder averaging.

At this point an important simplification occurs. Plugging in $G^{clean}(\mathbf{k},\omega_n)$ into Eq. (4.26), we see that $\hat{\Sigma}_{SCBA}(\mathbf{k},\omega_n)$ as a matrix only contains terms proportional to the identity and the matrix of the K-IVC pairing term $\sigma_x\tau_x\rho_z$. The terms arising due to the kinetic term, proportional to u in Eq. (4.21), cancel from the sum upon disorder averaging for the white noise distribution, Eq. (4.24). The Green's function can therefore be written as

$$G(\mathbf{k},\omega_n) = -\frac{i\tilde{\omega}_n + u(k_x\sigma_x\tau_z + k_y\sigma_y) + \tilde{\Delta}\sigma_x\tau_x\rho_z}{(u|\mathbf{k}|)^2 + \tilde{\Delta}^2 + \tilde{\omega}_n^2}, \tag{4.27}$$

where the parameters $\tilde{\omega_n}, \tilde{\Delta}$ are related to ω_n, Δ_{ivc} by the self-consistency equations

$$\begin{pmatrix} \tilde{\omega}_n \\ \tilde{\Delta} \end{pmatrix} = \begin{pmatrix} \omega_n \\ \Delta_{\mathrm{ivc}} \end{pmatrix} + \frac{\Gamma}{W} \int_0^W d\epsilon \epsilon \frac{1}{\epsilon^2 + \tilde{\Delta}^2 + \tilde{\omega}_n^2} \begin{pmatrix} \tilde{\omega}_n \\ \mp\tilde{\Delta} \end{pmatrix}, \tag{4.28}$$

where the minus sign holds for homostrain and the plus sign for heterostrain. We see that for heterostrain disorder, $(\tilde{\omega}_n, \tilde{\Delta})$ are simply proportional to (ω_n, Δ_{ivc}) with the same constant of proportionality.

The value of the K-IVC order parameter Δ_{ivc} is given by the mean-field gap equation

$$\Delta_{ivc} = -2\frac{k_b T\, U}{N_{\mathrm{UC}}} \sum_{\omega_n \mathbf{k}} Tr\{\sigma_x \tau_x \rho_z G\} = -2\frac{k_b T\, U}{N_{\mathrm{UC}}} \sum_{\omega_n \mathbf{k}} \frac{\tilde{\Delta}}{(u|\mathbf{k}|)^2 + \tilde{\Delta}^2 + \tilde{\omega}_n^2}, \tag{4.29}$$

where k_B is the Boltzmann constant, T is the temperature, and U is an interaction energy scale. Together, Eq. (4.29) and Eq. (4.28) have to be solved self-consistently.

As shown in Figure 2b of Ref. [1], increasing the strength of homostrain quickly reduces the value of the order parameter and the spectral gap. Strikingly, for certain values of disorder, the spectral gap vanishes, even though the inter-valley coherence order parameter Δ_{ivc} is still nonzero. This situation is analogous to the phenomenon of gapless superconductivity in s-wave superconductors with magnetic impurities [135]. In contrast, for heterostrain disorder, we have the Anderson theorem, protecting the K-IVC state from disorder.

5 Superconducting pockets in alternating twisted N-layer graphene

The results of this Chapter have been published as Ref. [3], co-authored by Yiran Zhang, Stefan Nadj-Perge, Felix von Oppen, and Cyprian Lewandowski. The research was conducted by the author of this thesis and was discussed with the other coauthors. Yiran Zhang and Stefan Nadj-Perge provided the experimental data in Fig. 5.2 and insights regarding the experiments.

In this Chapter, we study the interacting physics of alternating twisted N-layer graphene, introduced in Sec. 2.4. Our study is motivated by recent experiments on twisted N-layer graphene with up to five layers [31, 32]. As for twisted bilayer graphene, the phase diagrams of the multilayer systems featured prominent superconducting domes in the temperature-doping plane. However, while in TBG superconductivity typically terminates at filling $|\nu| = 3$, Ref. [31] observed that for $N = 5$, superconductivity persists up to a filling of five electrons per unit cell. Strikingly, such an extended superconducting pocket is at odds with a picture of decoupled sectors [78, 79, 150].

To understand the results of Refs. [31, 32] we employ mean-field theory to obtain analytical estimates and perform fully self-consistent Hartree-Fock calculations. While mean-field theory has inherent drawbacks and is an approximate technique, it has proven remarkably successful in the study of TBG [76, 110, 142, 143, 151], with certain models of TBG exhibiting Slater-determinant ground states at integer filling [77]. For a larger number of layers, the Hartree-Fock approximation accounts well for the screening of classical charge distributions, which we will argue play a crucial role in the physics of TNG.

Having understood the experimental results of Refs. [31, 32] for $N = 3, 4, 5$ layers, we apply the developed framework to study the twisted N-layer problem for larger values of N. We show that both in- and out-of-plane electrostatics play a crucial role in shaping the phase diagrams of TNG systems, providing a simple picture in terms of sector shifts in Sec. 5.2. For larger layer numbers, we show that electrostatically doping the moiré system requires a larger charge density on the metallic gates. This behaviour arises because it is necessary for the metallic gates to compensate for the charge redistribution due to interactions. This effect makes it increasingly prohibitive to electrostatically dope $N > 5$ multilayer structures into the regime where the magic flat band is optimally filled for superconductivity. This is shown in Fig. 5.1, where we also indicate estimates for the gate charge densities. Interestingly, we find that while going beyond $N = 5$ layers to study interaction effects of the $k = 1$ flat band presents little advan-

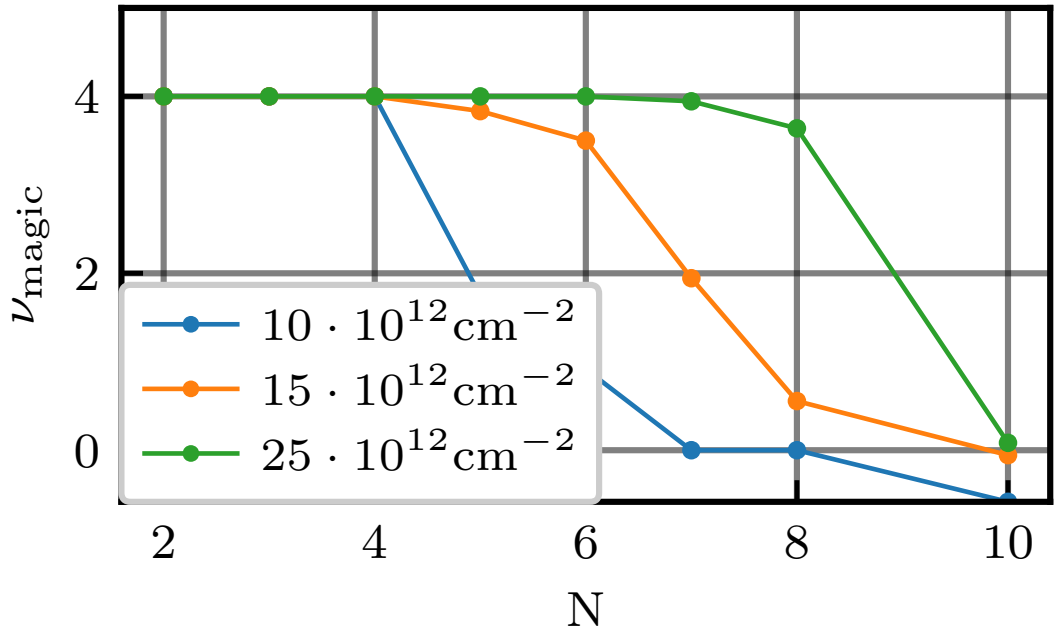

Figure 5.1: Band filling of the magic sector at different total gate densities. $25 \cdot 10^{12}\,\mathrm{cm}^{-2}$ is the threshold of dielectric breakdown in current hBN-based samples [152].

tage, focusing on the second-harmonic bands ($k = 2$) for $N \geq 5$ overcomes the prohibitive electrostatic barrier and yields very flat bands conducive to correlation effects.

This Chapter is structured as follows. Section 5.1 opens with a discussion of the experimental puzzle that this Chapter wishes to answer. Section 5.2 presents the main results of this chapter at an intuitive physical level. Section 5.3 outlines the formal description of the N-layer problem and introduces the Hartree-Fock machinery. In Sec. 5.4, we present Hartree-Fock calculations for $N = 3, 4, 5$, connecting with physical understanding of Sec. 5.2. Section 5.5 discusses the electronic properties of $N > 5$ devices in more detail. The concluding Sec. 5.6 presents a final discussion of the results.

5.1 Experimental motivation

An important physical effect in twisted alternating-angle graphene multilayers is the cascade of "resets" close to integer fillings of the flat bands. The resets already occur at relatively high temperatures, well above those required for the correlated superconducting and insulating states, and are deduced from measurements of the chemical potential [153, 154] as well as the Hall conductivity [30, 33]. The cascade of transitions can be explained in different ways [131, 151, 153–157], with Ref. [153] interpreting it as Stoner-like flavor (spin and valley) polarization. Within this picture, flat-band superconductivity is unlikely to exist when three of the four flavors are fully

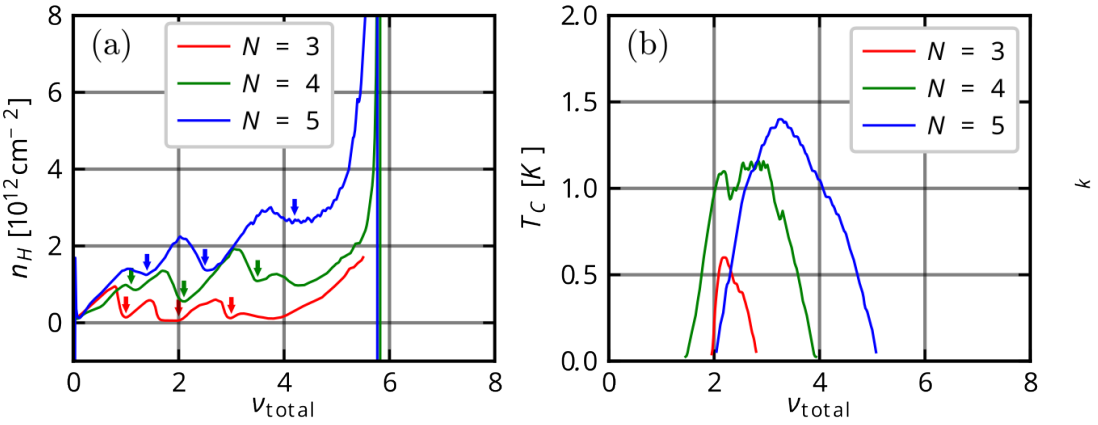

Figure 5.2: (a) Experimental data of the Hall density vs. total filling showing the cascade transitions (arrows) for $N = 3, 4, 5$. Data measured by the Nadj-Perge group and published in Ref. [31]. (b) Corresponding experimental data for T_C domes for $N = 3, 4, 5$. Data measured by the Nadj-Perge group and published in Ref. [31].

occupied and time-reversed partners at the Fermi level are absent. In TBG, this happens beyond $\nu = \pm 3$ (see further discussion in Sec. 5.3 regarding intervalley coherent orders). Irrespective of the detailed theoretical symmetry-breaking mechanism, this expectation is in line with experimental trends. In TBG, a cascade transition near $\nu = \pm 3$ typically serves as an upper filling bound for superconductivity [23, 30, 33, 158]. Similarly, a lower filling bound for superconductivity is the cascade transition at $\nu = \pm 2$.

Cascade phenomenology has also been reported for TNG systems with $N = 3, 4, 5$ layers [23, 31–33], cf., Fig. 5.2a. There, we show the experimentally measured Hall density data, highlighting the cascade transitions which manifest as dips in Hall density.

As discussed in Sec. 2.4, the band structure of TNG decomposes into decoupled sectors of TBG-like and (for N odd) monolayer-graphene (MLG)-like bands. When one of the TBG-like sectors is effectively at the magic angle, the cascade features can be understood as occurring in the magic sector, with the other sectors being filled uniformly [31, 32].

Startlingly, as shown in Fig. 5.2b and reported in Refs. [31, 32], superconductivity persists to higher total fillings (ν_{total}) in TQG (twisted quadrilayer graphene, $N = 4$) and TPG (twisted pentalayer graphene, $N = 5$), extending up to $\nu_{\text{total}} = 5$ for the $N = 5$ case of TPG. Simultaneously the cascade "resets" also set in at higher filling fractions.

Assuming that doping of the magic sector (ν_{magic}) is in the optimal range for superconductivity, i.e., approximately 2-3 electrons per moiré cell, these observations would imply substantial filling of the nonmagic sectors at odds with a simple band-structure picture. The nonmagic sectors are strongly dispersive, so that their noninteracting band structure would predict almost no filling. Specifically, complete filling of the magic bands ($\nu_{\text{magic}} = 4$) would be accompanied by a filling of less than ≈ 0.06 electrons per moiré unit cell in the nonmagic bands for TPG and

less than ≈ 0.02 electrons per moiré unit cell for TQG. (We measure fillings relative to charge neutrality.)

In order to obtain these estimates, we use the fact that the $\lfloor N/2 \rfloor$ TBG-like electronic sectors ($k = 1, 2, \ldots, \lfloor N/2 \rfloor$) have effective twist angles (see Section 2.4):

$$\theta_k^{\text{eff}} = \frac{\theta}{2\cos[\frac{\pi k}{N+1}]}, \tag{5.1}$$

which differ from the physical twist angle θ, shown in Fig. 5.3. This formula reveals the advantage of multilayers – one can obtain a sector effectively at the magic angle for devices at a larger twist angle θ. This is best exploited by choosing the $k = 1$ sector to lie effectively at the magic angle, which maximizes the physical twist angle. All the current experiments on multilayer alternating twist angle systems make this choice, and we shall also make it our default choice for analysis. However, we note that for large N, the choice $k_{\text{magic}} = 2$ also becomes feasible. We will return to this possibility in Sec. 5.5. Approximating the nonmagic sectors as Dirac cones, their filling is (see App. A.1.3)

$$\nu_{\text{non-magic}} = \sum_{k \in \text{nonmagic}} \nu_k \approx \sum_{k \in \text{nonmagic}} \frac{A_{\text{uc}} N_f c_k}{4\pi (\hbar v_D^{(k)})^2} \mu_k^2. \tag{5.2}$$

Here, $c_k = 2$ ($c_k = 1$) if the sector k is TBG-like (MLG-like), μ_k is the effective chemical potential in sector k, $N_f = 4$ is the number of flavors, and $v_D^{(k)}$ is the Dirac velocity in sector k. In the absence of interactions, $\mu_k = \mu_{\text{magic}}$ with μ_{magic} the magic sector Fermi energy. A filled magic sector corresponds to $\mu_{\text{magic}} \approx W/2$, where W is the noninteracting bandwidth. This bandwidth varies with strain, taking values $W \lesssim 20\,\text{meV}$. Even at the upper limit for W, we then find $\nu_{\text{non-magic}} \lesssim 0.06$ for TPG (using $v_D^{(k=2)} \approx 0.35 v_D$). For TQG, the $k = 2$ sector has an even larger detuning from the magic angle ($\theta_{k=2}^{\text{eff}} = 2.9°$), so that $v_D^{(k=2)} \approx 0.6 v_D$ and $\nu_{\text{non-magic}} \lesssim 0.02$. Therefore, the enhanced nonmagic-sector filling [31, 32] must be an interaction effect.

5.2 Physical understanding

Electron-electron interactions alter the above considerations predominantly through two terms in the Hamiltonian, as can be seen by examining the mean-field decomposition (see Sec. 5.3.2 and Sec. 5.3.3 for details)

$$\mathrm{H}_{\text{MF}} = \mathrm{H}_{\text{kin}} + \mathrm{H}_{\text{Hartree}} + \mathrm{H}_{\text{Fock}} + \mathrm{H}_{\text{layer}}, \tag{5.3}$$

where H_{kin} is the single-particle (kinetic) Hamiltonian, $\mathrm{H}_{\text{Hartree}}$ is the mean-field Hartree term, H_{Fock} is the Fock term, and $\mathrm{H}_{\text{layer}}$ is the mean-field layer potential term.

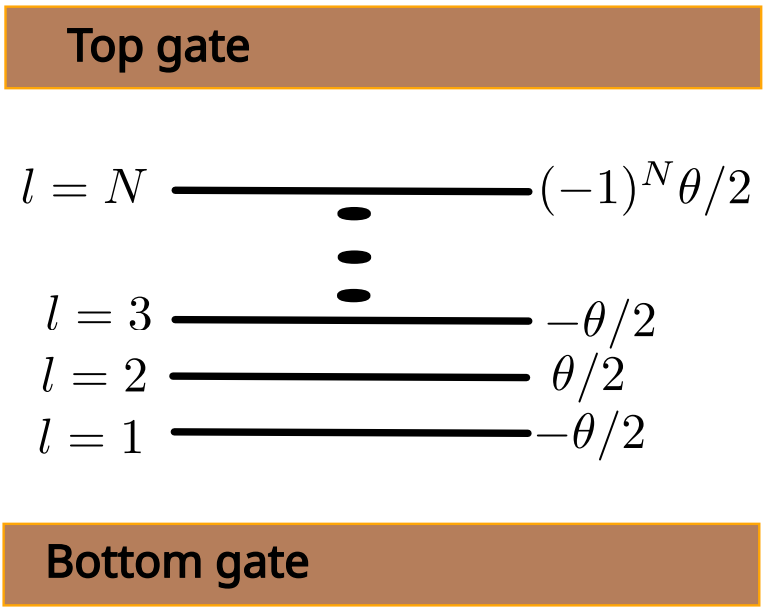

Figure 5.3: Device schematics. We consider N-layer graphene with alternating twist angles in a double-gated setup. Here θ is the physical twist angle.

First, interactions represented by the Hartree and Fock mean-field terms broaden the non-interacting magic bands, promote the onset of symmetry-breaking order, and, crucially for our analysis, induce filling-dependent upward shifts of the quasiparticle energies relative to non-magic sectors. This Hartree-dominated shift arises because the electron density of the TBG-like sectors is spatially inhomogeneous in the 2D plane, which is associated with a cost in Coulomb energy [151, 159–163]. Importantly, the inhomogeneity is particularly strong in the magic sector and decreases with detuning from the magic angle. Second, the contribution $\mathrm{H}_{\mathrm{layer}}$ is new to $N > 2$ layers and arises because the sectors have different vertical charge distributions across layers [31, 32] as shown in Fig. 2.4 of Sec. 2.4, which are given by the layer dependence of the wave functions, taking the form of standing waves analogous to a particle-in-a-box problem. The sector with lowest effective twist angle, $k = 1$, corresponds to the first harmonic, which is singly peaked at the center of the stack. The $k = 2$ sector is the second harmonic with a doubly-peaked structure, and so on. The different layer-dependent charge distributions imply that the sectors have different energies due to the electric potential produced by the gate charges.

For the devices investigated experimentally (magic sector $k = 1$), both H_{Hartree} and H_{layer} effects enhance the occupation of the non-magic sectors relative to the non-interacting band-structure scenario described above. The first mechanism postpones the occupation of the magic sector as it is broadened and shifted upward in energy as it is filled. A similar shift in energy also occurs for the second mechanism. The potential produced by the gate charges in combination with the induced charges in TNG has a maximum in the central layer. (Note that in the absence

of a displacement field, the electric field vanishes at the center by symmetry. Moreover, the potential drops towards the, say, positively charged gate electrodes above and below the TNG stack.) Due to this potential maximum, the energy is higher for sectors, in which charge is more localized near the central layer. Thus, this mechanism also predicts that the magic sector is pushed up in energy relative to the nonmagic sectors.

We can provide an estimate of this electrostatically induced band shifting, which will be verified in later Sections through extensive Hartree-Fock calculations. First we assume that in the presence of interactions, the overall band structure of each sector remains fixed (i.e., given by the non-interacting band structure) and only the chemical potential of each sector μ_k shifts as

$$\mu_k = \mu - U^{(k)} - G^{(k)} \,. \tag{5.4}$$

Here, $U^{(k)}$ and $G^{(k)}$ quantify the shifts due to H_{layer} and $\mathrm{H}_{\text{Hartree}}$, and μ is the chemical potential of the whole system. We take $G^{(k)} = 0$ for all sectors except the magic sector ($k = 1$) as it has the largest in-plane inhomogeneity (see App. A.1.1). In the magic sector [151, 159, 160, 164], the Hartree shift is approximately $G^{(k)} \sim e^2/(4\pi\epsilon_\parallel\epsilon_0 L_M)$, where L_M is the moiré period. For TPG, depending on dielectric constant, $G^{(k)}$ can be as large as $30\,\mathrm{meV}$, giving a filling of up to $\nu_{\text{non-magic}} \approx 1.1$ of the nonmagic sectors at full filling of the magic sector, $\nu_{\text{magic}} = 4$. This should be compared to the non-interacting estimate of $\nu_{\text{non-magic}} \approx 0.06$ given above.

Inclusion of the shift $U^{(k)}$ induced by H_{layer} can further increase the filling of $\nu_{\text{non-magic}}$. The term $\mathrm{H}_{\text{layer}}$ contributes nontrivially due to imperfect screening of the gate electrodes by the layers and becomes increasingly important as N grows. The energy shift $U^{(k)}$ of a sector k can be approximated by (see App. A.3.2)

$$U^{(k)} = e^2 \frac{d_l}{A_{\mathrm{UC}}\epsilon_0\epsilon_\perp} \sum_{k'} (C^{-1})_{k,k'}\nu_{k'} \tag{5.5}$$

for given sector fillings ν_k. Here, A_{UC} is the unit-cell area, d_l is the layer distance, and $\epsilon_\perp$ the out-of-plane dielectric constant of the graphene layers. The matrix C in sector space is a dimensionless capacitance-like matrix, which we tabulate for TQG, TPG, as well as large N in Table 5.1 (see App. A.3.2 for formulas for arbitrary N and derivations). For TPG, we obtain a shift of up to $45\,\mathrm{meV}$, allowing for a filling of up to $\nu_{\text{non-magic}} \approx 2.5$ for full filling of the magic sector, $\nu_{\text{magic}} = 4$ (see Sec. 5.3.2 for further discussion).

Modifications of the quasiparticle dispersion by H_{Fock} would tend to reduce the above estimates. However, we also highlight that the effects of the layer potential $\mathrm{H}_{\text{layer}}$ and the Hartree correction $\mathrm{H}_{\text{Hartree}}$ mutually reinforce each other. To illustrate this, consider the sector shift $U^{(1)} - U^{(2)} = 10\,\mathrm{meV}$ and $G^{(1)} = 10\,\mathrm{meV}$ and small bandwidth $W/2 = 2\,\mathrm{meV}$. Taken separately, each term would only yield a tiny $\nu_{\text{non-magic}} \approx 0.07$. On the other hand, taking $\mu_2 = 22\,\mathrm{meV}$ in Eq. (5.2) yields a four times larger $\nu_{\text{non-magic}} \approx 0.3$. This highlights the importance of considering both shift mechanisms simultaneously.

N	$(C^{-1})_{1,1}$	$(C^{-1})_{1,2} = (C^{-1})_{2,1}$	$(C^{-1})_{2,2}$
4	0.262	0.1	0.0382
5	0.403	0.208	0.125
$N \to \infty$	$0.147\,N$	$0.115\,N$	$0.099\,N$

Table 5.1: Inverse capacitance $(C^{-1})_{k,k'}$ for $k, k' \in \{1, 2\}$, evaluated for layer numbers $N = 4$, $N = 5$, and $N \to \infty$.

To conclude the qualitative analysis of this Section, we comment on the relative role the three interaction terms in Eq. (5.3) play as the layer number N increases. The inverse capacitance matrix $(C^{-1})_{k,k'}$ is a decreasing function of k and k'. Physically, larger-k sectors screen the gate field better, therefore generating smaller layer potentials. This monotonic decrease implies that $U^{(\text{magic})} - U^{(k)} > 0$ for any (nonmagic) $k > 1$. Thus, the effective chemical potentials μ_k of the nonmagic sectors increase, enhancing their occupations. Secondly, for fixed k and k', $(C^{-1})_{k,k'}$ scales linearly with the vertical extent (as the inverse capacitance of a parallel-plate capacitor) and thus with the number of layers N. This suggests that the layer potential grows in importance with N, eventually dominating over other contributions for large N. Indeed, other contributions to the mean-field Hamiltonian do not grow with the number of layers. This suggests that the layer potentials become dominant at large N and doping of the central $k = 1$ sector by gating will be preempted by dielectric breakdown [152], as shown in Fig. 5.1. We return to this analysis using Hartree-Fock calculations in subsequent Sections.

5.3 Model of alternating twisted N-layer graphene

In this Section, we recall the noninteracting model, specify the interaction, and discuss the mean-field decoupling. While we largely follow standard procedures for the mean-field description of moiré graphene [76, 110, 143, 151, 165–167], we allow for layer dependence of the interaction and include the layer potential term that is usually ignored.

5.3.1 Twisted graphene multilayers

We consider N-layer alternating angle twisted graphene, using the minimal model introduced in Sec. 2.4, which we recall here for convenience:

$$\mathrm{H}^K_{\text{kin}} = H^K_{\text{TNG}} = \begin{pmatrix} v_F \mathbf{k}\cdot\boldsymbol{\sigma} & T(\mathbf{r}) & 0 & \cdots & 0 \\ T^\dagger(\mathbf{r}) & v_F \mathbf{k}\cdot\boldsymbol{\sigma} & T^\dagger(\mathbf{r}) & & \\ 0 & T(\mathbf{r}) & v_F \mathbf{k}\cdot\boldsymbol{\sigma} & & \\ \vdots & & & \ddots & \end{pmatrix}. \tag{5.6}$$

Neglecting possible layer dependence, we account for lattice relaxation by choosing $w_{AA} = 80\text{meV}$, $w_{AB} = 110\text{meV}$ [150]. This model is a minimal description of N-layer systems, neglecting relative layer displacements [78, 168], next-nearest-layer hoppings [78], periodic strain [70], and layer dependence of lattice corrugation [150]. While these additional ingredients modify the quantitative details of the electronic spectrum, they do not alter the two key features, namely the inhomogeneous charge distribution and the inhomogeneous distribution of electronic sectors across layers. Both ingredients are crucial to capture the effect of interactions on the properties of the N-layered structure.

We recall that the single-particle Hamiltonian transforms into block-diagonal form using the basis outlined in Chapter 2, Section. 2.4. There are $\lfloor N/2 \rfloor$ TBG-like blocks with effective interlayer hoppings rescaled by a coefficient Λ_k. We can equivalently think of the sectors as corresponding to TBG with unscaled hoppings, but an effective twist angle

$$\theta_k^{\text{eff}} = \theta/\Lambda_k. \tag{5.7}$$

In this picture, the sector Hamiltonian is multiplied by an overall scale factor Λ_k. For N odd, in addition to the $\lfloor N/2 \rfloor$ TBG-like sectors, there is an additional sector, in which the band derives from the underlying graphene Dirac cone folded into the moiré Brillouin zone (BZ). We will denote this sector as the monolayer-graphene (MLG)-like sector. In what follows, we choose the physical angle θ such that there is one TBG-like sector – termed magic sector – at the magic angle, $\theta_k^{\text{eff}} = \theta^{\text{magic}} \approx 1.1^\circ$. In experiments to date, this would be the $k = 1$ sector, but in Sec. 5.5 we also consider the possibility of choosing $k_{\text{magic}} = 2$ as the magic sector. The weight distribution in Eq. (2.72) quantifies the charge distributions across layers for the various sectors, see Fig. 2.4. As discussed above, this is important for the electrostatic properties of the problem.

5.3.2 Layer-dependent Coulomb interaction

We assume a symmetric double-gated setup, shown in Fig. 5.3, as typically employed in experiment. For simplicity, we only consider symmetric gating, working at gate charge densities $en/2$ per gate, so that $-en$ is the charge density in TNG. This correspond to setting the displacement field $D = 0$. At a microscopic level, we use the standard Coulomb interaction

$$\mathrm{H}_{\text{int}}^{\text{bare}} = \frac{1}{2}\int d\mathbf{r} d\mathbf{r}' V(\mathbf{r}-\mathbf{r}') : \rho(\mathbf{r})\rho(\mathbf{r}') :, \tag{5.8}$$

where $V(\mathbf{r}-\mathbf{r}') = \frac{1}{4\pi\epsilon\epsilon_0}\frac{1}{|\mathbf{r}-\mathbf{r}'|}$, and where the density $\rho(\mathbf{r})$ includes free charges in both the graphene system and on the gates with the positive background subtracted (: ... : denotes normal ordering).

To obtain the effective interaction for TNG, we consider the charges to be constrained in $N+2$ layers labeled by an index L going from 0 to $N+1$ at vertical positions z_L. This corresponds to the physical situation of a sample with N graphene layers and two gate layers $L = 0, N+1$.

We take $z_0 = -d_s$, $z_{N+1} = d_s$, and $z_l = d_l(l - N/2)$ for $l = 1, \ldots, N$ corresponding to the graphene layers, where d_s is the gate sample distance and d_l is the constant interlayer distance of the TNG sample.

We decompose $\rho(\mathbf{r}) = \sum_L \rho_L(\mathbf{r})\delta(z - z_L)$, where $\rho_L(\mathbf{r})$ is the (2-dimensional) density in layer L. In Fourier space, we have

$$\mathrm{H}_{\mathrm{int}}^{\mathrm{bare}} = \frac{1}{2A} \sum_{\mathbf{q},L,J} V_{LJ}^{\mathrm{bare}}(\mathbf{q}) : \rho_{\mathbf{q},L}\rho_{-\mathbf{q},J} :, \tag{5.9}$$

where $\rho_{\mathbf{q},L}$ is the electron density in layer L at in-plane momentum $\mathbf{q}$, A is the 2-dimensional area of the sample, and where we sum also over layers 0 and $N + 1$ corresponding to the gates. V_{LJ}^{bare} is the bare Fourier-transformed 2D Coulomb interaction with vertical separation $d_{LJ} = |z_L - z_J|$, which reads

$$V_{LJ}^{\mathrm{bare}}(\mathbf{q}) = \frac{e^2}{2\epsilon\epsilon_0 q} \exp(-d_{LJ}q). \tag{5.10}$$

For $\mathbf{q} = 0$, we separate the divergent and finite parts as follows

$$V_{LJ}^{\mathrm{bare}}(\mathbf{q} \to 0) = \frac{e^2}{2\epsilon\epsilon_0} \left[O\left(\frac{1}{q}\right) - d_{LJ} \right]. \tag{5.11}$$

The divergent part is canceled if the total charge adds up to zero $\sum_L \rho_{\mathbf{q}=0,L} = 0$, and what remains of the $\mathbf{q} = 0$ term is $-\frac{e^2}{2\epsilon\epsilon_0} d_{LJ}$. Therefore we obtain, separating $\mathbf{q} = 0$:

$$\mathrm{H}_{\mathrm{int}}^{\mathrm{bare}} = \frac{1}{2A} \left[\sum_{\mathbf{q}\neq 0,L,J} V_{LJ}^{\mathrm{bare}}(\mathbf{q}) : \rho_{\mathbf{q},L}\rho_{-\mathbf{q},J} : - \sum_{L,J} \frac{e^2}{2\epsilon\epsilon_0} d_{LJ} : \rho_{\mathbf{q}=0,L}\rho_{\mathbf{q}=0,J} : \right]. \tag{5.12}$$

which still includes the gate charges. We can simplify the second term by using that the charge on the gates and in the sample are fixed, allowing us to replace $\frac{\rho_{\mathbf{q}=0,0}}{A} \to -\frac{n}{2}$, $\frac{\rho_{\mathbf{q}=0,N+1}}{A} \to -\frac{n}{2}$, and $\frac{\sum_{l=1}^{N} \rho_{\mathbf{q}=0,l}}{A} \to n$. Then the second term can be (up to a n dependent constant) more physically rewritten as the electrostatic energy of the perpendicular electric field between the layers $\sum_{l=1}^{N-1} A\epsilon_\perp\epsilon_0 d_l \frac{(E_{l,l+1}^{\perp})^2}{2}$, where the electric field is given by Gauss' law as:

$$E_{l,l+1}^{\perp} = -\frac{e}{\epsilon_0\epsilon} \left\{ \frac{1}{A} \sum_{l'=1}^{l} \langle \hat{\rho}_{\mathbf{q}=0,l'} \rangle - \frac{n}{2} \right\}. \tag{5.13}$$

Note that if we had not assumed symmetric gating, we would replace $-\frac{n}{2}$ by the charge on the bottom gate, as will be done in Chapter 6.

For the $\mathbf{q} \neq 0$ term, we assume the two gates are at positions $z = \pm d_s$ and integrate out the gate electrons, ending up with an effective screened interaction for the N layers. The effective interaction is obtained by solving the Poisson equation, where the gate electrons impose that the

gate positions $z = \pm d_s$ are equipotentials. This can be obtained using the method of images, as we now show.

First, we investigate the potential due to point charges. Consider the positions of image charges when a positive unit charge is placed at z_0. Due to the presence of two gates, there will be infinitely many image charges in the regions above d_s and below $-d_s$. We denote the z-coordinate of the position of the n-th image charge in the top gate ($z > d_s$) as d_n^{top}, while the z-coordinate of the position of the m-th image charge in the bottom gate will be d_m^{bottom}. The first image charge in the top gate will be at $d_1^{\text{top}} = 2d_s - z_0$, while the first image charge in the bottom gate at $d_1^{\text{bottom}} = -2d_s - z_0$, and they have negative unit charge. Next, the bottom gate is affected by the image charge in the top gate and vice versa, implying we need to place more and more charges. We, obtain the intertwined recurrence relation for the positions of the $n+1$-th image charges

$$d_{n+1}^{\text{top}} = 2d_s - d_n^{\text{bottom}} \tag{5.14}$$
$$d_{n+1}^{\text{bottom}} = -2d_s - d_n^{\text{top}}, \tag{5.15}$$

where the charge of the n-th image charge is $(-1)^n$. This recurrence is solved by :

$$d_n^{\text{top}} = 2nd_s + (-1)^n z_0 \tag{5.16}$$
$$d_n^{\text{bottom}} = -2nd_s + (-1)^n z_0. \tag{5.17}$$

The potential at vertical position z and an in-plane distance r away from the unit test charge is given by the sum of the potentials of the charge and all the image charges generated. We have

$$V(r,z,z_0) = \frac{1}{4\pi\epsilon\epsilon_0}\left[\frac{1}{\sqrt{r^2+(z-z_0)^2}} + \sum_{j=1}^{\infty}\frac{(-1)^j}{\sqrt{r^2+(2jd_s+(-1)^j z_0 - z)^2}} + \right.$$
$$\left. + \sum_{j=1}^{\infty}\frac{(-1)^j}{\sqrt{r^2+(2jd_s+z-(-1)^j z_0)^2}}\right]. \tag{5.18}$$

In Fourier space, we obtain:

$$V(q,z,z_0) = \frac{1}{2\epsilon\epsilon_0}\frac{1}{q}\left\{\exp(-q|z-z_0|) + \sum_{j=1}^{\infty}(-1)^j \exp\big[-q(2jd_s+(-1)^j z_0 - z)\big] + \right.$$
$$\left. + \sum_{j=1}^{\infty}(-1)^j \exp\big[-q(2jd_s-(-1)^j z_0 + z)\big]\right\}, \tag{5.19}$$

where we removed the absolute value in the image charge potentials since we are interested in the potential inside the sample, assuming $|z| < d_s, |z_0| < d_s$. The sum over j can be easily performed by separating into j odd and even, leading to the result:

$$V(q,z,z_0) = \frac{1}{2\epsilon\epsilon_0}\frac{1}{q}\cdot\left(\frac{e^{-q(z+z_0)}\left(-e^{2q(d_s+z+z_0)}-e^{2d_sq}+e^{2qz}+e^{2qz_0}\right)}{e^{4d_sq}-1}+e^{-q|z-z_0|}\right). \tag{5.20}$$

For $z = z_0 = 0$, $V(q,z,z_0)$ reduces to the $\tanh(qd_s)/q$ form usually used for double-gate screened interaction. On the other hand, with no screening ($d_s \to \infty$) we recover the bare interaction in Eq. (5.10). For an N-layer system with layers at positions $z_l = d_l(l - N/2)$, we obtain the effective $\mathbf{q} \neq 0$ layer-dependent screened interaction:

$$V_{l,l'}(\mathbf{q}) = \frac{1}{2\epsilon\epsilon_0}\frac{1}{q}\cdot\left(\frac{e^{-q(z_l+z_{l'})}\left(-e^{2q(d_s+z_l+z_{l'})}-e^{2d_sq}+e^{2qz_l}+e^{2qz_{l'}}\right)}{e^{4d_sq}-1}+e^{-q|z_l-z_{l'}|}\right). \tag{5.21}$$

Using this, the final result, our interacting Hamiltonian for the system reads:

$$\mathrm{H}_{\text{int}} = \frac{1}{2A}\sum_{\mathbf{q}\neq 0}\sum_{l,l'} V_{l,l'}(\mathbf{q}) : \rho_{\mathbf{q},l}\rho_{-\mathbf{q},l'} : + \sum_{l=1}^{N-1} A\epsilon_\perp\epsilon_0 d_l \frac{(E^\perp_{l,l+1})^2}{2}. \tag{5.22}$$

Note that here we allow the dielectric constant of the $\mathbf{q} = 0$ term ($\epsilon_\perp$) to differ from the dielectric constant entering $V_{l,l'}(\mathbf{q})$ ($\epsilon_\parallel$). Physically, the out-of-plane interaction reflects the out-of-plane response of graphene, while the $\mathbf{q} \neq 0$ component is governed by the dielectric properties of the substrate. For graphene layers, $\epsilon_\perp$ has been estimated to be around 2 [169, 170], while $\epsilon_\parallel$ is around 5 for hBN substrates [77, 160, 171, 172]. Larger values, accounting for remote band screening, have also been investigated [142, 143, 160]. We treat the dielectric constants as parameters. Without the second term, Eq. (5.22) is the standard in-plane Coulomb interaction of a 2D system with screening due to metallic gates. The second term is not usually included, but is important for multilayer systems as discussed in Sec. 5.2.

5.3.3 Mean-field decoupling

We perform our numerical calculations by restricting the full Hilbert space to a finite number of N_{active} bands with N_{flavor} spin/valley flavors, having single-particle wavefunctions $|u_{\mathbf{k},f,\beta}\rangle$, where the discretized momentum $\mathbf{k}$ lies in the first moiré Brillouin zone. Specific details of the numerical simulation are provided in Appendix A.4. We search for a $N_{\text{active}} \times N_{\text{active}}$ density matrix $[P_f(\mathbf{k})]_{\alpha\beta} = \langle c^\dagger_{\mathbf{k},f,\alpha} c_{\mathbf{k},f,\beta}\rangle$, where $\langle\hat{O}\rangle$ denotes the expectation value of an operator $\hat{O}$, and where $c_{\mathbf{k},f,\beta}$ annihilates a flavor-f electron in the single-particle band β at momentum $\mathbf{k}$.

Note that each single-particle state can be assigned to a sector $k \in \{1, \ldots, \lceil N/2 \rceil\}$, as a result of the sector decomposition detailed in Sec. 2.4. We keep N_{remote} remote bands, which generate additional Hartree and Fock interaction terms. In projecting onto a finite set of bands, we are assuming frozen completely filled bands below and completely empty bands above this set. To avoid overcounting of interactions already present in monolayer graphene and thus included in the BM model [76, 142, 167], we subtract a mean-field Hamiltonian corresponding to a reference density matrix $P^0_f(\mathbf{k})$. This is implemented in the mean-field equations by replacing every $P_f(\mathbf{k})$ with

$$\delta P_f(\mathbf{k}) = P_f(\mathbf{k}) - P^0_f(\mathbf{k}). \tag{5.23}$$

We choose the subtraction scheme [76, 110, 142, 167] in which $P^0_f(\mathbf{k})$ is the ground density matrix at charge neutrality with the interlayer hoppings switched off. For bands far below the charge-neutrality point, interlayer hoppings are ineffective and this density matrix approximates that of fully filled TNG bands. It therefore cancels with the remote-band-interaction term to a good approximation [76, 77], justifying retaining only a finite number N_{remote} of remote bands.

For the in-plane term, the mean-field decoupling extends the usual procedure detailed in previous studies [76, 78, 142, 143, 151, 165, 166] to include the layer dependence of $V_{l,l'}(\mathbf{q})$. The resulting Hartree term reads

$$\mathrm{H}_{\text{Hartree}} = \frac{1}{A} \sum_{l,l'} \sum_{\mathbf{G}} \hat{\rho}_{\mathbf{G},l} V_{l,l'}(\mathbf{G}) \langle \hat{\rho}_{-\mathbf{G},l'} \rangle, \tag{5.24}$$

where we introduce the projected layer density operator, $\hat{\rho}_{\mathbf{G},l} = \sum_{f\mathbf{k}} c^\dagger_{\mathbf{k},f} \Lambda^{fl}_{\mathbf{G}}(\mathbf{k}) c_{\mathbf{k},f}$, where $\left[\Lambda^{fl}_{\mathbf{G}}(\mathbf{k})\right]_{\alpha,\beta} = \left\langle u_{\mathbf{k},f,\alpha} \,\middle|\, e^{i\mathbf{G}\cdot\mathbf{r}} \mathbb{I}_l \,\middle|\, u_{\mathbf{k},f,\beta} \right\rangle$ is the overlap matrix between the Bloch wavefunctions of bands α and β at momentum $\mathbf{k}$ on layer l and in flavor f, where $\mathbb{I}_l$ is the projector on layer l. Note that we consider $c_{\mathbf{k},f}$ as a column vector. The mean-field expectation of the density operator is

$$\begin{aligned} \langle \hat{\rho}_{-\mathbf{G},l'} \rangle &= \sum_f \sum_{\mathbf{k}} \langle c^\dagger_{\mathbf{k},f} \Lambda^{fl'}_{-\mathbf{G}}(\mathbf{k}) c_{\mathbf{k},f} \rangle \\ &= \sum_f \sum_{\mathbf{k}} \mathrm{Tr}\left[\delta P^T_f(\mathbf{k}) \Lambda^{fl'}_{-\mathbf{G}}(\mathbf{k}) \right]. \end{aligned} \tag{5.25}$$

Here, the trace runs over the space of active bands. Similarly, the Fock term reads

$$\begin{aligned} \mathrm{H}_{\text{Fock}} = -\frac{1}{A} \sum_f \sum_{l,l'} \sum_{\mathbf{q},\mathbf{k}} V_{l,l'}(\mathbf{q}) \\ \times c^\dagger_{\mathbf{k},f} \left[\Lambda^{fl}_{\mathbf{q}}(\mathbf{k}) \delta P^T_f(\mathbf{k}+\mathbf{q}) \Lambda^{fl'}_{-\mathbf{q}}(\mathbf{k}+\mathbf{q}) \right] c_{\mathbf{k},f}, \end{aligned} \tag{5.26}$$

where in contrast to the Hartree term, each flavor interacts only with itself.

At the mean-field level, the charge distribution across the layers enters the Hamiltonian through

$$\mathrm{H}_{\text{layer}} = -e \sum_{l} \hat{\rho}_{\mathbf{q}=0,l} V_l, \tag{5.27}$$

where V_l is the electrostatic potential and $\hat{\rho}_{\mathbf{q}=0,l}$ the electron number (i.e., the $\mathbf{q} = 0$ Fourier component of the electron density $\hat{\rho}_{\mathbf{q},l}$) of layer l projected onto the active bands. The term $\mathrm{H}_{\text{layer}}$ contributes nontrivially due to imperfect screening of the gate electrodes by the layers and becomes increasingly important as N grows. App. A.2 details a formal derivation of $\mathrm{H}_{\text{layer}}$ in Eq. (5.27) by decoupling the out-of-plane term in Eq. (5.22). The difference of layer potentials

$$V_{l+1} - V_l = -d_l E^{\perp}_{l,l+1} \tag{5.28}$$

is related to the electric field, which is given by Gauss' law in Eq. (5.13). We fix the arbitrary constant of V_l by setting $V_1 + V_N = 0$.

Defining $U_l = -eV_l$ and $\mathbb{I}_l$ as the projector onto layer l, $\mathrm{H}_{\text{layer}}$ can be written more simply as follows

$$\mathrm{H}_{\text{layer}} = \sum_{l=1}^{N} U_l \, \mathbb{I}_l, \tag{5.29}$$

with the potential difference given simply as

$$U_{l+1} - U_l = -e^2 d_l \frac{-n/2 + \sum_{j \le l} n_j}{\epsilon_{\perp} \epsilon_0}, \tag{5.30}$$

where

$$n_j = \frac{1}{A} \langle \hat{\rho}_{\mathbf{q}=0,j} \rangle \tag{5.31}$$

is the net electron density on layer j.

We note in passing that Ref. [150] similarly considers interaction effects on the electronic spectrum of $N > 3$ systems. The nonmagic sectors are described as a set of equal Dirac cones with the chemical potential set by that of the flat bands. Their role in the mean-field calculation is reduced to providing static RPA screening for the magic sector as given by Refs. [173, 174]. This procedure focuses solely on describing interaction effects in the magic bands, but misses the impact of the nonmagic sectors on hybridizing the sectors and shifting their relative energies with the concomitant changes in filling.

Our analysis assumes that the symmetry breaking preserves the flavor index, precluding intervalley coherent states [76, 110, 147, 172] , which are likely the actual ground states [107, 133] of twisted bilayer graphene [175–177]. This limits our analysis to qualitative features of the phase diagram of N-layer alternating twisted bilayer graphene. This approach has been shown to reproduce experimental trends [131, 153]. As we will see, the phase diagram of TNG is mainly controlled by the interplay of the in-plane Hartree and layer potentials, which on the moiré

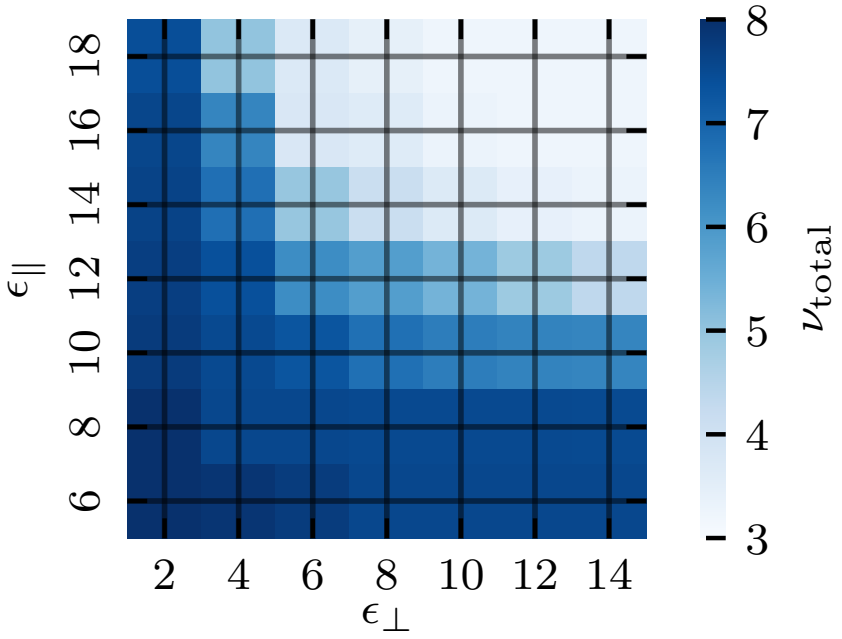

Figure 5.4: Colormap of ν_{total} needed to reach filling $\nu_{\text{magic}} = 3$ of the magic sector in the $\epsilon_\parallel$-$\epsilon_\perp$ plane.

scale, are insensitive to the subtle details of flavor-symmetry breaking [151]. We thus expect our results to apply even when different candidate ground states [76, 110, 147, 172] (such as intervalley coherent states) are considered for the magic sector.

Experimental samples are, to some extent, always strained [80, 178–182]. Strain increases the kinetic energy of the bands, suppressing interaction effects, and breaks C_3 symmetry, preventing gap opening by C_2T symmetry breaking. We incorporate strain as a constant vector potential, which alternates between layers (heterostrain [146]) as described in App. A.1.2. This simplified description of strain is sufficient to capture the broadening of the noninteracting bands as well as the C_3 symmetry breaking. Not considering intervalley coherence, we also preclude the incommensurate-Kekulé-spiral state [110, 167], for which there is some experimental support [106, 107]. Again, this is justified since electrostatic effects have larger energy scales and contribute over a wider temperature range.

5.4 Mean-field results for $N \leq 5$

We now apply the mean-field approach detailed above to alternating twisted N-layer structures with $N = 3, 4, 5$, confirming the qualitative reasoning discussed in Sec. 5.2. Figures 5.2a,b showed the experimental results for the filling dependence of the Hall density and of the superconducting T_C, respectively. Taken together, these data indicate a substantial filling of the

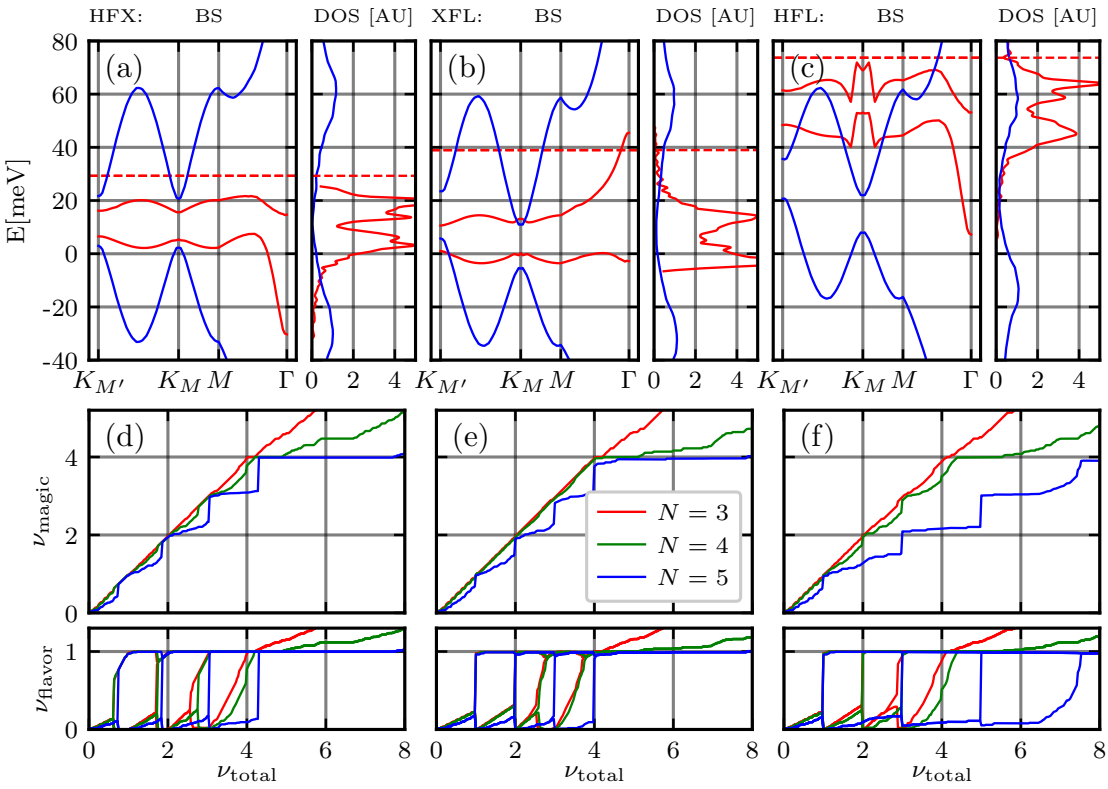

Figure 5.5: (a) Interacting structures and densities of states for TPG at $\nu_{\text{magic}} \approx 4$, including in-plane Hartree and Fock (HFX) terms from Eq. 5.3. Shown are the $k = 1$ magic sector (red) and $k = 2$ nonmagic TBG-like sector (blue). Dashed red lines denote the location of the Fermi level. (b) Same as (a) but with layer Hartree potentials and Fock (XFL) (c) Same as (a) but including all terms, that is, HFL. (d) Total magic sector filling (top) and flavor-resolved magic filling (bottom), showing the cascade with in-plane Hartree and Fock (HFX) for $N = 3, 4, 5$. (e) Same as (d), but with out-plane Hartree and Fock (XFL) (f) Same as (d), but including all the terms (HFL).

nonmagic sectors. As originally proposed in Refs. [31, 32], this enhanced filling can arise because of both, $\mathrm{H}_{\text{layer}}$ or $\mathrm{H}_{\text{Hartree}}$.

To disentangle the effects of $\mathrm{H}_{\text{layer}}$ and $\mathrm{H}_{\text{Hartree}}$, we first consider the total filling required for $\nu_{\text{magic}} = 3$ (taken here as a tentative upper bound for superconductivity) for TPG as a function of the dielectric constants $\epsilon_{\parallel}$ and $\epsilon_{\perp}$, see Fig. 5.4. To focus on the cascade physics, we include moderate strain ($\epsilon_{\text{strain}} = 0.2\%$), which explicitly breaks C_3 symmetry and suppresses the appearance of correlated insulating states. For strong interactions (small dielectric constants), the entire $k = 2$ nonmagic sector fills first before the magic sector starts to fill, incompatible with the onset of superconductivity for $\nu \approx 2$ in Fig. 5.2b. In the opposite, weakly interacting limit, only negligible filling of the nonmagic sectors is induced, precluding an extended superconducting pocket. Therefore, we use moderate $\epsilon_{\parallel} = 14$ and $\epsilon_{\perp} = 6$ in this Section. We refer the interested reader to the publication, Ref. [3], for other parameter choices.

To probe the interplay of H_{layer} and $H_{Hartree}$, Figs. 5.5a,d show numerical results retaining only the in-plane Hartree and Fock terms ("HFX") and Figs. 5.5b,e display corresponding results retaining only the out-of-plane (H_{layer}) and Fock terms ("XFL"). Finally, Figs. 5.5c,f include all terms ("HFL"). We first consider the band structures at full filling of the magic sector, plotted in Figs. 5.5a-c. Excluding the Hartree or layer potentials (HFX, Fig. 5.5a and XFL, Fig. 5.5b), we obtain only a minimal shift of the magic (red) vs. the nonmagic (blue) sectors. Interestingly, we find that in these approximations, the shifts due to $H_{Hartree}$ and H_{layer} are largely compensated by the effects of H_{Fock}. However, there is a substantial shift when including all terms (HFL, Fig. 5.5c). This highlights the importance of considering all of the terms together.

These trends are also reflected in the cascade plots in Figs. 5.5d-f for $N = 3, 4, 5$, which exhibit the flavor-resolved fillings as a function of ν_{total}. Figures 5.5d,e show results for XFL and HFX, respectively, and exhibit little effect of the nonmagic sectors on the cascade. This is consistent with the absence of a shift in Figs. 5.5a and b. In contrast, Fig. 5.5f shows increasingly delayed cascade transitions as the number of layers N grows. This again reflects the importance of incorporating the effects of both, H_{layer} and $H_{Hartree}$.

Numerically, for our choice of dielectric constants and $N = 5$, the $\nu_{magic} = 3$ cascade is pushed to $\nu_{total} \approx 5$, while the $\nu_{magic} = 2$ cascade happens at $\nu_{total} \approx 3$. While the $\nu_{magic} = 3$ cascade is consistent with experiment, the superconductivity data (Fig. 5.2b) suggest that the $\nu_{magic} = 2$ cascade already appears at $\nu_{total} \approx 2$. Fully reproducing the experimental data may require more accurate modeling of the devices or more accurate approximations, e.g., allowing for the appearance of intervalley correlated ground states[76, 106, 107, 110, 147, 172].

5.5 Large-N analysis

We now consider the interplay of the in-plane Hartree, Fock, and layer potentials in the experimentally unexplored cases of $N > 5$ and $k_{magic} = 2$. The key question we would like to explore is to what extent TNG reproduces the phenomenology of TBG, when charge-inhomogeneity-induced band shifts are included?

Figure 5.6 presents the main results of this Section for $\epsilon_{\parallel} = 10$ and $\epsilon_{\perp} = 6$. In Fig. 5.6a and Fig. 5.6b, we consider the ν_{total} needed to achieve complete filling of the magic sector, $\nu_{magic} = 4$. We compare the cases of $k_{magic} = 1$ (spectral weight peaked in the central layers, Fig. 5.6a) and $k_{magic} = 2$ sector (spectral weight predominantly away from the central layers, Fig. 5.6b). Each figure shows plots including (i) the in-plane Hartree and Fock (HFX), (ii) the layer potentials and Fock (XFL), and (iii) all terms combined (HFL). For $k_{magic} = 1$ (Fig. 5.6a), we see that the total filling required to completely fill the magic sector increases dramatically with N. This confirms our expectation that gating the $k_{magic} = 1$ sector becomes prohibitively difficult as the layer number increases.

Interestingly, when choosing $k = 2$ as the magic sector (Fig. 5.6b), the magic sector fills much more easily. This is a result of the fact that the potential due to the gate charges is maximal at

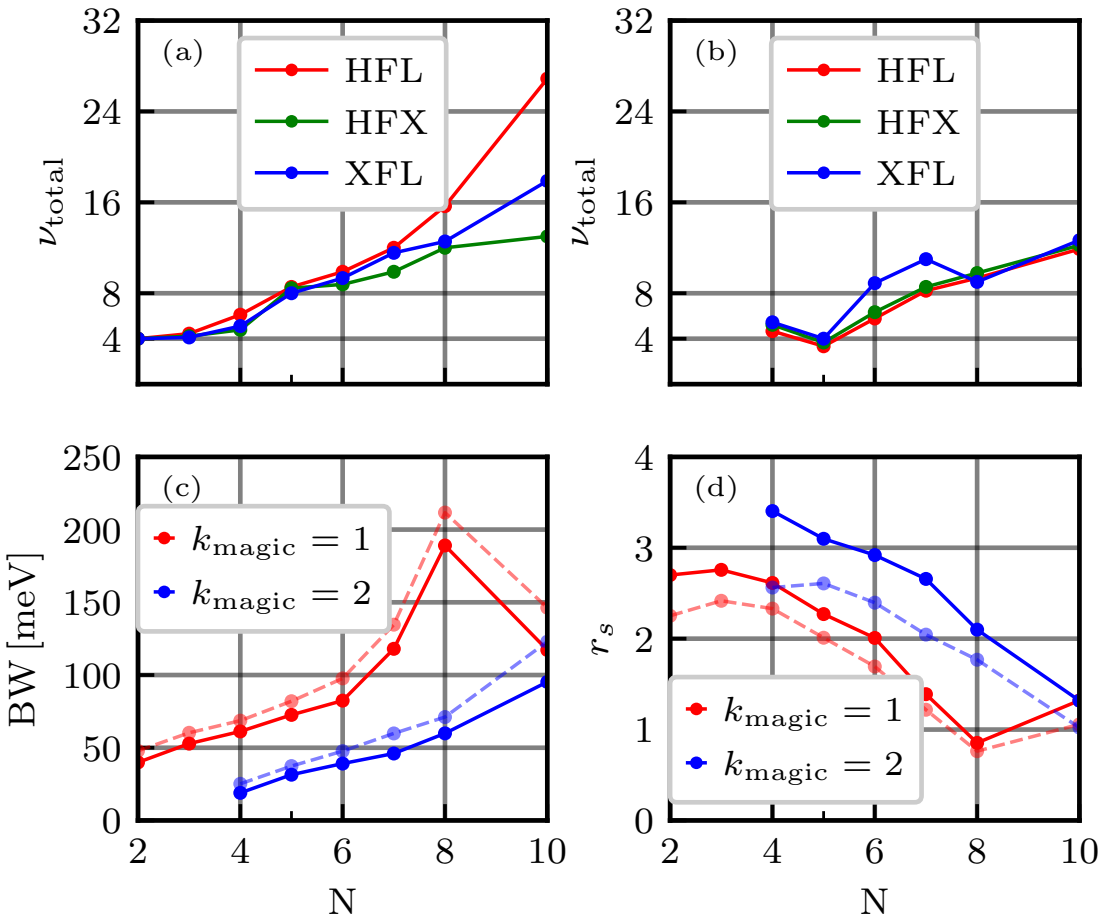

Figure 5.6: (a) ν_{total} as a function of layer number N at $\nu_{\text{magic}} = 4$ choosing $k = 1$ as the magic sector at $\epsilon_{\parallel} = 10$, $\epsilon_{\perp} = 6$, $\epsilon_{\text{strain}} = 0\%$. (b) Same as (a) for $k_{\text{magic}} = 2$. (c) Bandwidth at $\nu_{\text{magic}} = 4$ for the choice of $k_{\text{magic}} = 1$ (red) and $k_{\text{magic}} = 2$ (blue). Dashed curves are for finite strain $\epsilon_{\text{strain}} = 0.2\%$. (d) Effective interaction parameter r_s at $\nu_{\text{magic}} = 4$ for $k_{\text{magic}} = 1$ (red) and $k_{\text{magic}} = 2$ (blue). Dashed lines are at finite strain $\epsilon_{\text{strain}} = 0.2\%$.

the central layers, so that the $k = 1$ sector is more strongly shifted than the $k = 2$ sector. As a result, $k_{\text{magic}} = 2$ circumvents the electrostatic barrier present for gating the $k = 1$ sector, providing a promising platform to study TBG-like physics in TNG samples with larger N.

In Fig. 5.6c, we consider the bandwidth of the magic sector. We compute the interacting bandwidth of the completely filled magic bands at $\nu_{\text{magic}} = 4$ (see Ref. [3] for other parameter choices) defined as

$$\text{BW} = \max_{\mathbf{k}} E^{+}_{\mathbf{k}} - \min_{\mathbf{k}} E^{-}_{\mathbf{k}}, \tag{5.32}$$

where $E^{+}_{\mathbf{k}}$ ($E^{-}_{\mathbf{k}}$) are the band energies of the upper (lower) magic sector band. Choosing $k = 1$ (red) as the magic sector, we observe a substantial increase in bandwidth due to the in-plane Hartree and layer potentials. This suggests that even if the bands could be filled, the increased

bandwidth will suppress correlated physics associated with the flat-band regime. Choosing $k = 2$ (blue) as the magic sector, the bandwidth also increases with N, but less so than for $k_{\text{magic}} = 1$. This can be partially explained by the fact that much of the bandwidth is interaction driven and for a given N, $k_{\text{magic}} = 1$ has a smaller unit cell than $k_{\text{magic}} = 2$. To accurately gauge the importance of interactions in the magic bands, we need to compare the bandwidth to the interaction scale. The effective interaction scale depends on the vertical spread of charges in the sector of interest. Using that the interaction between charge distributions with wave vector $\mathbf{q}$ in two layers separated by a distance d is $(e^2/2\epsilon_\parallel\epsilon_0 q)e^{-qd}$ (cf. Eq. (5.10)), the effective interaction energy per flat-band electron can be estimated as

$$\begin{aligned}\frac{e^2}{4\pi\epsilon_\parallel\epsilon_0 L_M}\langle\exp(-\lambda G|z-z'|)\rangle = \\ = \frac{e^2}{4\pi\epsilon_\parallel\epsilon_0 L_M}\sum_{i,j} W_i^{(k)}\exp(-\lambda G d_l|i-j|)W_j^{(k)}\,.\end{aligned} \tag{5.33}$$

Here, the average in the first line is over the pairs of layers (located at z and z') accounting for the charge distribution of sector k over layers as described by $W_i^{(k)}$. We also used that the characteristic wave-vector scale G is given by the magnitude of the shortest reciprocal lattice vector $G = 4\pi/(\sqrt{3}L_M)$, i.e., the inverse of the moiré length L_M. In the exponent, λ accounts for the fact that the characteristic wave vector depends somewhat on the interaction effect of interest. We choose $\lambda = 1$ for Hartree effects, and $\lambda = \frac{1}{2}$ for correlation (Fock) effects.

We can now use the computed bandwidth to define a dimensionless measure of the interaction strength in the flat bands,

$$r_s = e^2\langle\exp\left\{(\frac{1}{2}G|z-z'|)\right\}\rangle/(4\pi\epsilon_\parallel\epsilon_0 L_M \text{BW}). \tag{5.34}$$

While this is still an oversimplified measure of interaction effects in flat bands [183], it serves as a useful metric in comparison to a similar analysis for TBG [184]. In Fig. 5.6d we plot the effective r_s as a function of layer number N. For $k_{\text{magic}} = 1$ (red full line) and zero strain, r_s decreases with increasing N, suggesting that devices with $N < 5$ are most likely to exhibit correlation effects. Strained $k_{\text{magic}} = 1$ data (red dashed line) highlight the advantage of $N > 2$. The importance of a given nominal value of strain diminishes with N. For this reason, r_s is larger for strained $N = 3$ than $N = 2$. Interestingly, we find that r_s is larger for $k_{\text{magic}} = 2$ (blue) than for $k_{\text{magic}} = 1$. This holds even for strained devices. For increasing N, again, there is a decrease in r_s, which nevertheless stays above the $k_{\text{magic}} = 1$ value.

To understand this peculiar behavior of r_s, we consider $N = 5$ and $k_{\text{magic}} = 2$ at zero strain. For $k = 2$ at the magic angle, the $k = 1$ sector is nominally below the magic angle, but still very flat. This results in a cascade-like transition, at which the $k = 2$ sector becomes almost completely filled, while the $k = 1$ sector has negative (hole) filling. Consequently, we find $\nu_{\text{total}} < 4$

at $\nu_{\text{magic}} = 4$. This transition is encouraged by the central charge distribution over layers, larger inhomogeneity (see App. A.1.1), and larger bandwidth of the nonmagic, $k = 1$ sector (whose effective twist angle is below the magic angle). After the cascade, the inhomogeneity of the holes from $k = 1$ partially cancels against the inhomogeneity of the $k = 2$ electrons, yielding a filled magic band with anomalously small Hartree broadening.

The behavior of r_s, together with the required doping dependence shown in Fig. 5.6a,b, suggest that to realize strongly interacting bands for large N multilayer devices, it is necessary to focus on sectors $k \neq 1$ such that the spectral weight is not localized near the center of the device structure. For example, for the $k = 2$ sector to be at the effective magic angle of $\theta_2^{\text{eff}} = 1.1°$, this would correspond to physical twist angles of $1.1°$, $1.37°$ for $N = 5, 6$-layer devices, respectively (see App. A.4 for further analysis).

Finally, we comment on the role of dielectric constants in large-N multilayers. In the literature, these constants are taken as fitting parameters and frequently vary between experiments. Thus, it is helpful to discuss the behavior of Fig. 5.6 as a function of the dielectric constants. The effect of a decreasing interaction strength on Fig. 5.6a is to shift all the curves downward. At zero strain, changing $\epsilon_{\|}$ from 10 to 14 leaves the cascade physics unchanged, since it comes from two sets of very flat single-particle bands ($k = 1$ and $k = 2$). At nonzero strain, decreasing interaction strength lowers r_s, as the strain-induced broadening becomes more relevant. We refer the interested reader to Ref. [3] for other parameter choices.

5.6 Summary and Discussion

In this Chapter, we demonstrated how in-plane Hartree and layer potentials control the phase diagram of alternating-angle twisted multilayer graphene. Compared with the experimental results of Ref. [31, 32], we showed that it is the interplay of these two effects that accounts for the filling enlargement of the superconducting pocket with layer number. In fact, we find that small-N devices are the preferred layered structures to study $k = 1$ flat-band physics. For $N > 5$, the magic sector present in the decoupling introduced in Ref. [78] becomes strongly modified by the presence of Hartree effects to the extent that electrostatic doping of that sector becomes challenging. In addition, the interacting bandwidth is enlarged by the in-plane and out-of-plane (layer) Hartree effects, likely precluding Fock-driven correlated phenomena.

The suppression of exchange-driven correlated phenomena by the Hartree effect relies on the mechanism of band shifting. Indeed this mechanism has been observed in the context of TTG, where shifting of the flat band with respect to the Dirac cone can be seen spectroscopically [80]. However, to date no scanning tunneling microscope (STM) experiments were carried out on $N > 3$ devices. Such experiments may allow one to verify the scenario developed here. This may also allow one to assess whether alternative theoretical explanations of the enlarged superconducting pocket, such as the more exotic scenarios discussed in Ref. [31], are necessary. We caution, however, that for STM measurements, one side of the sample is typically left uncov-

ered, so that there is only one gate on the opposite side. In this single-gate setup, it is impossible to vary displacement field and doping independently. Instead, varying gate voltage traces out a line in the filling-displacement field plane. Nonetheless, we expect the qualitative physics of band shifting to persist as it is a robust consequence of charge inhomogeneity. However, quantitative predictions must be adapted to the new device geometry.

Experiments on moiré graphene systems exhibit substantial particle-hole asymmetry, unlike our theoretical analysis. Specifically, in TBG correlated insulators appear to be more robust on the electron side than on the hole side. Similarly, superconductivity can also appear in a particle-hole asymmetric manner [158]. In the TPG samples studied in Ref. [31], superconductivity persists up to $\nu_{\text{total}} = 5$ on the electron side, but only down to $\nu_{\text{total}} = -4$ on the hole side. Particle-hole symmetry breaking can be incorporated into the BM model [71, 156, 185]. However we find this to be insufficient to reproduce the observed experimental trends. The presence of particle-hole symmetry is a common feature of theoretical efforts to date and requires further investigation.

While our results suggest that correlated phenomena are likely precluded for $N > 5$ samples with $k = 1$ magic sector, $k = 2$ flat bands appear more promising. We find that $k_{\text{magic}} = 2$ is subject to much weaker band reshuffling and thereby allows for effective electrostatic gating. Moreover, the $k = 2$ band can become unexpectedly flat. This suggests a resurgence of flat-band physics for large N in the $k = 2$ sector, which could in principle differ from that seen in TBG, for instance because the multiple nearly flat bands may conspire to reduce the Hartree-driven renormalizations that suppress the exchange effects.

6 Single gate dependence in Bernal-terminated graphene multilayers

The results of this Chapter will be included in a publication in preparation, Ref. [6], co-authored by Dacen Waters, Joshua Folk, Matthew Yankowitz, and Cyprian Lewandowski. The research has been conducted by the author of this thesis while discussing with the other coauthors. The experimental data plotted in this Chapter in Figures 6.1,6.2 have been provided by the Yankowitz lab.

In this chapter, motivated by surprising experimental observations, we study the interacting properties of graphene multilayers featuring a Bernal termination.

The unprecedented tunability afforded by doubly-gated two-dimensional structures allows for simultaneous *in-situ* control of charge density and perpendicular displacement field. These two, nominally very simple, experimental parameters allow one to explore a rich phase space realizing a wide variety of unexpected electronic phenomena. For example, in multilayer van der Waals systems, this has led to an avalanche of recent discoveries. Already the possibility to precisely tune the filling has led to remarkable results in moiré systems with large unit cells, including correlated insulators and superconductivity in twisted bilayer graphene [20–30], as well as fractional Chern insulators in twisted bilayer transition metal dichalcogenides [60–64]. The ability to tune displacement field has unveiled new, displacement-field-driven phases, most remarkably in systems based on rhombohedral or Bernal stacked graphene. In Bernal bilayer and rhombohedral trilayer graphene, an applied displacement field generates pockets with extremely high density of states, leading to flavor ferromagnetism [15, 186, 187] and unconventional superconductivity [14, 186, 188]. In rhombohedral pentalayer graphene under extreme displacement fields, the fascinating anomalous Hall crystal and fractional Chern insulator phases emerged recently [16, 189, 190]. Another fascinating class of systems are stacks of two Bernal multilayers on top of each other with a twist, such as twisted double-bilayer graphene. Such systems are strongly tunable by displacement field, leading to robust correlated insulating states [36–38, 67, 191, 192] and, very recently anomalous Hall crystal phases [193].

In this Chapter, we focus on a remarkable feature that has been visible since the earliest measurements of doubly-gated moiré graphene multilayers, but received little attention until now. This feature is the regular appearance of diagonal lines in the filling-displacement field (ν-D) plane, tracking contours of constant values of the top or bottom gate voltages, V_t or V_b, or,

equivalently, the top and bottom gate electron densities, n_t and n_b. This is a striking result, as it challenges the common assumption that the displacement field D and filling ν, rather than a single gate voltage, are the relevant parameters that define the boundaries of the experimental phase diagram. Devices exhibiting this feature include twisted double bilayer graphene [36–38, 191, 192], its derivatives [67, 193, 194], and rhombohedral pentalayer graphene aligned with hBN [16, 189, 190], where, most notably, the boundaries of the strongly correlated region of parameter space supporting the anomalous Hall crystal and fractional Chern insulators are determined by a single gate voltage only.

As we will show, the common microscopic denominator of these experiments is the presence of perfectly layer and sublattice polarized states at the Dirac point (one for each spin and valley), arising from the local Bernal stacking. As we will elucidate, these states, which we refer to as "surface states", form an important part of the flat bands that give rise to correlation effects. In particular, as our first finding, we reveal that the high density of states regions in parameter space in these systems are delimited by curves along which the surface states are at the Fermi level.

Secondly, the surface states' perfect layer polarization allows us to obtain an analytical understanding of their evolution in the $\nu - D$ plane. We uncover an electrostatic mechanism that causes the position of these surface states relative to the Fermi level to be tuned by the proximate gate only. Physically, this mechanism is rooted in the presence of other, vertically delocalized, states, that screen the effect of the distant gate on the surface states.

This Chapter is structured as follows. In Section 6.1, we introduce the problem, presenting experimental data on twisted double bilayer graphene and rhombohedral pentalayer graphene. In the next Section 6.2, we clarify the important role of surface states in shaping the band structures of Bernal terminated systems. Subsequently, in Section 6.3, we introduce the machinery to model systems under applied displacement field and present a simple electrostatic model to analytically understand the factors influencing the evolution of surface states in the $\nu - D$ plane, deriving conditions for the emergence of single-gate tracking behavior. We then apply this framework to twisted double bilayer graphene (Section 6.4), and rhombohedral pentalayer graphene (Section 6.5), utilizing self-consistent numerical simulations to confirm the physical understanding and reproducing experimental observations. We conclude this Chapter with an outlook and discussion in Sec. 6.6.

6.1 Experimental motivation

The paradigmatic system showing diagonal features in almost all devices is twisted double bilayer graphene (TDBG) [36–38, 67, 191, 192]. This system features two central moiré bands and hosts correlated insulating states. In Figure 6.1a, we show the longitudinal resistance map in the $\nu - D$ plane for one such device, highlighting with arrows the axes corresponding to the bottom (n_b, green), and top (n_t, black dashed) charge densities, which are (up to quantum capacitance corrections) proportional to the gate voltages. In addition to the vertical high resis-

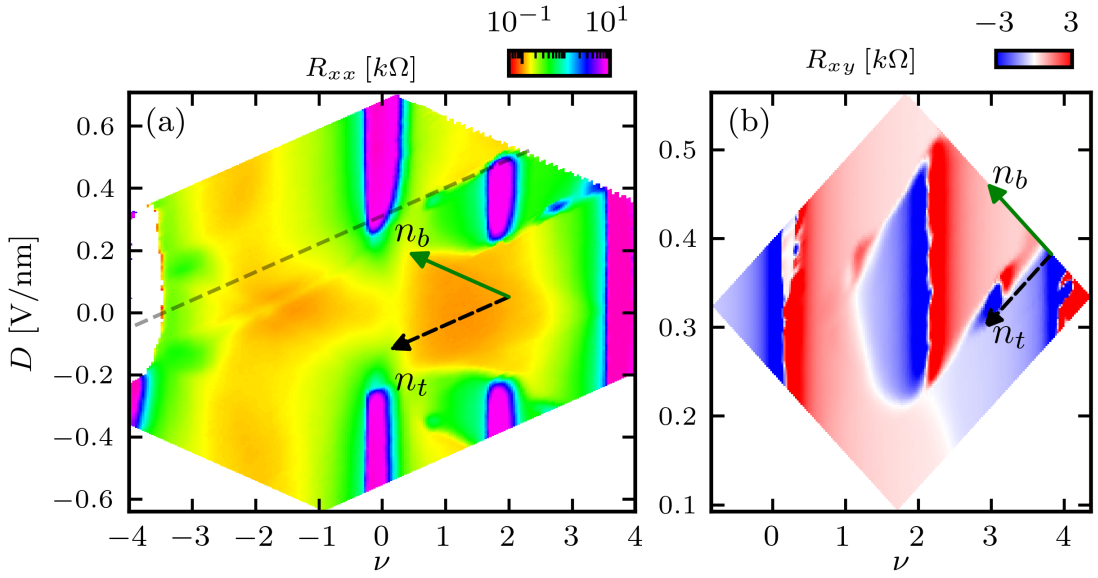

Figure 6.1: (a) Experimental R_{xx} map of twisted double bilayer graphene. The axes of bottom and top gates are shown in green and black, respecively. The onset of symmetry breaking is tuned by n_b. Data are provided by the Yankowitz Lab and are published in Ref. [36]. (b) Same as (a), but for R_{xy}. Data are provided by the Yankowitz Lab and are published in Ref. [36].

tance features corresponding to the insulating states at filling $\nu = 0, 2, 4$ (purple), there are two different diagonal features. First, inside the low resistance region (red) at negative filling ν, there is a high resistance line (yellow), which is almost perfectly independent of n_b. Second, the high resistance region of flavor symmetry breaking (green) appearing in proximity to the $\nu = 2$ correlated insulating state appears approximately bounded by lines of constant n_b. More insight into the nature of the symmetry broken phases can be obtained from a transverse resistance map, shown in Figure 6.1b. The entire region of flavor symmetry breaking is seen to consist of phases characterized by one-fold, two-fold, or three-fold flavor degeneracy. The most prominent one is the doubly-degenerate phase arising from the $\nu = 2$ insulator. Its phase boundaries, along which R_{xy} flips sign are seen to be primarily tuned by n_b, although n_t also has some effect. Another notable phase is the three-fold degenerate phase around $\nu = 3$ and $D = 0.3\,\mathrm{V/nm}$. The boundary of this phase to the phase with no flavor symmetry breaking is seen to be tuned almost exclusively by n_b.

A further fascinating example showing these features is rhombohedral pentalayer graphene aligned with hBN. We show its experimental phase diagram in Fig. 6.2, highlighting the diagonal features. The most striking one is the boundary of the high resistance (purple) region around $\nu = 1$ and $D = 0.9\,\mathrm{V/nm}$, which appears to be largely tuned by n_b. Excitingly, inside this high resistance region, the topological electronic crystal and fractional Chern insulator phases have been shown to occur [16, 190, 195].

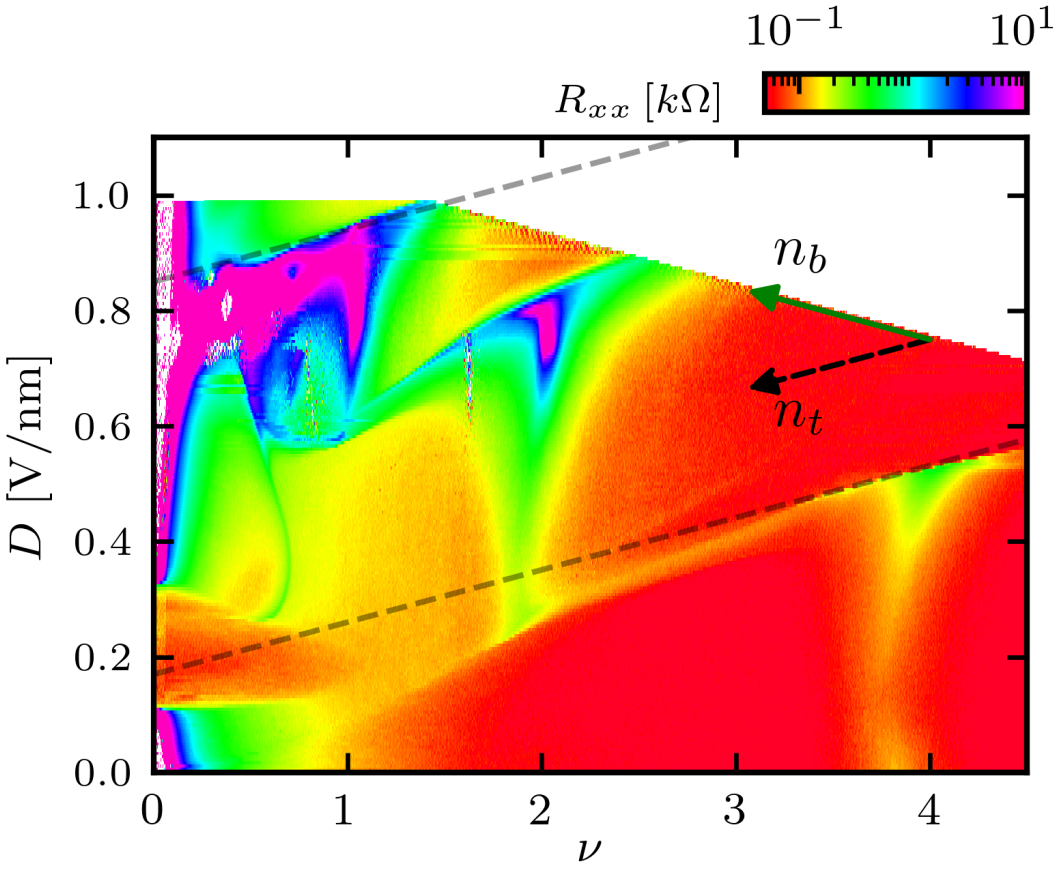

Figure 6.2: Experimental data on rhombohedral pentalayer graphene, provided by Yankowitz lab and presented in Ref. [190].

We note that already for these two systems exhibiting single-gate tracking, a certain degree of non-universality in the degree of single-gate tracking is apparent. Some phase boundaries track a single gate direction perfectly, while others only approximately. Other devices showing this single-gate tracking effect also exhibit diverse behaviors. In twisted monolayer-bilayer [194], single-gate tracking, while still approximately present, is less perfect. On the other hand, in twisted bilayer-trilayer graphene, the boundary of the $\nu = 1$ phase in [67, 193] is perfectly parallel to a single gate direction, similar to the $\nu = 1$ phase in moiré rhombohedral graphene multilayers [16, 190, 195], shown in Fig. 6.2. Intriguingly, both in twisted bilayer-trilayer, as well as rhombohedral pentalayer grpahene, the robustly tracking $\nu = 1$ phase is characterized by very strong correlations, manifesting in the formation of the anomalous Hall crystal phase [16, 190, 193, 195]. This suggests a connection between strong correlations and robust single gate tracking, which we will reexamine in what follows.

6.2 Perfectly layer-polarized states in Bernal-terminated systems

We focus on a class of 2D graphene multilayer systems featuring a Bernal termination, which is a Bernal stacking configuration at one of the terminating ends of the device. Focusing on a bottom termination and labeling the orbitals in the two terminating layers as $1A, 1B, 2A, 2B$, which denote the layer ($l = 1, 2$) and sublattice (A and B) degrees of freedom, local Bernal stacking implies that only $1B \rightarrow 2A$ tunneling is sizeable, and leads to a surface state at the Dirac point that is perfectly polarized to the bottom layer and does not mix with other states. Specifically, acting on wavefunctions expanded around the K-point

$$\Psi(\mathbf{r}) = [\Psi^{1,A}(\mathbf{r}), \Psi^{1,B}(\mathbf{r}), \Psi^{2,A}(\mathbf{r}), \Psi^{2,B}(\mathbf{r}), \ldots]^T, \tag{6.1}$$

the single-particle Hamiltonian of a Bernal-terminated device expanded around the K-point can be written as

$$\mathrm{H}^K_{\text{kin}} + \mathrm{H}_{\text{layer}} = \begin{pmatrix} U_1 & v_F\overline{k} & -v_4\overline{k} & -v_3 k & 0 & \cdots \\ v_F k & & & & & \\ -v_4 k & & & & & \\ -v_3\overline{k} & & & \cdots & & \\ 0 & & & & & \\ \vdots & & & & & \end{pmatrix} \tag{6.2}$$

where $\mathrm{H}^K_{\text{kin}}$ is the kinetic part, $\mathrm{H}_{\text{layer}}$ encodes the different potentials on each layer (these are independent of valley), $k = k_x + ik_y$ is the complex momentum operator, $\overline{k} = k_x - ik_y$ is its conjugate, v_F is the graphene Dirac velocity, $v_3, v_4 \ll v_F$ are the velocities for non-local interlayer tunneling, and U_l is the layer potential on layer l. Note that we only explicitly list matrix elements involving the $1A$ state, and treat the potentials U_l as parameters of the model at this point. Crucially, at the K-point ($\mathbf{k} = 0$), the $1A$ state is an exact eigenstate with energy U_1 that is completely decoupled from the other degrees of freedom. This state (one for each spin and valley), which we denote the surface state, is the key to understanding the peculiar behavior of graphene based systems, in which features are largely tuned by a single gate only. Its position relative to the Fermi level μ is given simply as $\mu - U_1$, and is a natural proxy for band flatness. So long as the surface state is part of the relevant band, $|\mu - U_1|$ sets a lower bound on the bandwidth. Conversely, if $|\mu - U_1| \approx 0$, the density of states is enhanced. Furthermore, while the surface state is strictly decoupled only at the K-point ($\mathbf{k} = 0$), layer polarization remains high even for small but finite $\mathbf{k}$, leading to strongly layer-polarized pocket deriving from the surface state. This pocket, while evolving largely independently at first, eventually has to merge with the rest of the bands. At this merging point of independent parts of the band structure, a

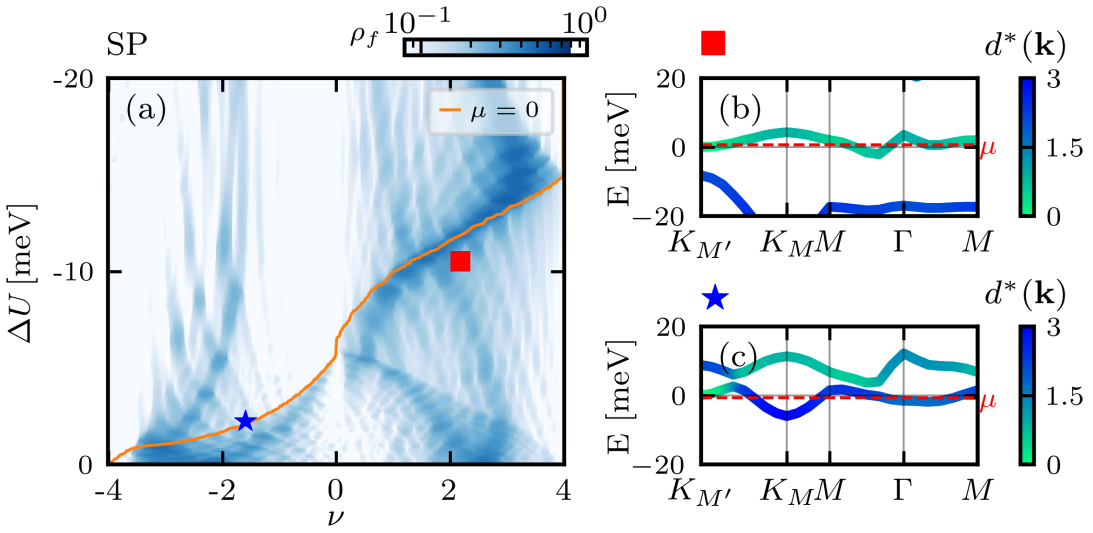

Figure 6.3: (a) Single-particle ΔU-ν map of the density of states per flavor ρ_f. The contour of the surface states due to the Bernal termination $\mu = 0$ is shown in orange. (b) Single particle band structures at the position of the red square in (c). Colorcode shows the average distance $d^*(\mathbf{k})$ from the bottommost layer. Note the bottom layer surface state has $d^*(K_{M'}) = 0$. (c) Same as (b), but at the position of the blue star of (a).

van Hove singularity necessarily develops. We note that for simplicity of notation, we will use the gauge $U_1 = 0$. In this gauge, the only quantity determining the surface state relevance to Fermi level physics is μ.

We now illustrate the effect of the surface state in twisted double bilayer graphene, which features two central moiré bands, where the conduction band is flatter than the valence band. We use the following continuum model in the K-valley

$$\mathrm{H}^K_{\text{kin}} + \mathrm{H}_{\text{layer}} = \begin{pmatrix} v_F\mathbf{k}\cdot\sigma + U_1\sigma_0 & t^\dagger(\mathbf{k}) & 0 & 0 \\ t(\mathbf{k}) & v_F\mathbf{k}\cdot\sigma + U_2\sigma_0 & T(\mathbf{r}) & 0 \\ 0 & T^\dagger(\mathbf{r}) & v_F\mathbf{k}\cdot\sigma + U_3\sigma_0 & t^\dagger(\mathbf{k}) \\ 0 & 0 & t(\mathbf{k}) & v_F\mathbf{k}\cdot\sigma + U_4\sigma_0 \end{pmatrix}, \tag{6.3}$$

where $T(\mathbf{r})$ is the moiré tunneling term for twisted bilayer graphene given in Eq. (2.56) of Chapter 2, and where the tunneling matrix for Bernal stacking is given as

$$t(\mathbf{k}) = \begin{pmatrix} -v_4 k & t_1 \\ -v_3\bar{k} & -v_4 k \end{pmatrix}, \tag{6.4}$$

with t_1 the strength of AB hopping when A is on top of B. In what follows, we use use the following parameters: $v_F = 542.1\,\mathrm{meV}\cdot\mathrm{nm}$, $v_3 = v_4 = 34\,\mathrm{meV}\cdot\mathrm{nm}$, $t_1 = 355.16\,\mathrm{meV}$, $w_{AB} = 110\,\mathrm{meV}$, and $w_{AA} = 0.7\cdot 110\,\mathrm{meV}$. Note that this model is precisely of the form of Eq. (6.2).

In Fig. 6.3a, we plot a heatmap of the density of states per flavor ρ_f for the single particle model as a function of filling factor ν and interlayer potential difference $\Delta U = U_{l+1} - U_l$, which is how an applied displacement field D is typically modeled.

A striking feature of this diagram is a high density of states (van Hove singularity) line at positive filling. Plotting also the $\mu = 0$ contour (orange) reveals that this density of states feature correlates with $\mu = 0$, at which point the surface state is at the Fermi level. The van Hove singularity curve also extends to negative filling, where it follows the $\mu = 0$ contour less closely. The correlation of $\mu = 0$ with a van Hove singularity is a natural consequence of the merging of the surface state pocket with the rest of the moiré bands.

To confirm this expectation, in Fig. 6.3b, we show the single particle band structure for $\nu > 0$, colorcoded by the average distance from the bottom layer $d^*(\mathbf{k})$. At this point in the phase diagram, the entire conduction band is strongly polarized to the bottom layer, so the van Hove singularity arising from the merger of the surface state pocket happens already for small detuning from the surface state. In contrast, for negative filling, shown Fig. 6.3c, the bulk bands are localized in the middle of the structure (cf. the colormap), so the surface state pocket is more robust, and the van Hove singularity consequently occurs further away from $\mu = 0$.

We remark that while feature lines are already present at this single particle level, they were obtained under the assumption of a constant interlayer potential difference ΔU. However, the potentials U_l are not directly experimentally tunable. Rather, what is tuned is the displacement field D. Therefore, in the following Section 6.3, we will introduce an accurate model relating U_l to D and show that a straightforward linear rescaling of the y-axis in Fig. 6.3a, setting $D \propto \Delta U$ with some arbitrarily chosen proportionality constant, is an unjustified approximation and misses the essential physics.

6.3 Electrostatic mechanism

In this Section set up the machinery to correctly describe the electrostatics of layered devices and describe the phase diagram in the ν-D plane accurately. We then use this machinery to obtain an analytical understanding of the evolution of surface states in doubly-gated multilayers.

6.3.1 Accurate model of doubly-gated systems

We consider a system with N layers labeled $l = 1, \ldots, N$ sandwiched between bottom and top gates, see Fig. 6.4a. Denote the net electron number densities in layer l as n_l, in the top gate as n_t, and in the bottom gate as n_b. Neglecting the effect of quantum capacitance, these gate densities are related to the top and bottom gate voltages as $n_t = -\frac{1}{e}C_{tg}V_t$ and $n_b = -\frac{1}{e}C_{bg}V_b$,

where C_{tg}/C_{bg} are the top/bottom gate capacitances per unit area (set by the device structure), and e is the electron charge. By overall charge neutrality, the sum of the gates fixes the total net electron density in the device as follows

$$n = \sum_{l=1}^{N} n_l = -(n_t + n_b), \tag{6.5}$$

while their difference corresponds to the experimentally accessible displacement field

$$D = e\frac{n_b - n_t}{2\epsilon_0}. \tag{6.6}$$

We decompose the full, second-quantized, interacting system Hamiltonian as follows:

$$\hat{H} = \mathrm{H}_{\text{kin}} + \mathrm{H}_{\text{layer}} + H_{\text{int},\mathbf{q}\neq 0}, \tag{6.7}$$

where H_{kin} is the kinetic part including the valley and spin degrees of freedom. $\mathrm{H}_{\text{layer}}$ describes the layer potentials

$$\mathrm{H}_{\text{layer}} = \sum_{l=1}^{N} U_l \, \mathbb{I}_l, \tag{6.8}$$

with $\mathbb{I}_l$ being the projector onto layer l. Importantly, in order to model the system accurately, the layer potentials U_l are self-consistent potentials, obtained by integrating Gauss' law between the layers:

$$U_{l+1} - U_l = -e^2 d_l \frac{n_b + \sum_{j\leq l} n_j}{\epsilon_\perp \epsilon_0}, \tag{6.9}$$

with d_l the interlayer distance and $\epsilon_\perp$ the out-of-plane dielectric constant. This equation is a simple generalization of Eq. (5.30) to the case of non-symmetric gating $n_t \neq n_b$. Crucially, these potentials have contributions due to both the gate charges and to the charges inside the sample. Finally, $H_{\text{int},\mathbf{q}\neq 0}$ is the finite-momentum Coulomb interaction

$$H_{\text{int},\mathbf{q}\neq 0} = \frac{1}{2A} \sum_{\mathbf{q}\neq 0} \sum_{i,j} V_{ij}(\mathbf{q}) : \rho_{\mathbf{q},i}\rho_{-\mathbf{q},j} :, \tag{6.10}$$

where $V_{ij}(\mathbf{q})$ is the Coulomb interaction at momentum $\mathbf{q}$ between layers i and j, which we will model using Eq. (5.21) derived in the previous Chapter 5, A is the system area, :: denotes normal ordering, and $\rho_{\mathbf{q},j}$ is the charge density in layer j at momentum $\mathbf{q}$.

This way of writing the Hamiltonian treats out-of-plane electric fields due to different charges (in the gates or in the sample) on the same footing, as indeed, the same Gauss' law relates them. It is readily seen that the conventional way of including displacement field $D = e\frac{n_b - n_t}{2\epsilon_0}$ as a constant potential difference $\Delta U = -d_l e D/\epsilon_\perp$ between the layers (as done in the single

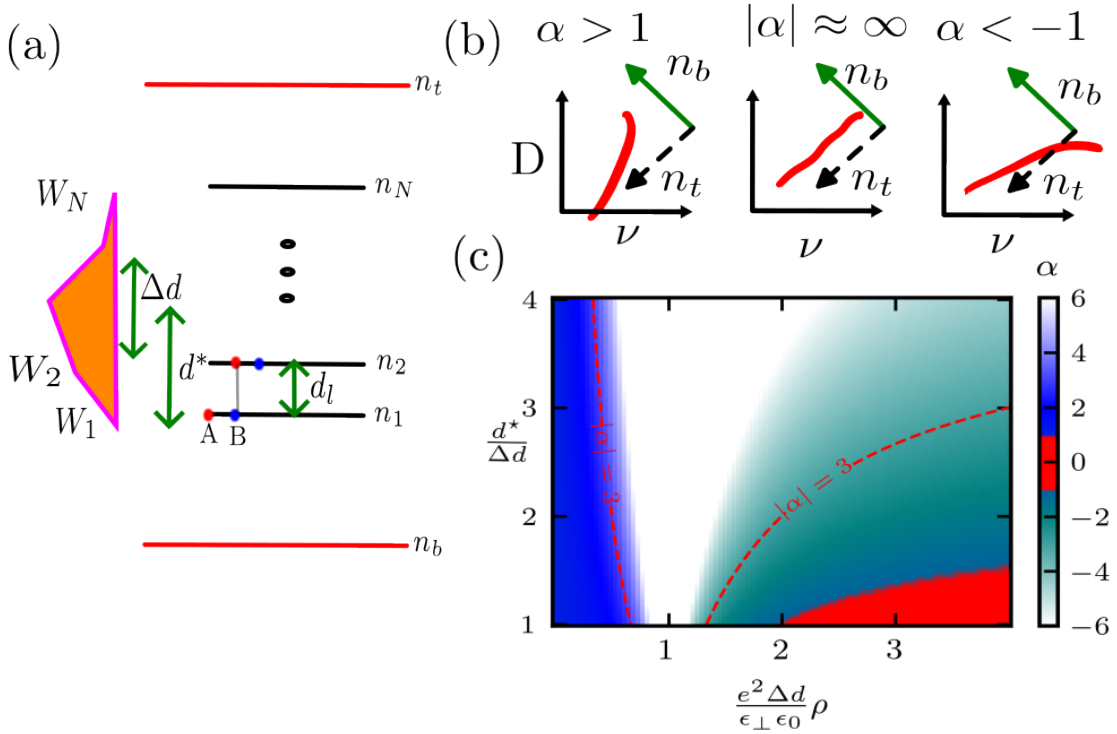

Figure 6.4: (a) Sketch of the theoretical setup, showing the gates and a layered material. We assume a Bernal termination at the bottom, where the bottom two layers have Bernal (AB) stacking, leading to surface states. The average distance of carriers from the bottom layer d^* and the average vertical spread Δd are shown. (b) Illustration of the behaviors expected for different values of α. (c) Map of α [Eq. (6.20)] as a function of $d^*/\Delta d$ and $\frac{e^2 \Delta d}{\epsilon_\perp \epsilon_0} \rho$. Contours of $|\alpha| = 3$ are shown in red.

particle calculation above) is inadequate by comparing with the full expression of Eq. (6.9). It misses contributions both due to the charges in the system, as well as due to the additional charges that accumulate on the gates upon doping (changing ν).

6.3.2 Physical understanding of the model: single sector

To gain a physical understanding of the forces at play in determining the chemical potential contours, we now consider the effect of the single particle terms H_{kin} and H_{layer} in Eq. (6.7). To analyze the chemical potential contours, we consider the change in chemical potential upon varying the gate charges

$$\mathrm{d}\mu = \frac{\partial \mu}{\partial n_b} \delta n_b + \frac{\partial \mu}{\partial n_t} \delta n_t, \tag{6.11}$$

where $\delta n_{t/b}$ are the increments in top/bottom gate densities, and where $\frac{\partial \mu}{\partial n_t}$ and $\frac{\partial \mu}{\partial n_b}$ are the compressibilities relative to the top and bottom gates, respectively. We assume a Fermi level density of states at constant layer potentials ρ and a distribution of charges W_l at the Fermi level

across the layers ($\sum_l W_l = 1$), as illustrated Fig. 6.4a. Note that both ρ and W_l depend on the instantaneous gate configurations, and that $\delta n_l = -(\delta n_t + \delta n_b)W_l$.

Upon varying the gate charges, the chemical potential changes (i) due to the compressibility $\frac{1}{\rho}$ at constant U_l and (ii) due to the change in layer potentials δU_l, which give additional shifts. Assuming all the states at the Fermi level to have the same distribution of charges W_l, the additional Fermi level shift due to the change in layer potentials is equal to the expectation of the change in the potentials δU_l upon doping:

$$-\frac{\partial \mu}{\partial n_b} = \frac{1}{\rho} - \sum_l W_l \frac{\partial U_l}{\partial n_b} \tag{6.12}$$

$$-\frac{\partial \mu}{\partial n_t} = \frac{1}{\rho} - \sum_l W_l \frac{\partial U_l}{\partial n_t}, \tag{6.13}$$

where $\frac{\partial U_l}{\partial n_b}$ and $\frac{\partial U_l}{\partial n_t}$ can be evaluated using Eq. (6.9). The change in the layer potentials upon changing the bottom gate charge by δn_b is

$$\delta U_l = \frac{\partial U_l}{\partial n_b}\delta n_b = -\frac{e^2 d_l}{\epsilon_\perp \epsilon_0}\left[(l-1) - \sum_{l'<l}(l-l')W_{l'}\right]\delta n_b, \tag{6.14}$$

while the change in the layer potentials upon changing the top gate charge by δn_t is

$$\delta U_l = \frac{\partial U_l}{\partial n_t}\delta n_t = \frac{e^2 d_l}{\epsilon_\perp \epsilon_0}\left[\sum_{l'<l}(l-l')W_{l'}\right]\delta n_t. \tag{6.15}$$

Defining the average distance from the bottom layer d^* and layer spread Δd as

$$d^* = d_l \sum_{l=1}^{N}(l-1)W_l \tag{6.16}$$

$$\Delta d = \frac{d_l}{2}\sum_{l,l'=1}^{N}|l'-l|W_l W_{l'}, \tag{6.17}$$

the compressibility for a single sector at the Fermi level can be written as

$$-\frac{\partial \mu}{\partial n_b} = \frac{1}{\rho} - \frac{e^2 \Delta d}{\epsilon_\perp \epsilon_0} + \frac{e^2 d^*}{\epsilon_\perp \epsilon_0} \tag{6.18}$$

$$-\frac{\partial \mu}{\partial n_t} = \frac{1}{\rho} - \frac{e^2 \Delta d}{\epsilon_\perp \epsilon_0}. \tag{6.19}$$

d^* and Δd the average distance of the charges at the Fermi level from the bottommost ($l = 1$) layer and their average vertical spread across the layers, respectively, see Fig. 6.4a for an illustration. Note that $d^* \geq \Delta d$.

These expressions can be physically understood as follows: in addition to the standard compressibility $\frac{1}{\rho}$, the states at the Fermi level experience electrostatic shifts due to $\mathrm{H}_{\text{layer}}$ of Eq. (6.8). Both gates induce the same layer distribution δn_l, leading to the self-interaction term proportional to Δd. The bottom gate, however, causes an additional shift proportional to the average distance from the bottom layer d^*. Note that this asymmetric behavior arises due to the choice $U_1 = 0$, which is natural for the bottom layer surface states. Importantly, for $\frac{1}{\rho} \approx \frac{e^2 \Delta d}{\epsilon_\perp \epsilon_0}$, the effect of the top gate is screened by the system.

For small changes in the gating, the chemical potential changes according to Eq. (6.11). Written in terms of

$$\alpha \equiv \frac{\partial \mu}{\partial n_b} \Big/ \frac{\partial \mu}{\partial n_t} = 1 + \frac{d^*}{\Delta d} \left(\frac{\epsilon_\perp \epsilon_0}{e^2 \Delta d} \frac{1}{\rho} - 1 \right)^{-1}, \tag{6.20}$$

it follows that constant chemical potential lines ($\mathrm{d}\mu = 0$) satisfy

$$\delta n_t = -\alpha \delta n_b. \tag{6.21}$$

The qualitative behavior of chemical potential contours is illustrated in Fig. 6.4b. Provided $|\alpha| \gg 1$, constant chemical potential lines correspond approximately to lines of constant bottom gate density, n_b. In other words, the chemical potential is predominantly tuned by n_b, so the surface states due to Bernal termination are primarily tuned by the bottom gate. For $\alpha > 1$, the contours tend towards verticality, while for $\alpha < -1$, they tend towards horizontality, cf. Fig. 6.4b.

It is instructive to analyze the parameter α as a function of the dimensionless parameters $\frac{d^*}{\Delta d} \geq 1$ and $\frac{e^2 \Delta d}{\epsilon_\perp \epsilon_0} \rho$, shown in Fig. 6.4c. In the non-interacting regime ($\epsilon_\perp = \infty$), we have $\alpha = 1$. Physically, for $\epsilon_\perp = \infty$, the gates are unable to induce any potential difference on the layers, so the chemical potential only depends on the filling ν. Increasing the strength of interaction, α increases and become large in a region in which the top gate is screened by the system electrons, characterized by the following condition

$$\frac{e^2 \Delta d}{\epsilon_\perp \epsilon_0} \rho \approx 1, \tag{6.22}$$

where we expect $\frac{e^2 \Delta d}{\epsilon_\perp \epsilon_0}$ to have a similar value across different graphene based systems. The range of ρ that gives a sizeable α is determined by the ratio $\frac{d^*}{\Delta d}$, with a larger ratio giving a more robust region, as seen by the diverging dashed red lines marking $|\alpha| = 3$ in Fig. 6.4c. Increasing the interaction even further, α flips sign and its absolute value steadily decreases. In this regime, the system overscreens the gate.

6.3.3 Physical understanding of the model: multiple sectors

Having analyzed a single sector, in this Subsection, we derive the dependence of the chemical potential on the two gates for multiple sectors. Consider different sectors labeled with an index k, where each sector has a layer distribution $W_l^{(k)}$, and density of states $\rho^{(k)}$. We now define a density of states matrix $\boldsymbol{\rho}$ as

$$\boldsymbol{\rho}_{kk} = \rho^{(k)}, \tag{6.23}$$

the matrix of layer spreads

$$\Delta \boldsymbol{D}_{ij} = \frac{e^2}{\epsilon_\perp \epsilon_0} \sum_{l'<l} W_l^{(i)} (l - l') W_{l'}^{(j)}, \tag{6.24}$$

where $\Delta \boldsymbol{D}_{ii} = \frac{e^2}{\epsilon_\perp \epsilon_0} \Delta d^{(i)}$ where $\Delta d^{(i)}$ is defined using the single-sector definition above, given in Eq. (6.17). The matrix of sector distances from the bottom layer is defined as

$$\boldsymbol{d}^*_{kj} = \frac{e^2}{\epsilon_\perp \epsilon_0} d^{*(k)} = \frac{e^2}{\epsilon_\perp \epsilon_0} \sum_l (l-1) W_l^{(k)}, \tag{6.25}$$

with $d^{*(k)}$ being the distance from the bottommost layer of the sector k. Following a similar analysis as for the case of a single sector above, we obtain the following results for the compressibilities

$$-\left(\frac{\partial \mu}{\partial n_b}\right)^{-1} = \sum_{i,j} \left[(\boldsymbol{\rho}^{-1} - \Delta \boldsymbol{D} + \boldsymbol{d}^*)^{-1} \right]_{i,j} \tag{6.26}$$

$$-\left(\frac{\partial \mu}{\partial n_t}\right)^{-1} = \sum_{i,j} \left[(\boldsymbol{\rho}^{-1} - \Delta \boldsymbol{D})^{-1} \right]_{i,j}. \tag{6.27}$$

In the weakly the weakly interacting limit $|\boldsymbol{d}^*| \ll |\boldsymbol{\rho}^{-1}|, |\Delta \boldsymbol{D}| \ll |\boldsymbol{\rho}^{-1}|$, we can obtain the inverses in Eqs. (6.26), (6.27) in a perturbative expansion. For example, expanding the matrix inverse in Eq. (6.27) obtains

$$(\boldsymbol{\rho}^{-1} - \Delta \boldsymbol{D})^{-1} = \boldsymbol{\rho} + \boldsymbol{\rho} \Delta \boldsymbol{D} \boldsymbol{\rho} + \mathcal{O}[\boldsymbol{\rho} (\Delta \boldsymbol{D} \boldsymbol{\rho})^2], \tag{6.28}$$

such that the compressibility is in this limit equal to

$$-\frac{\partial \mu}{\partial n_t} \approx \frac{1}{\sum_k \rho^{(k)}} - \frac{1}{\sum_k \rho^{(k)}} \sum_{ij} \rho_i (\Delta \boldsymbol{D})_{i,j} \rho_j = \frac{1}{\rho} - \frac{e^2 \Delta d}{\epsilon_\perp \epsilon_0}, \tag{6.29}$$

recovering the result of Eq. (6.19) upon identifying the total density of states $\rho = \sum_k \rho^{(k)}$ and Δd as the average over the Fermi surface over all the sectors with sector k weighted by $\frac{\rho^{(k)}}{\sum_k \rho^{(k)}}$.

An analogous manipulation on Eq. (6.26) recovers Eq. (6.18) in the limit $|\boldsymbol{d}^*| \ll |\boldsymbol{\rho}^{-1}|$ and $|\Delta \boldsymbol{D}| \ll |\boldsymbol{\rho}^{-1}|$.

We now apply this general framework to understand the evolution of the $\mu = 0$ contour, at which the surface state is at the Fermi level. This situation is naturally modeled using two sectors. One corresponding to the surface states, fully polarized to the bottom layer, having $W^{(1)}_{l=1} = 1$. The second sector corresponds to all the other states at the Fermi level, and has some layer-delocalized distribution $W^{(2)}_l$. In this limit, evaluating the compressibilities in Eq. (6.26) and Eq. (6.27) is straightforward, and we obtain

$$-\frac{\partial \mu}{\partial n_b} = \frac{1}{\mathfrak{C}}\left[\frac{1}{\rho^{(2)}} - \frac{e^2 \Delta d^{(2)}}{\epsilon_\perp \epsilon_0} + \frac{e^2 d^{*(2)}}{\epsilon_\perp \epsilon_0}\right] \tag{6.30}$$

$$-\frac{\partial \mu}{\partial n_t} = \frac{1}{\mathfrak{C}}\left[\frac{1}{\rho^{(2)}} - \frac{e^2 \Delta d^{(2)}}{\epsilon_\perp \epsilon_0}\right], \tag{6.31}$$

where $\mathfrak{C} = 1 + \frac{\rho^{(1)}}{\rho^{(2)}} + \frac{e^2 \rho^{(2)}}{\epsilon_\perp \epsilon_0}(d^{*(2)} - \Delta d^{(2)})$. Remarkably, up to a rescaling by $\mathfrak{C}$, these are the same results as for a single sector, but now all the quantities refer to sector $k = 2$ only. This implies that α for the $\mu = 0$ contour is

$$\alpha \equiv \frac{\partial \mu}{\partial n_b} \Big/ \frac{\partial \mu}{\partial n_t} = 1 + \frac{d^{*(2)}}{\Delta d^{(2)}}\left(\frac{\epsilon_\perp \epsilon_0}{e^2 \Delta d^{(2)}} \frac{1}{\rho^{(2)}} - 1\right)^{-1}, \tag{6.32}$$

which is the same as Eq. (6.32), but with all quantities defined with respect to sector $k = 2$. Physically, this result arises since along the $\mu = 0$ contour, the surface states' occupation does not change – their position with respect to the Fermi level is constant. Therefore, along the $\mu = 0$ contour, all the charge enters the $k = 2$ sector, meaning α should be defined with quantities referring to sector $k = 2$ only.

6.3.4 Role of $H_{\text{int},\mathbf{q}\neq 0}$

We conclude this Section by commenting on the role of the term $H_{\text{int},\mathbf{q}\neq 0}$ in Eq. (6.7), which we neglected above. The effect of this term is twofold. Firstly, there is the classical effect of the Hartree in-plane inhomogeneity, present in most moiré systems [179, 182, 196]. Its effect is to increase $\frac{1}{\rho}$ by a fixed amount due to an approximately constant Hartree shift energy scale G. The effect of this on the possible parameters in Fig. 6.4c is to put an upper cut-off on possible $\rho \lesssim \frac{1}{G}$ for a given system.

Secondly, $H_{\text{int},\mathbf{q}\neq 0}$ leads to all the strongly correlated physics observed experimentally. Already at the Hartree-Fock level, this obtains additional interaction induced shifts of the surface state, so that their position relative to the Fermi level is not determined purely by the Fermi level μ. Nevertheless, both the surface state and the Fermi level experience some shift due to the Fock term. However, it is a natural assumption that these two shifts are of similar size, so we expect the surface state properties to still be determined by the electrostatic mechanism above. In

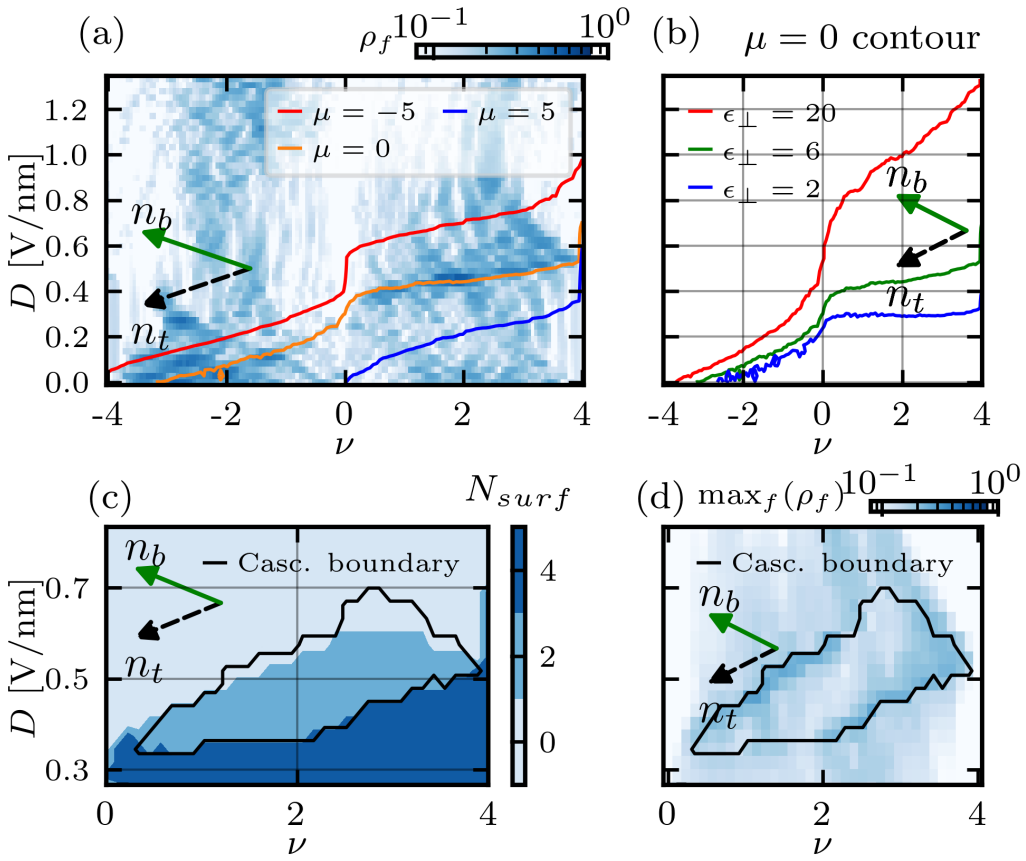

Figure 6.5: (a) Numerical $\nu - D$ colormap of the log of the density of states ρ (per spin-valley flavor) together with contours of $\mu = -5, 0, 5$meV. We work in the Hartree approximation with dielectric constant $\epsilon = \epsilon_\perp = 6$, see Supplement for details. (b) $\mu = 0$ line for three values of $\epsilon_\perp$ at $\epsilon = 6$. (c) Toy model cascade for $U = 5.9\,\text{meV}$ and $\epsilon = \epsilon_\perp = 6$, together with surface state occupation. (d) Same as (c) but showing ρ_f for the flavor with maximal density of states $\max_f(\rho_f)$.

fact, for a toy model Fock term that we will consider in the following Section, the Fock-induced surface state shift and Fock-induced Fermi level shift are the same.

6.4 Application to twisted double-bilayer graphene

We now illustrate these ideas on twisted double-bilayer graphene by solving Eq. (6.7) self-consistently, treating the finite $\mathbf{q}$ interaction in the Hartree approximation with in-plane dielectric constant $\epsilon = 6$. Specifically, we self-consistently solve the mean-field Hamiltonian $\hat{H} = \mathrm{H}_{\text{kin}} + H_\perp + \mathrm{H}_{\text{Hartree}}$, where the Hartree term reads

$$\mathrm{H}_{\text{Hartree}} = \frac{1}{A}\sum_{i,j}\sum_{\mathbf{G}} \rho_{\mathbf{G},i} V_{i,j}(\mathbf{G}) \langle \rho_{-\mathbf{G},j} \rangle, \tag{6.33}$$

where $\mathbf{G}$ are moiré reciprocal lattice vectors, and where $\langle \rho_{-\mathbf{G},j} \rangle$ denotes the expectation value of the momentum $-\mathbf{G}$ density in the mean-field state. Only simulating one spin-valley flavor, we recover results for $N_{\text{flavor}} = 4$ spin-valley flavors by multiplying the mean-field densities by N_{flavor}, modelling unbroken flavor symmetry. To avoid displacement field dependent bias, we choose at each momentum $\mathbf{k}$ on a Brillouin zone grid a basis of $N_{\mathbf{G}}$ plane waves per layer and sublattice. In this way, we expect the bands not included in our calculation to simply renormalize the dielectric constants $\epsilon_\perp$ and ϵ.

6.4.1 Results of self-consistent calculations

In Fig. 6.5a, we plot the resulting numerical $\nu - D$ map of the density of states, together with chemical potential contours for $\mu = 5, 0, -5$ meV, using an out-of-plane dielectric constant $\epsilon_\perp = 6$, which is chosen to account for the remote degrees of freedom not included in our numerics. A first important observation is that for $\nu < 0$, chemical potential contours very closely follow lines of constant n_b. This can be understood by noting that at negative filling, the surface state is part of the bottom moiré band, which is localized further away from the surface state. This band has $d^*/\Delta d \approx 3$, cf. Fig. 6.3c, giving a more robust region of large $|\alpha|$ in Fig. 6.4c.

At positive filling, the states are much more polarized to the outermost layer, cf. Fig. 6.3d, giving a small $d^*/\Delta d$. Consequently, the tracking is less robust, with the $\mu = 0\,\text{meV}$ contour being almost horizontal ($\alpha \approx -1$), consistent with the large density of states due to the proximate van Hove singularity. In contrast, the $\mu = \pm 5\,\text{meV}$ contours are more vertical as a result of their lower density of states, in line with our analytical expectation of Eq. (6.20).

To further confirm our physical analysis above, it is instructive to compare the results for the surface state $\mu = 0$ contour for different $\epsilon_\perp$, shown in Fig. 6.5b. There, it is seen that at $\nu < 0$, large $|\alpha|$ robustly persists for all the parameters studied, in line with the large width of the white region in Fig. 6.4b for $d^*/\Delta d \approx 3$. On the other hand, at positive filling, the behavior of the contour changes from being almost horizontal ($\alpha = -1$) for $\epsilon_\perp = 2$ to having positive α for $\epsilon_\perp = 20$, converging towards verticality ($\alpha = 1$) for $\epsilon_\perp = \infty$, so it does not seem to robustly track a single gate.

The robust tracking at $\nu < 0$ explains the negative filling diagonal feature seen in Fig. 6.1a, which we interpret as the point at which the surface state pocket is at the Fermi level. On the other hand, we do not observe robust gate tracking of the surface state at $\nu > 0$ in this Hartree calculation. However, since around the $\mu = 0$ contour there is a van Hove singularity in a flat band, we expect that the flavor degenerate phase currently considered will be unstable towards flavor symmetry breaking, which we consider in the following Subsection.

6.4.2 Role of flavor symmetry breaking

To study flavor symmetry breaking, we use a minimal mean-field model for flavor symmetry breaking, which simply shifts each flavor according to its current filling [197]

$$H_{Fock} = -U_{\text{Fock}}\text{Diag}(\nu_{K\uparrow}, \nu_{K\downarrow}, \nu_{K'\uparrow}, \nu_{K'\downarrow}), \tag{6.34}$$

with ν_f the filling of flavor f relative to charge neutrality and U_{Fock} an energy scale quantifying the strength of interactions. To simplify even further, we only consider spin-degenerate symmetry breaking, imposing $\nu_{K'\downarrow} = \nu_{K'\uparrow}$ and $\nu_{K\downarrow} = \nu_{K\uparrow}$. By optimizing the division of charges among the two valleys at $U_{\text{Fock}} = 5.9\,\text{mev}$ for different ν and D, we obtain obtain the phase diagram of Fig. 6.5c, highlighting the boundary of the region where cascade occurs. We also colorcode the surface state occupation N_{surf}, defined as the total number of electrons in the bottom layer surface states across all the four spin-valley flavors. We see that the cascade boundary closely tracks changes in the surface state occupation. As we have seen above, the point at which surface state filling changes is proximate to the density of states peak. Reaching this peak in the symmetry broken phase, then, leads to an instability towards the symmetry unbroken phase. To confirm this intuition, in Fig. 6.5d, we plot the density of states of the dominant flavor, $\max_f(\rho_f)$, showing that the cascade transitions from the symmetry broken phases are preceded by an increase in the density of states due to the van Hove singularity, which arises when the surface state is close to the Fermi level.

Importantly, the surface state evolution in this model is still described by our framework above, but with a reduced density of states in the symmetry broken phase due to the reduced number of flavors at the Fermi level. In the diagram of Fig. 6.4c, this means that symmetry breaking causes a flow of the system parameters towards the left side of the plot, where $\alpha > 0$. And indeed, U_{Fock} turns the negative α in the symmetry unbroken phase (Fig. 6.5a) into a large and positive α in the symmetry broken phase, in line with the experimental phenomenology, cf. Fig. 6.1b.

6.5 Application to rhombohedral pentalayer graphene aligned with hexagonal boron nitride

We now consider rhombohedral pentalayer graphene aligned with hBN, whose experimental phase diagram we showed in Fig. 6.2. While at large D all the states in this system are strongly layer polarized, there is still a Bernal termination, and therefore decoupled surface-layer polarized states must exist that are only sensitive to the chemical potential. In this system, the anomalous Hall crystal, whose origins are presently hotly discussed, forms for displacement field values corresponding to electrons localizing at the side far from the moiré interface. On the other hand, insulators exist even at the single particle level for displacement field values corresponding to electrons localizing on the hBN-proximate side. Since the single gate dependence of phase

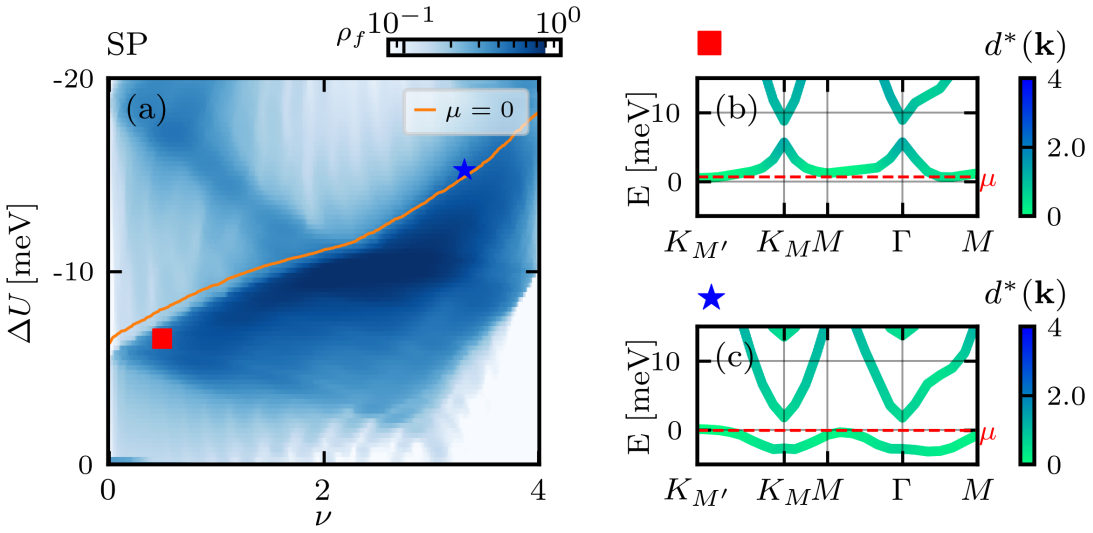

Figure 6.6: (a) Numerical $\nu - D$ contour map of chemical potential μ in the single particle regime for rhombohedral pentalayer graphene aligned with hexagonal boron nitride. (b) Plot of the band structures at the red square point of (b). Fermi level μ is shown by the red dashed line. (c) Plot of the band structures at the blue star point of (b).

boundaries occurs for both sides equally well, we focus on the moiré proximate side, allowing us to neglect the complex role exchange effects play.

As basis of our analysis, we use the single-particle model of Ref. [198] for hBN graphene orientation $\xi = 1$ and twist angle $\theta = 0.77°$. The parameters of this model are listed in Table I of Ref. [198].

In Fig. 6.6a, we show the single particle density of states, together with the $\mu = 0$ contour, which is seen to be approximately diagonal. As for twisted double bilayer graphene, this $\mu = 0$ contour tracks a high density of states region, this time forming its boundary.

In Figs. 6.6b,c, we plot the band structures at two points in the map of Fig. 6.6a, where, similarly to TDBG, the high density of states region arises from the joining of the states arising from the surface state pocket and the rest of the bands.

Focusing on the moiré proximate side justifies an approach based on the single particle bands H_{kin} and H_{layer}, while treating the interaction at the Hartree level, as introduced in Sec. 6.4. Working in this approximation, we plot the interacting density of states in Fig. 6.7, together with chemical potential contours. It is seen that the constant μ contours, which form the boundary of the high density of states region, are tracking a single gate. This suggests that the gate screening mechanism is also relevant for rhombohedral pentalayer graphene.

We now speculate on the interplay of surface states, screening effects and the anomalous Hall crystal. It is an experimental fact that features with $\alpha < 0$ are not observed, while according to Fig. 6.4c, α tends to be larger in more strongly correlated devices with higher density of states.

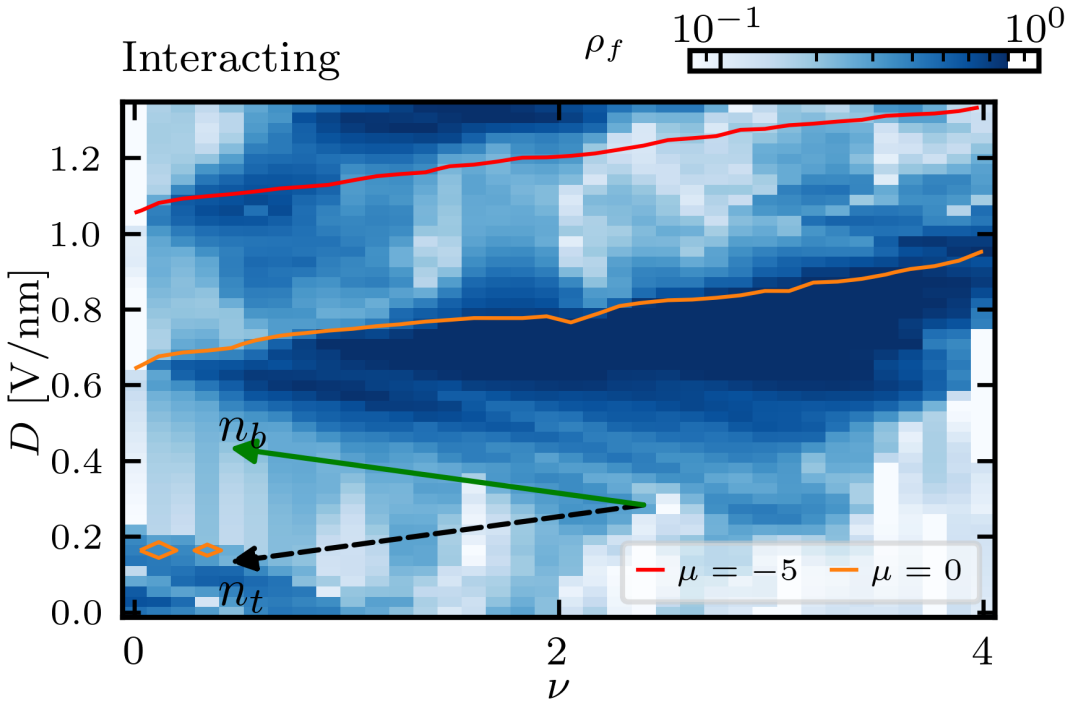

Figure 6.7: Numerical $\nu - D$ contour map of chemical potential μ in the Hartree approximation for rhombohedral pentalayer graphene aligned with hexagonal boron nitride.

Since correlation effects in the anomalous Hall crystal phase are of paramount importance, we expect a large α, as seen in Fig. 6.2.

6.6 Discussion

To conclude, motivated by unexplained experimental trends, we uncovered a powerful approach to study multilayer graphene structures with a Bernal termination. Using the analytical properties of the decoupled "surface states" allows their evolution in the $\nu - D$ plane to be tracked, providing an understanding for the experimentally observed diagonal features.

We focused on the regime in which the bottom layer surface states are relevant, which occurs for positive displacement field, for which electrons tend to reside in the lower layers. The same effect occurs with regards to the top layer surface states, but at opposite sign of displacement field.

It is worth noting that in our analysis of Sec. 6.2, the surface state is completely decoupled from other states. However, a periodic potential will induce a coupling between the surface state at the K-point and other states at different momenta offset by a reciprocal lattice vector $\mathbf{g}$, leading to an additional shift of the surface state. Nevertheless, we expect this effect to be small,

being suppressed by a factor $\frac{V_{\mathbf{g}}}{v_F|\mathbf{g}|} \ll 1$, where $V_{\mathbf{g}}$ is the strength of the periodic potential at wavevector $\mathbf{g}$.

An interesting further direction is to consider the role of the surface states in the recently discussed ratchet effect, in which hysteretic gating behavior is observed in graphene based devices [199, 200].

7 Real-space textures of wavefunctions

In this Chapter, we study the real-space wavefunctions of moiré materials, with a focus on twisted bilayer graphene and twisted bilayer transition metal dichalcogenides. We are motivated by the fact that the real-space textures of moiré wavefunctions are directly experimentally accessible in local tunneling experiments as a result of the large moiré unit cell. The results of this Chapter will be included in a publication in preparation, Ref. [7].

Wavefunctions of layered moiré systems typically possess multiple components, and therefore define smooth maps from the real-space moiré unit cell into $\mathbb{C}^N$, where N is the number of components. Furthermore, these wavefunctions are periodic in real-space unit cell at zero applied magnetic field, and quasiperiodic when a nonzero integer number Φ of magnetic flux quanta per unit cell is applied.

Two important examples of systems possessing multicomponent wavefunctions are twisted bilayer graphene (TBG) and twisted transition metal dichalcogenides (TMDs). TBG wavefunctions have four components in each valley – two for each sublattice and layer, while wavefunctions of twisted bilayer TMDs have two – one for each layer. Interestingly, for both these systems, there is a limit, in which their low energy wavefunctions are given in terms of Landau levels. For twisted bilayer graphene, this is the chiral limit [73], in which interlayer hopping within the same sublattice is neglected. In this limit, the flat band wavefunctions have an exact Landau level representation. For twisted bilayer transition metal dichalcogenides (TMDs), it is the adiabatic approximation [201, 202], in which the Hamiltonian is projected onto the direction of the effective Zeeman field defined by the tunneling and potential terms. Because this Zeeman field defines a skyrmion texture in the unit cell, the ensuing effective Hamiltonian is characterized by an emergent magnetic field of one flux quantum per unit cell, and the wavefunctions are therefore given as linear combinations of Landau levels.

In what follows, we study the connection between real space textures of multicomponent wavefunctions and their representability in terms of Landau levels. To characterize the textures of wavefunctions, we first focus on nowhere vanishing wavefunctions, defining an associated real-space Berry connection, Berry curvature, and Chern number. Surprisingly, we find that at zero applied magnetic field, any wavefunction without zeroes in the unit cell has to have zero real-space Chern number. More generally, the real-space Chern number of nowhere vanishing wavefunctions is tied to the number of applied flux quanta per unit cell Φ.

Further, we find that the real-space Chern number can still be defined for some wavefunctions with zeroes in the unit cell, characterizing those for which this is possible as a product of a nowhere vanishing spinor wavefunction and a scalar wavefunction. Crucially, the two factors

can experience different magnetic fields, Φ_1 and Φ_2, which are nevertheless tied to the applied field as $\Phi_1 + \Phi_2 = \Phi$. The real-space Chern number of such wavefunctions is then given by the flux experienced by the spinor part, Φ_1, and, crucially, is no longer necessarily equal to the applied flux. In particular, we obtain that a nonzero real-space Chern number at $\Phi = 0$ is possible exactly when the scalar part experiences a nonzero magnetic field, meaning $\Phi_2 \neq 0$, and implying that it is expressible in terms of Landau levels, which necessarily have a zero in the unit cell.

For twisted bilayer TMDs, we find that a nonzero real-space Chern number is realized precisely in the adiabatic approximation, in which the wavefunctions map onto Landau levels, and the wavefunction exactly follows the real-space skyrmion defined by the effective Zeeman field. In this regime, the wavefunctions necessarily possess zeroes in the unit cell. However, we find that these zeroes are generically removed when going beyond the adiabatic approximation, leading to a vanishing real-space Chern number in any realistic situation.

For twisted bilayer graphene in the chiral limit, we find as well that in the regime in which its wavefunctions map onto Landau levels, the real-space Chern number is nonzero. However, similarly to twisted TMDs, we find that going beyond the ideal chiral limit the real-space zeroes are removed and the real-space Chern number evaporates.

This Chapter is structured as follows. In Section 7.1, we present a general theory of real-space topology of multicomponent wavefunctions. In Section 7.2, we introduce the ideal band wavefunctions, which have an exact Landau level representation, and discuss an example in the form of twisted bilayer graphene in the chiral limit. In Section 7.3, we introduce the wavefunctions of twisted bilayer TMDs, focusing on the adiabatic approach in which they can be related to Landau levels, interpreting this relation in light of the theory introduced in Sec. 7.1. In Section 7.4, we present arguments in support of the generic vanishing of the real-space Chern number at zero applied magnetic field, and illustrate on examples of twisted bilayer TMDs and TBG in the chiral limit. We conclude with a discussion in Section 7.5, emphasizing the experimental relevance of our results.

7.1 Real-space textures of wavefunctions

Consider a general N-by-N continuum Hamiltonian in two spatial dimensions, where the N components typically correspond to layer, sublattice, spin (pseudospin), or any additional degrees of freedom. We consider a situation when an integer number of flux quanta per unit cell Φ are applied. In this situation, the system retains the original lattice periodicity with lattice vectors $\mathbf{a}_1, \mathbf{a}_2$, and the eigenstates of its Hamiltonian are (magnetic) translation eigenstates labelled by a band index and a momentum $\mathbf{k}$ in the Brillouin zone.

The eigenstates are given in terms of N-component Bloch spinors:

$$u_{\mathbf{k}}(\mathbf{r}) = [u^1_{\mathbf{k}}(\mathbf{r}), u^2_{\mathbf{k}}(\mathbf{r}), \ldots, u^N_{\mathbf{k}}(\mathbf{r})]^T, \tag{7.1}$$

which are (quasi) periodic functions in the unit cell, satisfying

$$u_{\mathbf{k}}(\mathbf{r}+\mathbf{a}_1) = u_{\mathbf{k}}(\mathbf{r}) \tag{7.2}$$
$$u_{\mathbf{k}}(\mathbf{r}+\mathbf{a}_2) = e^{i\gamma(\mathbf{r})}u_{\mathbf{k}}(\mathbf{r}) \tag{7.3}$$

for lattice vectors $\mathbf{a}_1, \mathbf{a}_2$. The additional phase $\gamma(\mathbf{r})$ arises in a finite magnetic field in a generalized Landau gauge. In this gauge, in which the electromagnetic vector potential is translationally invariant in the $\mathbf{a}_1$ direction, this phase takes the form [1]

$$\gamma(\mathbf{r}) = \frac{2\pi\Phi}{|\mathbf{a}_1|^2}\,\mathbf{r}\cdot\mathbf{a}_1. \tag{7.4}$$

We note that $\gamma(\mathbf{r})$ satisfies $\int_{\mathbf{R}}^{\mathbf{R}+\mathbf{a}_1} d\mathbf{r}\cdot\,\partial_{\mathbf{r}}\gamma(\mathbf{r}) = 2\pi\Phi$, encoding the magnetic field enclosed. We further note that the full wavefunction is obtained from $u_{\mathbf{k}}(\mathbf{r})$ as $e^{i\mathbf{k}\cdot\mathbf{r}}u_{\mathbf{k}}(\mathbf{r})$.

Away from the zeroes of $u_{\mathbf{k}}(\mathbf{r})$, we define the normalized function $\chi_{\mathbf{k}}(\mathbf{r})$ as

$$\chi_{\mathbf{k}}(\mathbf{r}) = \frac{u_{\mathbf{k}}(\mathbf{r})}{|u_{\mathbf{k}}(\mathbf{r})|}. \tag{7.5}$$

This normalized function $\chi_{\mathbf{k}}(\mathbf{r})$ allows us to define a real-space Berry connection corresponding to the wavefunction $u_{\mathbf{k}}(\mathbf{r})$, treating $\mathbf{r}$ as a parameter:

$$A_{\mathbf{k}}(\mathbf{r}) = -i\,\chi^{\dagger}_{\mathbf{k}}(\mathbf{r})\partial_{\mathbf{r}}\chi_{\mathbf{k}}(\mathbf{r}), \tag{7.6}$$

which corresponds to the additional geometric phase obtained upon adiabatically following $\chi_{\mathbf{k}}(\mathbf{r})$ in real space. The associated Berry curvature is defined in the usual way

$$B_{\mathbf{k}}(\mathbf{r}) = \nabla_{\mathbf{r}} \times A_{\mathbf{k}}(\mathbf{r}), \tag{7.7}$$

and is invariant under gauge transformations $\chi \to e^{i\theta(\mathbf{r})}\chi$, where $\theta(\mathbf{r})$ an arbitrary function. Note that physically, multiplying by $e^{i\theta(\mathbf{r})}$ is not a gauge transformation as the resulting wavefunction is physically different. Nevertheless, they all lead to the same real-space Berry curvature. The Berry curvature upon integrating gives the real space Chern number

$$C(\mathbf{k}) = \frac{1}{2\pi}\int_{\mathrm{UC}} d\mathbf{r} B_{\mathbf{k}}(\mathbf{r}) \in \mathbb{Z}, \tag{7.8}$$

where UC denotes the unit cell.

[1] The generalized Landau gauge has the electromagnetic vector potential $\mathbf{A}(\mathbf{r}) = \frac{\hbar}{e}(\mathbf{G}_2\cdot\mathbf{r})\mathbf{a}_1/|\mathbf{a}_1|^2$. Here $\mathbf{G}_2$ is the reciprocal basis vector satisfying $\mathbf{G}_2\cdot\mathbf{a}_1 = 0$ and $\mathbf{G}_2\cdot\mathbf{a}_2 = 2\pi$. This vector potential is periodic in the $\mathbf{a}_1$ direction, leading to the periodic boundary conditions of Eq. (7.2). Upon translation by $\mathbf{a}_2$, on the other hand, $\mathbf{A}(\mathbf{r})$ changes as $\mathbf{A}(\mathbf{r}+\mathbf{a}_2) - \mathbf{A}(\mathbf{r}) = \frac{\hbar}{e|\mathbf{a}_1|^2}(\mathbf{G}_2\cdot\mathbf{a}_2)\mathbf{a}_1 = 2\pi\frac{\hbar}{e|\mathbf{a}_1|^2}\,\mathbf{a}_1 = 2\pi\frac{\hbar}{e}\frac{1}{|\mathbf{a}_1|^2}\partial_{\mathbf{r}}(\mathbf{a}_1\cdot\mathbf{r})$. The last equality allows $\gamma(\mathbf{r})$ to be determined, giving the result of Eq. (7.4).

The (quasi) periodicity expressed in Eq. (7.3) fixes the integrated Berry connection along the boundary of the unit cell as

$$\oint_{\partial \mathrm{UC}} d\mathbf{r} \cdot A_{\mathbf{k}}(\mathbf{r}) = 2\pi\Phi, \tag{7.9}$$

corresponding to the Aharonov-Bohm phase when going around the unit cell, which encloses Φ flux quanta.

We now distinguish between scalar ($N = 1$) and spinor ($N > 1$) cases.

For scalar wavefunctions, which are complex numbers, the condition Eq. (7.9) implies that the argument of the wavefunction winds by $2\pi\Phi$ when going around the unit cell. This phase winding necessarily leads to zeroes (vortices) inside the unit cell with total vorticity Φ. Mathematically, these zeroes arise due to homotopy constraints [2]. A natural basis for these scalar wavefunctions is given by Landau levels.

For spinor wavefunctions, first consider the case where the wavefunction is nowhere vanishing. In this case, the normalized spinor $\chi_{\mathbf{k}}(\mathbf{r})$ is well defined inside the entire unit cell, permitting the application of Stokes' theorem to determine the Chern number. Eq. (7.9) then obtains the value of the real space Chern number for non-vanishing spinors as

$$C(\mathbf{k}) \overset{u_{\mathbf{k}}(\mathbf{r})\neq 0}{=} \Phi, \tag{7.10}$$

so that the real-space Chern number is tied to the number of flux quanta per unit cell. In particular, it has to vanish at zero magnetic field.

Let us now consider spinor wavefunctions that have zeroes in the unit cell. The real space Chern number can still be defined provided a well defined spinor can be assigned to the wavefunction. The most general such wavefunction can be written as a product of a nonzero spinor part and a possibly vanishing scalar part

$$u^{\Phi}_{\mathbf{k}}(\mathbf{r}) = \chi^{\Phi_1}_{\mathbf{k}}(\mathbf{r})\psi^{\Phi_2}_{\mathbf{k}}(\mathbf{r}), \tag{7.11}$$

where $\Phi = \Phi_1 + \Phi_2$ and $\chi^{\Phi_1}_{\mathbf{k}}$ is a spinor wavefunction at flux Φ_1 [satisfying Eq. (7.3) at flux Φ_1], that is normalized at every point $\mathbf{r}$ in the unit cell, and $\psi^{\Phi_2}_{\mathbf{k}}$ is a scalar (single-component, $N = 1$) wavefunction at flux Φ_2 [satisfying Eq. (7.3) at flux Φ_2]. The real-space Chern number of this wavefunction is determined by its spinor component $\chi^{\Phi_1}_{\mathbf{k}}$ only and is given by

$$C(\mathbf{k}) = \Phi_1, \tag{7.12}$$

[2] This can be proved as follows. The function $\mathfrak{u}_{0,\mathbf{k}}(\mathbf{r})$ defines a map (not periodic) from the unit cell to complex numbers $\mathbb{C}$. If this function is non-vanishing everywhere, it becomes a map from the unit cell to non-zero complex numbers $\mathbb{C}^\times = \mathbb{C} - \{0\}$. The latter has nontrivial fundamental group $\pi_1(\mathbb{C}^\times) = \mathbb{Z}$, describing the phase rotation of $\mathfrak{u}_{0,\mathbf{k}}(\mathbf{r})$ along a loop. Since we can deform a loop along the unit cell boundary to a single point by shrinking the loop through the interior of the unit cell, this loop must belong to the trivial element $0 \in \pi_1(\mathbb{C}^\times) = \mathbb{Z}$, contradicting the non-trivial phase winding due to the magnetic translation.

which differs from Eq. (7.10) for $\Phi_2 \neq 0$. In this case, the wavefunction necessarily has a zero in the unit cell as a result of the nonzero flux Φ_2 experienced by the scalar part $\psi_{\mathbf{k}}^{\Phi_2}(\mathbf{r})$.

To prove Eq. (7.11), suppose that a smooth normalized spinor $\chi_{\mathbf{k}}(\mathbf{r})$ can be assigned to a smooth wavefunction $u_{\mathbf{k}}(\mathbf{r})$. The existence of such a spinor in the unit cell is a necessary condition to define a real space Chern number. We further require that $\chi_{\mathbf{k}}(\mathbf{r}) \propto u_{\mathbf{k}}(\mathbf{r})/|u_{\mathbf{k}}(\mathbf{r})|$ wherever $u_{\mathbf{k}}(\mathbf{r}) \neq 0$. Crucially, to be well defined at the zeroes of $u_{\mathbf{k}}(\mathbf{r})$, $\chi_{\mathbf{k}}(\mathbf{r})$ will possibly have to differ from $u_{\mathbf{k}}(\mathbf{r})/|u_{\mathbf{k}}(\mathbf{r})|$ by a non-trivial phase factor around them. Defining $\psi_{\mathbf{k}}(\mathbf{r}) = \chi_{\mathbf{k}}^{\dagger}(\mathbf{r})u_{\mathbf{k}}(\mathbf{r})$, which is smooth as the product of two smooth functions, we can write

$$u_{\mathbf{k}}(\mathbf{r}) = \chi_{\mathbf{k}}(\mathbf{r})\psi_{\mathbf{k}}(\mathbf{r}). \tag{7.13}$$

Now consider the integral of the Berry connection of $\chi_{\mathbf{k}}(\mathbf{r})$ across the boundary of the unit cell. This has to be equal to an integer multiple of 2π, because $\chi_{\mathbf{k}}(\mathbf{r})$ can only change by a phase upon translating by a lattice vector [3]. We denote the value of this integral as $2\pi\Phi_1$, where Φ_1 is an integer. We now define

$$\chi_{\mathbf{k}}^{\Phi_1}(\mathbf{r}) = e^{i\Gamma(\mathbf{r})}\chi_{\mathbf{k}}(\mathbf{r}), \tag{7.14}$$

where the smooth function $\Gamma(\mathbf{r})$ is chosen in order for $\chi_{\mathbf{k}}^{\Phi_1}(\mathbf{r})$ to satisfy the (quasi) periodic boundary conditions of Eq. (7.2) and Eq. (7.3) at flux Φ_1. Such a function can always be found as the Berry connection of $\chi_{\mathbf{k}}(\mathbf{r})$ integrated across the boundary of the unit cell evaluates to $2\pi\Phi_1$. We further define $\psi_{\mathbf{k}}^{\Phi_2}(\mathbf{r})$ with $\Phi_2 = \Phi - \Phi_1$ as

$$\psi_{\mathbf{k}}^{\Phi_2}(\mathbf{r}) = e^{-i\Gamma(\mathbf{r})}\psi_{\mathbf{k}}(\mathbf{r}), \tag{7.15}$$

which is obtained by multiplying the wavefunction $\psi_{\mathbf{k}}(\mathbf{r})$ scalar with the opposite phase to $\chi_{\mathbf{k}}(\mathbf{r})$. We finally obtain the decomposition of Eq. (7.11) when noting that $\psi_{\mathbf{k}}^{\Phi_2}(\mathbf{r})$ now satisfies the Bloch boundary conditions of Eq. (7.2) and Eq. (7.3) at flux $\Phi_2 = \Phi - \Phi_1$. This follows, since the product with $\chi_{\mathbf{k}}^{\Phi_1}(\mathbf{r})$ has to recover the boundary conditions of $u_{\mathbf{k}}(\mathbf{r})$.

As an application, we see that a finite real-space Chern number at zero applied field is possible if we allow the wavefunction to have zeroes, which arise due to the scalar part $\psi_{\mathbf{k}}^{\Phi_2}(\mathbf{r})$ Namely, if $C(\mathbf{k}) = \Phi_1 \neq 0$, we have $\Phi_2 = -\Phi_1 \neq 0$. In this case, the scalar part of the wavefunction $\psi_{\mathbf{k}}^{\Phi_2}(\mathbf{r})$ is experiencing an effective magnetic field of flux Φ_2. It is therefore naturally expressed in terms of Landau levels and, according to our discussion of scalar ($N = 1$) wavefunctions above, nonzero Φ_2 implies zeroes in the unit cell, with total vorticity Φ_2.

We reiterate that if the wavefunction is everywhere nonzero, the Chern number at $\Phi = 0$ has to vanish, by merit of Eq. (7.10). On the other hand, at finite applied flux, a nonzero Chern number is possible even without zeroes in the wavefunction, as demonstrated in Eq. (7.10).

[3] Note that we assume the zeroes of $u_{\mathbf{k}}(\mathbf{r})$ are away from the unit cell boundary, which can always be achieved by an appropriate choice of unit cell.

7.2 Landau level-like wavefunctions: Ideal bands

We now introduce a class of wavefunctions that naturally yield Landau-level like states – the ideal band wavefunctions. Ideal bands are believed to be well suited for hosting fractional Chern insulator phases [203–210], allowing Laughlin-like trial states to be constructed [205]. At zero applied magnetic field $\Phi = 0$, their wavefunctions possess an exact Landau level representation [204]

$$u_{\mathbf{k}}^{IDEAL}(\mathbf{r}) = N_{\mathbf{k}}\mathcal{B}(\mathbf{r})\mathfrak{u}_{0,\mathbf{k}}^{\Phi=1}(\mathbf{r}), \tag{7.16}$$

where $\mathfrak{u}_{0,\mathbf{k}}^{\Phi=1}(\mathbf{r})$ is the zeroth Landau level wavefunction at momentum $\mathbf{k}$ for magnetic field of one flux quantum per unit cell, $N_{\mathbf{k}}$ is a normalization constant and $\mathcal{B}(\mathbf{r})$ is a scalar or vector function. Note that the Landau level wavefunction $\mathfrak{u}_{0,\mathbf{k}}^{\Phi=1}(\mathbf{r})$ is quasiperiodic, satisfying Eq. (7.3) with $\Phi = 1$. This Landau level quasiperiodicity implies that $\mathcal{B}(\mathbf{r})$ is necessarily also quasiperiodic, experiencing flux $\Phi = -1$. For a spinor $\mathcal{B}(\mathbf{r})$, we see that this wavefunction is of the form of Eq. (7.11) with the identification

$$\psi_{\mathbf{k}}^{\Phi_2=1}(\mathbf{r}) = N_{\mathbf{k}}|\mathcal{B}(\mathbf{r})|\mathfrak{u}_{0,\mathbf{k}}^{\Phi=1}(\mathbf{r}) \tag{7.17}$$

$$\chi^{\Phi_1=-1}(\mathbf{r}) = \mathcal{B}(\mathbf{r})/|\mathcal{B}(\mathbf{r})| \tag{7.18}$$

and therefore possesses real space Chern number $C(\mathbf{k}) = -1$.

An important example of ideal bands is twisted bilayer graphene [described by the Hamiltonian of Eq. (2.57)] in the chiral limit, in which intrasublattice tunneling w_{AA} in Eq. (2.56) is set to zero $w_{AA} = 0$ [73]. In this regime, there is a new chiral antisymmetry σ_z.

In this chiral limit, it is advantageous to rewrite the Hamiltonian in a basis which groups states with the same σ_z eigenvalue. Acting on the following four-component wavefunctions $\Psi_{\text{chiral}}(\mathbf{r}) = [\Psi^{b,A}(\mathbf{r}), \Psi^{t,A}(\mathbf{r}), \Psi^{b,B}(\mathbf{r}), \Psi^{t,B}(\mathbf{r})]^T$, the Hamiltonian for chiral TBG in the K valley reads

$$H_{\text{chiral}}^{K} = \begin{pmatrix} 0 & \mathcal{D}^{\dagger}(\mathbf{r}) \\ \mathcal{D}(\mathbf{r}) & 0 \end{pmatrix}, \tag{7.19}$$

where the operator on the off-diagonal is given by

$$\mathcal{D}(\mathbf{r}) = \begin{pmatrix} v_F k & w_{AB}\left[\sum_{j=1}^{3} e^{i2\pi j/3} e^{i\mathbf{q}_j\cdot\mathbf{r}}\right] \\ \left[\sum_{j=1}^{3} e^{-i2\pi j/3} e^{i\mathbf{q}_j\cdot\mathbf{r}}\right] & v_F k \end{pmatrix}, \tag{7.20}$$

where $k = \mathbf{k}|_x + i\mathbf{k}|_y = -i(\partial_x + i\partial_y)$ is the complex momentum, where v_F is the graphene Dirac velocity, w_{AB} is the strength of intersublattice tunneling, and the vectors $\mathbf{q}_1, \mathbf{q}_2, \mathbf{q}_3$ are defined in Eqs. (2.48),(2.49), and (2.50), and shown in Fig 2.3a.

In this system, ideal flat bands emerge at certain magic angles. To see how this occurs, consider any zero-energy solution polarized to the A-sublattice. Importantly, these zero-energy solutions

are zero modes of the operator $\mathcal{D}(\mathbf{r})$. An important property of this operator is that if it has a sublattice polarized zero mode $\begin{pmatrix} \Psi^{b,A}(\mathbf{r}) \\ \Psi^{t,A}(\mathbf{r}) \end{pmatrix}$, satisfying

$$\mathcal{D}(\mathbf{r}) \begin{pmatrix} \Psi^{b,A}(\mathbf{r}) \\ \Psi^{t,A}(\mathbf{r}) \end{pmatrix} = 0. \tag{7.21}$$

Then also the zero mode wavefunction multiplied by $z = x + iy$ is a zero mode

$$\mathcal{D}(\mathbf{r}) z \begin{pmatrix} \Psi^{b,A}(\mathbf{r}) \\ \Psi^{t,A}(\mathbf{r}) \end{pmatrix} = 0, \tag{7.22}$$

which follows because the operator of Eq. (7.20) contains only anti-holomorphic derivatives.

In fact, two such zero-energy solutions are guaranteed to exist at the mini-Dirac points K_M and $K_{M'}$ by using the sublattice antisymmetry $\mathcal{C} = \sigma_z$ and $C_{2z}\mathcal{T}$, with opposite sublattice polarizations – these arise from the original Dirac points of the two layers forming the twisted structure. At the magic angles of chiral TBG, the two-component K_M wavefunction has a zero in the unit cell. This allows the property expressed in Eq. (7.22) to be used to construct zero energy wavefunctions at different momenta, leading to an exactly flat band [73], with a second flat band obtainable by the application of $C_{2z}\mathcal{T}$. In this construction, the mapping to Landau levels of Eq. (7.16) arises quite naturally, since the zeroth Landau level wavefunctions in the symmetric gauge have the same property as Eq. (7.22). For a rigorous derivation of the representation Eq. (7.16) for chiral twisted bilayer graphene, we refer to the literature [73, 205].

7.3 Landau level-like wavefunctions: TMDs

Another class of wavefunctions which are naturally expressed in terms of Landau levels are twisted transition metal dichalcogenides, whose continuum model was introduced in Sec.2.2. These systems can be intuitively understood as parabolically dispersing holes moving in a pseudospin Zeeman field denoted $\mathbf{\Delta}(\mathbf{r})$ and a scalar potential $\Delta_0(\mathbf{r})$. In the K-valley, the Hamiltonian reads:

$$H^K_{\text{tTMD}} = -\frac{(\hbar\mathbf{k})^2}{2m^*}\sigma_0 + \mathbf{\Delta}(\mathbf{r}) \cdot \boldsymbol{\sigma} + \Delta_0(\mathbf{r})\sigma_0, \tag{7.23}$$

where m^* is the effective mass of the holes, and where $\sigma_{0,x,y,z}$ are the Pauli matrices, and where in contrast to Sec. 2.2 we are working in a convention where momentum in each layer is mea-

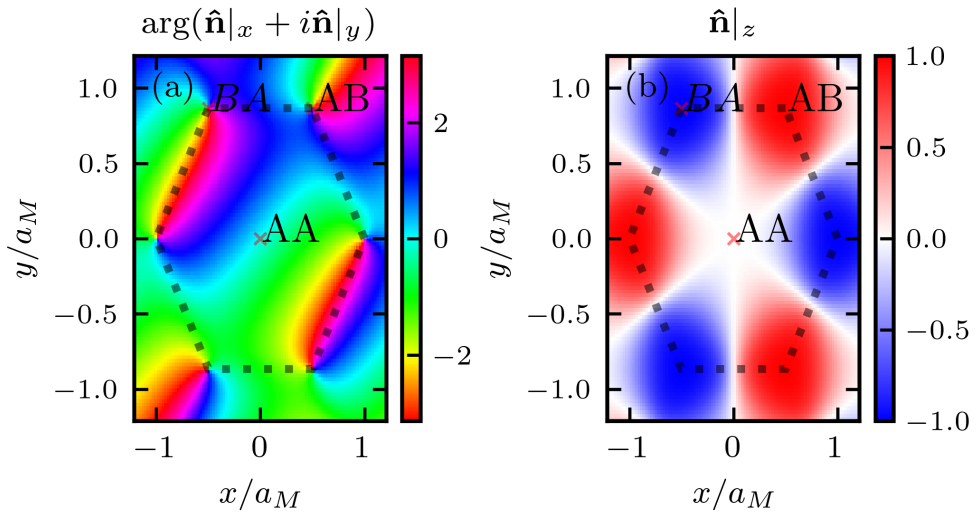

Figure 7.1: (a) Unit cell map of the in-plane angle of the texture $\boldsymbol{n} = \boldsymbol{\Delta}/|\boldsymbol{\Delta}|$ (Eq. (7.29)). (b) Same as (a) but for the z-component.

sured with respect to its K-point. In terms of the layer potentials and interlayer tunneling from Eq. (2.36) of Sec. 2.2, we have

$$\Delta_0 = \frac{1}{2}[V_t(\mathbf{r}) + V_b(\mathbf{r})] \tag{7.24}$$

$$\Delta_x = \mathrm{Re}\left[e^{i(\mathbf{K}^t - \mathbf{K}^b)\cdot\mathbf{r}} T(\mathbf{r})\right] \tag{7.25}$$

$$\Delta_y = -\mathrm{Im}\left[e^{i(\mathbf{K}^t - \mathbf{K}^b)\cdot\mathbf{r}} T(\mathbf{r})\right] \tag{7.26}$$

$$\Delta_z = \frac{1}{2}[V_b(\mathbf{r}) - V_t(\mathbf{r})], \tag{7.27}$$

where $T(\mathbf{r})$ is given in Eq. (2.35), and where the additional factor $e^{i(\mathbf{K}^t - \mathbf{K}^b)\cdot\mathbf{r}}$ is due to measuring momenta in each layer with respect to its respective K-point.

Importantly, the texture of the pseudo-Zeeman field typically has a nonzero real-space Pontryagin index:

$$C[\boldsymbol{\Delta}(\mathbf{r})] = \frac{1}{4\pi}\int_{UC} d\mathbf{r}\, \hat{\mathbf{n}}(\mathbf{r}) \cdot \partial_x \hat{\mathbf{n}}(\mathbf{r}) \times \partial_y \hat{\mathbf{n}}(\mathbf{r}), \tag{7.28}$$

which is defined using the unit vector

$$\hat{\mathbf{n}}(\mathbf{r}) = \boldsymbol{\Delta}(\mathbf{r})/|\boldsymbol{\Delta}(\mathbf{r})|. \tag{7.29}$$

We show the texture corresponding to WSe_2 of the model of Ref. [68] in Figs. 7.1a,b. This texture has $C[\boldsymbol{\Delta}(\mathbf{r})] = -1$, since as the unit cell is traversed, the vector $\hat{\mathbf{n}}(\mathbf{r})$ covers the entire unit

sphere once. For the two-component TMD wavefunctions, the real space Chern number of Eq. (7.8) can be also written in terms of the direction of the vector defined by the location of the wavefunction on the Bloch sphere

$$\hat{\boldsymbol{m}}(\mathbf{r}) = \chi^{\dagger}_{\mathbf{k}}(\mathbf{r})\boldsymbol{\sigma}\chi_{\mathbf{k}}(\mathbf{r}), \tag{7.30}$$

with the Chern number $C(\mathbf{k})$ given by the integral of the Pontryagin index as in Eq. (7.28). As we will see, this value is not necessarily equal to the value obtained for the texture $C[\boldsymbol{\Delta}(\mathbf{r})]$.

The adiabatic *approach* [201, 202] performs a rotation aligning the z-direction of the layer pseudospin at every $\mathbf{r}$ with the direction of $\boldsymbol{\Delta}(\mathbf{r})$, achieved by a unitary transformation $U(\mathbf{r})$, which satisfies

$$U^{\dagger}(\mathbf{r})\boldsymbol{\Delta}(\mathbf{r})U(\mathbf{r}) = |\boldsymbol{\Delta}(\mathbf{r})|\sigma_z, \tag{7.31}$$

where the columns of $U(\mathbf{r})$ are two orthogonal normalized spinors, denoted $\chi^{+}(\mathbf{r})$ and $\chi^{-}(\mathbf{r})$, satisfying

$$\boldsymbol{\Delta}(\mathbf{r}) \cdot \boldsymbol{\sigma}\, \chi^{+}(\mathbf{r}) = |\boldsymbol{\Delta}(\mathbf{r})|\chi^{+}(\mathbf{r}) \tag{7.32}$$

$$\boldsymbol{\Delta}(\mathbf{r}) \cdot \boldsymbol{\sigma}\chi^{-}(\mathbf{r}) = -|\boldsymbol{\Delta}(\mathbf{r})|\chi^{-}(\mathbf{r}), \tag{7.33}$$

so that the unitary can be written as $U(\mathbf{r}) = [\chi^{+}(\mathbf{r}) \;\; \chi^{-}(\mathbf{r})]$. The rotated Hamiltonian reads:

$$U^{\dagger}(\mathbf{r})H^{K}_{tTMD}U(\mathbf{r}) = -\frac{\hbar^2\big(\mathbf{k} - iU^{\dagger}\partial_{\mathbf{r}}U\big)^2}{2m^*} + |\Delta(\mathbf{r})|\sigma_z + \Delta_0(\mathbf{r})\sigma_0, \tag{7.34}$$

where the non-Abelian Berry connection $-iU^{\dagger}\partial_{\mathbf{r}}U$ arises from the kinetic term due to the spatial dependence of the transformation $U(\mathbf{r})$. This term has three consequences.

The first consequence is an emergent magnetic vector potential $\tilde{\mathbf{A}}(\mathbf{r})$ for the low-energy [aligned, (1,1)] block. It is explicitly given by the Berry connection of $\chi^{+}(\mathbf{r})$ as

$$\tilde{\mathbf{A}}(\mathbf{r}) = \frac{\hbar}{e}i\big[U^{\dagger}\partial_{\mathbf{r}}U\big]_{1,1} = \frac{\hbar}{e}i\big[\chi^{+}(\mathbf{r})\big]^{\dagger}\partial_{\mathbf{r}}\chi^{+}(\mathbf{r}), \tag{7.35}$$

which leads to an effective magnetic field

$$\tilde{B}(\mathbf{r}) = \nabla \times \tilde{\mathbf{A}}(\mathbf{r}) = -\frac{\hbar}{2e}\hat{\mathbf{n}}(\mathbf{r}) \cdot \partial_x\hat{\mathbf{n}}(\mathbf{r}) \times \partial_y\hat{\mathbf{n}}(\mathbf{r}), \tag{7.36}$$

proportional to the Pontryagin index density. The total flux enclosed per unit cell is

$$\int_{\mathrm{UC}} d\mathbf{r}\, \tilde{B}(\mathbf{r}) = -\frac{h}{e}C[\boldsymbol{\Delta}(\mathbf{r})], \tag{7.37}$$

giving one flux quantum per unit cell [201, 202] for the texture of WSe_2 in Figs. 7.1a,b. The high-energy (2,2) block experiences an opposite magnetic field. Using this, a natural basis of wave-

functions at momentum $\mathbf{k}$ for the original Hamiltonian of Eq. (7.28) is then given by Landau levels in positive and negative magnetic fields multiplying the spinor $\chi^{\pm}(\mathbf{r})$ [211]. Explicitly, for $\chi^{+}(\mathbf{r})$, we have the wavefunctions $\chi^{+}(\mathbf{r})\mathfrak{u}_{l,\mathbf{k}}^{\Phi=1}(\mathbf{r})$ for $l = 0, 1, \ldots$, while for $\chi^{-}(\mathbf{r})$, we have the wavefunctions $\chi^{-}(\mathbf{r})\mathfrak{u}_{l,\mathbf{k}}^{\Phi=-1}(\mathbf{r})$ for $l = 0, 1, \ldots$.

The second consequence is an additional scalar potential $-D(\mathbf{r})$ for both the aligned and antialigned sector, denoted the kinetic potential

$$D(\mathbf{r}) = -\sum_{i=x,y} \frac{\hbar^2 \left[U^\dagger \partial_i U\right]_{1,2} \left[U^\dagger \partial_i U\right]_{2,1}}{2m^*} \tag{7.38}$$

$$= \frac{\hbar^2}{8m^*} \sum_{i=x,y} [\partial_i \hat{\mathbf{n}}(\mathbf{r})]^2, \tag{7.39}$$

where in the second line, we expressed the potential in terms of the Zeeman field direction $\hat{\mathbf{n}}(\mathbf{r})$.

The third consequence is a coupling between the aligned and antialigned sectors due to the off-diagonal components of $U^\dagger(\mathbf{r})\partial_{\mathbf{r}} U(\mathbf{r})$.

The adiabatic *approximation* projects onto the low-energy subspace which is at every position aligned with the Zeeman field $\mathbf{\Delta}(\mathbf{r})$, optimizing the Zeeman part of the energy. In the rotated Hamiltonian, Eq. (7.34), this amounts to only considering the (1,1) block, and gives the following adiabatic approximation Hamiltonian [201, 202]

$$H^K_{\text{Adiabatic}} = -\frac{(\hbar\mathbf{k} - e\tilde{\mathbf{A}}(\mathbf{r}))^2}{2m^*} - D(\mathbf{r}) + |\Delta(\mathbf{r})| + \Delta_0(\mathbf{r}). \tag{7.40}$$

At a wavefunction level in the unrotated Hamiltonian of Eq. (7.23), the adiabatic approximation amounts to approximating the full wavefunction as

$$u^{Ad}_{\mathbf{k}}(\mathbf{r}) = \chi^{+}(\mathbf{r}) \sum_l c_l^{\mathbf{k}} \mathfrak{u}_{l,\mathbf{k}}^{\Phi=1}(\mathbf{r}) \tag{7.41}$$

with some coefficients $c_l^{\mathbf{k}}$. We see that this is again of the form of Eq. (7.11), provided we identify $\chi_{\mathbf{k}}^{\Phi_1=-1}(\mathbf{r}) = \chi_{+}(\mathbf{r})$ and $\psi_{\mathbf{k}}^{\Phi_2=1}(\mathbf{r}) = \sum_l c_l^{\mathbf{k}} \mathfrak{u}_{l,\mathbf{k}}^{\Phi=1}(\mathbf{r})$. In this adiabatic approximation, $\hat{\boldsymbol{n}}(\mathbf{r})$ of Eq. (7.29) and $\hat{\boldsymbol{m}}(\mathbf{r})$ of Eq. (7.30) coincide and the wavefunction precisely follows the texture of $\mathbf{\Delta}(\mathbf{r})$, having the same invariant as the texture $C(\mathbf{k}) = -1 = C[\mathbf{\Delta}(\mathbf{r})]$.

We note that even when the adiabatic approximation fails due to a $\mathbf{\Delta}(\mathbf{r})$ that has fast variations in the unit cell, the writing in Eq. (7.41) can still be relevant for states that approximate zeroth or higher Landau levels [65, 212–216], possibly replacing $\chi^{+}(\mathbf{r})$ with a spinor that is obtained variationally [211].

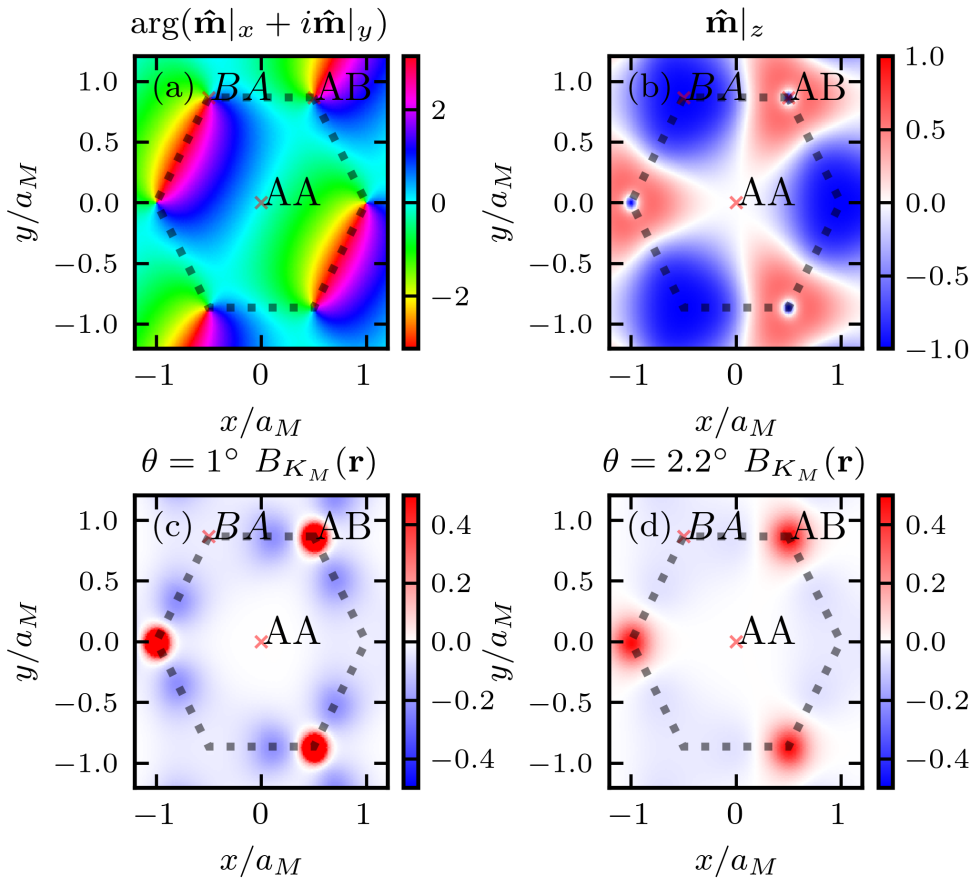

Figure 7.2: (a) Unit cell map of the in-plane angle of the texture of $\hat{\boldsymbol{m}}(\mathbf{r})$ defined by the top K_M wavefunction of WSe_2 at $\theta = 1^\circ$, defined in in Eq. (7.30). (b) Same as (a) but for the z-polarization in the unit cell. (c) Real space Berry curvature at the K_M point at $\theta = 1^\circ$. (d) Same as (c), but at $\theta = 2.2^\circ$.

7.4 Stability of nonzero real-space Chern number to perturbations

Having introduced two examples where a nonzero real-space Chern number naturally emerges, we now connect these examples to our considerations in Sec. 7.1, where we showed that a nonzero real-space Chern number is only possible if the wavefunction has a zero in the unit cell.

We therefore consider the stability to perturbations of the zeroes of the wavefunction in Eq. (7.11). To that end, let us write a general perturbed wavefunction as

$$u_{\mathbf{k}}(\mathbf{r}) = \chi_{\mathbf{k}}^{\Phi_1}(\mathbf{r})\psi_{\mathbf{k}}^{\Phi_2}(\mathbf{r}) + \epsilon\Delta u_{\mathbf{k}}(\mathbf{r}), \tag{7.42}$$

where $\Delta u_{\mathbf{k}}(\mathbf{r})$ is a perturbing wavefunction and ϵ is a small perturbation parameter. Importantly, we expect $\Delta u_{\mathbf{k}}(\mathbf{r})$ to be a generic wavefunction, which is not necessarily aligned with $\chi_{\mathbf{k}}^{\Phi_1}(\mathbf{r})$. We decompose $\Delta u_{\mathbf{k}}(\mathbf{r})$ into two orthogonal components as follows

$$\Delta u_{\mathbf{k}}(\mathbf{r}) = \Delta u_{\mathbf{k}}^{\parallel}(\mathbf{r}) + \Delta u_{\mathbf{k}}^{\perp}(\mathbf{r}), \tag{7.43}$$

where the aligned component is

$$\Delta u_{\mathbf{k}}^{\parallel}(\mathbf{r}) = \chi_{\mathbf{k}}^{\Phi_1}(\mathbf{r}) \Big\{ \big[\chi_{\mathbf{k}}^{\Phi_1}(\mathbf{r})\big]^{\dagger} \Delta u_{\mathbf{k}}(\mathbf{r}) \Big\}, \tag{7.44}$$

and the orthogonal component is

$$\Delta u_{\mathbf{k}}^{\perp}(\mathbf{r}) = \Delta u_{\mathbf{k}}(\mathbf{r}) - \Delta u_{\mathbf{k}}^{\parallel}(\mathbf{r}), \tag{7.45}$$

which is orthogonal to the spinor of the ideal wavefunction at every point in space

$$\big[\chi_{\mathbf{k}}^{\Phi_1}(\mathbf{r})\big]^{\dagger} \Delta u_{\mathbf{k}}^{\perp}(\mathbf{r}) = 0. \tag{7.46}$$

A first observation is that the admixture of $\Delta u_{\mathbf{k}}^{\parallel}(\mathbf{r})$ preserves the structure of Eq. (7.11), and therefore also the real-space Chern number. In particular, we can absorb $\epsilon \Delta u_{\mathbf{k}}^{\parallel}(\mathbf{r})$ into the unperturbed wavefunction. On the other hand, the admixture of $\Delta u_{\mathbf{k}}^{\perp}(\mathbf{r})$ will generically remove any zeroes. To see that, consider the norm squared of the perturbed wavefunction

$$|u_{\mathbf{k}}(\mathbf{r})|^2 = |\psi_{\mathbf{k}}^{\Phi_2}(\mathbf{r})|^2 + \epsilon^2 |\Delta u_{\mathbf{k}}^{\perp}(\mathbf{r})|^2, \tag{7.47}$$

which was obtained using orthogonality property of $\Delta u_{\mathbf{k}}^{\perp}(\mathbf{r})$. We see that the full wavefunction can only have a zero if both $\psi_{\mathbf{k}}^{\Phi_2}(\mathbf{r})$ and $\Delta u_{\mathbf{k}}^{\perp}(\mathbf{r})$ are simultaneously zero. Since we do not generically expect the zeroes of a perturbing wavefunction to coincide with the original wavefunction, zeroes of $\psi_{\mathbf{k}}^{\Phi_2}(\mathbf{r})$ will typically be removed.

We therefore find that zeroes of the wavefunction Eq. (7.11) are generically removed upon admixing generic wavefunctions, which contain spinors orthogonal to $\chi_{\mathbf{k}}^{\Phi_1}(\mathbf{r})$. This removal of zeroes in turn leads to the real-space Chern number collapsing to the behavior for non-vanishing wavefunctions, given in Eq. (7.10), in which it is tied to the applied magnetic flux. We remark that at high symmetry points in the Brillouin zone, zeroes of wavefunctions can be protected by symmetries, rendering them stable to symmetry-preserving perturbations.

7.4.1 Illustration 1: TMDs

The removal of zeroes by admixture is best illustrated for twisted bilayer TMDs. There, the adiabatic approximation assumes a wavefunction of the form of Eq. (7.41), effectively projecting on the Hilbert space of wavefunctions with spinor components given by $\chi^{+}(\mathbf{r})$. Going beyond the

adiabatic *approximation* by allowing the admixing of wavefunctions with spinors proportional to χ^- is, according to our general arguments, generically bound to remove zeroes. Therefore we expect that generically, the real-space Chern number of the wavefunctions of twisted bilayer TMDs is will vanish, even when the adiabatic wavefunction suggests otherwise.

To illustrate this, in Figs. 7.2a,b we show the real-space texture $\hat{\boldsymbol{m}}(\mathbf{r})$ of the full wavefunction at the K_M point for the topmost band for WSe_2 at $\theta = 1°$. Note that nominally, the adiabatic approximation is expected to be very accurate at these small twist angles [201, 202]. And indeed, the texture $\hat{\boldsymbol{m}}(\mathbf{r})$ largely follows the texture $\boldsymbol{n}(\mathbf{r})$ defined by the Zeeman field, shown in Figs. 7.1a,b. However, exactly at the BA stacking point, rather than being fully polarized to the top layer like the underlying texture $\boldsymbol{n}(\mathbf{r})$, it has the opposite layer polarization.

As expected on general grounds, this arises due to the admixing of a perpendicular spinor in the full wavefunction. At the adiabatic wavefunction zeroes, the perpendicular spinor dominates, leading to a sudden flipping of the spinor direction close to those zeroes. Plotting the real-space Berry curvature $B_{\mathbf{k}}(\mathbf{r})$ in Fig. 7.2c reveals that the flip in the spinor direction leads to a strongly concentrated Berry curvature at the AB stacking points. For larger twist angles ($\theta = 2.2°$), the adiabatic approximation becomes less accurate, with wavefunctions characterized by a large admixing of the $\chi^-(\mathbf{r})$ component. In this regime, the sharp feature at the AB stacking point is smeared out, as seen in Fig. 7.2d.

While we illustrated the fragility of the real-space Chern number at the K_M point, we have checked that this vanishing of Chern number is generic for states across the Brillouin zone. Only at the high-symmetry Γ point, we obtain $C(\Gamma) = -1$, which arises because at the Γ point, the zero in the adiabatic approximation is symmetry protected in the full model.

7.4.2 Illustration 2: Ideal bands in chiral TBG

For ideal bands, we expect similarly that the real-space Chern number will vanish due to the admixing of other wavefunctions, which happens in any realistic system. We now illustrate this for chiral twisted bilayer graphene. We recall that at the magic angle, there are two degenerate ideal flat bands of opposite Chern number, which have opposite sublattice polarization. To split the degeneracy and obtain ideal detached flat Chern bands, it is enough to apply a staggered mass, introducing a polarizing term $\sigma_z m_s$. In Fig. 7.3a, we illustrate the real-space Berry curvature for the K_M B-sublattice wavefunction for TBG in the chiral limit at the magic angle $\theta = 1.09°$, where the degeneracy between the two flat bands was lifted by a large sublattice potential $m_s = 60\,\mathrm{meV}$. We see that the Berry curvature is everywhere positive and find that it integrates to $C(\mathbf{k}) = 1$. This reflects the ideality of the bands of chiral TBG, being given in terms of Landau levels.

Since the ideal wavefunctions are fully sublattice polarized, a natural way to remove the zero is to admix states in the other sublattice. This happens naturally when going beyond the chiral limit, introducing a small nonzero intrasublattice tunneling $w_{AA} = 5\,\mathrm{meV}$, but keeping a strong polarizing potential $m_s = 60\,\mathrm{meV}$. We show the resulting Berry curvature distribution

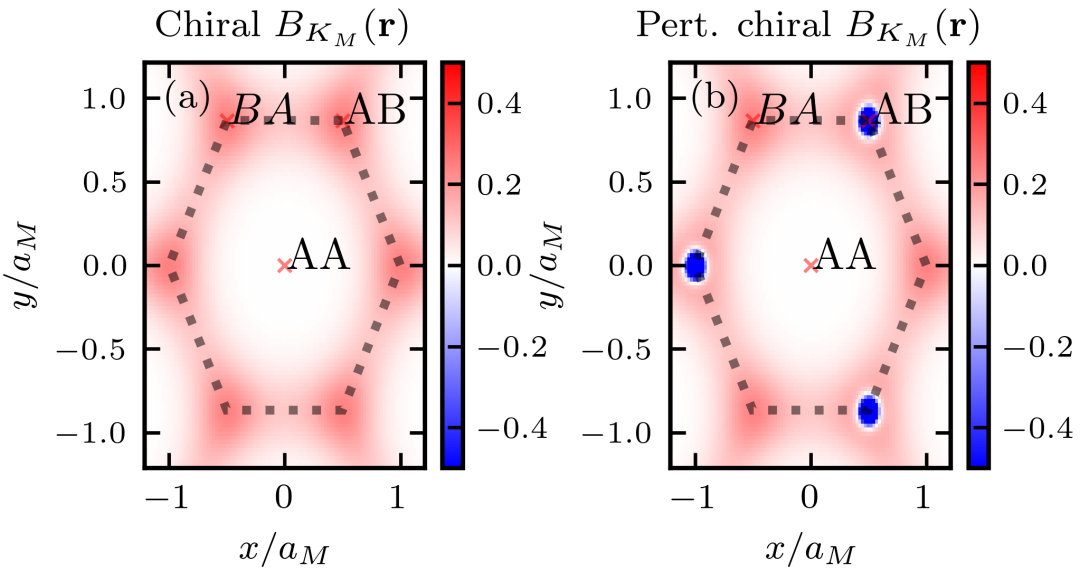

Figure 7.3: (a) Unit cell map of the real-space Berry curvature for the flat band K_M wavefunction of TBG at the magic angle of the chiral limit ($w_{AA} = 0$) with a sublattice potential mass term $m_s\sigma_z$, $m_s = 60\,\mathrm{meV}$. (b) Same as (a) but slightly perturbed away from the chiral limit with $w_{AA} = 5\,\mathrm{meV}$.

for the K_M, mostly B-polarized, state in Fig. 7.3b, showing that at the BA point, a sharp peak of negative Berry curvature emerges, leading to the vanishing of the total real-space Chern number.

7.5 Discussion

To conclude, we found that the real-space Chern number of spinor wavefunctions is generically tied to the magnetic flux, satisfying $C(\mathbf{k}) = \Phi$. It is only in fine tuned cases that the real-space Chern number can differ from the applied flux. Having identified two such fine-tuned examples, the chiral limit of twisted bilayer graphene and the adiabatic approximation to transition metal dichalcogenides, we showed how the real-space Chern number at zero flux $\Phi = 0$ vanishes when perturbing away from these ideal limits.

We note that this generic vanishing of real-space Chern number should be experimentally observable [217], in particular for bands far away from the ideal/adiabatic limits. On the other hand, for bands close to the ideal/adiabatic limits, experimental observation of the generic vanishing of the real-space Chern number is challenging. This is because the cancellation of the real-space Chern number happens in a region where the ideal wavefunction has a zero, so the full wavefunction density is very small when the perturbation parameter ϵ, characterizing the deviation from ideality in Eq. (7.42), is small. This renders the explicit observation of the features shown in Figs. 7.2b,7.3b experimentally difficult.

8 Hofstadter butterfly in twisted transition metal dichalcogenides

The results of this Chapter have been published as Ref. [4], co-authored by Kang Yang, Felix von Oppen and Christophe Mora. The research was conducted by the author of this thesis while discussing with the coauthors.

When magnetic flux of the order of a flux quantum $\Phi_0 = h/e$ threads the unit cell of a lattice, the energy spectrum exhibits a remarkable fractal structure, referred to as the Hofstadter butterfly [218]. Reaching this regime for standard materials requires unrealistically large applied magnetic fields B. The advent of moiré materials which feature large unit cells enabled the Hofstadter regime to be probed experimentally, with signatures observed in bilayer graphene on hBN [219], twisted bilayer graphene [220–222], and transition metal dichalcogenide heterobilayers [223].

The experimental realization of twisted bilayer graphene [20] spearheaded these developments [22–30, 153, 154]. Twisted bilayer graphene exhibits flat bands at twist angles close to the magic angle of $\theta = 1.05°$ [19], providing additional interest in its Hofstadter physics. The band structure at large magnetic fields was shown to exhibit rich structure [224–227], with salient features appearing at magnetic fields corresponding to an integer number of flux quanta threading the unit cell. At these points, the Hofstadter problem retains the periodicity of the underlying lattice [226], and the system displays reentrant flat bands, resulting in an interaction-driven phenomenology, which is similar to that at zero magnetic field [222]. Shortly after twisted bilayer graphene, twisted transition metal dichalcogenide (TMD) bilayers emerged as another remarkable moiré platform, featuring flat topological bands [55, 68, 228, 229] and permitting the observation of Mott insulators [56], superconductivity [57, 58], quantum criticality [59], and, most remarkably, the integer and fractional quantum anomalous Hall effects [60–64]. Very recently, a TMD bilayer has been proposed to exhibit a fractional quantum spin Hall effect of holes [65] and shown to feature multiple flat bands of equal Chern number in a given valley [65, 66]. These experimental findings were accompanied by intense theoretical efforts. Due to flavor polarization, topological bands exhibit an anomalous Hall effect at integer fillings [230–233], with magnetic field tuning the fine balance between competing states [234]. The fractional quantum anomalous Hall effect can form in partially filled Chern bands and is now firmly established in exact diagonalization studies [232, 235–240], greatly broadening the scope of fractional states in twisted graphenes [241].

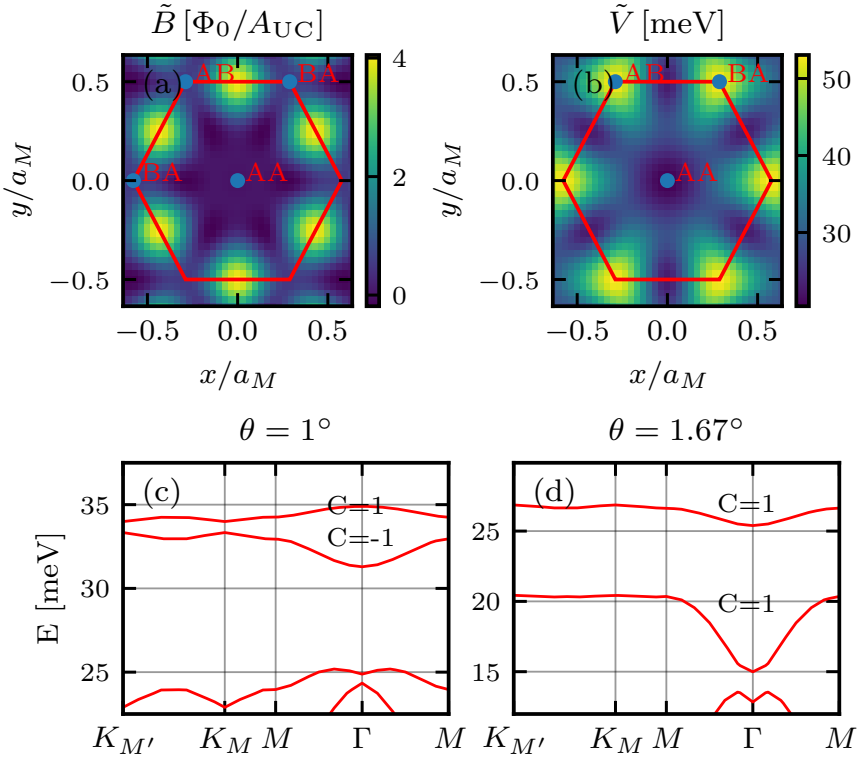

Figure 8.1: (a) Effective magnetic field $\tilde{B}(\mathbf{r}) = \nabla \times \tilde{A}(\mathbf{r})$ entering the adiabatic model in Eq. (8.1), measured in units of flux quanta ($\Phi_0 = h/e$) per unit cell (A_{UC}). The moiré unit cell with the AA, AB, and BA stacking locations is highlighted in red. The effective magnetic field is peaked at the midpoints between AB and BA stacking. (b) Effective moiré potential $\tilde{V}(\mathbf{r})$ entering the adiabatic model. (c) Band structure of twisted bilayer WSe_2. Plots in panels (a-c) are for a twist angle of $\theta = 1°$ using model parameters from Ref. [68]. (d) Same as (c) but at a twist angle of $\theta = 1.67°$.

Motivated by these exciting developments, we study the effects of a strong magnetic field on topological bands in twisted TMDs. We employ a continuum model [55, 68] for each valley of the twisted-TMD band structure and develop a gauge-independent framework to compute the spectrum as a function of magnetic field (Hofstadter butterfly). While our framework is generally applicable, we focus specifically on models of twisted bilayer WSe_2 and $MoTe_2$.

We first investigate a minimal model of WSe_2, pointing out a remarkable similarity between the Hofstadter butterflies for WSe_2 at small twist angles and the celebrated Haldane model [242, 243], and shedding light on the various topological phase transitions as a function of magnetic flux. We find that in many ways, the model with an external magnetic field corresponding to $\Phi = -1$ flux quanta per moiré unit cell can be viewed as a natural parent model for understanding the TMD band structures. In particular, we find that up to a twist angle of $\sim 2°$, the band structure at $\Phi = -1$ is robustly described by a Haldane model. This contrasts with the zero-flux case, where a topological phase transition [68] already occurs at a twist angle of

$\sim 1.5°$. Beyond this transition, the two topmost bands acquire equal Chern numbers, which is no longer compatible with the two-band approximation of the Haldane model. We show that these equal-Chern bands arise from the parabolic band top at flux $\Phi = -1$. Notably, the entire topmost band at $\Phi = -1$ resembles a free-particle dispersion, allowing a single Landau level to develop into a detached flat Chern band at zero flux, and providing ideal conditions for fractional quantum Hall liquids to form.

We then apply our framework to a more elaborate model, which provides a realistic description of the band structure of twisted bilayer $MoTe_2$ at twist angle $\theta = 2.1°$, close to the value in a recent experiment [65]. This model features three low-lying bands of equal Chern number per valley, in agreement with experiment. It has been proposed to feature non-Abelian topological order in the second topmost band, analogous to the first Landau level [65, 212–216]. We show that at $\Phi = -1$, the band structure is remarkably close to that of a backfolded free-electron dispersion for a large range of energies, allowing its two lowest Landau levels to persist all the way to $\Phi = 0$. In this picture, the lowest two bands at $\Phi = 0$ are Landau levels of the nearly free electrons at $\Phi = -1$, so that the $\Phi = -1$ band structure may serve as a natural parent model to understand the appearance of non-Abelian phases [65, 212–216].

Beyond twisted bilayer TMDs, our results for twisted bilayer $MoTe_2$ establish the Hofstadter spectra as a valuable general characterization method for Chern bands and their connection to Landau levels, complementing earlier approaches focusing on their quantum geometry [203–210]

The special role played by the $\Phi = -1$ band structure is best motivated by the adiabatic picture of twisted bilayer TMDs [201, 202], which we introduced in Section 7.3 of the preceding Chapter 7.

This model describes the band structure of one valley using a model of electrons with effective mass m^* subject to a potential $\tilde{V}(\mathbf{r}) = -D(\mathbf{r}) + |\Delta(\mathbf{r})| + \Delta_0(\mathbf{r})$ and an effective magnetic field $\tilde{B}(\mathbf{r}) = \nabla \times \tilde{\boldsymbol{A}}(\mathbf{r})$, both of which are moiré periodic. The corresponding Hamiltonian for the K-valley takes the form

$$H^K_{\text{Adiabatic}} = -\frac{(\hbar\mathbf{k} - e\tilde{\mathbf{A}}(\mathbf{r}))^2}{2m^*} + \tilde{V}(\mathbf{r}). \tag{8.1}$$

The valley-odd effective magnetic field emerges after projecting to the low-energy states of the potential and tunneling terms of the full continuum Hamiltonian, exploiting their slow spatial variation. These can be written as an effective Zeeman field acting on the layer degree of freedom, with the direction $\hat{\mathbf{n}}(\mathbf{r})$ describing a moiré periodic texture. The effective magnetic field, shown in Fig. 8.1a, is given by the Pontryagin-index density associated with this skyrmion-like texture,

$$\tilde{B}(\mathbf{r}) = -\frac{\hbar}{2e}\hat{\mathbf{n}}(\mathbf{r}) \cdot \partial_x\hat{\mathbf{n}}(\mathbf{r}) \times \partial_y\hat{\mathbf{n}}(\mathbf{r}), \tag{8.2}$$

and corresponds to an average of one flux quantum per unit cell. The moiré-periodic scalar potential $\tilde{V}(\mathbf{r})$ experienced by the electrons, shown in Fig. 8.1b, combines the effective Zeeman energy and a scalar potential originating from the adiabatic approximation,

$$D(\mathbf{r}) = \frac{\hbar^2}{8m^*} \sum_{i=x,y} [\partial_i \hat{\mathbf{n}}(\mathbf{r})]^2, \tag{8.3}$$

which is proportional to the trace of the quantum geometric tensor of the adiabatically polarized states as a function of $\mathbf{r}$.

Within the adiabatic model, the external magnetic field simply adds to the effective field, $\tilde{B}(\mathbf{r}) \to B_{\text{tot}}(\mathbf{r}) = \tilde{B}(\mathbf{r}) + B$ [202]. This immediately implies that on average, an externally applied field corresponding to $\Phi = -1$ flux quanta per unit cell cancels the effective magnetic field. At this *point of net zero flux*, the model in a single valley reduces to a band structure without average magnetic field and can be solved using a Bloch basis for the original lattice unit cell. This simplification makes $\Phi = -1$ a natural starting point to understand the magnetic-field-dependent spectrum. Note that in the other valley, the effective magnetic field $\tilde{B}(\mathbf{r})$ carries the opposite sign, so a cancellation in that valley occurs for opposite applied flux $\Phi = 1$.

Within the adiabatic picture, it is natural to describe the band structure of twisted bilayer WSe_2 at $\Phi = -1$ in terms of a Haldane model. The periodic potential $\tilde{V}(\mathbf{r})$ localizes particles into site orbitals on a hexagonal lattice, cf. Fig. 8.1b. The next-nearest neighbor hopping between these orbitals will have nonzero phases due to the inhomogeneous part of the emergent magnetic field. The departure of the external magnetic flux from $\Phi = -1$, i.e., the *net flux*, tunes these phases. Indeed, for sufficiently low twist angles, we find very good agreement between the exact magnetic-field spectra obtained from the original continuum model and those computed from the Haldane model. Specifically, both models exhibit a similar sequence of topological phase transitions, which are expected whenever the phase of the next-nearest neighbor hopping amplitude changes sign. The site orbitals delocalize with increasing twist angle. As a result, the Haldane model must be extended to include longer-range hoppings and becomes more sensitive to the net flux. A direct consequence is that the Haldane model at *net zero flux* ($\Phi = -1$) is much more robust against an increase in the twist angle than at $\Phi = 0$.

For larger twist angles, the adiabatic model suggests an alternative description at $\Phi = -1$. The kinetic term in Eq. (8.1) becomes dominant, corresponding to holes in a weak periodic potential. The resulting band structure naturally resembles backfolded free particle bands with small gaps. Even though the adiabatic picture breaks down upon increasing the twist angle [201, 202, 244], we still find good agreement with a parabolic band for the topmost band of WSe_2 at $\theta = 1.67°$. For $MoTe_2$, fast oscillations in the effective Zeeman field direction $\hat{\mathbf{n}}(\mathbf{r})$ render the adiabatic approximation inapplicable, yet the two topmost bands at the point of *net zero flux* ($\Phi = -1$) are nearly parabolic.

This Chapter is structured as follows. In Sec. 8.1, we recall the continuum TMD model and outline its solution in the presence of an external magnetic field. In Sec. 8.2, we analyze the

model for WSe_2 in the small twist angle regime, which is well approximated within a tight-binding approach. Larger twist angles are considered in Sec. 8.3. Section 8.4 investigates a corresponding model for $MoTe_2$, featuring Chern bands that are akin to the first Landau level. We conclude with a discussion, highlighting the general applicability and experimental relevance of our findings.

8.1 Band structures in a magnetic field

8.1.1 TMD continuum model

Let us recall from Sec. 2.2 that the band structure of twisted homobilayer TMDs in valley K can be described by the continuum Hamiltonian [55, 68]

$$H_{\text{sp}}^K = \begin{pmatrix} -\frac{\hbar^2(\mathbf{k}-\mathbf{K}^b)^2}{2m^*} + V_b(\mathbf{r}) & T(\mathbf{r}) \\ T^\dagger(\mathbf{r}) & -\frac{\hbar^2(\mathbf{k}-\mathbf{K}^t)^2}{2m^*} + V_t(\mathbf{r}) \end{pmatrix}, \tag{8.4}$$

where m^* is the effective mass of the valence band, $\mathbf{K}^{t/b} = (0, \pm 4\pi \sin(\theta/2)/(3a_0))$ are the momenta of the band extrema of the top and bottom layers with a_0 the TMD lattice constant, $V_{t/b}(\mathbf{r})$ are the potentials in the top/bottom layers, and $T(\mathbf{r})$ describes interlayer tunneling. In the first harmonic approximation, these take the form

$$V_b(\mathbf{r}) = V e^{i\psi}(e^{i\mathbf{g}_1\cdot\mathbf{r}} + e^{i\mathbf{g}_3\cdot\mathbf{r}} + e^{i\mathbf{g}_5\cdot\mathbf{r}}) + h.c. \tag{8.5}$$

$$V_t(\mathbf{r}) = V_b(-\mathbf{r}) \tag{8.6}$$

$$T(\mathbf{r}) = w(1 + e^{i\mathbf{g}_5\cdot\mathbf{r}} + e^{i\mathbf{g}_6\cdot\mathbf{r}}), \tag{8.7}$$

with tunneling strength w, potential strength V, the phase ψ, and the six reciprocal vectors $\mathbf{g}_j$ defined as the $j-1$ counterclockwise C_{6z} rotations of $\mathbf{g}_1 = (4\pi\theta/(\sqrt{3}a_0), 0)$, shown in Fig. 2.1. The moiré lattice constant $a_M = \frac{a_0}{2\sin(\theta/2)}$ is much larger than the bare TMD lattice constant a_0.

The form of the Hamiltonian is fixed by the C_{3z}, C_{2y}, and time-reversal ($\mathcal{T}$) symmetries of a twisted TMD homobilayer, as shown in Sec. 2.2. In the first harmonic approximation, there is an additonal 3D inversion symmetry acting as $\sigma_x H_{\text{sp}}^K(\mathbf{r})\sigma_x = H_{\text{sp}}^K(-\mathbf{r})$, which, however, is broken by higher harmonic terms [1] [232, 245]. Note that $C_{2y}\mathcal{T}$ remains a good symmetry in the presence of an externally applied magnetic field, even though C_{2y} and $\mathcal{T}$ are both broken individually.

Many different parameter choices have been proposed in the literature for relevant twisted TMDs [55, 68, 239]. For most of this work, we consider a minimal model of twisted WSe_2 in the first harmonic approximation from Ref. [68] as an illustrative example. The parameters of

[1] C_{2y} fixes $V_b(x,y) = V_t(-x,y)$ only. If only first harmonics are considered, this turns out to be the same as $V(\mathbf{r}) = V(-\mathbf{r})$, see Eq. (8.6) in the text.

this model are $(a_0, m^*, V, \psi, w) = (0.332\,\mathrm{nm}, 0.43\,\mathrm{m_e}, 9\,\mathrm{meV}, -128^\circ, 18\,\mathrm{meV})$, with m_e the bare electron mass. The band structure of twisted WSe_2 depends sensitively on twist angle. At small twist angles, it has two low-energy Chern bands of opposite Chern number separated from other bands by a large gap, as shown for $\theta \approx 1^\circ$ in Fig. 8.1c. In this regime, the two bands are accurately described by a Haldane model [55, 246]. As the twist angle is increased, the lower of the two bands approaches the remote bands, while the upper band flattens, reaching the magic angle at $\theta \approx 1.43^\circ$ [68]. After a band crossing at $\theta \approx 1.5^\circ$, the Chern number of the lower band switches sign, so that the two topmost bands have equal Chern number. We illustrate the band structure in this regime in Fig. 8.1d for $\theta = 1.67^\circ$.

In Sec. 8.4, we extend our discussion to a realistic model of $MoTe_2$ at $\theta = 2.1^\circ$, which includes higher harmonics for the tunneling and layer potential terms [212, 216]. Specifically, we add the second harmonic potential

$$V_b^{(2)}(\mathbf{r}) = V_t^{(2)}(\mathbf{r}) = V_2\left[e^{i(\mathbf{g}_1+\mathbf{g}_2)\cdot\mathbf{r}} + e^{i(\mathbf{g}_3+\mathbf{g}_4)\cdot\mathbf{r}} + e^{i(\mathbf{g}_5+\mathbf{g}_6)\cdot\mathbf{r}}\right] + h.c. \tag{8.8}$$

to $V_b(\mathbf{r})$ and $V_t(\mathbf{r})$ as well as the second harmonic tunneling

$$T^{(2)}(\mathbf{r}) = w_2\left[e^{i\mathbf{g}_1\cdot\mathbf{r}} + e^{i\mathbf{g}_4\cdot\mathbf{r}} + e^{i(\mathbf{g}_3+\mathbf{g}_2)\cdot\mathbf{r}}\right] \tag{8.9}$$

to $T(\mathbf{r})$. We use parameters $(a_0, m^*, V, \psi, w, V_2, w_2) = (0.3472\,\mathrm{nm}, 0.62\,\mathrm{m_e}, 20.51\,\mathrm{meV}, -61.49^\circ, -7.01\,\mathrm{meV}, -9.08\,\mathrm{meV}, 11.08\,\mathrm{meV})$ [212], which fit the band structure obtained from ab initio calculations [216].

8.1.2 Gauge-independent calculation of magnetic Bloch bands

We introduce an external magnetic field B into the continuum model in Eq. (8.4) by substituting momentum with kinetic momentum, $\mathbf{k} \to \mathbf{\Pi} = \mathbf{k} - e\mathbf{A}/\hbar$. The kinetic momentum obeys

$$[\Pi_x, \Pi_y] = ieB/\hbar = \frac{i}{l_B^2}, \tag{8.10}$$

where $l_B = \sqrt{\hbar/eB}$ is the magnetic length satisfying $2\pi l_B^2 B = \Phi_0$. Working at a rational flux $\Phi = \frac{p}{q}$ per moiré unit cell (measured in units of Φ_0), we have $\frac{1}{l_B^2} = 2\pi\frac{p}{q}\frac{1}{A_{\mathrm{UC}}}$, where $A_{\mathrm{UC}} = |\mathbf{a}_1 \times \mathbf{a}_2|$ is the area of the moiré unit cell with elementary lattice vectors $\mathbf{a}_i$. We denote the basis vectors of the corresponding reciprocal lattice as $\mathbf{G}_1$ and $\mathbf{G}_2$, which satisfy $\mathbf{a}_i \cdot \mathbf{G}_j = 2\pi\delta_{ij}$. (In our numerics, we use $\mathbf{G}_1 = \mathbf{g}_5$ and $\mathbf{G}_2 = \mathbf{g}_1$.) We express the Hamiltonian in the Landau level basis [224, 225], working in a gauge-independent formalism. We recall the magnetic translation operators

$$T_{\mathbf{a}} = \exp\left[i\mathbf{a}\cdot\left(\mathbf{\Pi} + \frac{1}{l_B^2}\hat{\boldsymbol{z}}\times\mathbf{r}\right)\right] \tag{8.11}$$

($\hat{\boldsymbol{z}}$ is the unit vector in the z-direction), which satisfy

$$T_{\mathbf{a}}T_{\mathbf{a}'} = \exp\left(i\frac{\mathbf{a}\times\mathbf{a}'}{l_B^2}\right)T_{\mathbf{a}'}T_{\mathbf{a}}. \tag{8.12}$$

where $\mathbf{a}\times\mathbf{a}'$ stands for the (oriented) area spanned by the two in-plane vectors. The operators $T_{\mathbf{a}}$ and $T_{\mathbf{a}'}$ commute if this area is threaded by an integer number of flux quanta. We now choose translations by $q\mathbf{a}_1$ and $\frac{1}{p}\mathbf{a}_2$, which enclose precisely one flux quantum, to define our basis. Specifically, we choose a Landau-level basis of simultaneous eigenstates of $\mathbf{\Pi}^2$, $T_{q\mathbf{a}_1}$, and $T_{\mathbf{a}_2/p}$ [247]. The basis states $|n,\mathbf{k}\rangle$ are characterized by a Landau level index n and momentum $\mathbf{k}$, defined through

$$(\Pi_x^2+\Pi_y^2)\,|n,\mathbf{k}\rangle = (n+\frac{1}{2})\frac{1}{l_B^2}\,|n,\mathbf{k}\rangle \tag{8.13}$$

$$T_{q\mathbf{a}_1}\,|n,\mathbf{k}\rangle = \exp(iq\mathbf{a}_1\cdot\mathbf{k})\,|n,\mathbf{k}\rangle \tag{8.14}$$

$$T_{\mathbf{a}_2/p}\,|n,\mathbf{k}\rangle = \exp\left(i\frac{1}{p}\mathbf{a}_2\cdot\mathbf{k}\right)|n,\mathbf{k}\rangle\,. \tag{8.15}$$

We expand the momentum $\mathbf{k}$ in the basis vectors $\mathbf{G}_1$ and $\mathbf{G}_2$ of the reciprocal lattice as

$$\mathbf{k} = k_1\frac{1}{q}\mathbf{G}_1 + k_2 p\mathbf{G}_2, \tag{8.16}$$

with coefficients $k_1, k_2 \in [0,1)$ defining the Landau-level Brillouin zone. (Note that, as defined, the Landau-level Brillouin zone is p times larger than the conventional magnetic Brillouin zone.)

We now construct this basis starting from the state invariant under magnetic translations, $|n,0\rangle$. To that end, we use that the exponential of the guiding center operator

$$\mathbf{R} = \mathbf{r} - l_B^2(\hat{z}\times\mathbf{\Pi}) \tag{8.17}$$

implements a momentum boost [204], and is related to magnetic translations through

$$T_{l_B^2(\hat{z}\times\mathbf{q})} = e^{i\mathbf{q}\cdot\mathbf{R}}. \tag{8.18}$$

We use these operators acting on $|n,0\rangle$ to explicitly construct states for any $\mathbf{k}$ in the Landau-level Brillouin zone,

$$|n,\mathbf{k}\rangle = e^{ik_2p\mathbf{G}_2\cdot\mathbf{R}}e^{ik_1\frac{1}{q}\mathbf{G}_1\cdot\mathbf{R}}\,|n,0\rangle\,, \tag{8.19}$$

where Eqs. (8.14) and (8.15) follow using Eqs. (8.18) and (8.12). We define states with $\mathbf{k}$ outside the Landau-level Brillouin zone by the periodic extension $|n,\mathbf{k}\rangle = |n,\mathbf{k}+p\mathbf{G}_2\rangle = |n,\mathbf{k}+\frac{1}{q}\mathbf{G}_1\rangle$. With this convention, the states at the Landau-level Brillouin zone boundaries

are not continuous. This reflects the topology of Landau levels as states translated across the entire Landau-level Brillouin zone are related by an irremovable $U(1)$ phase.

The solution now proceeds by expressing the Hamiltonian in the above basis. The kinetic term only acts on the Landau level index and is independent of momentum $\mathbf{k}$. On the other hand, the moiré potential and tunneling terms depend on the momentum, requiring us to evaluate the matrix element of $\exp(i\mathbf{g}\cdot\mathbf{r})$,

$$\langle n'\mathbf{k}' \,|\, \exp(i\mathbf{g}\cdot\mathbf{r}) \,|\, n\mathbf{k}\rangle = \left\langle n' \left| \exp\left(i\frac{\Pi\times\mathbf{g}}{B}\right) \right| n \right\rangle \langle \mathbf{k}' \,|\, \exp(i\mathbf{g}\cdot\mathbf{R}) \,|\, \mathbf{k}\rangle, \tag{8.20}$$

where we separated the position operator into its kinetic momentum and guiding center components. The vector $\mathbf{g}$ is an element of the moiré reciprocal lattice.

The first term in Eq. (8.20) is a standard expectation value in Landau levels, and is given in terms of Laguerre polynomials [248]. For $n' \leq n$:

$$\left\langle n' \left| \exp\left(i\frac{\Pi\times\mathbf{g}}{B}\right) \right| n \right\rangle = (z^*)^{n'-n}\sqrt{\frac{n'!}{n!}} L_{n'}^{n-n'}(|z|^2)\exp\left(-|z|^2/2\right), \tag{8.21}$$

with $z = [(\mathbf{g})_x + i(\mathbf{g})_y]\frac{l_B}{\sqrt{2}}$ and $L_{n'}^{n-n'}(|z|^2)$ is the associated Laguerre polynomial. For $n' > n$, we use $\langle n'|\exp\left(i\frac{\Pi\times\mathbf{g}}{B}\right)|n\rangle = \left[\langle n|\exp\left(-i\frac{\Pi\times\mathbf{g}}{B}\right)|n'\rangle\right]^*$.

To evaluate the second term in Eq. (8.20), we expand the vector $\mathbf{g}$ using a basis of the reciprocal lattice, $\mathbf{g} = m_1\mathbf{G}_1 + m_2\mathbf{G}_2$, with integers m_1, m_2. Using this, we separate the exponential

$$\exp(i\mathbf{g}\cdot\mathbf{R}) = c_1 \exp(im_1\mathbf{G}_1\cdot\mathbf{R})\exp(im_2\mathbf{G}_2\cdot\mathbf{R}), \tag{8.22}$$

where $c_1 = \exp\left(-\pi i m_1 m_2 \frac{q}{p}\right)$ is the commutator from the Baker–Campbell–Hausdorff formula, which states that $e^{X+Y} = e^X e^Y e^{-\frac{1}{2}[X,Y]}$ for operators X and Y whose commutator $[X,Y]$ is a number. At this point our basis definition, Eq. (8.19) facilitates the evaluation. For one, $\exp(im_2\mathbf{G}_2\cdot\mathbf{R})$ changes $\mathbf{k} \to \mathbf{k} + m_2\mathbf{G}_2$. If this momentum lies outside the Landau level Brillouin zone, compared to the basis definition of Eq. (8.19), there is an extra factor $\exp(i\lfloor k_2 + m_2/p\rfloor p\mathbf{G}_2\cdot\mathbf{R})$, where $\lfloor x\rfloor$ denotes the integer part of the number x. This operator is in fact proportional to a translation by $-q\mathbf{a}_1$ (using the relation of Eq. (8.18)), and can be easily evaluated using the translation properties of our basis states, Eq. (8.14). We have

$$\begin{aligned} e^{im_2\mathbf{G}_2\cdot\mathbf{R}}\,|\mathbf{k}\rangle &= e^{i\lfloor k_2+m_2/p\rfloor p\mathbf{G}_2\cdot\mathbf{R}}\,|\mathbf{k}+m_2\mathbf{G}_2\rangle \\ &= (T_{-q\mathbf{a}_1})^{\lfloor k_2+m_2/p\rfloor}\,|\mathbf{k}+m_2\mathbf{G}_2\rangle \\ &= e^{-i2\pi k_1\lfloor k_2+m_2/p\rfloor}\,|\mathbf{k}+m_2\mathbf{G}_2\rangle\,. \end{aligned} \tag{8.23}$$

Next, we apply $\exp(im_1\mathbf{G}_1\cdot\mathbf{R})$ leading to

$$\begin{aligned} e^{im_1\mathbf{G}_1\cdot\mathbf{R}}\,|\mathbf{k}+m_2\mathbf{G}_2\rangle &= T_{\frac{q}{p}m_1\mathbf{a}_2}\,|\mathbf{k}+m_2\mathbf{G}_2\rangle \\ &= e^{i2\pi(k_2p+m_2)\frac{q}{p}m_1}\,|\mathbf{k}+m_2\mathbf{G}_2\rangle\,, \end{aligned} \tag{8.24}$$

where we used Eq. (8.18) in the first line. Putting everything together:

$$\begin{aligned} \langle\mathbf{k}'\,|\,\exp(i\mathbf{g}\cdot\mathbf{R})\,|\,\mathbf{k}\rangle = \delta_{\mathbf{k}',\mathbf{k}+m_2\mathbf{G}_2}\exp\left(-i\pi m_1m_2\frac{q}{p}\right) \\ \exp(-i2\pi k_1\lfloor k_2+m_2/p\rfloor)\exp\left\{i2\pi(k_2p+m_2)\frac{q}{p}m_1\right\}, \end{aligned} \tag{8.25}$$

so that momentum is conserved up to multiples of $\mathbf{G}_2$. The orbit consists of p momenta $\mathbf{k}$, $\mathbf{k}+\mathbf{G}_2$, …, $\mathbf{k}+(p-1)\mathbf{G}_2$, which need to be kept in the calculation. In total, therefore, at flux p/q per unit cell, at a given momentum keeping N_{LL} Landau levels, we obtain a matrix of dimension $2\cdot N_{LL}\cdot p$, where 2 is the number of layers.

We emphasize that our approach is completely independent of the electromagnetic gauge chosen. Going beyond Ref. [249], which also works in a gauge-free manner, we obtain the matrix element [Eq. (8.25)] in closed form in a much simpler fashion, owing to the advantageous basis construction of Eq. (8.19). We note that for small fluxes, as well as for fluxes close to simple fractions, the hybrid Wannier function approach of [234, 250] can be used to improve performance.

8.2 Twisted WSe_2 in a magnetic field: tight binding regime

Our first main result, the magnetic field dependent energy spectrum for the continuum model of WSe_2 at a twist angle $\theta = 1°$, is shown in Fig. 8.2a, focusing on the two topmost detached bands. It has been argued that the spectrum at zero flux is well reproduced by the Haldane model [55, 68],

Figure 8.2a shows that the *point of net zero flux* ($\Phi = -1$) plays a special role. First, the net effective magnetic field vanishes on average at $\Phi = -1$. This is reflected in the fact that the spectrum attains its global maximum at this point. Second, due to the absence of an average magnetic field, the spectrum at this point can be modelled by a Haldane model in its originally envisaged form [242]. The Haldane model emerges in the adiabatic approximation from orbitals forming a hexagonal lattice localized in the AB and BA regions of the unit cell (Fig. 8.1b), with hopping phases arising due to the remnant inhomogeneous part of the effective magnetic field. By fitting the two topmost bands with Chern number sequence $(1,-1)$, we obtain a Haldane model with nearest-neighbor hopping $t_1 = 0.75\,\mathrm{meV}$ and next-nearest-neighbor hopping $|t_2| = 0.045\,\mathrm{meV}$ with phase $\phi^{TB} \approx -40°$, where $t_2 = -e^{i\phi^{TB}}|t_2|$.

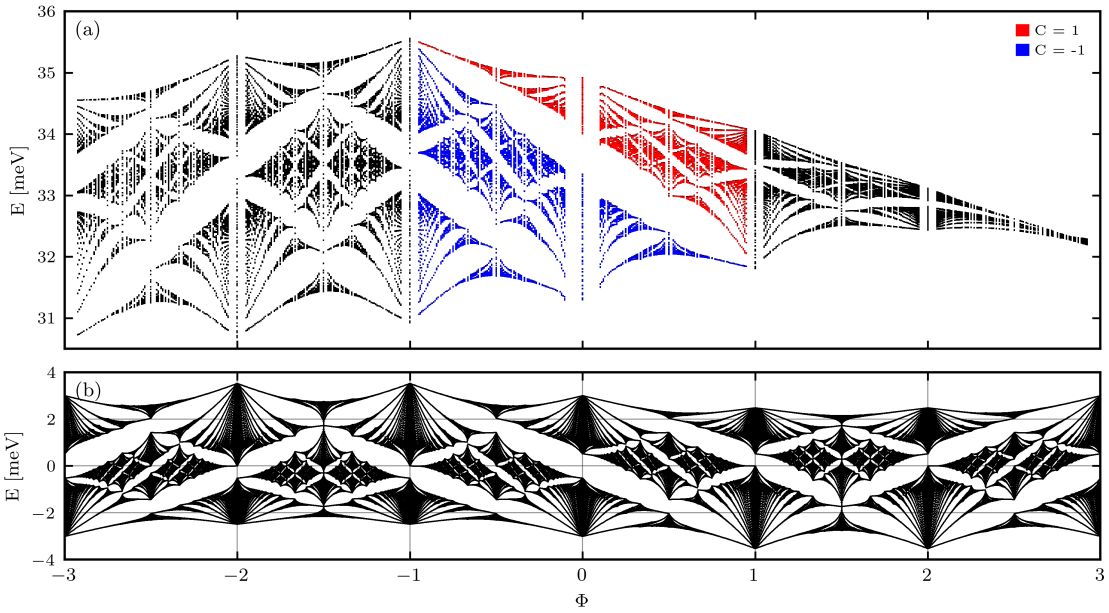

Figure 8.2: (a) Energy level diagram for twisted bilayer WSe_2 vs. applied magnetic field at twist angle $\theta = 1°$. The topmost $C = 1$ band is highlighted in red and the second topmost $C = -1$ band in blue. (b) Energy level diagram for the topological Haldane model with next-nearest-hopping phase $\phi^{TB} = -\pi/6$ at $\Phi = -1$.

Longer range hoppings decay quickly and have little effect on the band structure at this twist angle.

In the Haldane model, Peierls substitution implies that the next-nearest-neighbor hopping phase ϕ^{TB} changes as $\phi^{TB} \to \phi^{TB} - 2\pi/6$ as an additional flux quantum is threaded, $\Phi \to \Phi + 1$. Topological phase transitions occur at $\phi^{TB} = 0, \pi$. For our $\Phi = -1$ fit, this line of reasoning would suggest the Chern number sequence to remain $(1, -1)$ for $\Phi = -1, 0, 1$ and switch to $(-1, 1)$ for $\Phi = -3, -2, 2$, which agrees with the full continuum-model calculation. We caution, however, that while the topology agrees with the prediction of the Peierls substitution, the actual best-fit tight binding phases do not follow the predictions of the Peierls substitution, except between $\Phi = -1$ and $\Phi = -2$. This breakdown of the Peierls substitution was highlighted in Ref. [251] in the context of cold atoms. Nevertheless, we find that the magnetic field dependent energy spectrum of a tight-binding Haldane model [243], shown in Fig. 8.2b, exhibits a striking qualitative resemblance to Fig. 8.2a.

The behavior between integer fluxes can be understood using the Středa formula [252]

$$\frac{d\nu}{d\Phi} = C, \tag{8.26}$$

which relates Chern number C to the change in the number of states per unit cell ν inside a band upon varying flux Φ. We illustrate the Středa formula by tracking the two bands at zero

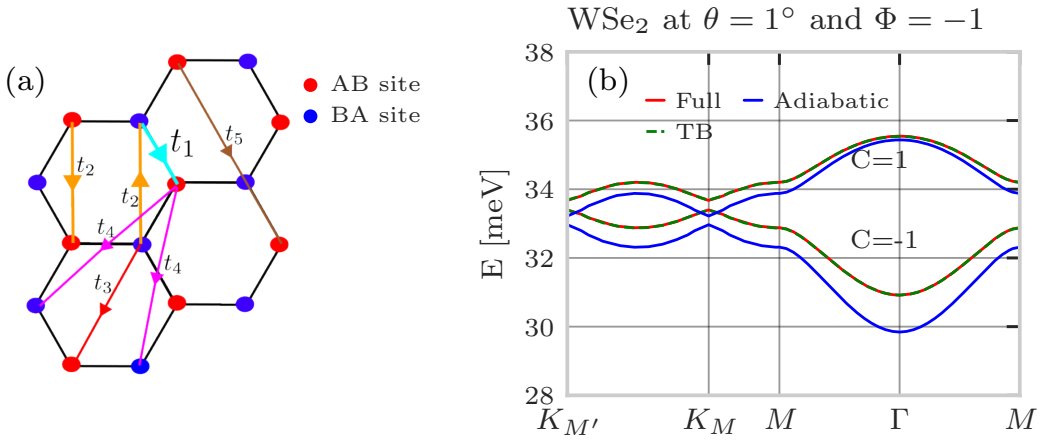

Figure 8.3: (a) Scheme of the hexagonal lattice model used to fit the two topmost bands of twisted bilayer WSe_2 at the *point of net zero flux* ($\Phi = -1$), showing the hoppings t_1, t_2, t_3, t_4, t_5. (b) Two topmost bands of twisted bilayer WSe_2 at twist angle $\theta = 1°$ and flux $\Phi = -1$. Full band structure is shown in red, adiabatic approximation in blue, and a tight-binding fit to the full band structure in dashed green.

flux, highlighting the $C = 1$ band in red and the second highest $C = -1$ band in blue in Fig. 8.2a. At $\Phi = 1$, the top $C = 1$ band expands to $\nu = 2$, whereas the bottom $C = -1$ band goes extinct, necessitating a gap closing since the two bands are detached [253]. The situation is reversed at $\Phi = -1$, where the $C = -1$ band expands to $\nu = 2$, while the $C = 1$ band disappears, forcing a gap closing. The energy level diagram also shows that the Chern bands at zero flux in fact emerge as lowest Landau levels from parabolic band edges, as can be clearly seen near flux $\Phi = 1$ for the $C = -1$ band (blue) and near flux $\Phi = -1$ for the $C = 1$ band (red).

Another interesting region is between fluxes $\Phi = -1$ and $\Phi = -2$, since the Chern number sequence is opposite at these two fluxes. This leads to tension at flux $\Phi = -3/2$ at which the bottom $C = 1$ band emerging from $\Phi = -2$ collides with the $C = -1$ band emerging from $\Phi = -1$. More precisely, the Středa formula predicts the bottom bands at both $\Phi = -2$ and $\Phi = -1$, with opposite Chern numbers, to expand to $\nu = 3/2$ states per unit cell. This necessitates a gap closing. In the continuum model, the gap emerging from $\Phi = -1$ is closing at $\Phi = -3/2$. In the Haldane model, we used a symmetric value of $\phi^{TB} = -\pi/6$ at $\Phi = -1$, leading to the simultaneous closing of the gaps arising from both $\Phi = -2$ and $\Phi = -1$, cf. Fig. 8.2b.

Remarkably, while at small twist angles, a Haldane description is possible at any applied flux, at the *point of net zero flux* ($\Phi = -1$), this description remains valid for an extended range of twist angles. Longer-range hoppings become necessary to fit the topmost two bands of the adiabatic band structures, but the character of a hexagonal lattice remains as does the topological character of the Haldane model. In contrast, at zero flux $\Phi = 0$, the emergent magnetic field induces a topological phase transition after which the bands develop a topology incompatible with a two-band model [246], resulting in two bands of equal Chern number.

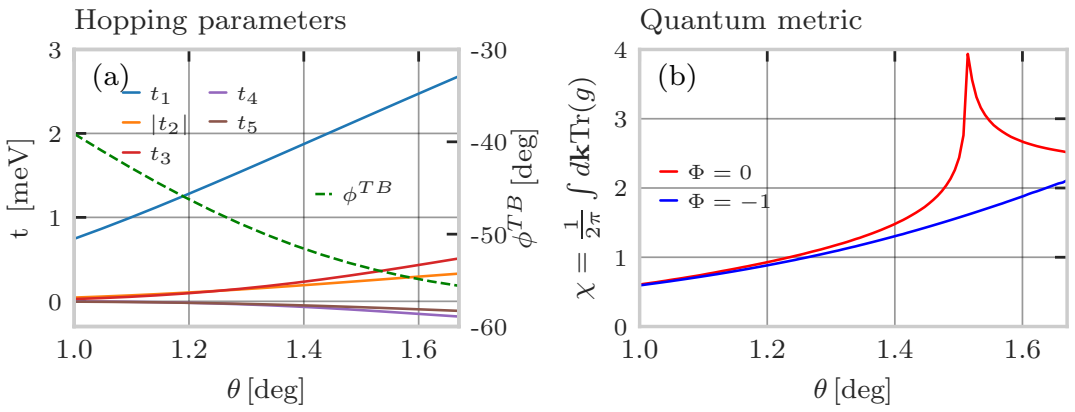

Figure 8.4: (a) Left axis: Twist angle dependence of the hoppings obtained from the tight-binding fit to the topmost two bands at flux $\Phi = -1$. Right axis: Phase of next-nearest hopping $\phi^{TB} = \arg(-t_2)$. (b) $\chi = \frac{1}{2\pi}\int d\mathbf{k}\mathrm{Tr}(g)$, the integrated trace of the quantum metric of the topmost two bands at flux $\Phi = -1$ (blue) and $\Phi = 0$ (red).

To illustrate this point, we fit the band structure at *net zero flux* ($\Phi = -1$) using a hexagonal tight-binding model, illustrated in Fig. 8.3a, retaining up to fifth-nearest-neighbor hoppings. We present the fit at $\theta = 1^\circ$ in Fig. 8.3b, with the full continuum bands shown in red and the tight-binding fit depicted in dashed green. We also show the adiabatic band structure in blue, confirming that at this twist angle, the adiabatic approximation is well within its regime of validity. In Fig. 8.4a, we plot the hoppings obtained by fitting the bands to the tight-binding model, showing the increase in hopping integrals with twist angle. Nevertheless, the model remains relatively short-range. In contrast, at zero flux, $\Phi = 0$, the two-band tight binding description becomes invalid at $\theta \approx 1.5^\circ$ [68, 246]. This sharp difference in locality between $\Phi = -1$ and $\Phi = 0$ is further brought out by looking at the integrated trace of the quantum metric $\chi = \frac{1}{2\pi}\int d\mathbf{k}\mathrm{Tr}(g)$ of the two topmost bands, shown in Fig. 8.4b. The average quantum metric measures the localization of wavefunctions [254] and shows that for larger twist angles, the two topmost bands are more localized at *net zero flux* ($\Phi = -1$) than at $\Phi = 0$. In fact, at $\Phi = 0$, upon crossing the topological phase transition, χ diverges logarithmically [255, 256].

8.3 Larger twist angles: towards nearly free electrons

The Hofstadter spectrum at a larger twist angle of $\theta = 1.67^\circ$ (see Fig. 8.5a) differs dramatically from the one at $\theta = 1^\circ$ in Fig. 8.2a. The two topmost bands at zero flux now have the same Chern number $C = 1$ (cf. Fig. 8.1d), so that the Středa formula, Eq. (8.26), predicts their filling ν to vary in the same way. Both disappear at $\Phi = -1$ and the topmost band (shown in red) expands to two states per unit cell at flux $\Phi = 1$ without any enforced gap closing as in the tight-binding regime discussed above.

We now focus on *net zero flux* ($\Phi = -1$), from which the zero-flux Chern bands emerge. We plot the band structure (red) in Fig. 8.5b, together with the adiabatic approximation bands (blue). The adiabatic approximation becomes less accurate for increasing twist angle [202]. However, it still captures essential features of the full band structure at $\theta = 1.67°$. For increasing twist angle, the electrons can escape the potential traps formed by the adiabatic potential $\tilde{V}(\mathbf{r})$ and the kinetic energy term in Eq. (8.1) becomes the dominant energy scale. As a result, the adiabatic band structure becomes describable in the nearly-free electron (weak periodic potential) approach. Indeed, the adiabatic bands (blue) are close to the backfolded bare kinetic energy $-\frac{\hbar^2\mathbf{k}^2}{2m^*}$ (dashed green in Fig. 8.5b), with degeneracies lifted by the periodic potential and the remnant effective magnetic field.

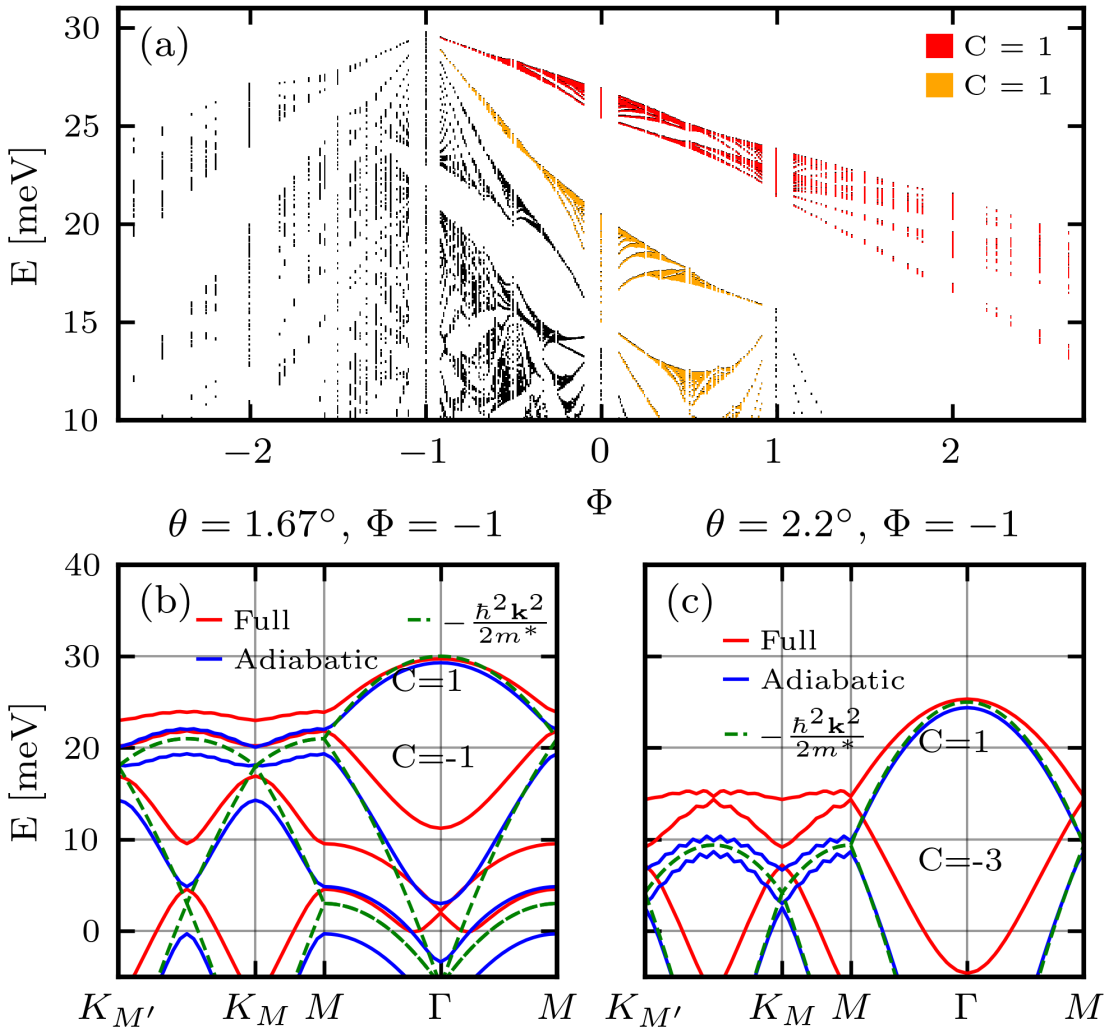

Figure 8.5: (a) Energy level diagram as a function of an applied magnetic field for twisted bilayer WSe_2 at twist angle $\theta = 1.67°$, showing the topmost $C = 1$ band in red and second topmost $C = 1$ band in orange. (b) Band structure at $\theta = 1.67°$ and flux $\Phi = -1$. The full band structure is shown in red, adiabatic in blue, and a backfolded free electron dispersion in dashed green. Note that the topmost branch of the backfolded free electron bands are doubly degenerate along the $K_{M'} - K_M - M$ line in the Brillouin zone, cf. the discussion in Appendix B.1. (c) Same as (b), but at $\theta = 2.2°$.

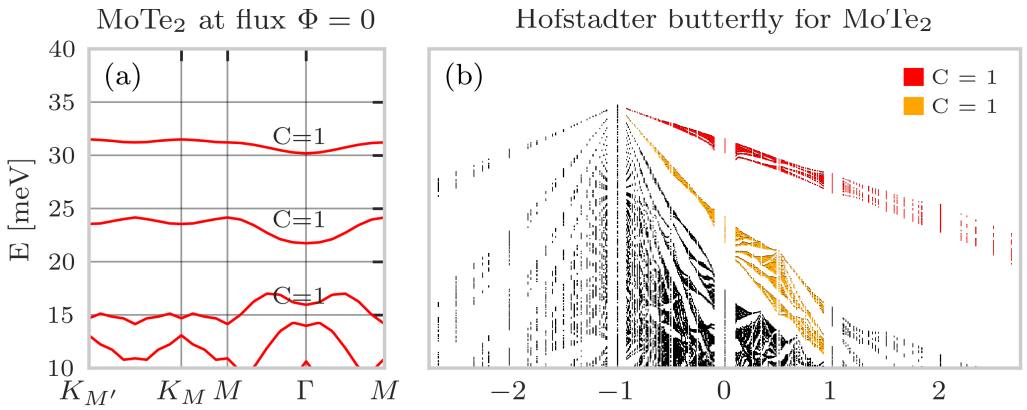

Figure 8.6: (a) Zero field band structure for a realistic model of twisted bilayer $MoTe_2$ at twist angle $\theta = 2.1°$. We include second harmonic terms following [212, 216]. (b) Energy spectra as a function of magnetic field for the same system, highlighting the topmost $C = 1$ band in red and second topmost $C = 1$ band in orange. (c) Band structure at $\Phi = -1$ (red) and backfolded free parabolic bands of the underlying $MoTe_2$ (dotted green), shifted by a constant in energy. Note that the topmost branch of the backfolded free electron bands are doubly degenerate along the $K_{M'} - K_M - M$ line in the Brillouin zone, cf. the discussion in Appendix B.1.

Like in the tight-binding regime, the Chern bands at $\Phi = 0$ emerge as Landau levels from the parabolic band maximum at $\Phi = -1$. However, as understood above, at $\Phi = -1$, the band structure in fact resembles backfolded free-electron bands, valid up to a filling of $\nu = 1$ electron per unit cell. This provides enough states for the zeroth Landau level to persist to zero flux, $\Phi = 0$, and create a band suitable for fractional quantum Hall liquids. For the second Chern band, on the other hand, the deviations of the $\Phi = -1$ band structure from pure parabolic lead to a notable dispersion at $\Phi = 0$.

To connect the present discussion to that of Section 8.2, we use the nearly-free electron picture to confirm that the Haldane-like topology of the topmost two bands at flux $\Phi = -1$ remains stable up to large twist angles. In App. B.2, we obtain the topology of the topmost bands using symmetry indicators [257] in the adiabatic picture. We find that the Haldane sequence of Chern numbers $(+1, -1)$ is remarkably robust, persisting up to $\theta \approx 1.96°$. At this twist angle, there is a band crossing of the second and third bands at the K_M and $K_{M'}$ points, which changes the Chern number of the second band to $C = -3$. We find that in the full continuum model, this topological phase transition occurs at $\theta \approx 2.02°$, in surprisingly good agreement given the worsening of the adiabatic approximation for increasing twist angles. We show the bands in the $(+1, -3)$ regime in Fig. 8.5c for a twist angle of $\theta = 2.2°$, exhibiting strong deviations between the full (red) and the adiabatic bands (blue).

8.4 Twisted $MoTe_2$ at $\theta = 2.1°$: emergent nearly free electrons at flux $\Phi = -1$.

Very recently, twisted bilayer $MoTe_2$ has been argued to host first Landau level analogs with non-Abelian states [65, 212–216]. At $\theta = 2.1°$, density functional theory [212, 216] predicts the three topmost bands to have the same Chern number, with the two top bands well detached from the remainder of the spectrum, see Fig. 8.6a for a continuum band structure. In order to fit the ab initio band structure, second-harmonic terms need to be included [212, 215, 216], see Sec. 8.1 for details. The energy level diagram as a function of magnetic field, shown in Fig. 8.6b, is qualitatively similar to that of WSe_2 at larger twist angles (cf. Fig. 8.5a), with the two topmost Chern bands (highlighted in red and orange) clearly emerging from flux $\Phi = -1$. Importantly, the second Chern band (shown in orange) is clearly detached for $MoTe_2$.

As for WSe_2, we can obtain insight into the origin of these topological bands by studying the $\Phi = -1$ band structure. As shown in red in Fig. 8.7, the band structure exhibits a distinct non-degenerate parabolic band maximum. Remarkably, a comparison to the bare TMD dispersion $-\frac{\hbar^2\mathbf{k}^2}{2m^*}$ (dashed green lines) reveals a striking similarity with the full band structure for the two topmost bands. Note that the double degeneracy of the topmost branch of the free-electron bands along the $K_{M'} - K_M - M$ path in the Brillouin zone is lifted in the full band structure.

Since the bands at flux $\Phi = -1$ are almost parabolic up to a filling of $\nu = 2$, we expect at least two Landau-level-like bands when adding one flux quantum per unit cell. This is in agreement with recent arguments for the band structure at zero applied flux [212]. We note that due to the rapidly varying potential profile, the adiabatic approximation breaks down for this model. Nevertheless, the bands at *net zero flux* ($\Phi = -1$) remain describable within the nearly free electron model similar to Eq. (8.1). It is this feature of the $\Phi = -1$ band structure that implies that the two topmost bands at zero flux ($\Phi = 0$) can be understood as the two lowest Landau levels of a nearly free electron system. As a consequence, many remarkable phenomena associated with the fractional quantum Hall effect are likely to carry over.

The most important difference from the fractional quantum Hall effect is the presence of a time-reversed partner in the K'-valley. This allows the possibility of time-reversal-symmetry preserving topological order, which has recently been proposed [65].

We comment on Ref. [214], which used the adiabatic approximation bands for a model without higher harmonics to argue for first-Landau level physics. As we have seen, the adiabatic approximation for larger twist angles naturally predicts Landau levels, as the $\Phi = -1$ band structure becomes nearly free. However, the approximation itself breaks down for these large twist angles. We have shown however, without invoking the adiabatic approximation, that a realistic model of $MoTe_2$ leads to nearly free bands at $\Phi = -1$.

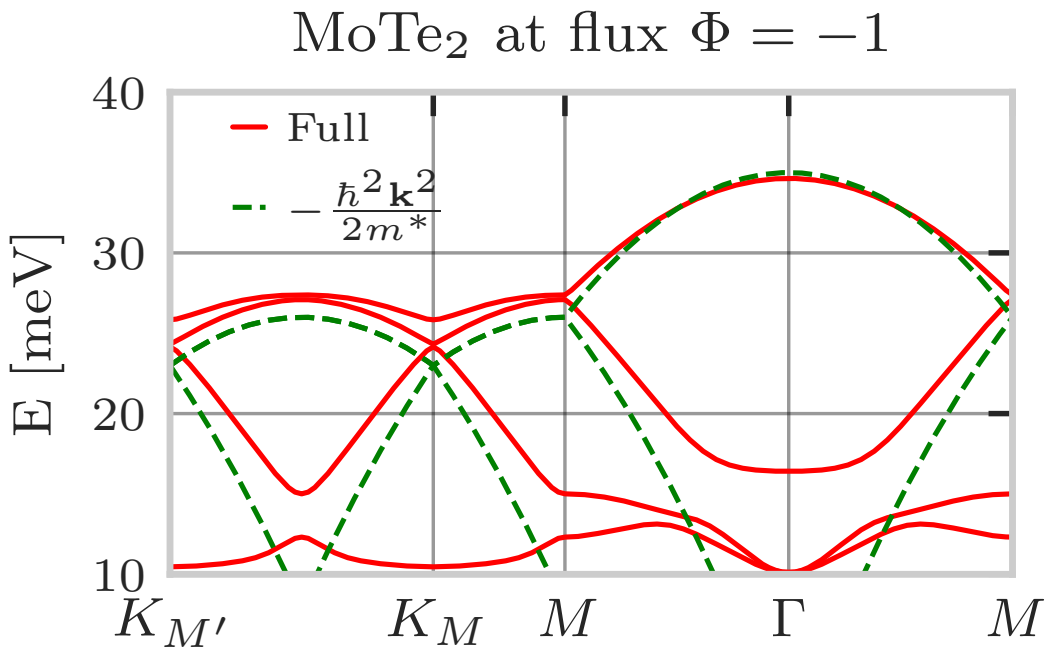

Figure 8.7: Band structure of twisted bilayer $MoTe_2$ at $\Phi = -1$ (red), and backfolded free parabolic bands of the underlying $MoTe_2$ (dotted green), shifted by a constant in energy. Note that the topmost branch of the backfolded free electron bands are doubly degenerate along the $K_{M'} - K_M - M$ line in the Brillouin zone, cf. the discussion in Appendix B.1.

8.5 Discussion

In summary, we studied twisted transition metal dichalcogenide bilayers in an out-of-plane magnetic field. We first studied a minimal model of twisted WSe_2 in the localized, Haldane regime, in which the magnetic field spectra qualitatively match those of the Haldane model in a magnetic field. We showed that compared to the zero flux case, the bands at the *point of net zero flux* ($\Phi = -1$) admit a Haldane description for an extended range of twist angles. The zero flux $C = 1$ bands emerge as Landau levels from the bands at negative unit flux quantum per unit cell ($\Phi = -1$). At larger twist angles, the bands at $\Phi = -1$ resemble electrons in a weak periodic potential, a fact naturally explained in the adiabatic approximation.

For a realistic model of $MoTe_2$, we found that the bands at $\Phi = -1$ are essentially obtained by backfolding a parabolic dispersion, giving a clear physical picture for the second topmost band at zero flux as the first Landau level of this dispersion. This finding is of immediate relevance for the study of fractionalized states, as it provides a simple picture for the zeroth and first Landau level nature of the bands at $\Phi = 0$. This allows the phenomenology from the fractional quantum Hall effect to be translated into the present context, with the crucial enrichment that

in TMDs, there are two time-reversed copies, rendering the fractional quantum spin Hall effect a possibility [65].

For half filled TMD bands, experiment suggests an interpretation in terms of a composite Fermi liquid [61]. In fact, to lowest order, the mean-field band structure of composite fermions at half filling is precisely the $\Phi = -1$ band structure. Thus, our results imply that they have a strongly dispersive nature, which is a necessary condition for a composite fermion liquid to occur [258–262].

We now comment on the experimental relevance of our findings. In actual samples both, the K and K' valleys coexist and doped holes distribute among them by optimizing the single particle and interaction energies. At finite applied flux, the single particle spectra of the two valleys differ drastically – the energy levels in the K'-valley at flux Φ are the same as the energy levels in the K-valley at flux $-\Phi$. While immaterial for and hence not included in our single-valley calculations, Zeeman splitting is significant when considering both valleys of TMDs [263], giving an additional energy splitting between the valleys at finite magnetic field. Thus, the precise way holes distribute among the two valleys is a subtle interplay of orbital, Zeeman, and interaction effects [234]. In the small twist angle regime with valley polarization, the Haldane-like Hofstadter spectrum should be observable in magnetotransport, with Landau fans emerging from integer applied fluxes. A tantalizing possibility would be the observation of the topological phase transition between fluxes $\Phi = -1$ and $\Phi = -2$ per unit cell, at which two Landau fans collide. For larger twist angle WSe_2 and $MoTe_2$ at $\theta = 2.1°$, we recover a parabolic dispersion in the K-valley at flux $\Phi = -1$ coexisting with a flat detached $C = 1$ band in valley K'. The reentrant free electron band of valley K should be observable when the chemical potential is inside a gap for valley K'.

Our study paves the way to analyze arbitrary Chern bands and establish their connection to Landau levels by studying the Hofstadter spectra. For $C = \pm 1$ bands, one has to trace their evolution between $\Phi = -1$ and $\Phi = 0$. Provided the band of interest can be traced all the way to $\Phi = -1$, the way it emerges from the band structure at $\Phi = -1$ allows it to be identified as a Landau level. The ideality of this level at $\Phi = 0$ can be obtained from the similarity of the $\Phi = -1$ band structure with an elementary band structure, such as a Dirac cone or parabolic free electron band. This provides a powerful complement to analytical approaches [204, 205, 207, 208].

As an interesting application, let us compare TMD band structures with those of twisted bilayer graphene in the chiral limit. For a given spin and valley flavor, there are two sublattice polarized zero-energy bands with opposite Chern numbers, a $C = 1$ band on the A-sublattice and a $C = -1$ band on the B-sublattice. Thus, at $\Phi = 1$, the A-sublattice band gains one state per unit cell, while the B-sublattice band disappears. Particle-hole symmetry necessitates this vanishing of the $C = -1$ band to be accompanied by a gap closing with the remote bands [227, 264, 265]. This enforces a Dirac cone in the band structure at $\Phi = 1$. For fluxes $\Phi < 1$, the B-sublattice band emerges as the zeroth Landau level of this Dirac cone. For $\Phi > 1$, there is a Chern number $C = 1$, A-sublattice polarized zeroth Landau level, so that the zero-energy

bands have a total Chern number of $C = 2$ with $\nu = 2\Phi$ states per unit cell, similar to the Landau level spectrum in the absence of a moiré tunneling term. The particle-hole symmetry and the ensuing emergence of the low-lying Chern bands from a Dirac cone explain why no analogs of higher Landau levels for a quadratic dispersion are present in twisted bilayer graphene. In contrast, for twisted TMDs, particle-hole symmetry is absent, allowing for a parabolic band extremum and enabling higher Landau levels to emanate from it.

Conclusions

This thesis has explored the diverse world of layered materials, with a particular focus on moiré systems and their emergent phenomena. The author hopes that by now the reader will be convinced of the fascinating richness of this field.

This thesis started with introducing moiré models in Chapter 2, which are derived based on only few underlying principles. Yet, most of the essential physics of moiré systems is already contained at this simple level of description. For twisted transition metal dichalcogenides, it is the physics of flat Chern bands, which emerge as a result of a skyrmionic real-space layer-pseudospin texture. For twisted bilayer graphene, it is the physics of magic angles, arising from interference between interlayer tunneling and kinetic terms, wherein the bandwidth abruptly drops at the special twist angle of $\theta = 1.1°$. An interesting extension was to add more layers, forming a structure with alternating twist angles, which obtains flat bands at larger physical twist angles.

The next Chapter 3 showed how scanning tunneling microscopy could reveal signatures of exciton-induced interband coherence in monolayer and bilayer TMDs, opening a pathway to experimentally observe these elusive quantum states. Studying exciton condensates accurately using surface probes such as scanning tunneling microscopy was only made possible by the layered nature of the materials, harnessing the fruits of the revolution that has been underway for the last twenty years.

This thesis then transitioned in Chapter 4 to study the interplay between disorder and the Kramers intervalley coherent state in twisted bilayer graphene. This study is particularly pressing, as disorder is ubiquitous in moiré devices. By deriving an Anderson theorem for this state, we provided insights into the robustness of the Kramers intervalley coherent state against disorder, drawing a parallel to s-wave superconductors.

Expanding to larger numbers of layers, in Chapter 5, we explored the emergent effects that arise for alternating twist arrangements when more layers are added. The crucial insight was that for larger number of layers, the three-dimensional nature of the material dominates the electronic properties. Importantly, it was found that three-dimensionality is important already for $N = 5$ layers, shaping the experimental phase diagram.

The next Chapter 6 explored the effects of three-dimensionality for another class of systems, including twisted double bilayer graphene and rhombohedral pentalayer graphene. It uncovered the remarkable underlying physics of the experimentally observed diagonal features in the filling-displacement field plane, achieving so by linking these phenomena to the local Bernal stacking common to these systems.

In the next Chapter 7, we studied multi-component moiré wavefunctions in real space, with applications to twisted graphene devices and to twisted bilayer transition metal dichalcogenides. Multi-component wavefunctions allow an integer real-space Chern number to be defined. Our main finding was that this real-space Chern number generically vanishes, being nonzero in fine-tuned, but important, examples.

Finally, in Chapter 8, we uncovered the rich structure of twisted transition metal dichalcogenides under applied magnetic fields. Here again, two dimensional materials are of particular interest, since electrons in a magnetic field are confined to a single plane. In one dimension, the magnetic field is only a boundary condition, while in three dimensional materials, the third (out-of-plane) direction only adds an unnecessary complication. Twisted bilayers greatly enhance the material unit cell, allowing the strong-field regime to be probed.

This thesis illustrates the profound richness of moiré systems, demonstrating their capacity to provide a fascinating arena to explore fundamental physics.

Acknowledgments

Firstly, I acknowledge the generous support of the CRC183 collaboration, as well as the opportunity to attend the numerous CRC183-funded events and interact with members of institutes at Cologne, Copenhagen, and Rehovot.

I thank my supervisor, Felix von Oppen, for the great freedom that I enjoyed during my PhD. I also thank Felix for teaching me not to settle, and to always try to understand.

I thank my collaborators Kang Yang, Cyprian Lewandowski, Christophe Mora, Gal Shavit, Yuval Oreg, Dacen Waters, Matt Yankowitz, Josh Folk, Stevan Nadj-Perge, Yuval Oreg, Zekang Zhou, Kenji Watanabe, Takashi Taniguchi, and Mitali Banerjee.

I thank my dear colleagues in Trakt 4 for their company.

I thank everyone else.

Appendix A

A.1 Properties of the single-particle TNG Hamiltonian

A.1.1 Twist angle dependence of the in-plane charge inhomogeneity

In Fig. A.1, we plot the dependence of the average wavefunction overlap

$$\overline{\langle u_{\mathbf{k}+\mathbf{G},f,\alpha}|u_{\mathbf{k},f,\alpha}\rangle} = \frac{1}{N_{\mathbf{k}}}\frac{1}{N_{\mathbf{G}}}\sum_{\mathbf{k},\mathbf{G}}\frac{1}{2}\sum_{\alpha=1,2}|\langle u_{\mathbf{k}+\mathbf{G},f,\alpha}|u_{\mathbf{k},f,\alpha}\rangle| \tag{A.1}$$

on twist angle for $N = 2$ (this result applies to any TBG-like sector) for the two central flat bands. Here the sum over $\mathbf{G}$ runs over the $N_{\mathbf{G}} = 6$ shortest nonzero reciprocal lattice vectors and $\mathbf{k}$ are in the first Brillouin zone, with $N_{\mathbf{k}} = 144$ the number of $\mathbf{k}$ points in the numerical calculation grid. This average overlap increases with decreasing twist angle. Its meaning can be understood from Eq. (5.24). The larger the wavevector $\mathbf{G}$ overlap, the more strongly a sector couples to the in-plane inhomogeneity at wavevector $-\mathbf{G}$. Conversely, sectors with a larger overlap at wavevector $\mathbf{G}$ generate a larger mean-field inhomogeneity at $-\mathbf{G}$. This implies that for $k_{\text{magic}} = 1$, the magic sector feels the in-plane potential most strongly and is most effective at generating it.

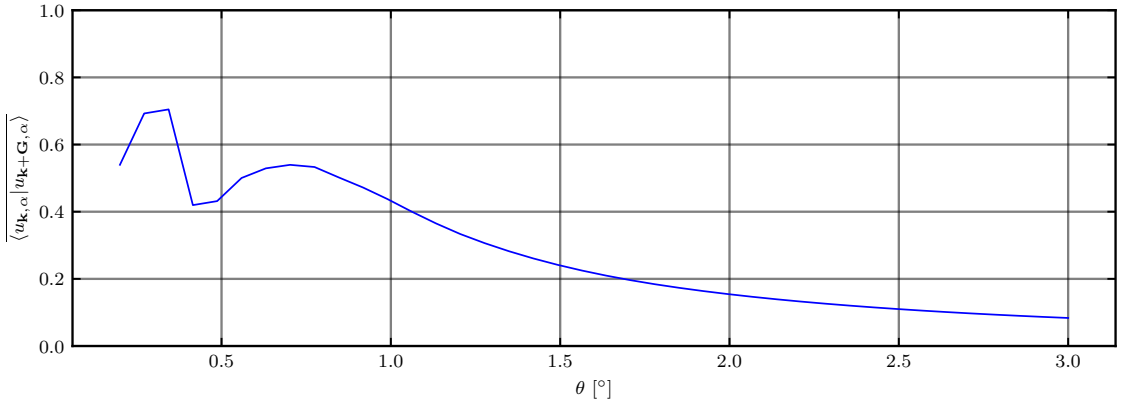

Figure A.1: Dependence of $\overline{\langle u_{\mathbf{k}+\mathbf{G},f,\alpha}|u_{\mathbf{k}},f,\alpha\rangle}$, a quantity that controls the in-plane Hartree correction, on twist angle for $N = 2$

A.1.2 Strain

In TBG, heterostrain drastically increases the single particle bandwidth [146], changes the nature of correlated states [110, 147], and can induce in-gap states, see Chapter 4. The procedure for implementing heterostrain in TBG involves adding vector potentials due to the changes in graphene hoppings and distorting the moiré Brillouin zone, altering the momentum space distance between the two layers of Dirac cones and the moiré reciprocal vectors. Since, for a bilayer, any layer-dependent strain can be decomposed as the sum of hetero and homostrain, and homostrain has negligible effect, including heterostrain in this way is a generic procedure that captures qualitative physical trends. In systems with more than two layers, there are more nongeneric layer dependencies possible. As the purpose of our modeling is to introduce a mechanism for broadening the single-particle bandwidth, we consider a simple procedure and only add the vector potentials induced by the graphene hoppings, choosing an antisymmetric layer structure:

$$\mathbf{A}_l = (-1)^l \mathbf{A}_0, \tag{A.2}$$

where the single-layer vector potential is given by

$$\mathbf{A}_0 = \frac{\sqrt{3}}{2a}\beta(\epsilon_{xx} - \epsilon_{yy}, -2\epsilon_{xy}), \tag{A.3}$$

with a being the monolayer graphene lattice constant and $\beta \approx 3.12$ the hopping modulus factor [146]. We choose $\epsilon_{xx} = \epsilon_{\text{strain}}, \epsilon_{xy} = 0$ and $\epsilon_{yy} = -0.16 \cdot \epsilon_{\text{strain}}$ (0.16 is the Poisson ratio for graphene), varying ϵ_{strain} from 0 to $0.2 \cdot 10^{-2}$. This layer structure is motivated by the fact that it acts just like a heterostrain vector the potential within each bilayer-like sector at zero displacement field. The above-defined vector potentials couple via minimal coupling to the momentum operator [146].

A.1.3 Density of states for nonmagic sectors in the Dirac cone approximation

In this Section, we evaluate the numerical constants that appear in the expression for density of states (DOS) for a Dirac cone dispersion to obtain estimates for the DOS of the nonmagic sectors, as used in Section II of the main text. To this end, let us evaluate the prefactor of Eq. (5.2) with v_D instead of $v_D^{(k)}$:

$$\frac{A_{\text{uc}}}{4\pi(\hbar v_D)^2} = \frac{\sqrt{3}(0.246\text{nm})^2/(8\sin^2(\theta/2))}{4\pi(6.582 \cdot 10^{-16}\text{eVs} \cdot 10^6 \text{ms}^{-1})^2} = 31.6/\theta^2 \text{eV}^{-2}, \tag{A.4}$$

where in the last equality, the twist angle θ should be expressed in degrees. For the $k = 2$ nonmagic sector in TPG, we have $N_f = 4$, $c_{k=2} = 2$,$\theta = 1.9°$, $v_D^{(k=2)} = 0.35 v_D$. We note in passing that Ref. [19] finds a smaller Dirac velocity. This is because here we account for lattice

corrugation by taking $w_{AA}/w_{AB} = \frac{8}{11}$, while in Ref. [19] the unrelaxed value, $w_{AA}/w_{AB} = 1$, is taken. Plugging into Eq. (A.4), we obtain

$$\nu_{k=2}^{TPG} = (5.71 \cdot 10^{-4}\mathrm{meV}^{-2})\mu_2^2. \tag{A.5}$$

As an example, for $\mu_2 = 10\mathrm{meV}$, using Eq. (5.2) we obtain filling $\nu_2 \lesssim 0.06$. As noted in the main text, for $\nu_2 \gtrsim 0.5$, we use the numerically computed full non-interacting density of states which involves a DOS peak at the van Hove singularity.

A.2 Mean-field decoupling of out-of-plane electric field term

Here we detail the mean-field decoupling the out-of-plane ($\mathbf{q} = 0$) term. For notational simplicity, we work out the general form before projecting onto a fixed number of active bands. We perform the mean-field decoupling of $\mathrm{H}_{\mathrm{int}}^{(\mathbf{q}=0)}$:

$$\mathrm{H}_{\mathrm{int}}^{(\mathbf{q}=0)} = -\frac{1}{2A}\sum_{L,J}\frac{e^2}{2\epsilon_\perp\epsilon_0}d_{LJ}\rho_{\mathbf{q}=0,L}\rho_{\mathbf{q}=0,J} \;= \sum_{l=1}^{N-1} A\epsilon_\perp\epsilon_0 d_l\frac{(E_{l,l+1}^\perp)^2}{2} + \text{ Const}\,, \tag{A.6}$$

which was derived assuming a fixed amount of charge on the gates, but still includes it explicitly (by summing I, J from 0 to $N+1$). We dropped the normal ordering symbol since it only matters for $I = J$, for which the vertical distance d_{IJ} vanishes. Let us recall the three constraints

- $\rho_{0,0} = -A\frac{n}{2}$
- $\rho_{0,N+1} = -A\frac{n}{2}$
- $\sum_{l=1}^{N}\rho_{0,l} = An$

For the mean-field decoupling, we use the $\mathbf{q} = 0$ layer density form of the interaction. Following standard procedures, there will be the Hartree term, which corresponds to classical electrostatics

$$\mathrm{H}_{\mathrm{layer}}^{\mathrm{Hartree}} = -\sum_{L\neq J}\frac{e^2}{2\epsilon_\perp\epsilon_0 A}d_{LJ}\rho_{\mathbf{q}=0,L}\langle\rho_{\mathbf{q}=0,J}\rangle = \sum_{l=1}^{N}\rho_{0,l}(-eV_l)\,, \tag{A.7}$$

where we changed sum over L (from 0 to $N+1$, including gates) to a sum over l (from 1 to N) since the gates have a fixed charge. Therefore, the potentials are given by

$$V_l = \frac{e}{2\epsilon_\perp\epsilon_0 A}\sum_{J=0}^{N+1} d_{lJ}\langle\rho_{\mathbf{q}=0,J}\rangle. \tag{A.8}$$

It is insightful to consider the potential difference between two neighboring layers

$$V_{l+1} - V_l = \frac{e}{2\epsilon_\perp \epsilon_0 A} \sum_J (d_{l+1,J} - d_{l,J}) \langle \rho_{\mathbf{q}=0,J} \rangle \,, \tag{A.9}$$

where

$$d_{l+1,J} - d_{l,J} = \begin{cases} d_l & \text{for } l \geq J \\ -d_l & \text{for } l < J. \end{cases} \tag{A.10}$$

With this relation, we can rewrite Eq. (A.9)

$$V_{l+1} - V_l = d_l \frac{e}{2\epsilon_\perp \epsilon_0 A} \left[\sum_{J \leq l} \langle \rho_{\mathbf{q}=0,J} \rangle - \sum_{J > l} \langle \rho_{\mathbf{q}=0,J} \rangle \right]. \tag{A.11}$$

Since $\rho_0 = \rho_{N+1} = -nA/2$, the gate charge terms cancel. Further, since the total charge on the sample is fixed, we also have

$$-\sum_{l<J\leq N} \langle \rho_{\mathbf{q}=0,J} \rangle = \sum_{1\leq J\leq l} \langle \rho_{\mathbf{q}=0,J} \rangle - nA. \tag{A.12}$$

which yields

$$V_{l+1} - V_l = d_l \frac{e}{\epsilon_0 \epsilon} \left\{ \frac{1}{A} \sum_{l'=1}^{l} \langle \hat{\rho}_{0,l'} \rangle - \frac{n}{2} \right\} = -d_l E^{\perp}_{l,l+1}. \tag{A.13}$$

In the above expression, we identified that the interlayer electric field is given by Gauss' law, Eq. (5.13).

Next we consider the $\mathbf{q} = 0$ Fock term. As the Fock term involves an integral over a range momenta and is intensive, if we fix a single momentum term $\mathbf{q} = 0$ (as we do for the interlayer potential term), it will vanish in the thermodynamic limit. Therefore we only need to keep the $\mathbf{q} = 0$ Hartree term. Finally, in our numerics, we project on a finite number of bands replacing $\rho_{l,0}$ by $\hat{\rho}_{l,0}$.

A.3 Analytical results on the layer potentials

A.3.1 Layer potentials in sector basis

In this Section, we consider the mean-field layer potential term, and rewrite it in the sector basis. We use the unprojected form of the layer Hamiltonian:

$$\mathrm{H}^{\text{unprojected}}_{\text{layer}} = \sum_l \rho_{0,l}(-eV_l), \tag{A.14}$$

but the conclusions will also hold after projection. To proceed, we need to write

$$\rho_{0,l} = \sum_{f,\mathbf{k},z} d^\dagger_{f,l,\mathbf{k},z} d_{f,l,\mathbf{k},z}, \tag{A.15}$$

where $d^\dagger_{f,l,\mathbf{k},z}$ creates an electron in flavor f, layer l, momentum $\mathbf{k}$ and a joint sublattice/spin index z. Since the transformation into sectors does not affect flavor, momentum, or sublattice and spin, we will in the following omit their labels. Using the sector decomposition we can go from layer basis to sector basis using the unitary basis transformation V_{TNG}, defined in Eq. (2.71) as follows:

$$f^\dagger_s = \sum_l d^\dagger_l (V_{\text{TNG}})_{ls}, \tag{A.16}$$

where $f^\dagger_s$, $s \in \{1, \dots, N\}$ creates an electron in the effective layer s, which can either have support in the odd physical layers or even. We therefore rewrite

$$\sum_l \rho_{l,0}(-eV_l) = \sum_{s,s'} f^\dagger_s f_{s'} \sum_l (V_{\text{TNG}})_{ls} (V_{\text{TNG}})_{ls'} (-eV_l). \tag{A.17}$$

To emphasize the sector (recall for N layers there are $\lceil N/2 \rceil$ sectors labeled by index k) diagonal and off-diagonal terms, we now switch s for a multi-index k, i, where $k \in \{1, \dots, \lceil N/2 \rceil\}$ labels the sector, and i labels the effective odd or even layer of that sector. For an MLG-like sector, this index is trivial. With this rewriting, we write suggestively

$$\begin{aligned}\sum_l \rho_{l,0}(-eV_l) = \sum_{k,i} f^\dagger_{k,i} f_{k,i} \sum_l (V_{\text{TNG}})_{l,ki} (V_{\text{TNG}})_{l,ki} (-eV_l) + \\ + \sum_{k \neq k',i} f^\dagger_{k,i} f_{k',i} \sum_l (V_{\text{TNG}})_{l,ki} (V_{\text{TNG}})_{l,k'i} (-eV_l),\end{aligned} \tag{A.18}$$

where we used the fact that $(V_{\text{TNG}})_{l,ki} (V_{\text{TNG}})_{l,k'i'} \propto \delta_{i,i'}$, so that there are no layer index (i, i') off-diagonal terms. On the other hand, odd and even layer index preserving terms are allowed.

Sector diagonal terms — In this Section, we focus on the sector diagonal terms, which correspond to the first term in the Equation (A.18). For a TBG-like sector k, this term is a potential

$$V_1 = \sum_l (V_{\text{TNG}})_{l,k1} (V_{\text{TNG}})_{l,k1} (-eV_l) \tag{A.19}$$

on the effective odd layer and

$$V_2 = \sum_l (V_{\text{TNG}})_{l,k2} (V_{\text{TNG}})_{l,k2} (-eV_l) \tag{A.20}$$

on the effective even layer. Decomposing the effective layer potential matrix $\begin{pmatrix} V_1 & 0 \\ 0 & V_2 \end{pmatrix}$ into layer-even and layer-odd components, we obtain that the effect of layer potentials within a sector is twofold. It causes a shift of the whole sector by $U^{(k)} = \frac{V_1+V_2}{2}$ and an interlayer potential difference $D_k = V_1 - V_2$ between the effective odd and even layers. We can obtain an analytical formula for the sector shift in terms of the matrix $(V_{\text{TNG}})_{l,ki}$ and therefore also in terms of the vectors $R^{(k)}$, $L^{(k)}$.

$$U^{(k)} = \frac{1}{2}\sum_{l,i}(V_{\text{TNG}})_{l,ki}(V_{\text{TNG}})_{l,ki}(-eV_l). \tag{A.21}$$

In the above, we identify

$$\frac{1}{2}\sum_{i}(V_{\text{TNG}})_{l,ki}(V_{\text{TNG}})_{l,ki} = W_l^{(k)} \tag{A.22}$$

as the layer distribution weights $W_l^{(k)}$, plotted in Figure 2.4. The final formula for the shift of the sector $U^{(k)}$ therefore reads:

$$U^{(k)} = \sum_{l} W_l^{(k)}(-eV_l). \tag{A.23}$$

The derivation of the interlayer potential difference proceeds analogously, so we only give the expression, which differs by an extra $(-1)^l$ in the sum over layers

$$D_k = 2\sum_{l}(-1)^l\, W_l^{(k)}(-eV_l). \tag{A.24}$$

This $(-1)^l$ leads to a cancellation when compared to $U^{(k)}$.

Sector off-diagonal terms — We now turn to the sector mixing terms, which correspond to the $k \neq k'$ term in Eq. (A.18). Given that the potential difference between layers can become quite sizeable for large filling, sector mixing will become important for large N. If sector mixing is small, one can directly relate the physics to the TBG physics. On the other hand, for large sector mixing, such direct mapping is no longer possible, and the bands become rather different from bare TBG-like bands. However, these bands may still favor superconductivity and strong correlation physics, as seen in TTG under a displacement field. One advantage arises for N odd. In that case, opposite mirror symmetry eigenvalues forbid mixing between adjacent sectors (k and $k+1$, say).

A.3.2 Evaluation of sector shifts

Given the layer structure of the sectors, we can obtain a mean-field layer Hartree shift $\Delta U^{(k)}$ analytically. We start with the layer distributions for sector k, obtained in Sec. 2.4 we obtain

the sector shift $U^{(k)}$ in terms of the weights $W_l^{(k)}$ and the layer potentials V_l. We obtain the layer potentials by using that a sector with filling ν_k has on average the following layer number density distribution

$$\langle \hat{\rho}_{0,l} \rangle = \frac{1}{A_{\mathrm{UC}}} W_l^{(k)} \nu_k. \tag{A.25}$$

Knowing this, and using Eq. (5.13) the electric field between two layers caused by sector filling ν_k (which causes an electron density $e\nu_k/(2A_{\mathrm{UC}})$ on the gates) becomes

$$E_{i,i+1}^{\perp} = -e \frac{-1/2 + \sum_{l=1}^{i} W_l^{(k)}}{A_{\mathrm{UC}} \epsilon_0 \epsilon_\perp} \nu_k. \tag{A.26}$$

Using the formula in Eq. (2.72), we evaluate the sum of the weights

$$\sum_{l=1}^{i} W_l^{(k)} = \frac{1}{N+1} \left[i + 1/2 - \frac{\sin[\pi k (2i+1)/(N+1)]}{2 \sin[\pi k/(N+1)]} \right]. \tag{A.27}$$

As a check, for $i = N$, we obtain $\sum_{l=1}^{N} W_l^{(k)} = 1$, while for N even, $i = N/2$, we get $\sum_{l=1}^{N} W_l^{(k)} = 1/2$, so that $E_{i,i+1} = 0$ in the middle spacing. Using that $V_{l+1} - V_l = -d_l E_{l,l+1}$, we can now integrate the electric field to calculate the electron energy shift $-eV_l^{(k)}$ in layer l due to the filling of sector k:

$$-eV_{l+1}^{(k)} = \nu_k \frac{e^2 d_l}{\epsilon_0 \epsilon_\perp} \left\{ l \cdot \left[\frac{N-l-1}{2(N+1)} \right] + \frac{\cos[2\pi k/(N+1)] - \cos[2\pi k (l+1)/(N+1)]}{4(N+1)\sin^2[\pi k/(N+1)]} \right\}. \tag{A.28}$$

We note that the maximal potential magnitude is in the middle of the sample, which is intuitive, given that charge of a single sign is being distributed across the layers.

Having obtained the layer shifts due to the filling of a single sector k, we can now add the contributions due to all the sectors and obtain $-eV_l$. Using this, we get the sector shifts $U^{(k)}$, and therefore also the numerical coefficients $\left(\frac{1}{C}\right)_{k,k'}$ giving the shifts of sectors in terms of the sector fillings

$$U^{(k)} = \sum_l W_l^{(k)} (-eV_l) \tag{A.29}$$

$$= \sum_{lk'} \frac{W_l^{(k)} \nu_{k'} e^2 d_l}{\epsilon_0 \epsilon_\perp} \left\{ l \left[\frac{N-l-1}{2(N+1)} \right] + \frac{\cos\left[\frac{2\pi k'}{N+1}\right] - \cos\left[\frac{2\pi k'(l+1)}{N+1}\right]}{4(N+1)\sin^2\left[\frac{\pi k'}{N+1}\right]} \right\}. \tag{A.30}$$

N	$\left(\frac{1}{C}\right)_{1,1}$	$\left(\frac{1}{C}\right)_{1,2} = \left(\frac{1}{C}\right)_{2,1}$	$\left(\frac{1}{C}\right)_{2,2}$
4	$2\phi^4/(2+2\phi^2)^2$	$2\phi^2/(2+2\phi^2)^2$	$2/(2+2\phi^2)^2$
5	$29/72$	$15/72$	$9/72$
$N \to \infty$	$N(1/12 + 5/(8\pi^2))$	$N(1/12 + 5/(16\pi^2))$	$N(1/12 + 5/(32\pi^2))$

Table A.1: Inverse capacitance $\left(\frac{1}{C}\right)_{k,k'}$ for $N = 4, 5$ layers and large N for $k, k' \in \{1, 2\}$ in expression form.

Recalling the definition of $\left(\frac{1}{C}\right)_{k,k'}$ from Equation (5.5), we can identify $\left(\frac{1}{C}\right)_{k,k'}$ as

$$\left(\frac{1}{C}\right)_{k,k'} = \sum_l W_l^{(k)} \left\{ l \cdot \left[\frac{N-l-1}{2(N+1)}\right] + \frac{\cos[2\pi k'/(N+1)] - \cos[2\pi k'(l+1)/(N+1)]}{4(N+1)\sin^2[\pi k'/(N+1)]} \right\}. \tag{A.31}$$

This equation is used to generate the Table 5.1 in the main text for $N = 4, 5$. At fixed k, k', but taking $N \to \infty$, we can obtain $\left(\frac{1}{C}\right)_{k,k'}$ analytically by going from a sum to an integral in Eq. (A.31). This immediately reveals a scaling with N. We get for the dominant $O(N)$ terms:

$$\left(\frac{1}{C}\right)_{k,k'} = N \int_0^1 dy \sin^2(\pi k y) \left\{ y(1-y) + \frac{1 - \cos(2\pi k' y)}{2\pi^2 (k')^2} \right\}. \tag{A.32}$$

Note that the integral over y depends only on k and k', with the entire N dependence factored out in the front. Evaluating this integral for $k, k' = 1, 2$, we obtain the large N entry in Table 5.1. In Table A.1, we give the results for $\left(\frac{1}{C}\right)_{k,k'}$ in expression form, rather than evaluated numerically as in the main text.

For reference, we evaluate the numerical constants:

$$\frac{e^2 d_l}{A_{uc}\epsilon_0} = \frac{e^2 \cdot 0.3\text{nm}}{\frac{\sqrt{3}\cdot 0.243^2}{2(\pi/180)^2\theta^2}\text{nm}^2 \cdot e^2 \cdot 55.263\,\text{keV}^{-1}\text{nm}^{-1}} = 32.34\theta^2_{\text{physical}}\text{meV}, \tag{A.33}$$

with θ in degrees and where we used vacuum permittivity $\epsilon_0 = 55.263\,\text{e}^2\text{keV}^{-1}\text{nm}^{-1}$ and interlayer distance $d_l = 0.3\text{nm}$. This yields

$$U^{(k)} = \left[32.34 \frac{\theta^2_{\text{physical}}}{\epsilon_\perp} \sum_{k'}^{n_o} \left(\frac{1}{C}\right)_{k,k'} \nu_{k'} \right] \text{meV}\,. \tag{A.34}$$

A.3.3 Application to TPG

For twisted pentalayer graphene, the weights of the $k = 1, 2, 3$ sectors are

$$W_l^{(k=1)} = \frac{1}{12}(1, 3, 4, 3, 1)_l \tag{A.35}$$

$$W_l^{(k=2)} = \frac{1}{4}(1, 1, 0, 1, 1)_l \tag{A.36}$$

$$W_l^{(k=3)} = \frac{1}{3}(1, 0, 1, 0, 1)_l. \tag{A.37}$$

Evaluating, using $\theta = 1.9°$, interlayer $\epsilon_\perp \in [2, 12]$, the nonmagic effective chemical potential increases by

$$U^{(1)} - U^{(2)} = 3.24/\epsilon_\perp \left[3\nu_2 + 7\nu_{\text{magic}}\right] \text{meV}. \tag{A.38}$$

Supposing that $\nu_{\text{magic}} = 4$, we obtain a range of $U^{(1)} - U^{(2)} \approx 7 - 45\,\text{meV}$ increase of the effective nonmagic sector chemical potential due to Hartree layer potentials.

We now consider effects of the layer potentials beyond simple sector shifts, which are:

- Intrasector potential difference, both for $k = 1$ and $k = 2$
- A term mixing $k = 1$ and $k = 3$ – magic and MLG-like, acting like an external displacement field in TTG

We can readily evaluate the magnitudes of all these terms assuming fixed sector filling using the results from the previous Section. We evaluate $-eV_l$ in terms of $\nu_1 = \nu_{\text{magic}}$ and ν_2:

$$-eV_l = \frac{e^2 d_l}{\epsilon_0 \epsilon_\perp A_{\text{UC}}} \left[\nu_2 \left(0, \frac{1}{4}, \frac{1}{4}, \frac{1}{4}, 0\right)_l + \nu_1 \left(0, \frac{5}{12}, \frac{7}{12}, \frac{5}{12}, 0\right)_l \right]. \tag{A.39}$$

With this in hand, we can evaluate:

$$D_1 = -\frac{e^2 d_l}{\epsilon_0 \epsilon_\perp A_{\text{UC}}} \left[\frac{1}{12}\nu_2 + \frac{1}{36}\nu_1 \right], \tag{A.40}$$

for the magic sector and:

$$D_2 = -\frac{e^2 d_l}{\epsilon_0 \epsilon_\perp A_{\text{UC}}} \left[\frac{1}{4}\nu_2 + \frac{5}{12}\nu_1 \right], \tag{A.41}$$

for the nonmagic TBG-like sector, significantly larger than D_1. By mirror symmetry, the $k = 2$ sector does not mix any other sector. Let us however evaluate the mixing term of $k = 1$ and $k = 3$. This is the term:

$$H_{13} = f^\dagger_{k=1,i=1} f_{k'=3,i=1} \sum_l (V_{\text{TNG}})_{l,k=1,i=1} (V_{\text{TNG}})_{l,k'=3,i=1} (-eV_l) + \text{h. c.} \tag{A.42}$$

from Equation. (A.18), which we readily evaluate using $-eV_l$:

$$H_{13} = -\frac{e^2 d_l}{\epsilon_0 \epsilon_\perp A_{\mathrm{UC}}} \left[\frac{\sqrt{3}}{8}\nu_2 + \frac{7\sqrt{3}}{24}\nu_1 \right] f^\dagger_{k=1,i=1} f_{k'=3,i=1} + \text{h. c.} \tag{A.43}$$

H_{13} has exactly the same effect as a displacement field in TTG. However, rather than being explicitly tunable in a doubly-gated setup, it is self-generated and doping dependent.

A.4 Methods

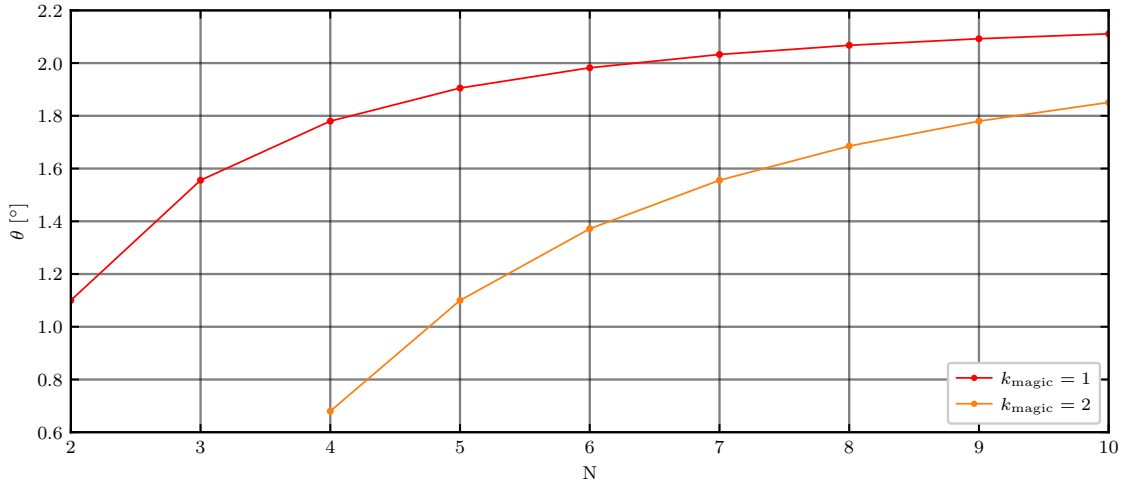

Figure A.1: Physical twist angle for choosing $k_{\mathrm{magic}} = 1$ (red) or $k_{\mathrm{magic}} = 2$ (orange) as a function of the layer number N.

To obtain the numerical results, we perform self-consistent Hartree-Fock. Our default choice will be a 12×12 $\mathbf{k}$-space grid. Our $\mathbf{q} \neq 0$ interaction is the double-gate screened, layer dependent (see Sec. 5.3.2) Coulomb interaction, with gate distance $d_s = 40\mathrm{nm}$ and interlayer distance $d_l = 0.3\mathrm{nm}$. We choose our physical twist angles by the following formula:

$$\theta = 2\cos\left[\frac{\pi k_{\mathrm{magic}}}{N+1}\right] \cdot 1.1^\circ, \tag{A.44}$$

chosen so that the effective twist angle of sector k_{magic}, is the magic angle, $\theta^{\mathrm{eff}}_{k_{\mathrm{magic}}} = 1.1^\circ$. In Fig. A.1 we plot relation Eq. (A.44) for the different choices $k_{\mathrm{magic}} = 1, 2$ (see also Ref. [78] for an equivalent plot). This demonstrates that achieving the regime where $k = 2$ is in the magic regime for $N \geq 5$ is feasible due to the realistic physical twist angles of $\theta > 1^\circ$ thus avoiding lattice reconstruction effects.

A.4.1 $N \leq 5$

For the $N \leq 5$ analysis, we consider $N_{\text{active}} = 10$ bands and calculate the remote Hartree and Fock contribution using $N_{\text{remote}} = 14$ bands below and above the active bands. For the heatmap and cascade plots, Figs. 5.5d,e,f, we simulate all four spin/valley flavors, inducing flavor symmetry-breaking by proposing symmetry-broken trial states at integer fillings. For the illustrative band structure and density of states plots, Figs. 5.5a,b,c, we use a larger 24×24 grid, but do not include flavor symmetry breaking. We show the band structures close to $\nu_{\text{magic}} = 4$. The cascade and band structure plots are performed at $\epsilon_{\parallel} = 14$ and $\epsilon_{\perp} = 6$.

A.4.2 $N \geq 5$

For the $N \geq 5$ analysis, we consider $N_{\text{active}} = \max[10, 2N]$ bands and calculate the remote Hartree and Fock contribution using $N_{\text{remote}} = \max[10, 3N]$ bands below and above the active bands. This dependence is motivated by the fact that adding a layer adds a band, which we want to include in our analysis, to account for nonmagic sector screening. We caution, however, that the precise choice is somewhat arbitrary.

For Fig. 5.1, we work at zero strain and $\epsilon_{\parallel} = 10$, $\epsilon_{\perp} = 6$. For Figs. 5.6, we also work at zero strain and $\epsilon_{\parallel} = 10$, $\epsilon_{\perp} = 6$. In Figs. 5.6c,d we show both zero strain and $\epsilon_{\text{strain}} = 0.2\%$ results.

A.4.3 Stability of Hartree-Fock with $\mathrm{H}_{\text{layer}}$

In our Hartree-Fock numerics, we ran into an instability for large $\mathrm{H}_{\text{layer}}$ terms (large filling of large N in combination with a small out-of-plane constant $\epsilon_{\perp}$). Our system oscillates between states with vertical polarization to the top and to the bottom of the sample. Clearly such spontaneously polarized states fail at screening the gate electric field and are therefore high energy (see Eq. (5.22)). We can understand the appearance of such oscillations by considering mean-field $\mathrm{H}_{\text{layer}}$ for a state polarized to the top layer in an infinite density of states system. In the mean field of such a state, the lowest energy state is the state polarized to the bottom layer. In this way, there appears an oscillation between opposing vertical polarizations upon iterating Hartree-Fock. Other terms in Eq. (5.3) make this instability weaker. For example, a finite density of states induces an energy cost to filling one layer excessively. We find that explicitly imposing $V_1 = V_N = 0$ by adding a constant gradient removes this instability, at the cost of a slight inaccuracy. Numerically, we find that the gradient is small, typically below $\frac{1}{\epsilon_{\perp}}\mathrm{meV}$.

Appendix B

B.1 Degeneracies of backfolded parabolic bands

The degeneracies of backfolded parabolic bands (Fig. B.1a) in the moiré Brillouin zone are best understood by examining copies of the parabolic dispersion shifted by reciprocal lattice vectors $\mathbf{g}$. The value of that copy at a given point $\mathbf{k}$ in the Brillouin zone is proportional to the square of the distance from the shift vector $\mathbf{g}$. For example, around the $K_{M'}$ point, the three points Γ, $\mathbf{g}_1$, and $\mathbf{g}_2$, shown in Fig. B.1b, are relevant for the topmost backfolded bands. There is a threefold degeneracy at $\mathbf{k} = K_{M'}$. The distance of $K_{M'}$ from Γ, $\mathbf{g}_1$ and $\mathbf{g}_2$ is equal, being related by C_3 rotation around $K_{M'}$. As pictured in Fig. B.1c, for a point $\mathbf{k}$ along the $K_{M'} - K_M$ high-symmetry line, the distances to Γ and $\Gamma + \mathbf{g}_1$ remain equal and decrease, while the distance to $\Gamma + \mathbf{g}_2$ increases. As a result, the threefold degeneracy at the $K_{M'}$ point is lifted into a 2+1 degeneracy from top to bottom, see Fig. B.1a, along $K_{M'} - K_M$. The same lifting occurs along $K_M - M$. At a generic point $\mathbf{k}$ away from high symmetry lines (Fig. B.1d), there is no degeneracy – the distances from Γ, $\mathbf{g}_1$, and $\mathbf{g}_2$ are all different.

B.2 Nearly free electrons at $\Phi = -1$

We now turn to the nearly free electron approach for the adiabatic model of Eq. (8.1) in an externally applied flux $\Phi = -1$, where the dominant term is the kinetic energy, and the potential $\tilde{V}(\mathbf{r})$ and vector potential $\tilde{\mathbf{A}}(\mathbf{r})$ act as perturbations.

B.2.1 Definition of natural units and Fourier expansion

We define a natural energy unit for terms arising from the kinetic term, evaluating for WSe_2:

$$\mathrm{Ry}^* = \frac{\hbar^2 |\mathbf{K}_M|^2}{2m^*} = (\theta[^\circ])^2 4.3\,\mathrm{meV}, \tag{B.1}$$

where $|\mathbf{K}_M| = 8\pi \sin(\theta/2)/(3a_0)$ is the magnitude of the moiré K_M point in the Brillouin zone, which we use to define a dimensionless derivative $\tilde{\partial}_i = \frac{1}{|\mathbf{K}_M|}\partial_i$, such that $|\mathbf{K}_M|\tilde{\partial}_i = \partial_i$, with the advantage that dimensionless derivatives of $\hat{\boldsymbol{n}}$ are twist angle independent. The effective potential is given as

$$\tilde{V}(\mathbf{r}) = -D(\mathbf{r}) + |\boldsymbol{\Delta}(\mathbf{r})| + \Delta_0(\mathbf{r}) \tag{B.2}$$

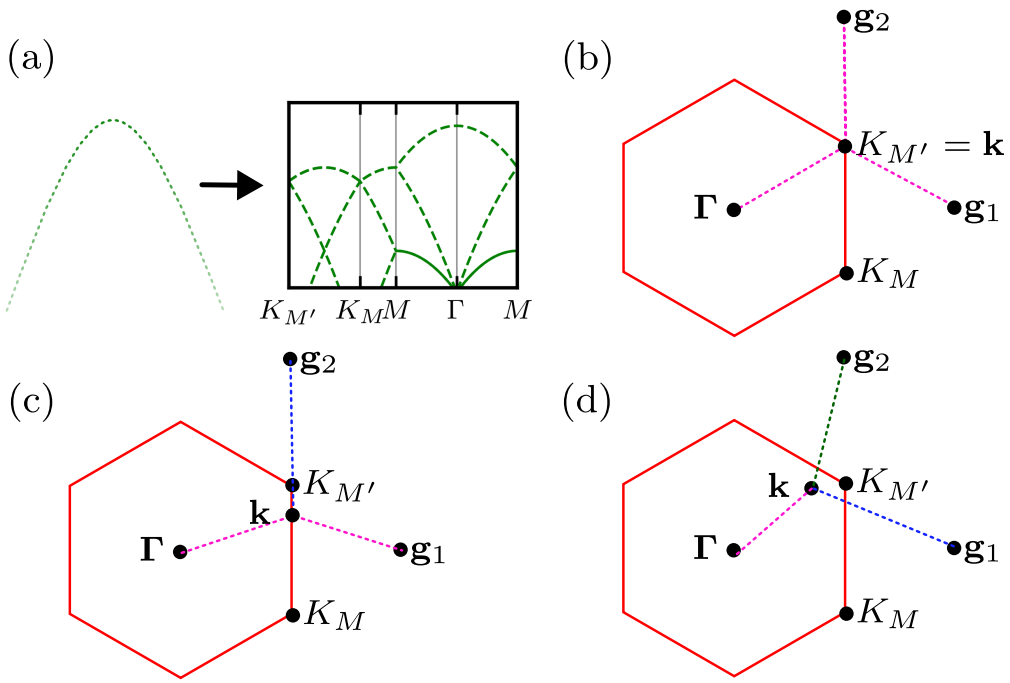

Figure B.1: (a) Illustration of the backfolding of a free electron dispersion into the Brillouin zone. (b) For a point $\mathbf{k} = K_{M'}$ at the moiré Brillouin zone corner, there is a threefold degeneracy of the topmost branch of the backfolded bands, as the distances of $\mathbf{k}$ to Γ, $\mathbf{g}_1$ and $\mathbf{g}_2$, shown in purple, are all equal. (c) For a point $\mathbf{k}$ along the $K_M - K_{M'}$ line, the degeneracy is partially lifted. The distances to Γ and $\mathbf{g}_1$ (purple) are equal, while the distance to $\mathbf{g}_2$ (blue) is different. (d) For a generic point $\mathbf{k}$ in the Brillouin zone, there is no degeneracy, as the distances are all different.

and we separate it into two parts. First, the kinetic potential term $D(\mathbf{r})$ is written as:

$$\begin{aligned} D(\mathbf{r}) &= \mathrm{Ry}^* \frac{1}{4} \sum_{i=x,y} (\tilde{\partial}_i \hat{\mathbf{n}})^2 \\ &= \mathrm{Ry}^* \sum_{\mathbf{g}} \delta_{\mathbf{g}} e^{i\mathbf{g}\cdot\mathbf{r}}, \end{aligned} \tag{B.3}$$

where $\delta_{\mathbf{g}}$ are twist-angle independent numbers depending only on model parameters. Second, the Zeeman potentials can also be expanded:

$$|\mathbf{\Delta}(\mathbf{r})| + \Delta_0(\mathbf{r}) = \sum_{\mathbf{g}} \Delta_{\mathbf{g}} e^{i\mathbf{g}\cdot\mathbf{r}}, \tag{B.4}$$

where $\Delta_{\mathbf{g}}$ has no twist angle dependence. In total, the potential term can be written as a Fourier series as:

$$\tilde{V}(\mathbf{r}) = \sum_{\mathbf{g}} (-\mathrm{Ry}^* \delta_{\mathbf{g}} + \Delta_{\mathbf{g}}) e^{i\mathbf{g}\cdot\mathbf{r}}. \tag{B.5}$$

Note that in this way, the kinetic potential term $D(\mathbf{r})$ has the twist angle dependence explicitly pulled out in the form of a factor of Ry^*. The effective magnetic field is written as

$$\nabla \times \tilde{\mathbf{A}}(\mathbf{r}) = \tilde{B} = -|\mathbf{K}_M|^2 \frac{\hbar}{e} \frac{1}{2} \hat{\boldsymbol{n}} \cdot \left(\tilde{\partial}_x \hat{\boldsymbol{n}} \times \tilde{\partial}_y \hat{\boldsymbol{n}} \right), \tag{B.6}$$

where the minus sign compared to [202] is because in our convention $B > 0$ gives $C = 1$ for electrons. Writing as a Fourier series, we obtain

$$\frac{1}{2} \hat{\boldsymbol{n}} \cdot \left(\tilde{\partial}_x \hat{\boldsymbol{n}} \times \tilde{\partial}_y \hat{\boldsymbol{n}} \right) = \sum_{\mathbf{g}} \beta_{\mathbf{g}} e^{i\mathbf{g}\cdot\mathbf{r}}. \tag{B.7}$$

At $\Phi = -1$ the effective magnetic field is on average cancelled by the external one, meaning we need to remove the $\mathbf{g} = 0$ term in the sum to obtain the total magnetic field experienced by the electrons:

$$B_{\mathrm{tot}}(\mathbf{r}) = -|\mathbf{K}_M|^2 \frac{\hbar}{e} \sum_{\mathbf{g} \neq 0} \beta_{\mathbf{g}} e^{i\mathbf{g}\cdot\mathbf{r}}, \tag{B.8}$$

where $\beta_{\mathbf{g}}$ is twist angle-independent. This leads to the vector potential at $\Phi = -1$:

$$\tilde{\mathbf{A}}(\mathbf{r}) = -|\mathbf{K}_M|^2 \frac{\hbar}{e} \sum_{\mathbf{g} \neq 0} \frac{i\mathbf{g} \times \hat{z}}{|\mathbf{g}|^2} \beta_{\mathbf{g}} e^{i\mathbf{g}\cdot\mathbf{r}}. \tag{B.9}$$

We now need to evaluate the vector potential terms in Eq. (8.1). As $|\beta_{\mathbf{g}}| \ll 1$, we neglect the diamagnetic term which contains factors of β^2, obtaining for the paramagnetic [linear in $\tilde{\mathbf{A}}(\mathbf{r})$] matrix element

$$\begin{aligned}
\langle \mathbf{k}_2 | H_{\mathrm{para}} | \mathbf{k}_1 \rangle &= \frac{e\hbar}{2m^*} \langle \mathbf{k}_2 | \tilde{\mathbf{A}}(\mathbf{r}) \cdot \mathbf{k} + \mathbf{k} \cdot \tilde{\mathbf{A}}(\mathbf{r}) | \mathbf{k}_1 \rangle & \text{(B.10)} \\
&= -i\mathrm{Ry}^* \frac{(\mathbf{k}_1 + \mathbf{k}_2) \times (\mathbf{k}_2 - \mathbf{k}_1)}{|\mathbf{k}_2 - \mathbf{k}_1|^2} \beta_{\mathbf{k}_2 - \mathbf{k}_1} & \text{(B.11)} \\
&= -i\mathrm{Ry}^* \frac{2\mathbf{k}_1 \times \mathbf{k}_2}{|\mathbf{k}_2 - \mathbf{k}_1|^2} \beta_{\mathbf{k}_2 - \mathbf{k}_1}. & \text{(B.12)}
\end{aligned}$$

We use the symmetry indicators of band topology [257], which for a C_{6z}-symmetric system give the Chern number C_i of a band i as:

$$e^{i\pi C_i/3} = \eta_i(\Gamma)\theta_i(K_M)\zeta_i(M), \tag{B.13}$$

where $\eta_i(\mathbf{k})$, $\theta_i(\mathbf{k})$ and $\zeta_i(\mathbf{k})$ are the C_{6z}, C_{3z} and C_{2z} eigenvalues of band i at momentum $\mathbf{k}$. In what follows, we evaluate the eigenvalues by considering the effective Hamiltonians inside the highest energy degenerate subspaces at high symmetry momenta. Focusing on WSe_2 use the values of Fourier coefficients listed in Table B.1.

i	Δ_i	δ_i	β_i
1	$-2.61\,\mathrm{meV}$	-0.12	-0.11
2	$1.34\,\mathrm{meV}$	-0.06	-0.05
3	$-1.13\,\mathrm{meV}$	0.14	0.14

Table B.1: Coefficients β,δ and Δ of the adiabatic model of WSe_2.

.

B.2.2 Hamiltonian at the M-point

At a given M point there are only two relevant states, denoted $M^{(1)}$ and $M^{(2)}$ in Fig. B.2a. They are connected by a lowest magnitude reciprocal vector, giving a hopping

$$t = \Delta_1 - \delta_1 E_0, \tag{B.14}$$

which is necessarily real due to C_{2z}. This gives energies

$$\epsilon_\pm = \pm(\Delta_1 - \delta_1 E_0), \tag{B.15}$$

with C_{2z} eigenvalues ± 1. Above, we omitted a constant energy shift as it does not affect the ordering of the states. For small twist angles (small E_0), the topmost band has C_{2z} eigenvalue -1 (note that both Δ_1 and δ_1 are negative) and the second band $+1$. As twist angle increases, at the point $\Delta_1 - \delta_1 E_0 = 0$, which happens at $\theta \approx 2.25°$, the eigenvalues swap places. Summarizing, for $\theta \lessapprox 2.25°$:

$$\zeta_1(M) = -1 \tag{B.16}$$
$$\zeta_2(M) = 1, \tag{B.17}$$

while for larger angles:

$$\zeta_1(M) = 1 \tag{B.18}$$
$$\zeta_2(M) = -1. \tag{B.19}$$

B.2.3 Hamiltonian at the K_M-point: a three-site model

At the K_M point, are only three relevant momenta, denoted $K^{(1)}$, $K^{(2)}$ and $K^{(3)}$ in Fig. B.2a. They are connected by a hopping t_1^K, and the Hamiltonian is

$$H_{K_M} = -E_0 + \begin{pmatrix} 0 & (t_1^K)^* & t_1^K \\ t_1^K & 0 & (t_1^K)^* \\ (t_1^K)^* & t_1^K & 0 \end{pmatrix}, \tag{B.20}$$

where t_1^K is given as

$$t_1^K = \Delta_1 + E_0(-\delta_1 - i\frac{1}{\sqrt{3}}\beta_1). \tag{B.21}$$

The eigenstates are labeled by their C_{3z} eigenvalues, $1, \omega = e^{2\pi i/3}, \omega^* = e^{4\pi i/3}$, and have energies (omitting an overall constant):

$$\epsilon_1 = 2[\Delta_1 - \delta_1 E_0] \tag{B.22}$$
$$\epsilon_\omega = -\Delta_1 + E_0(\delta_1 + \beta_1) \tag{B.23}$$
$$\epsilon_{\omega^*} = -\Delta_1 + E_0(\delta_1 - \beta_1), \tag{B.24}$$

that are equal to:

$$\epsilon_1[\text{meV}] = -5.22 + 0.24E_0 \tag{B.25}$$
$$\epsilon_\omega[\text{meV}] = 2.61 - 0.23E_0 \tag{B.26}$$
$$\epsilon_{\omega^*}[\text{meV}] = 2.61 - 0.01E_0. \tag{B.27}$$

Therefore, for small twist angle ω^* and ω states are the highest and second highest energy states, respectively. The second highest state of eigenvalue ω crosses with the eigenvalue 1 state at $\theta \approx 1.96°$ Summarizing, for $\theta \lessapprox 1.96°$:

$$\theta_1(K_M) = e^{4\pi i/3} \tag{B.28}$$
$$\theta_2(K_M) = e^{2\pi i/3}, \tag{B.29}$$

while for larger angles

$$\theta_1(K_M) = e^{4\pi i/3} \tag{B.30}$$
$$\theta_2(K_M) = 1, \tag{B.31}$$

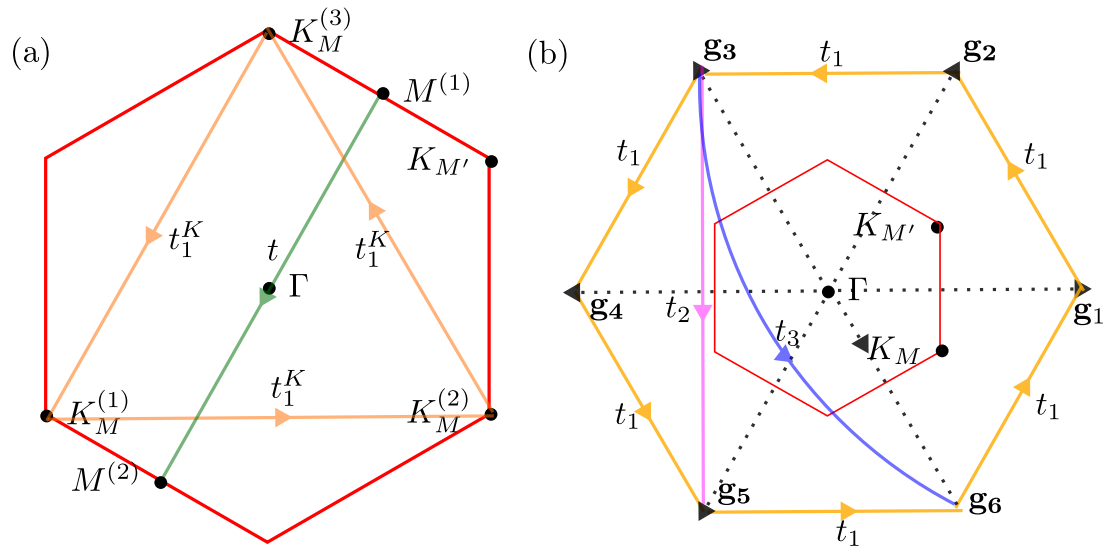

Figure B.2: (a) Moiré Brillouin zone, showing two degenerate M points $M^{(1)}$ and $M^{(2)}$ coupled by a hopping t and three degenerate $|\mathbf{K}_M|$ points, coupled by hopping t_1^K. (b) Six relevant momenta for the second highest state at the Γ point. They are coupled by nearest neighbor hopping t_1, next-nearest neighbor hopping t_2 and third nearest neighbor hopping t_3.

B.2.4 Hamiltonian at the moiré Γ-point: a six-site model

The Γ point extremum itself, which is part of the topmost band trivial representation of C_{6z}, giving $\eta_1 = 1$ for all twist angle. For the second topmost state at the moiré Γ point, six momenta are relevant, given by $\mathbf{g}_1, \ldots, \mathbf{g}_6$, with $|\mathbf{g}_i| = \sqrt{3}|\mathbf{K}_M|$ for $i = 1, \ldots 6$. We plot them in Fig. B.2b, together with the nearest, next-nearest and third-nearest neighbor hoppings t_1, t_2 and t_3. The Hamiltonian at this point is:

$$H_{|\mathbf{K}_M|} = -\sqrt{3}E_0 + \begin{pmatrix} 0 & t_1^* & t_2^* & t_3 & t_2 & t_1 \\ t_1 & 0 & t_1^* & t_2^* & t_3 & t_2 \\ t_2 & t_1 & 0 & t_1^* & t_2^* & t_3 \\ t_3 & t_2 & t_1 & 0 & t_1^* & t_2^* \\ t_2^* & t_3 & t_2 & t_1 & 0 & t_1^* \\ t_1^* & t_2^* & t_3 & t_2 & t_1 & 0 \end{pmatrix}, \tag{B.32}$$

where t_1 is given by

$$t_1 = \Delta_1 + E_0(-\delta_1 - i\sqrt{3}\beta_1), \tag{B.33}$$

with the only difference to t_1^K in Eq. (B.21) being the geometric factor $\sqrt{3}$ multiplying β_1. The other hoppings are:

$$t_2 = \Delta_2 + E_0(-\delta_2 - i\frac{1}{\sqrt{3}}\beta_2) \tag{B.34}$$

$$t_3 = \Delta_3 + E_0(-\delta_3), \tag{B.35}$$

where we note that t_3 is real due to C_{2z} symmetry.

To solve, we use the C_{6z} symmetry, so that solutions can be labelled by C_{6z} eigenvalues $e^{i\frac{\pi}{3}m}$, where m is the angular momentum. Firstly, t_3 causes a large splitting between different C_{2z} sectors, caused by the dip of $\tilde{V}(\mathbf{r})$ at the midpoint between AB and BA sites of the unit cell, and the magnitude of this splitting increases with twist angle. Since t_3 is negative, the upper branch has C_{2z} eigenvalue -1, corresponding to angular momenta $m = 1, 3, 5$. The energies of these states are (up to an overall constant):

$$\epsilon_{m=1} = -t_3 + 2\mathrm{Re}\big[(t_1 - t_2^*)e^{i\pi/3}\big] \tag{B.36}$$

$$\epsilon_{m=3} = -t_3 + 2\mathrm{Re}[-t_1 + t_2] \tag{B.37}$$

$$\epsilon_{m=5} = -t_3 + 2\mathrm{Re}\big[(t_1 - t_2^*)e^{-i\pi/3}\big], \tag{B.38}$$

which we can numerically evaluate for WSe_2 to be:

$$\epsilon_{m=1}[\mathrm{meV}] \approx -t_3 + 2 \cdot [-1.97 - 0.15E_0] \tag{B.39}$$

$$\epsilon_{m=3}[\mathrm{meV}] \approx -t_3 + 2 \cdot [3.95 - 0.06E_0] \tag{B.40}$$

$$\epsilon_{m=5}[\mathrm{meV}] \approx -t_3 + 2 \cdot [-1.97 + 0.2E_0], \tag{B.41}$$

where we do not evaluate t_3 as it is the same for all states. We see that the $m = 3$ state is by far highest in energy up to $\theta = 2.5°$. Therefore, we have for realistic angles:

$$\eta_1(\Gamma) = 1 \tag{B.42}$$

$$\eta_2(\Gamma) = -1, \tag{B.43}$$

B.2.5 Topology

Putting the results together, we have for $\theta \lessapprox 1.96°$ the Chern number sequence:

$$C_1 = 1 \mod 6 \tag{B.44}$$

$$C_2 = -1 \mod 6. \tag{B.45}$$

For $\theta \gtrapprox 1.96^\circ$, we have

$$C_1 = 1 \mod 6 \tag{B.46}$$

$$C_2 = -3 \mod 6, \tag{B.47}$$

predicting the correct phase transition and obtaining the twist angle of the transition to reasonable accuracy compared with the full model, in which it happens at $\theta \approx 2.02^\circ$. From the symmetry-indicator analysis, we also infer that the gap closing at $\theta \approx 2.02^\circ$ between the second and the third band occurs through two Dirac cones at K_M and $K_{M'}$.

Bibliography

1. G. Shavit, K. Kolář, C. Mora, F. von Oppen, and Y. Oreg, "Strain disorder and gapless intervalley coherent phase in twisted bilayer graphene", Physical Review B **107**:8, L081403 (2023).
2. K. Kolář, G. Shavit, C. Mora, Y. Oreg, and F. von Oppen, "Anderson's theorem for correlated insulating states in twisted bilayer graphene", Physical Review Letters **130**:7, 076204 (2023).
3. K. Kolář, Y. Zhang, S. Nadj-Perge, F. von Oppen, and C. Lewandowski, "Electrostatic fate of N-layer moiré graphene", Physical Review B **108**:19, 195148 (2023).
4. K. Kolář, K. Yang, F. von Oppen, and C. Mora, "Hofstadter spectrum of chern bands in twisted transition metal dichalcogenides", Physical Review B **110**:11, 115114 (2024).
5. K. Kolář and F. von Oppen, "Tunneling signatures of interband coherence in exciton condensates", in preparation (2024).
6. K. Kolář, D. Waters, J. Folk, M. Yankowitz, and C. Lewandowski, "The rise of single-gate behavior in bernal-terminated graphene multilayers", in preparation (2024).
7. K. Kolář, K. Yang, F. von Oppen, and C. Mora, "Real-space topology of wavefunctions and absence thereof", in preparation.
8. K. S. Novoselov, A. K. Geim, S. V. Morozov, D. Jiang, Y. Zhang, S. V. Dubonos, I. V. Grigorieva, and A. A. Firsov, "Electric Field Effect in Atomically Thin Carbon Films", Science **306**:5696, 666–669 (2004).
9. A. K. Geim, "Graphene: Status and Prospects", Science **324**:5934, 1530–1534 (2009).
10. K. S. Novoselov, A. K. Geim, S. V. Morozov, D. Jiang, M. I. Katsnelson, I. V. Grigorieva, S. V. Dubonos, and A. A. Firsov, "Two-dimensional gas of massless Dirac fermions in graphene", Nature **438**:7065, 197–200 (2005).
11. W. Bao, L. Jing, J. Velasco, Y. Lee, G. Liu, D. Tran, B. Standley, M. Aykol, S. B. Cronin, D. Smirnov, M. Koshino, E. McCann, M. Bockrath, and C. N. Lau, "Stacking-dependent band gap and quantum transport in trilayer graphene", Nature Physics **7**:12, 948–952 (2011).
12. J. B. Oostinga, H. B. Heersche, X. Liu, A. F. Morpurgo, and L. M. K. Vandersypen, "Gate-induced insulating state in bilayer graphene devices", Nature Materials **7**:2, 151–157 (2008).
13. C. H. Lui, Z. Li, K. F. Mak, E. Cappelluti, and T. F. Heinz, "Observation of an electrically tunable band gap in trilayer graphene", Nature Physics **7**:12, 944–947 (2011).
14. H. Zhou, T. Xie, T. Taniguchi, K. Watanabe, and A. F. Young, "Superconductivity in rhombohedral trilayer graphene", Nature **598**:7881, 434–438 (2021).

15. H. Zhou, T. Xie, A. Ghazaryan, T. Holder, J. R. Ehrets, E. M. Spanton, T. Taniguchi, K. Watanabe, E. Berg, M. Serbyn, and A. F. Young, "Half- and quarter-metals in rhombohedral trilayer graphene", Nature **598**:7881, 429–433 (2021).

16. Z. Lu, T. Han, Y. Yao, A. P. Reddy, J. Yang, J. Seo, K. Watanabe, T. Taniguchi, L. Fu, and L. Ju, "Fractional quantum anomalous hall effect in multilayer graphene", Nature **626**:8000, 759–764 (2024).

17. N. B. Kopnin, T. T. Heikkilä, and G. E. Volovik, "High-temperature surface superconductivity in topological flat-band systems", Physical Review B **83**:22, 220503 (2011).

18. J. M. B. Lopes dos Santos, N. M. R. Peres, and A. H. Castro Neto, "Graphene Bilayer with a Twist: Electronic Structure", Physical Review Letters **99**:25, 256802 (2007).

19. R. Bistritzer and A. H. MacDonald, "Moire bands in twisted double-layer graphene", Proceedings of the National Academy of Sciences **108**:30, 12233–12237 (2011).

20. Y. Cao, V. Fatemi, A. Demir, S. Fang, S. L. Tomarken, J. Y. Luo, J. D. Sanchez-Yamagishi, K. Watanabe, T. Taniguchi, E. Kaxiras, R. C. Ashoori, and P. Jarillo-Herrero, "Correlated insulator behaviour at half-filling in magic-angle graphene superlattices", Nature **556**:7699, 80–84 (2018).

21. Y. Cao, V. Fatemi, S. Fang, K. Watanabe, T. Taniguchi, E. Kaxiras, and P. Jarillo-Herrero, "Unconventional superconductivity in magic-angle graphene superlattices", Nature **556**:7699, 43–50 (2018).

22. M. Yankowitz, S. Chen, H. Polshyn, Y. Zhang, K. Watanabe, T. Taniguchi, D. Graf, A. F. Young, and C. R. Dean, "Tuning superconductivity in twisted bilayer graphene", Science **363**:6431, 1059–1064 (2019).

23. Z. Hao, A. M. Zimmerman, P. Ledwith, E. Khalaf, D. H. Najafabadi, K. Watanabe, T. Taniguchi, A. Vishwanath, and P. Kim, "Electric field–tunable superconductivity in alternating-twist magic-angle trilayer graphene", Science **371**:6534, 1133–1138 (2021).

24. M. Oh, K. P. Nuckolls, D. Wong, R. L. Lee, X. Liu, K. Watanabe, T. Taniguchi, and A. Yazdani, "Evidence for unconventional superconductivity in twisted bilayer graphene", Nature **600**:7888, 240–245 (2021).

25. X. Lu, P. Stepanov, W. Yang, M. Xie, M. A. Aamir, I. Das, C. Urgell, K. Watanabe, T. Taniguchi, G. Zhang, A. Bachtold, A. H. MacDonald, and D. K. Efetov, "Superconductors, orbital magnets and correlated states in magic-angle bilayer graphene", Nature **574**:7780, 653–657 (2019).

26. Y. Cao, D. Rodan-Legrain, J. M. Park, N. F. Q. Yuan, K. Watanabe, T. Taniguchi, R. M. Fernandes, L. Fu, and P. Jarillo-Herrero, "Nematicity and competing orders in superconducting magic-angle graphene", Science **372**:6539, 264–271 (2021).

27. X. Liu, Z. Wang, K. Watanabe, T. Taniguchi, O. Vafek, and J. I. A. Li, "Tuning electron correlation in magic-angle twisted bilayer graphene using coulomb screening", Science **371**:6535, 1261–1265 (2021).

28. H. S. Arora, R. Polski, Y. Zhang, A. Thomson, Y. Choi, H. Kim, Z. Lin, I. Z. Wilson, X. Xu, J.-H. Chu, K. Watanabe, T. Taniguchi, J. Alicea, and S. Nadj-Perge, "Superconductivity in metallic twisted bilayer graphene stabilized by wse2", Nature **583**:7816, 379–384 (2020).

29. P. Stepanov, I. Das, X. Lu, A. Fahimniya, K. Watanabe, T. Taniguchi, F. H. L. Koppens, J. Lischner, L. Levitov, and D. K. Efetov, "Untying the insulating and superconducting orders in magic-angle graphene", Nature **583**:7816, 375–378 (2020).

30. Y. Saito, J. Ge, K. Watanabe, T. Taniguchi, and A. F. Young, "Independent superconductors and correlated insulators in twisted bilayer graphene", Nature Physics **16**:9, 926–930 (2020).

31. Y. Zhang, R. Polski, C. Lewandowski, A. Thomson, Y. Peng, Y. Choi, H. Kim, K. Watanabe, T. Taniguchi, J. Alicea, F. von Oppen, G. Refael, and S. Nadj-Perge, "Promotion of superconductivity in magic-angle graphene multilayers", Science **377**:6614, 1538–1543 (2022).

32. J. M. Park, Y. Cao, L.-Q. Xia, S. Sun, K. Watanabe, T. Taniguchi, and P. Jarillo-Herrero, "Robust superconductivity in magic-angle multilayer graphene family", Nature Materials **21**:8, 877–883 (2022).

33. J. M. Park, Y. Cao, K. Watanabe, T. Taniguchi, and P. Jarillo-Herrero, "Tunable strongly coupled superconductivity in magic-angle twisted trilayer graphene", Nature **590**:7845, 249–255 (2021).

34. Y. Cao, J. M. Park, K. Watanabe, T. Taniguchi, and P. Jarillo-Herrero, "Pauli-limit violation and re-entrant superconductivity in moiré graphene", Nature **595**:7868, 526–531 (2021).

35. L.-Q. Xia, S. C. de la Barrera, A. Uri, A. Sharpe, Y. H. Kwan, Z. Zhu, K. Watanabe, T. Taniguchi, D. Goldhaber-Gordon, L. Fu, T. Devakul, and P. Jarillo-Herrero, *Helical trilayer graphene: a moiré platform for strongly-interacting topological bands*, (18, 2023) `http://arxiv.org/abs/2310.12204` (visited on 10/31/2023), pre-published.

36. M. He, Y. Li, J. Cai, Y. Liu, K. Watanabe, T. Taniguchi, X. Xu, and M. Yankowitz, "Symmetry breaking in twisted double bilayer graphene", Nature Physics **17**:1, 26–30 (2021).

37. G. W. Burg, J. Zhu, T. Taniguchi, K. Watanabe, A. H. MacDonald, and E. Tutuc, "Correlated Insulating States in Twisted Double Bilayer Graphene", Physical Review Letters **123**:19, 197702 (2019).

38. Y. Cao, D. Rodan-Legrain, O. Rubies-Bigorda, J. M. Park, K. Watanabe, T. Taniguchi, and P. Jarillo-Herrero, "Tunable correlated states and spin-polarized phases in twisted bilayer–bilayer graphene", Nature **583**:7815, 215–220 (2020).

39. K. F. Mak, C. Lee, J. Hone, J. Shan, and T. F. Heinz, "Atomically Thin ${\mathrm{MoS}}_{2}$: A New Direct-Gap Semiconductor", Physical Review Letters **105**:13, 136805 (2010).

40. S. Z. Butler, S. M. Hollen, L. Cao, Y. Cui, J. A. Gupta, H. R. Gutiérrez, T. F. Heinz, S. S. Hong, J. Huang, A. F. Ismach, E. Johnston-Halperin, M. Kuno, V. V. Plashnitsa, R. D. Robinson, R. S. Ruoff, S. Salahuddin, J. Shan, L. Shi, M. G. Spencer, M. Terrones, W. Windl, and J. E. Goldberger, "Progress, Challenges, and Opportunities in Two-Dimensional Materials Beyond Graphene", ACS Nano **7**:4, 2898–2926 (2013).

41. G. Wang, A. Chernikov, M. M. Glazov, T. F. Heinz, X. Marie, T. Amand, and B. Urbaszek, "Colloquium: Excitons in atomically thin transition metal dichalcogenides", Reviews of Modern Physics **90**:2, 021001 (2018).

42. Q. Gao, Y.-h. Chan, Y. Wang, H. Zhang, P. Jinxu, S. Cui, Y. Yang, Z. Liu, D. Shen, Z. Sun, J. Jiang, T. C. Chiang, and P. Chen, "Evidence of high-temperature exciton condensation in a two-dimensional semimetal", Nature Communications **14**:1, 994 (2023).

43. Y. Jia, P. Wang, C.-L. Chiu, Z. Song, G. Yu, B. Jäck, S. Lei, S. Klemenz, F. A. Cevallos, M. Onyszczak, N. Fishchenko, X. Liu, G. Farahi, F. Xie, Y. Xu, K. Watanabe, T. Taniguchi, B. A. Bernevig, R. J. Cava, L. M. Schoop, A. Yazdani, and S. Wu, "Evidence for a Monolayer Excitonic Insulator", Nature Physics **18**:1, 87–93 (2022).

44. B. Sun, W. Zhao, T. Palomaki, Z. Fei, E. Runburg, P. Malinowski, X. Huang, J. Cenker, Y.-T. Cui, J.-H. Chu, X. Xu, S. S. Ataei, D. Varsano, M. Palummo, E. Molinari, M. Rontani, and D. H. Cobden, "Evidence for equilibrium exciton condensation in monolayer wte2", Nature Physics **18**:1, 94–99 (2022).

45. D. Jérome, T. M. Rice, and W. Kohn, "Excitonic Insulator", Physical Review **158**:2, 462–475 (1967).

46. B. I. Halperin and T. M. Rice, "The Excitonic State at the Semiconductor-Semimetal Transition", Journal of Physics C: Solid State Physics **21**, 115–192 (1968).

47. L. V. Keldysh and A. N. Kozlov, "Collective Properties of Excitons in Semiconductors", Soviet Journal of Experimental and Theoretical Physics **27**, 521 (1968).

48. A. N. Kozlov and L. A. Maksimov, "The Metal-Dielectric Divalent Crystal Phase Transition", JETP, Vol. 21, No. 4, p. 790 (October 1965), 6 (1965).

49. L. Ma, P. X. Nguyen, Z. Wang, Y. Zeng, K. Watanabe, T. Taniguchi, A. H. MacDonald, K. F. Mak, and J. Shan, "Strongly correlated excitonic insulator in atomic double layers", Nature **598**:7882, 585–589 (2021).

50. Z. Wang, D. A. Rhodes, K. Watanabe, T. Taniguchi, J. C. Hone, J. Shan, and K. F. Mak, "Evidence of high-temperature exciton condensation in two-dimensional atomic double layers", Nature **574**:7776, 76–80 (2019).

51. R. Qi, A. Y. Joe, Z. Zhang, Y. Zeng, T. Zheng, Q. Feng, E. Regan, J. Xie, Z. Lu, T. Taniguchi, K. Watanabe, S. Tongay, M. F. Crommie, A. H. MacDonald, and F. Wang, *Thermodynamic behavior of correlated electron-hole fluids in van der waals heterostructures*, (22, 2023) `http://arxiv.org/abs/2306.13265` (visited on 07/17/2023), pre-published.

52. W. Zhao, K. Kang, Y. Zhang, P. Knüppel, Z. Tao, L. Li, C. L. Tschirhart, E. Redekop, K. Watanabe, T. Taniguchi, A. F. Young, J. Shan, and K. F. Mak, "Realization of the haldane chern insulator in a moiré lattice", Nature Physics **20**:2, 275–280 (2024).

53. K. F. Mak, T. Li, S. Jiang, B. Shen, Y. Zhang, L. Li, T. Devakul, K. Watanabe, T. Taniguchi, L. Fu, and J. Shan, "Quantum anomalous Hall effect from intertwined moiré bands", (2021).

54. Y. Tang, L. Li, T. Li, Y. Xu, S. Liu, K. Barmak, K. Watanabe, T. Taniguchi, A. H. MacDonald, J. Shan, and K. F. Mak, "Simulation of Hubbard model physics in WSe2/WS2 moiré superlattices", Nature **579**:7799, 353–358 (2020).

55. F. Wu, T. Lovorn, E. Tutuc, I. Martin, and A. H. MacDonald, "Topological insulators in twisted transition metal dichalcogenide homobilayers", Physical Review Letters **122**:8, 086402 (2019).

56. L. Wang, E.-M. Shih, A. Ghiotto, L. Xian, D. A. Rhodes, C. Tan, M. Claassen, D. M. Kennes, Y. Bai, B. Kim, K. Watanabe, T. Taniguchi, X. Zhu, J. Hone, A. Rubio, A. N. Pasupathy, and C. R. Dean, "Correlated electronic phases in twisted bilayer transition metal dichalcogenides", Nature Materials **19**:8, 861–866 (2020).

57. Y. Xia, Z. Han, K. Watanabe, T. Taniguchi, J. Shan, and K. F. Mak, *Unconventional superconductivity in twisted bilayer wse2*, (23, 2024) `http://arxiv.org/abs/2405.14784` (visited on 05/24/2024), pre-published.

58. Y. Guo, J. Pack, J. Swann, L. Holtzman, M. Cothrine, K. Watanabe, T. Taniguchi, D. Mandrus, K. Barmak, J. Hone, A. J. Millis, A. N. Pasupathy, and C. R. Dean, *Superconductivity in twisted bilayer wse_2*, (5, 2024) `http://arxiv.org/abs/2406.03418` (visited on 06/06/2024), pre-published.

59. A. Ghiotto, E.-M. Shih, G. S. S. G. Pereira, D. A. Rhodes, B. Kim, J. Zang, A. J. Millis, K. Watanabe, T. Taniguchi, J. C. Hone, L. Wang, C. R. Dean, and A. N. Pasupathy, "Quantum criticality in twisted transition metal dichalcogenides", Nature **597**:7876, 345–349 (2021).

60. J. Cai, E. Anderson, C. Wang, X. Zhang, X. Liu, W. Holtzmann, Y. Zhang, F. Fan, T. Taniguchi, K. Watanabe, Y. Ran, T. Cao, L. Fu, D. Xiao, W. Yao, and X. Xu, "Signatures of fractional quantum anomalous hall states in twisted mote2", Nature **622**:7981, 63–68 (2023).

61. H. Park, J. Cai, E. Anderson, Y. Zhang, J. Zhu, X. Liu, C. Wang, W. Holtzmann, C. Hu, Z. Liu, T. Taniguchi, K. Watanabe, J.-H. Chu, T. Cao, L. Fu, W. Yao, C.-Z. Chang, D. Cobden, D. Xiao, and X. Xu, "Observation of fractionally quantized anomalous hall effect", Nature **622**:7981, 74–79 (2023).

62. Y. Zeng, Z. Xia, K. Kang, J. Zhu, P. Knüppel, C. Vaswani, K. Watanabe, T. Taniguchi, K. F. Mak, and J. Shan, "Thermodynamic evidence of fractional chern insulator in moiré mote2", Nature **622**:7981, 69–73 (2023).

63. F. Xu, Z. Sun, T. Jia, C. Liu, C. Xu, C. Li, Y. Gu, K. Watanabe, T. Taniguchi, B. Tong, J. Jia, Z. Shi, S. Jiang, Y. Zhang, X. Liu, and T. Li, "Observation of integer and fractional quantum anomalous hall effects in twisted bilayer $MoTe_2$", Physical Review X **13**:3, 031037 (2023).

64. B. A. Foutty, C. R. Kometter, T. Devakul, A. P. Reddy, K. Watanabe, T. Taniguchi, L. Fu, and B. E. Feldman, "Mapping twist-tuned multiband topology in bilayer wse2", Science **384**:6693, 343–347 (2024).

65. K. Kang, B. Shen, Y. Qiu, Y. Zeng, Z. Xia, K. Watanabe, T. Taniguchi, J. Shan, and K. F. Mak, "Evidence of the fractional quantum spin hall effect in moiré mote2", Nature **628**:8008, 522–526 (2024).

66. K. Kang, Y. Qiu, K. Watanabe, T. Taniguchi, J. Shan, and K. F. Mak, *Observation of the double quantum spin hall phase in moiré wse2*, (6, 2024) http://arxiv.org/abs/2402.04196 (visited on 02/11/2024), pre-published.

67. D. Waters, R. Su, E. Thompson, A. Okounkova, E. Arreguin-Martinez, M. He, K. Hinds, K. Watanabe, T. Taniguchi, X. Xu, Y.-H. Zhang, J. Folk, and M. Yankowitz, *Topological flat bands in a family of multilayer graphene moiré lattices*, (9, 2024) http://arxiv.org/abs/2405.05913 (visited on 06/05/2024), pre-published.

68. T. Devakul, V. Crépel, Y. Zhang, and L. Fu, "Magic in twisted transition metal dichalcogenide bilayers", Nature Communications **12**:1, 6730 (2021).

69. H. C. Po, L. Zou, T. Senthil, and A. Vishwanath, "Faithful Tight-binding Models and Fragile Topology of Magic-angle Bilayer Graphene", Physical Review B **99**:19, 195455 (2019).

70. M. Koshino and N. N. T. Nam, "Effective continuum model for relaxed twisted bilayer graphene and moir\'e electron-phonon interaction", Physical Review B **101**:19, 195425 (2020).

71. J. Kang and O. Vafek, "Pseudomagnetic fields, particle-hole asymmetry, and microscopic effective continuum hamiltonians of twisted bilayer graphene", Physical Review B **107**:7, 075408 (2023).

72. O. Vafek and J. Kang, "Continuum effective hamiltonian for graphene bilayers for an arbitrary smooth lattice deformation from microscopic theories", Physical Review B **107**:7, 075123 (2023).

73. G. Tarnopolsky, A. J. Kruchkov, and A. Vishwanath, "Origin of Magic Angles in Twisted Bilayer Graphene", Physical Review Letters **122**:10, 106405 (2019).

74. J. Kang and O. Vafek, "Symmetry, maximally localized Wannier states, and low energy model for the twisted bilayer graphene narrow bands", Physical Review X **8**:3, 031088 (2018).

75. Z.-D. Song, B. Lian, N. Regnault, and B. A. Bernevig, "TBG II: Stable Symmetry Anomaly in Twisted Bilayer Graphene", Physical Review B **103**:20, 205412 (2021).

76. N. Bultinck, E. Khalaf, S. Liu, S. Chatterjee, A. Vishwanath, and M. P. Zaletel, "Ground State and Hidden Symmetry of Magic Angle Graphene at Even Integer Filling", Physical Review X **10**:3, 031034 (2020).

77. B. A. Bernevig, Z.-D. Song, N. Regnault, and B. Lian, "TBG III: Interacting Hamiltonian and Exact Symmetries of Twisted Bilayer Graphene", Physical Review B **103**:20, 205413 (2021).

78. E. Khalaf, A. J. Kruchkov, G. Tarnopolsky, and A. Vishwanath, "Magic angle hierarchy in twisted graphene multilayers", Physical Review B **100**:8, 085109 (2019).

79. S. Carr, C. Li, Z. Zhu, E. Kaxiras, S. Sachdev, and A. Kruchkov, "Ultraheavy and Ultrarelativistic Dirac Quasiparticles in Sandwiched Graphenes", Nano Letters **20**:5, 3030–3038 (2020).

80. H. Kim, Y. Choi, C. Lewandowski, A. Thomson, Y. Zhang, R. Polski, K. Watanabe, T. Taniguchi, J. Alicea, and S. Nadj-Perge, "Evidence for unconventional superconductivity in twisted trilayer graphene", Nature **606**:7914, 494–500 (2022).

81. M. S. Hossain, T. A. Cochran, Y.-X. Jiang, S. Zhang, H. Wu, X. Liu, X. Zheng, B. Kim, G. Cheng, Q. Zhang, M. Litskevich, J. Zhang, Z.-J. Cheng, J. Liu, J.-X. Yin, X. P. Yang, J. Denlinger, M. Tallarida, J. Dai, E. Vescovo, A. Rajapitamahuni, H. Miao, N. Yao, Y. Peng, Y. Yao, Z. Wang, L. Balicas, T. Neupert, and M. Z. Hasan, *Discovery of a topological exciton insulator with tunable momentum order*, (25, 2023) http://arxiv.org/abs/2312.15862 (visited on 08/08/2024), pre-published.

82. J. Huang, B. Jiang, J. Yao, D. Yan, X. Lei, J. Gao, Z. Guo, F. Jin, Y. Li, Z. Yuan, C. Chai, H. Sheng, M. Pan, F. Chen, J. Liu, S. Gao, G. Qu, B. Liu, Z. Jiang, Z. Liu, X. Ma, S. Zhou, Y. Huang, C. Yun, Q. Zhang, S. Li, S. Jin, H. Ding, J. Shen, D. Su, Y. Shi, Z. Wang, and T. Qian, "Evidence for an excitonic insulator state in $Ta_2Pd_3Te_5$", Physical Review X **14**:1, 011046 (2024).

83. K. Seki, Y. Wakisaka, T. Kaneko, T. Toriyama, T. Konishi, T. Sudayama, N. L. Saini, M. Arita, H. Namatame, M. Taniguchi, N. Katayama, M. Nohara, H. Takagi, T. Mizokawa, and Y. Ohta, "Excitonic Bose-Einstein condensation in ${\mathrm{Ta}}_{2}{\mathrm{NiSe}}_{5}$ above room temperature", Physical Review B **90**:15, 155116 (2014).

84. Q. He, X. Que, L. Zhou, M. Isobe, D. Huang, and H. Takagi, "Tunneling-tip-induced collapse of the charge gap in the excitonic insulator ${\mathrm{Ta}}_{2}{\mathrm{NiSe}}_{5}$", Physical Review Research **3**:3, L032074 (2021).

85. Y. F. Lu, H. Kono, T. I. Larkin, A. W. Rost, T. Takayama, A. V. Boris, B. Keimer, and H. Takagi, "Zero-gap semiconductor to excitonic insulator transition in Ta2NiSe5", Nature Communications **8**:1, 14408 (2017).

86. K. Kim, H. Kim, J. Kim, C. Kwon, J. S. Kim, and B. J. Kim, "Direct observation of excitonic instability in Ta2NiSe5", Nature Communications **12**:1, 1969 (2021).

87. H. Cercellier, C. Monney, F. Clerc, C. Battaglia, L. Despont, M. G. Garnier, H. Beck, P. Aebi, L. Patthey, H. Berger, and L. Forró, "Evidence for an Excitonic Insulator Phase in $1T\mathrm{\text{\ensuremath{-}}}{\mathrm{TiSe}}_{2}$", Physical Review Letters **99**:14, 146403 (2007).

88. A. Kogar, M. S. Rak, S. Vig, A. A. Husain, F. Flicker, Y. I. Joe, L. Venema, G. J. MacDougall, T. C. Chiang, E. Fradkin, J. van Wezel, and P. Abbamonte, "Signatures of exciton condensation in a transition metal dichalcogenide", Science **358**:6368, 1314–1317 (2017).

89. K. Rossnagel, "On the origin of charge-density waves in select layered transition-metal dichalcogenides", Journal of Physics: Condensed Matter **23**:21, 213001 (2011).

90. C. Comte and P. Nozières, "Exciton Bose condensation : the ground state of an electron-hole gas - I. Mean field description of a simplified model", Journal de Physique **43**:7, 1069–1081 (1982).

91. L. Windgätter, M. Rösner, G. Mazza, H. Hübener, A. Georges, A. J. Millis, S. Latini, and A. Rubio, "Common microscopic origin of the phase transitions in Ta2NiS5 and the excitonic insulator candidate Ta2NiSe5", npj Computational Materials **7**:1, 1–14 (2021).

92. E. Baldini, A. Zong, D. Choi, C. Lee, M. H. Michael, L. Windgaetter, I. I. Mazin, S. Latini, D. Azoury, B. Lv, A. Kogar, Y. Su, Y. Wang, Y. Lu, T. Takayama, H. Takagi, A. J. Millis, A. Rubio, E. Demler, and N. Gedik, "The spontaneous symmetry breaking in ta2nise5 is structural in nature", Proceedings of the National Academy of Sciences **120**:17, e2221688120 (2023).

93. P. B. Littlewood and X. Zhu, "Possibilities for exciton condensation in semiconductor quantum-well structures", Physica Scripta **T68**, 56–67 (1996).

94. S. Gupta, A. Kutana, and B. I. Yakobson, "Heterobilayers of 2D materials as a platform for excitonic superfluidity", Nature Communications **11**:1, 2989 (2020).

95. Y. H. Kwan, T. Devakul, S. L. Sondhi, and S. A. Parameswaran, "Theory of competing excitonic orders in insulating ${\mathrm{WTe}}_{2}$ monolayers", Physical Review B **104**:12, 125133 (2021).

96. J. Lee, C.-J. Kang, M. J. Eom, J. S. Kim, B. I. Min, and H. W. Yeom, "Strong interband interaction in the excitonic insulator phase of ${\mathrm{Ta}}_{2}{\mathrm{NiSe}}_{5}$", Physical Review B **99**:7, 075408 (2019).

97. M. Xie and A. H. MacDonald, "Electrical Reservoirs for Bilayer Excitons", Physical Review Letters **121**:6, 067702 (2018).

98. Y. Zeng and A. H. MacDonald, "Electrically controlled two-dimensional electron-hole fluids", Physical Review B **102**:8, 085154 (2020).

99. R. Qi, A. Y. Joe, Z. Zhang, J. Xie, Q. Feng, Z. Lu, Z. Wang, T. Taniguchi, K. Watanabe, S. Tongay, and F. Wang, *Perfect coulomb drag and exciton transport in an excitonic insulator*, (26, 2023) `http://arxiv.org/abs/2309.15357` (visited on 04/17/2024), pre-published.

100. P. X. Nguyen, L. Ma, R. Chaturvedi, K. Watanabe, T. Taniguchi, J. Shan, and K. F. Mak, *Perfect coulomb drag in a dipolar excitonic insulator*, (26, 2023) `http://arxiv.org/abs/2309.14940` (visited on 04/17/2024), pre-published.

101. J. Eisenstein, "Exciton Condensation in Bilayer Quantum Hall Systems", Annual Review of Condensed Matter Physics **5**:1, 159–181 (2014).

102. D. Nandi, A. D. K. Finck, J. P. Eisenstein, L. N. Pfeiffer, and K. W. West, "Exciton condensation and perfect Coulomb drag", Nature **488**:7412, 481–484 (2012).

103. M. Kellogg, J. P. Eisenstein, L. N. Pfeiffer, and K. W. West, "Vanishing Hall Resistance at High Magnetic Field in a Double-Layer Two-Dimensional Electron System", Physical Review Letters **93**:3, 036801 (2004).

104. E. Tutuc, M. Shayegan, and D. A. Huse, "Counterflow Measurements in Strongly Correlated GaAs Hole Bilayers: Evidence for Electron-Hole Pairing", Physical Review Letters **93**:3, 036802 (2004).

105. X. Liu, G. Farahi, C.-L. Chiu, Z. Papic, K. Watanabe, T. Taniguchi, M. P. Zaletel, and A. Yazdani, "Visualizing Broken Symmetry and Topological Defects in a Quantum Hall Ferromagnet", 23, 2021.

106. H. Kim, Y. Choi, É. Lantagne-Hurtubise, C. Lewandowski, A. Thomson, L. Kong, H. Zhou, E. Baum, Y. Zhang, L. Holleis, K. Watanabe, T. Taniguchi, A. F. Young, J. Alicea, and S. Nadj-Perge, "Imaging inter-valley coherent order in magic-angle twisted trilayer graphene", Nature, 1–7 (2023).

107. K. P. Nuckolls, R. L. Lee, M. Oh, D. Wong, T. Soejima, J. P. Hong, D. Călugăru, J. Herzog-Arbeitman, B. A. Bernevig, K. Watanabe, T. Taniguchi, N. Regnault, M. P. Zaletel, and A. Yazdani, "Quantum textures of the many-body wavefunctions in magic-angle graphene", Nature **620**:7974, 525–532 (2023).

108. D. Călugăru, N. Regnault, M. Oh, K. P. Nuckolls, D. Wong, R. L. Lee, A. Yazdani, O. Vafek, and B. A. Bernevig, "Spectroscopy of Twisted Bilayer Graphene Correlated Insulators", 28, 2021.

109. J. P. Hong, T. Soejima, and M. P. Zaletel, "Detecting symmetry breaking in magic angle graphene using scanning tunneling microscopy", 27, 2021.

110. Y. H. Kwan, G. Wagner, T. Soejima, M. P. Zaletel, S. H. Simon, S. A. Parameswaran, and N. Bultinck, "Kekul\'e Spiral Order at All Nonzero Integer Fillings in Twisted Bilayer Graphene", Physical Review X **11**:4, 041063 (2021).

111. R. Maezono, P. López Ríos, T. Ogawa, and R. J. Needs, "Excitons and biexcitons in symmetric electron-hole bilayers", Physical Review Letters **110**:21, 216407 (2013).

112. S. De Palo, F. Rapisarda, and G. Senatore, "Excitonic Condensation in a Symmetric Electron-Hole Bilayer", Physical Review Letters **88**:20, 206401 (2002).

113. X. Zhu, P. B. Littlewood, M. S. Hybertsen, and T. M. Rice, "Exciton Condensate in Semiconductor Quantum Well Structures", Physical Review Letters **74**:9, 1633–1636 (1995).

114. M. M. Fogler, L. V. Butov, and K. S. Novoselov, "High-temperature superfluidity with indirect excitons in van der Waals heterostructures", Nature Communications **5**:1, 4555 (2014).

115. V. Fock, "Näherungsmethode zur Lösung des quantenmechanischen Mehrkörperproblems", Zeitschrift für Physik **61**:1, 126–148 (1930).

116. T. Koopmans, "Über die Zuordnung von Wellenfunktionen und Eigenwerten zu den Einzelnen Elektronen Eines Atoms", Physica **1**:1, 104–113 (1934).

117. S. De Palo, F. Tramonto, S. Moroni, and G. Senatore, "Quadriexcitons and excitonic condensate in a symmetric electron-hole bilayer with valley degeneracy", Physical Review B **107**:4, L041409 (2023).

118. R. M. Lee, N. D. Drummond, and R. J. Needs, "Exciton-exciton interaction and biexciton formation in bilayer systems", Physical Review B **79**:12, 125308 (2009).

119. C. Schindler and R. Zimmermann, "Analysis of the exciton-exciton interaction in semiconductor quantum wells", Physical Review B **78**:4, 045313 (2008).

120. L. V. Keldysh, "The electron-hole liquid in semiconductors", Contemporary Physics **27**:5, 395–428 (1986).

121. Y. Lozovik and O. Berman, "Phase transitions in a system of two coupled quantum wells", JETP Letters **64**, 573–579 (1996).

122. D. Neilson, A. Perali, and A. R. Hamilton, "Excitonic superfluidity and screening in electron-hole bilayer systems", Physical Review B **89**:6, 060502 (2014).

123. P. López Ríos, A. Perali, R. J. Needs, and D. Neilson, "Evidence from Quantum Monte Carlo Simulations of Large-Gap Superfluidity and BCS-BEC Crossover in Double Electron-Hole Layers", Physical Review Letters **120**:17, 177701 (2018).

124. F. Pascucci, S. Conti, A. Perali, J. Tempere, and D. Neilson, *Effects of intra-layer correlations on electron-hole double-layer superfluidity*, (18, 2023) `http://arxiv.org/abs/2310.12117` (visited on 01/22/2024), pre-published.

125. A. Perali, D. Neilson, and A. R. Hamilton, "High-Temperature Superfluidity in Double-Bilayer Graphene", Physical Review Letters **110**:14, 146803 (2013).

126. F.-C. Wu, F. Xue, and A. H. MacDonald, "Theory of two-dimensional spatially indirect equilibrium exciton condensates", Physical Review B **92**:16, 165121 (2015).

127. Z. Zhang, J. Xie, W. Zhao, R. Qi, C. Sanborn, S. Wang, S. Kahn, K. Watanabe, T. Taniguchi, A. Zettl, M. Crommie, and F. Wang, "Engineering correlated insulators in bilayer graphene with a remote coulomb superlattice", Nature Materials, 1–7 (2024).

128. X. Zhu, M. S. Hybertsen, and P. B. Littlewood, "Electron-hole system revisited: A variational quantum Monte Carlo study", Physical Review B **54**:19, 13575–13580 (1996).

129. K. Asano and T. Yoshioka, "Exciton–Mott Physics in Two-Dimensional Electron–Hole Systems: Phase Diagram and Single-Particle Spectra", Journal of the Physical Society of Japan **83**:8, 084702 (2014).

130. H. Ochoa, "Strain-induced excitonic instability in twisted bilayer graphene", Physical Review B **102**:20, 201107 (2020).

131. G. Shavit, E. Berg, A. Stern, and Y. Oreg, "Theory of Correlated Insulators and Superconductivity in Twisted Bilayer Graphene", Physical Review Letters **127**:24, 247703 (2021).

132. J. S. Hofmann, E. Khalaf, A. Vishwanath, E. Berg, and J. Y. Lee, "Fermionic Monte Carlo Study of a Realistic Model of Twisted Bilayer Graphene", Physical Review X **12**:1, 011061 (2022).

133. J. Yu, B. A. Foutty, Y. H. Kwan, M. E. Barber, K. Watanabe, T. Taniguchi, Z.-X. Shen, S. A. Parameswaran, and B. E. Feldman, "Spin skyrmion gaps as signatures of strong-coupling insulators in magic-angle twisted bilayer graphene", Nature Communications **14**:1, 6679 (2023).

134. P. W. Anderson, "Theory of dirty superconductors", Journal of Physics and Chemistry of Solids **11**:1, 26–30 (1959).

135. K. Maki, "Gapless Superconductivity", in *Superconductivity*, Routledge, 1969.

136. E. I. Timmons, S. Teknowijoyo, M. Kończykowski, O. Cavani, M. A. Tanatar, S. Ghimire, K. Cho, Y. Lee, L. Ke, N. H. Jo, S. L. Bud'ko, P. C. Canfield, P. P. Orth, M. S. Scheurer, and R. Prozorov, "Electron irradiation effects on superconductivity in ${\mathrm{PdTe}}_{2}$: An application of a generalized Anderson theorem", Physical Review Research **2**:2, 023140 (2020).

137. L. Andersen, A. Ramires, Z. Wang, T. Lorenz, and Y. Ando, "Generalized Anderson's theorem for superconductors derived from topological insulators", Science Advances **6**:9, eaay6502 (2020).

138. L. Yu, "Bound State in Superconductors With Paramagnetic Impurities", Acta Phys. Sin. **Vol: 21** (1965).

139. H. Shiba, "Classical Spins in Superconductors", Progress of Theoretical Physics **40**:3, 435–451 (1968).

140. A. I. Rusinov, "On the Theory of Gapless Superconductivity in Alloys Containing Paramagnetic Impurities", Soviet Journal of Experimental and Theoretical Physics **29**, 1101 (1969).

141. A. V. Balatsky, I. Vekhter, and J.-X. Zhu, "Impurity-induced states in conventional and unconventional superconductors", Reviews of Modern Physics **78**:2, 373–433 (2006).

142. M. Xie and A. H. MacDonald, "On the nature of the correlated insulator states in twisted bilayer graphene", Physical Review Letters **124**:9, 097601 (2020).

143. S. Liu, E. Khalaf, J. Y. Lee, and A. Vishwanath, "Nematic topological semimetal and insulator in magic angle bilayer graphene at charge neutrality", Physical Review Research **3**:1, 013033 (2021).

144. H. C. Po, L. Zou, A. Vishwanath, and T. Senthil, "Origin of Mott Insulating Behavior and Superconductivity in Twisted Bilayer Graphene", Physical Review X **8**:3, 031089 (2018).

145. B. Lian, Z.-D. Song, N. Regnault, D. K. Efetov, A. Yazdani, and B. A. Bernevig, "TBG IV: Exact Insulator Ground States and Phase Diagram of Twisted Bilayer Graphene", Physical Review B **103**:20, 205414 (2021).

146. Z. Bi, N. F. Q. Yuan, and L. Fu, "Designing flat bands by strain", Physical Review B **100**:3, 035448 (2019).

147. D. E. Parker, T. Soejima, J. Hauschild, M. P. Zaletel, and N. Bultinck, "Strain-induced quantum phase transitions in magic angle graphene", Physical Review Letters **127**:2, 027601 (2021).

148. L. Balents, "General continuum model for twisted bilayer graphene and arbitrary smooth deformations", SciPost Physics **7**:4, 048 (2019).

149. A. Abrikosov and L. Gor'kov, "On the Theory of Superconducting Alloys; I. The Electrodynamics of Alloys at Absolute Zero", JETP **8**:6, 1090 (1959).

150. P. J. Ledwith, E. Khalaf, Z. Zhu, S. Carr, E. Kaxiras, and A. Vishwanath, "TB or not TB? Contrasting properties of twisted bilayer graphene and the alternating twist n-layer structures ($n=3, 4, 5, \dots$)", 23, 2021.

151. T. Cea and F. Guinea, "Band structure and insulating states driven by Coulomb interaction in twisted bilayer graphene", Physical Review B **102**:4, 045107 (2020).

152. A. Pierret, D. Mele, H. Graef, J. Palomo, T. Taniguchi, K. Watanabe, Y. Li, B. Toury, C. Journet, P. Steyer, V. Garnier, A. Loiseau, J.-M. Berroir, E. Bocquillon, G. Fève, C. Voisin, E. Baudin, M. Rosticher, and B. Plaçais, "Dielectric permittivity, conductivity and breakdown field of hexagonal boron nitride", Materials Research Express **9**:6, 065901 (2022).

153. U. Zondiner, A. Rozen, D. Rodan-Legrain, Y. Cao, R. Queiroz, T. Taniguchi, K. Watanabe, Y. Oreg, F. von Oppen, A. Stern, E. Berg, P. Jarillo-Herrero, and S. Ilani, "Cascade of phase transitions and dirac revivals in magic-angle graphene", Nature **582**:7811, 203–208 (2020).

154. D. Wong, K. P. Nuckolls, M. Oh, B. Lian, Y. Xie, S. Jeon, K. Watanabe, T. Taniguchi, B. A. Bernevig, and A. Yazdani, "Cascade of electronic transitions in magic-angle twisted bilayer graphene", Nature **582**:7811, 198–202 (2020).

155. J. Kang, B. A. Bernevig, and O. Vafek, "Cascades between Light and Heavy Fermions in the Normal State of Magic-Angle Twisted Bilayer Graphene", Physical Review Letters **127**:26, 266402 (2021).

156. M. Xie and A. H. MacDonald, "Weak-Field Hall Resistivity and Spin-Valley Flavor Symmetry Breaking in Magic-Angle Twisted Bilayer Graphene", Physical Review Letters **127**:19, 196401 (2021).

157. A. Datta, M. J. Calderón, A. Camjayi, and E. Bascones, *Heavy quasiparticles and cascades without symmetry breaking in twisted bilayer graphene*, (30, 2023) `http://arxiv.org/abs/2301.13024` (visited on 04/22/2023), pre-published.

158. R. Polski, Y. Zhang, Y. Peng, H. S. Arora, Y. Choi, H. Kim, K. Watanabe, T. Taniguchi, G. Refael, F. von Oppen, and S. Nadj-Perge, *Hierarchy of symmetry breaking correlated phases in twisted bilayer graphene*, (10, 2022) `http://arxiv.org/abs/2205.05225` (visited on 07/17/2022), pre-published.

159. F. Guinea and N. R. Walet, "Electrostatic effects, band distortions, and superconductivity in twisted graphene bilayers", Proceedings of the National Academy of Sciences **115**:52, 13174–13179 (2018).

160. T. Cea, N. R. Walet, and F. Guinea, "Electronic band structure and pinning of Fermi energy to Van Hove singularities in twisted bilayer graphene: A self-consistent approach", Physical Review B **100**:20, 205113 (2019).

161. L. Rademaker, D. A. Abanin, and P. Mellado, "Charge smoothening and band flattening due to Hartree corrections in twisted bilayer graphene", Physical Review B **100**:20, 205114 (2019).

162. Z. A. H. Goodwin, V. Vitale, X. Liang, A. A. Mostofi, and J. Lischner, "Hartree theory calculations of quasiparticle properties in twisted bilayer graphene", Electronic Structure **2**:3, 034001 (2020).

163. P. A. Pantaleón, T. Cea, R. Brown, N. R. Walet, and F. Guinea, "Narrow bands, electrostatic interactions and band topology in graphene stacks", 2D Materials **8**:4, 044006 (2021).

164. T. Cea, P. A. Pantaleón, N. R. Walet, and F. Guinea, "Electrostatic interactions in twisted bilayer graphene", Nano Materials Science, Special Issue on Graphene and 2D Alternative Materials **4**:1, 27–35 (2022).

165. F. Xie, N. Regnault, D. Călugăru, B. A. Bernevig, and B. Lian, "Twisted symmetric trilayer graphene. II. Projected Hartree-Fock study", Physical Review B **104**:11, 115167 (2021).

166. M. Christos, S. Sachdev, and M. S. Scheurer, "Correlated Insulators, Semimetals, and Superconductivity in Twisted Trilayer Graphene", Physical Review X **12**:2, 021018 (2022).

167. G. Wagner, Y. H. Kwan, N. Bultinck, S. H. Simon, and S. A. Parameswaran, "Global phase diagram of the normal state of twisted bilayer graphene", Physical Review Letters **128**:15, 156401 (2022).

168. W. Qin and A. H. MacDonald, "In-Plane Critical Magnetic Fields in Magic-Angle Twisted Trilayer Graphene", Physical Review Letters **127**:9, 097001 (2021).

169. F. Guinea, "Charge distribution and screening in layered graphene systems", Physical Review B **75**:23, 235433 (2007).

170. A. Ghazaryan, T. Holder, E. Berg, and M. Serbyn, "Multilayer graphenes as a platform for interaction-driven physics and topological superconductivity", Physical Review B **107**:10, 104502 (2023).

171. A. Laturia, M. L. Van de Put, and W. G. Vandenberghe, "Dielectric properties of hexagonal boron nitride and transition metal dichalcogenides: from monolayer to bulk", npj 2D Materials and Applications **2**:1, 1–7 (2018).

172. J. Kang and O. Vafek, "Strong Coupling Phases of Partially Filled Twisted Bilayer Graphene Narrow Bands", Physical Review Letters **122**:24, 246401 (2019).

173. B. Wunsch, T. Stauber, F. Sols, and F. Guinea, "Dynamical polarization of graphene at finite doping", New Journal of Physics **8**:12, 318 (2006).

174. E. H. Hwang and S. Das Sarma, "Dielectric function, screening, and plasmons in two-dimensional graphene", Physical Review B **75**:20, 205418 (2007).

175. P. Potasz, M. Xie, and A. H. MacDonald, "Exact Diagonalization for Magic-Angle Twisted Bilayer Graphene", Physical Review Letters **127**:14, 147203 (2021).

176. F. Xie, A. Cowsik, Z.-D. Song, B. Lian, B. A. Bernevig, and N. Regnault, "TBG VI: An Exact Diagonalization Study of Twisted Bilayer Graphene at Non-Zero Integer Fillings", Physical Review B **103**:20, 205416 (2021).

177. T. Wang, D. E. Parker, T. Soejima, J. Hauschild, S. Anand, N. Bultinck, and M. P. Zaletel, *Kekulé spiral order in magic-angle graphene: a density matrix renormalization group study*, (26, 2022) `http://arxiv.org/abs/2211.02693` (visited on 11/21/2023), pre-published.

178. N. P. Kazmierczak, M. Van Winkle, C. Ophus, K. C. Bustillo, S. Carr, H. G. Brown, J. Ciston, T. Taniguchi, K. Watanabe, and D. K. Bediako, "Strain fields in twisted bilayer graphene", Nature Materials **20**:7, 956–963 (2021).

179. Y. Xie, B. Lian, B. Jäck, X. Liu, C.-L. Chiu, K. Watanabe, T. Taniguchi, B. A. Bernevig, and A. Yazdani, "Spectroscopic signatures of many-body correlations in magic-angle twisted bilayer graphene", Nature **572**:7767, 101–105 (2019).

180. Y. Jiang, X. Lai, K. Watanabe, T. Taniguchi, K. Haule, J. Mao, and E. Y. Andrei, "Charge order and broken rotational symmetry in magic-angle twisted bilayer graphene", Nature **573**:7772, 91–95 (2019).

181. A. Kerelsky, L. J. McGilly, D. M. Kennes, L. Xian, M. Yankowitz, S. Chen, K. Watanabe, T. Taniguchi, J. Hone, C. Dean, A. Rubio, and A. N. Pasupathy, "Maximized electron interactions at the magic angle in twisted bilayer graphene", Nature **572**:7767, 95–100 (2019).

182. Y. Choi, J. Kemmer, Y. Peng, A. Thomson, H. Arora, R. Polski, Y. Zhang, H. Ren, J. Alicea, G. Refael, F. von Oppen, K. Watanabe, T. Taniguchi, and S. Nadj-Perge, "Electronic correlations in twisted bilayer graphene near the magic angle", Nature Physics **15**:11, 1174–1180 (2019).

183. Z.-D. Song and B. A. Bernevig, "Magic-angle twisted bilayer graphene as a topological heavy fermion problem", Physical Review Letters **129**:4, 047601 (2022).

184. M. J. Klug, "Charge order and Mott insulating ground states in small-angle twisted bilayer graphene", New Journal of Physics **22**:7, 073016 (2020).

185. S. Carr, S. Fang, Z. Zhu, and E. Kaxiras, "Exact continuum model for low-energy electronic states of twisted bilayer graphene", Physical Review Research **1**:1, 013001 (2019).

186. H. Zhou, L. Holleis, Y. Saito, L. Cohen, W. Huynh, C. L. Patterson, F. Yang, T. Taniguchi, K. Watanabe, and A. F. Young, "Isospin magnetism and spin-triplet superconductivity in Bernal bilayer graphene", 30, 2021.

187. S. C. de la Barrera, S. Aronson, Z. Zheng, K. Watanabe, T. Taniguchi, Q. Ma, P. Jarillo-Herrero, and R. Ashoori, "Cascade of isospin phase transitions in Bernal bilayer graphene at zero magnetic field", 26, 2021.

188. Y. Zhang, R. Polski, A. Thomson, É. Lantagne-Hurtubise, C. Lewandowski, H. Zhou, K. Watanabe, T. Taniguchi, J. Alicea, and S. Nadj-Perge, *Spin-orbit enhanced superconductivity in bernal bilayer graphene*, (10, 2022) `http://arxiv.org/abs/2205.05087` (visited on 06/15/2022), pre-published.

189. Z. Lu, T. Han, Y. Yao, J. Yang, J. Seo, L. Shi, S. Ye, K. Watanabe, T. Taniguchi, and L. Ju, *Extended quantum anomalous hall states in graphene/hbn moiré superlattices*, (19, 2024) `http://arxiv.org/abs/2408.10203` (visited on 08/20/2024), pre-published.

190. D. Waters, A. Okounkova, R. Su, B. Zhou, J. Yao, K. Watanabe, T. Taniguchi, X. Xu, Y.-H. Zhang, J. Folk, and M. Yankowitz, *Interplay of electronic crystals with integer and fractional chern insulators in moiré pentalayer graphene*, (19, 2024) `http://arxiv.org/abs/2408.10133` (visited on 08/26/2024), pre-published.

191. X. Liu, Z. Hao, E. Khalaf, J. Y. Lee, Y. Ronen, H. Yoo, D. Haei Najafabadi, K. Watanabe, T. Taniguchi, A. Vishwanath, and P. Kim, "Tunable spin-polarized correlated states in twisted double bilayer graphene", Nature **583**:7815, 221–225 (2020).

192. M. Kuiri, C. Coleman, Z. Gao, A. Vishnuradhan, K. Watanabe, T. Taniguchi, J. Zhu, A. H. MacDonald, and J. Folk, "Spontaneous time-reversal symmetry breaking in twisted double bilayer graphene", Nature Communications **13**:1, 6468 (2022).

193. R. Su, D. Waters, B. Zhou, K. Watanabe, T. Taniguchi, Y.-H. Zhang, M. Yankowitz, and J. Folk, *Generalized anomalous hall crystals in twisted bilayer-trilayer graphene*, (25, 2024) http://arxiv.org/abs/2406.17766 (visited on 06/28/2024), pre-published.

194. S. Xu, M. M. Al Ezzi, N. Balakrishnan, A. Garcia-Ruiz, B. Tsim, C. Mullan, J. Barrier, N. Xin, B. A. Piot, T. Taniguchi, K. Watanabe, A. Carvalho, A. Mishchenko, A. K. Geim, V. I. Fal'ko, S. Adam, A. H. C. Neto, K. S. Novoselov, and Y. Shi, "Tunable van Hove singularities and correlated states in twisted monolayer–bilayer graphene", Nature Physics **17**:5, 619–626 (2021).

195. Y. Choi, Y. Choi, M. Valentini, C. L. Patterson, L. F. W. Holleis, O. I. Sheekey, H. Stoyanov, X. Cheng, T. Taniguchi, K. Watanabe, and A. F. Young, *Electric field control of superconductivity and quantized anomalous Hall effects in rhombohedral tetralayer graphene*, (22, 2024) http://arxiv.org/abs/2408.12584 (visited on 10/30/2024), pre-published.

196. K. P. Nuckolls, M. Oh, D. Wong, B. Lian, K. Watanabe, T. Taniguchi, B. A. Bernevig, and A. Yazdani, "Strongly correlated Chern insulators in magic-angle twisted bilayer graphene", Nature **588**:7839, 610–615 (2020).

197. U. Zondiner, A. Rozen, D. Rodan-Legrain, Y. Cao, R. Queiroz, T. Taniguchi, K. Watanabe, Y. Oreg, F. von Oppen, A. Stern, E. Berg, P. Jarillo-Herrero, and S. Ilani, "Cascade of phase transitions and Dirac revivals in magic-angle graphene", Nature **582**:7811, 203–208 (2020).

198. J. Herzog-Arbeitman, Y. Wang, J. Liu, P. M. Tam, Z. Qi, Y. Jia, D. K. Efetov, O. Vafek, N. Regnault, H. Weng, Q. Wu, B. A. Bernevig, and J. Yu, *Moiré fractional chern insulators ii: first-principles calculations and continuum models of rhombohedral graphene superlattices*, (21, 2023) http://arxiv.org/abs/2311.12920 (visited on 01/06/2024), pre-published.

199. D. Waters, D. Waleffe, E. Thompson, E. Arreguin-Martinez, J. Fonseca, T. Poirier, J. H. Edgar, K. Watanabe, T. Taniguchi, X. Xu, D. Cobden, and M. Yankowitz, *On the origin of anomalous hysteresis in graphite/boron nitride transistors*, (3, 2024) http://arxiv.org/abs/2410.02699 (visited on 10/04/2024), pre-published.

200. L. Chen, H. Long, H. Wu, R. Mei, Z. Su, M. Feng, J.-B. Wu, K. Watanabe, T. Taniguchi, X. Cao, Z. Wei, P.-H. Tan, and Y. Shi, *Anomalous gate-tunable capacitance in graphene moiré heterostructures*, arXiv.org, (7, 2024) https://arxiv.org/abs/2405.03976v1 (visited on 10/04/2024).

201. D. Zhai and W. Yao, "Theory of tunable flux lattices in the homobilayer moiré of twisted and uniformly strained transition metal dichalcogenides", Physical Review Materials **4**:9, 094002 (2020).

202. N. Morales-Durán, N. Wei, J. Shi, and A. H. MacDonald, "Magic angles and fractional chern insulators in twisted homobilayer transition metal dichalcogenides", Physical Review Letters **132**:9, 096602 (2024).

203. R. Roy, "Band geometry of fractional topological insulators", Physical Review B **90**:16, 165139 (2014).

204. J. Wang, J. Cano, A. J. Millis, Z. Liu, and B. Yang, "Exact landau level description of geometry and interaction in a flatband", Physical Review Letters **127**:24, 246403 (2021).

205. P. J. Ledwith, G. Tarnopolsky, E. Khalaf, and A. Vishwanath, "Fractional chern insulator states in twisted bilayer graphene: an analytical approach", Physical Review Research **2**:2, 023237 (2020).

206. A. Abouelkomsan, K. Yang, and E. J. Bergholtz, "Quantum metric induced phases in moiré materials", Physical Review Research **5**:1, L012015 (2023).

207. M. Fujimoto, D. E. Parker, J. Dong, E. Khalaf, A. Vishwanath, and P. Ledwith, *Higher vortexability: zero field realization of higher landau levels*, (29, 2024) http://arxiv.org/abs/2403.00856 (visited on 03/13/2024), pre-published.

208. Z. Liu, B. Mera, M. Fujimoto, T. Ozawa, and J. Wang, *Theory of generalized landau levels and implication for non-abelian states*, (23, 2024) http://arxiv.org/abs/2405.14479 (visited on 05/24/2024), pre-published.

209. J. Wang, S. Klevtsov, and Z. Liu, "Origin of model fractional chern insulators in all topological ideal flatbands: explicit color-entangled wave function and exact density algebra", Physical Review Research **5**:2, 023167 (2023).

210. B. Estienne, N. Regnault, and V. Crépel, "Ideal chern bands as landau levels in curved space", Physical Review Research **5**:3, L032048 (2023).

211. B. Li and F. Wu, *Variational mapping of chern bands to landau levels: application to fractional chern insulators in twisted mote$_2$*, (30, 2024) http://arxiv.org/abs/2405.20307 (visited on 05/31/2024), pre-published.

212. C.-E. Ahn, W. Lee, K. Yananose, Y. Kim, and G. Y. Cho, *First landau level physics in second moiré band of 2.1° twisted bilayer mote$_2$*, (28, 2024) http://arxiv.org/abs/2403.19155 (visited on 04/09/2024), pre-published.

213. C. Wang, X.-W. Zhang, X. Liu, J. Wang, T. Cao, and D. Xiao, *Higher landau-level analogues and signatures of non-abelian states in twisted bilayer mote$_2$*, (8, 2024) http://arxiv.org/abs/2404.05697 (visited on 04/09/2024), pre-published.

214. A. P. Reddy, N. Paul, A. Abouelkomsan, and L. Fu, *Non-abelian fractionalization in topological minibands*, (19, 2024) http://arxiv.org/abs/2403.00059 (visited on 04/05/2024), pre-published.

215. C. Xu, N. Mao, T. Zeng, and Y. Zhang, *Multiple chern bands in twisted mote$_2$ and possible non-abelian states*, (25, 2024) http://arxiv.org/abs/2403.17003 (visited on 04/05/2024), pre-published.

216. X.-W. Zhang, C. Wang, X. Liu, Y. Fan, T. Cao, and D. Xiao, *Polarization-driven band topology evolution in twisted mote$_2$ and wse$_2$*, (27, 2024) http://arxiv.org/abs/2311.12776 (visited on 04/03/2024), pre-published.

217. F. Zhang, N. Morales-Durán, Y. Li, W. Yao, J.-J. Su, Y.-C. Lin, C. Dong, H. Kim, J. A. Robinson, A. H. Macdonald, and C.-K. Shih, *Direct observation of layer skyrmions in twisted WSe2 bilayers*, (28, 2024) http://arxiv.org/abs/2406.20036 (visited on 10/17/2024), pre-published.

218. D. R. Hofstadter, "Energy levels and wave functions of bloch electrons in rational and irrational magnetic fields", Physical Review B **14**:6, 2239–2249 (1976).

219. C. R. Dean, L. Wang, P. Maher, C. Forsythe, F. Ghahari, Y. Gao, J. Katoch, M. Ishigami, P. Moon, M. Koshino, T. Taniguchi, K. Watanabe, K. L. Shepard, J. Hone, and P. Kim, "Hofstadter's butterfly and the fractal quantum hall effect in moiré superlattices", Nature **497**:7451, 598–602 (2013).

220. J. Yu, B. A. Foutty, Z. Han, M. E. Barber, Y. Schattner, K. Watanabe, T. Taniguchi, P. Phillips, Z.-X. Shen, S. A. Kivelson, and B. E. Feldman, "Correlated hofstadter spectrum and flavour phase diagram in magic-angle twisted bilayer graphene", Nature Physics (2022).

221. Y. Saito, J. Ge, L. Rademaker, K. Watanabe, T. Taniguchi, D. A. Abanin, and A. F. Young, "Hofstadter subband ferromagnetism and symmetry broken chern insulators in twisted bilayer graphene", Nature Physics **17**:4, 478–481 (2021).

222. I. Das, C. Shen, A. Jaoui, J. Herzog-Arbeitman, A. Chew, C.-W. Cho, K. Watanabe, T. Taniguchi, B. A. Piot, B. A. Bernevig, and D. K. Efetov, "Observation of reentrant correlated insulators and interaction-driven fermi-surface reconstructions at one magnetic flux quantum per moiré unit cell in magic-angle twisted bilayer graphene", Physical Review Letters **128**:21, 217701 (2022).

223. C. R. Kometter, J. Yu, T. Devakul, A. P. Reddy, Y. Zhang, B. A. Foutty, K. Watanabe, T. Taniguchi, L. Fu, and B. E. Feldman, "Hofstadter states and re-entrant charge order in a semiconductor moiré lattice", Nature Physics **19**:12, 1861–1867 (2023).

224. R. Bistritzer and A. H. MacDonald, "Moiré butterflies in twisted bilayer graphene", Physical Review B **84**:3, 035440 (2011).

225. K. Hejazi, C. Liu, and L. Balents, "Landau levels in twisted bilayer graphene and semiclassical orbits", Physical Review B **100**:3, 035115 (2019).

226. J. Herzog-Arbeitman, A. Chew, D. K. Efetov, and B. A. Bernevig, "Reentrant Correlated Insulators in Twisted Bilayer Graphene at 25 T ($2\ensuremath{\pi}$ Flux)", Physical Review Letters **129**:7, 076401 (2022).

227. Y. Sheffer and A. Stern, "Chiral magic-angle twisted bilayer graphene in a magnetic field: landau level correspondence, exact wave functions, and fractional chern insulators", Physical Review B **104**:12, L121405 (2021).

228. V. Crépel, N. Regnault, and R. Queiroz, "Chiral limit and origin of topological flat bands in twisted transition metal dichalcogenide homobilayers", Communications Physics **7**:1, 1–6 (2024).

229. B. T. Zhou, S. Egan, and M. Franz, "Moiré flat chern bands and correlated quantum anomalous hall states generated by spin-orbit couplings in twisted homobilayer MoS_2", Physical Review Research **4**:1, L012032 (2022).

230. Y. Jia, J. Yu, J. Liu, J. Herzog-Arbeitman, Z. Qi, H. Pi, N. Regnault, H. Weng, B. A. Bernevig, and Q. Wu, "Moiré fractional chern insulators. i. first-principles calculations and continuum models of twisted bilayer $MoTe_2$", Physical Review B **109**:20, 205121 (2024).

231. T. Wang, M. Wang, W. Kim, S. G. Louie, L. Fu, and M. P. Zaletel, *Topology, magnetism and charge order in twisted mote2 at higher integer hole fillings*, (19, 2023) `http://arxiv.org/abs/2312.12531` (visited on 06/03/2024), pre-published.

232. J. Yu, J. Herzog-Arbeitman, M. Wang, O. Vafek, B. A. Bernevig, and N. Regnault, "Fractional chern insulators versus nonmagnetic states in twisted bilayer $MoTe_2$", Physical Review B **109**:4, 045147 (2024).

233. B. Li, W.-X. Qiu, and F. Wu, "Electrically tuned topology and magnetism in twisted bilayer $MoTe_2$ at $\nu_h = 1$", Physical Review B **109**:4, L041106 (2024).

234. M. Wang, X. Wang, and O. Vafek, *Interacting phase diagram of twisted bilayer mote$_2$ in magnetic field*, (23, 2024) http://arxiv.org/abs/2405.14811 (visited on 05/24/2024), pre-published.

235. H. Li, U. Kumar, K. Sun, and S.-Z. Lin, "Spontaneous fractional Chern insulators in transition metal dichalcogenide moir\'e superlattices", Physical Review Research **3**:3, L032070 (2021).

236. V. Crépel and L. Fu, "Anomalous hall metal and fractional chern insulator in twisted transition metal dichalcogenides", Physical Review B **107**:20, L201109 (2023).

237. B. Andrews and A. Soluyanov, "Fractional quantum Hall states for moir\'e superstructures in the Hofstadter regime", Physical Review B **101**:23, 235312 (2020).

238. A. P. Reddy, F. Alsallom, Y. Zhang, T. Devakul, and L. Fu, "Fractional quantum anomalous hall states in twisted bilayer $MoTe_2$ and WSe_2", Physical Review B **108**:8, 085117 (2023).

239. C. Wang, X.-W. Zhang, X. Liu, Y. He, X. Xu, Y. Ran, T. Cao, and D. Xiao, "Fractional chern insulator in twisted bilayer $MoTe_2$", Physical Review Letters **132**:3, 036501 (2024).

240. N. Mao, C. Xu, J. Li, T. Bao, P. Liu, Y. Xu, C. Felser, L. Fu, and Y. Zhang, "Transfer learning relaxation, electronic structure and continuum model for twisted bilayer mote2", Communications Physics **7**:1, 1–7 (2024).

241. A. Abouelkomsan, Z. Liu, and E. J. Bergholtz, "Particle-Hole Duality, Emergent Fermi Liquids, and Fractional Chern Insulators in Moir\'e Flatbands", Physical Review Letters **124**:10, 106803 (2020).

242. F. D. M. Haldane, "Model for a quantum hall effect without landau levels: condensed-matter realization of the "parity anomaly"", Physical Review Letters **61**:18, 2015–2018 (1988).

243. J.-M. Hou and W.-X. Yang, "Next-nearest-neighbor-tunneling-induced symmetry breaking of hofstadter's butterfly spectrum for ultracold atoms on the honeycomb lattice", Physics Letters A **373**:31, 2774–2777 (2009).

244. J. Shi, N. Morales-Durán, E. Khalaf, and A. H. MacDonald, "Adiabatic approximation and aharonov-casher bands in twisted homobilayer transition metal dichalcogenides", Physical Review B **110**:3, 035130 (2024).

245. J. Wang, Y. Zheng, A. J. Millis, and J. Cano, "Chiral approximation to twisted bilayer graphene: Exact intravalley inversion symmetry, nodal structure, and implications for higher magic angles", Physical Review Research **3**:2, 023155 (2021).

246. V. Crépel and A. Millis, "Bridging the small and large in twisted transition metal dichalcogenide homobilayers: a tight binding model capturing orbital interference and topology across a wide range of twist angles", Physical Review Research **6**:3, 033127 (2024).

247. F. D. M. Haldane and E. H. Rezayi, "Periodic laughlin-jastrow wave functions for the fractional quantized hall effect", Physical Review B **31**:4, 2529–2531 (1985).

248. G. Murthy and R. Shankar, "Hamiltonian theories of the fractional quantum hall effect", Reviews of Modern Physics **75**:4, 1101–1158 (2003).

249. J. Herzog-Arbeitman, A. Chew, and B. A. Bernevig, "Magnetic bloch theorem and reentrant flat bands in twisted bilayer graphene at 2π flux", Physical Review B **106**:8, 085140 (2022).

250. X. Wang and O. Vafek, "Narrow bands in magnetic field and strong-coupling hofstadter spectra", Physical Review B **106**:12, L121111 (2022).

251. J. Ibañez-Azpiroz, A. Eiguren, A. Bergara, G. Pettini, and M. Modugno, "Breakdown of the peierls substitution for the haldane model with ultracold atoms", Physical Review A **90**:3, 033609 (2014).

252. P. Středa, "Theory of quantised hall conductivity in two dimensions", Journal of Physics C: Solid State Physics **15**:22, L717 (1982).

253. J. Herzog-Arbeitman, Z.-D. Song, N. Regnault, and B. A. Bernevig, "Hofstadter topology: noncrystalline topological materials at high flux", Physical Review Letters **125**:23, 236804 (2020).

254. N. Marzari and D. Vanderbilt, "Maximally localized generalized wannier functions for composite energy bands", Physical Review B **56**:20, 12847–12865 (1997).

255. S. Matsuura and S. Ryu, "Momentum space metric, nonlocal operator, and topological insulators", Physical Review B **82**:24, 245113 (2010).

256. M. S. M. de Sousa, A. L. Cruz, and W. Chen, "Mapping quantum geometry and quantum phase transitions to real space by a fidelity marker", Physical Review B **107**:20, 205133 (2023).

257. C. Fang, M. J. Gilbert, and B. A. Bernevig, "Bulk topological invariants in noninteracting point group symmetric insulators", Physical Review B **86**:11, 115112 (2012).

258. G. Möller and N. R. Cooper, "Fractional Chern Insulators in Harper-Hofstadter Bands with Higher Chern Number", Physical Review Letters **115**:12, 126401 (2015).

259. J. Dong, J. Wang, P. J. Ledwith, A. Vishwanath, and D. E. Parker, "Composite fermi liquid at zero magnetic field in twisted $MoTe_2$", Physical Review Letters **131**:13, 136502 (2023).

260. H. Goldman, A. P. Reddy, N. Paul, and L. Fu, "Zero-field composite fermi liquid in twisted semiconductor bilayers", Physical Review Letters **131**:13, 136501 (2023).

261. A. Stern and L. Fu, *Transport properties of a half-filled chern band at the electron and composite fermion phases*, (28, 2023) `http://arxiv.org/abs/2311.16761` (visited on 01/17/2024), pre-published.

262. T. Lu and L. H. Santos, *Fractional chern insulators in twisted bilayer mote$_2$: a composite fermion perspective*, (5, 2024) `http://arxiv.org/abs/2406.03530` (visited on 06/10/2024), pre-published.

263. C. Robert, H. Dery, L. Ren, D. Van Tuan, E. Courtade, M. Yang, B. Urbaszek, D. Lagarde, K. Watanabe, T. Taniguchi, T. Amand, and X. Marie, "Measurement of conduction and valence bands g-factors in a transition metal dichalcogenide monolayer", Physical Review Letters **126**:6, 067403 (2021).

264. F. K. Popov and A. Milekhin, "Hidden wave function of twisted bilayer graphene: the flat band as a landau level", Physical Review B **103**:15, 155150 (2021).

265. A. Datta, D. Guerci, M. O. Goerbig, and C. Mora, "Helical trilayer graphene in magnetic field: chern mosaic and higher chern number ideal flat bands", Physical Review B **110**:7, 075417 (2024).